

# UC Berkeley

## UC Berkeley Electronic Theses and Dissertations

### Title

Faint Coronal Hard X-rays From Accelerated Electrons in Solar Flares

### Permalink

<https://escholarship.org/uc/item/64k848ff>

### Author

Glesener, Lindsay Erin

### Publication Date

2012

Peer reviewed|Thesis/dissertation

**Faint Coronal Hard X-rays From Accelerated Electrons in Solar Flares**

by

Lindsay Erin Glesener

A dissertation submitted in partial satisfaction of the

requirements for the degree of

Doctor of Philosophy

in

Physics

in the

Graduate Division

of the

University of California, Berkeley

Committee in charge:

Professor Robert P. Lin, Co-chair  
Doctor Säm Krucker, Co-chair  
Professor Stuart D. Bale, Co-chair  
Professor Gibor Basri  
Professor Steven E. Boggs

Fall 2012

**Faint Coronal Hard X-rays From Accelerated Electrons in Solar Flares**

Copyright 2012  
by  
Lindsay Erin Glesener

## Abstract

Faint Coronal Hard X-rays From Accelerated Electrons in Solar Flares

by

Lindsay Erin Glesener

Doctor of Philosophy in Physics

University of California, Berkeley

Professor Robert P. Lin, Co-chair

Doctor Säm Krucker, Co-chair

Professor Stuart D. Bale, Co-chair

Solar flares are huge explosions on the Sun that release a tremendous amount of energy from the coronal magnetic field, up to  $10^{33}$  ergs, in a short time (100–1000 seconds), with much of the energy going into accelerated electrons and ions. An efficient acceleration mechanism is needed, but the details of this mechanism remain relatively unknown. A fraction of this explosive energy reaches the Earth in the form of energetic particles, producing geomagnetic storms and posing dangers to spaceborne instruments, astronauts, and Earthbound power grids. There are thus practical reasons, as well as intellectual ones, for wishing to understand this extraordinary form of energy release.

Through imaging spectroscopy of the hard X-ray (HXR) emission from solar flares, the behavior of flare-accelerated electrons can be studied. The *Reuven Ramaty High Energy Solar Spectroscopic Imager (RHESSI)* spacecraft launched in 2002 with the goal of better understanding flare particle acceleration. Using rotation modulation collimators, *RHESSI* is able to cover a wide energy range (3 keV–17 MeV) with fine angular and energy resolutions. *RHESSI*'s success in the last 10 years in investigating the relationship between energetic electrons and ions, the nature of faint sources in the corona, the energy distribution of flares, and several other topics have significantly advanced the understanding of flares.

But along with the wealth of information revealed by *RHESSI* come some clear observational challenges. Very few, if any, *RHESSI* observations have come close to imaging the electron acceleration region itself. This is undoubtedly due to a lack of both sensitivity (HXRs from electron beams in the tenuous corona are faint) and dynamic range (HXR sources at chromospheric flare footpoints are much brighter and tend to obscure faint coronal sources). Greater sensitivity is also required to investigate the role that small flares in the quiet Sun could play in heating the corona.

The *Focusing Optics X-ray Solar Imager (FOXSI)* is a developing project to address these observational difficulties. *FOXSI* is a sounding rocket payload developed under NASA's Low Cost Access to Space program. The project spearheads a shift to using direct imaging via focusing grazing-incidence HXR optics rather than the indirect Fourier techniques used

by *RHESSI* and its predecessors. Such optics can attain higher sensitivity since photons are focused onto a small detector volume and have significantly better dynamic range than Fourier methods do. On November 2, 2012 the *FOXSI* rocket payload was flown for a 6-minute observation and successfully imaged a solar flare, providing the first focused HXR spectroscopic images of the Sun above 5 keV.

The motivation, construction, testing, and flight of *FOXSI* will be described in this text, along with case studies on the use of *RHESSI* to analyze unique coronal HXR sources from two solar flares.

## Dedication

These pages have been finished with many tears, for we have lost a great scientist and an inspiring man with the passing of my advisor Bob Lin. Bob was dear to everyone who knew him and I am very lucky to have known and have been taught by this extraordinary man.

In a draft of thesis acknowledgements written before his sudden stroke, I had this to say about him: “My advisor, Bob Lin, is an inspiration to me with the enthusiasm and creativity with which he approaches his work. Bob is someone you want to be like: he has an encyclopedic knowledge gained from a lifetime of hard work; he treats everyone he meets with kindness and respect, and he enjoys his life.” Looking back at these words, I could not agree more. Bob was distinctive because of his intelligence, his kindness, and his love of his life and his work. He created a healthy and encouraging environment for his students and employees. He will always have my unending gratitude, and in the course of the career ahead of me I will make every effort to make him proud.

While Bob was with us he taught me much about the field of space physics. In death he continues to teach me much about life.

# Contents

<b>List of Figures</b>	<b>vi</b>
<b>List of Tables</b>	<b>xviii</b>
<b>Acknowledgments</b>	<b>xx</b>
<b>1 Introduction</b>	<b>1</b>
1.1 Welcome . . . . .	1
1.2 Solar structure . . . . .	2
1.3 Solar flares . . . . .	5
1.4 What's ahead . . . . .	8
<b>2 Solar flare processes</b>	<b>9</b>
2.1 Introduction . . . . .	9
2.2 The standard flare model . . . . .	9
2.2.1 Reconnection . . . . .	10
2.2.2 Standard flare geometry . . . . .	13
2.2.3 Interchange reconnection . . . . .	14
2.3 Flare acceleration mechanisms . . . . .	16
2.4 The coronal heating problem . . . . .	18
2.4.1 Flare heating . . . . .	20
2.4.2 Nanoflare heating . . . . .	20
2.5 Methods of observation . . . . .	23
2.5.1 X-ray emission from the Sun . . . . .	23
2.5.2 Radio emission . . . . .	27
2.5.3 Time evolution of flares . . . . .	28
<b>3 The Reuven Ramaty High Energy Solar Spectroscopic Imager (RHESSI)</b>	<b>30</b>
3.1 Introduction . . . . .	30
3.2 Imaging system . . . . .	31
3.3 Spectrometer . . . . .	36
3.4 Software . . . . .	38

3.4.1	Image reconstruction methods . . . . .	39
3.4.2	Spectroscopy . . . . .	42
<b>4</b>	<b>Hard X-ray Observations of a Jet and Accelerated Electrons in the Corona</b>	<b>44</b>
4.1	Introduction . . . . .	44
4.2	Observations . . . . .	48
4.2.1	<i>TRACE</i> EUV observations . . . . .	48
4.2.2	<i>RHESSI</i> HXR observations . . . . .	50
4.2.3	Radio observations . . . . .	53
4.3	Discussion . . . . .	54
4.3.1	Evidence for interchange reconnection . . . . .	54
4.3.2	HXR emission from the jet . . . . .	56
4.4	Summary . . . . .	60
<b>5</b>	<b>Energetics and Heating in a Solar Plasma Ejection Observed By <i>RHESSI</i> and <i>AIA</i></b>	<b>62</b>
5.1	Introduction . . . . .	63
5.2	Observations . . . . .	65
5.2.1	<i>AIA</i> observations of ejected plasma . . . . .	65
5.2.2	<i>RHESSI</i> HXRs from the ejecta . . . . .	71
5.3	Discussion . . . . .	73
5.3.1	Thermal energy . . . . .	74
5.3.2	Collisional energy loss . . . . .	74
5.3.3	Electron injection profile . . . . .	76
5.4	Summary . . . . .	76
<b>6</b>	<b>Introduction to the Focusing Optics X-ray Solar Imager (<i>FOXSI</i>)</b>	<b>78</b>
6.1	Scientific Motivation . . . . .	78
6.1.1	Coronal sources . . . . .	79
6.1.2	Nanoflares and coronal heating . . . . .	81
6.2	Advantages of focusing optics . . . . .	82
6.3	The <i>FOXSI</i> sounding rocket . . . . .	83
6.3.1	<i>FOXSI</i> optics . . . . .	84
6.3.2	<i>FOXSI</i> detectors . . . . .	85
6.4	<i>FOXSI</i> 's science goals . . . . .	85
6.4.1	Active region temperatures . . . . .	86
6.4.2	Nonthermal emission from quiet Sun nanoflares . . . . .	88
6.5	Chapter summary . . . . .	89
<b>7</b>	<b>Focusing Hard X-ray Optics for <i>FOXSI</i></b>	<b>91</b>
7.1	Introduction to X-ray Focusing Telescopes . . . . .	91
7.1.1	X-ray reflectivity . . . . .	91

7.1.2	Focusing optics geometries . . . . .	98
7.2	Heritage of the <i>FOXSI</i> optics . . . . .	101
7.2.1	The <i>HERO</i> balloon program . . . . .	101
7.3	Description of the <i>FOXSI</i> optics . . . . .	104
7.4	<i>FOXSI</i> optics testing and results . . . . .	106
7.4.1	Calibration setup . . . . .	106
7.4.2	Point spread function . . . . .	107
7.4.3	Half power diameter . . . . .	107
7.4.4	Effective area . . . . .	109
7.4.5	X-ray alignment with <i>FOXSI</i> detectors . . . . .	111
7.5	Conclusion . . . . .	115
<b>8</b>	<b>Double-sided Silicon Strip Detectors for FOXSI</b>	<b>116</b>
8.1	Introduction to semiconductor radiation detectors . . . . .	116
8.1.1	Signal formation in a semiconductor . . . . .	117
8.1.2	The effect of impurities . . . . .	120
8.1.3	Semiconductor junctions . . . . .	121
8.1.4	Leakage current . . . . .	123
8.1.5	Semiconductor detector geometries . . . . .	124
8.1.6	Semiconductor detector materials . . . . .	127
8.1.7	Producing an energy spectrum . . . . .	128
8.2	The <i>FOXSI</i> detector system . . . . .	132
8.2.1	The <i>FOXSI</i> DSSD . . . . .	132
8.2.2	The <i>FOXSI</i> VATA451 readout ASIC . . . . .	133
8.2.3	Prototype testing at ISAS/JAXA . . . . .	136
8.2.4	The <i>FOXSI</i> readout system . . . . .	136
8.3	<i>FOXSI</i> detector testing and calibration . . . . .	144
8.3.1	Experimental setup . . . . .	144
8.3.2	Noisy strips . . . . .	145
8.3.3	Gain calibration . . . . .	145
8.3.4	Low-energy efficiency . . . . .	146
8.3.5	Imaging tests . . . . .	149
8.3.6	Livetime measurement . . . . .	152
8.3.7	Thermal vacuum tests . . . . .	153
8.4	Chapter summary . . . . .	155
<b>9</b>	<b>FOXSI's first flight</b>	<b>157</b>
9.1	The <i>FOXSI</i> payload . . . . .	157
9.1.1	Experiment section . . . . .	157
9.1.2	Other systems . . . . .	158
9.2	Flight . . . . .	159
9.2.1	Targeting . . . . .	159

---

9.2.2	Recovery and post-flight state of health . . . . .	161
9.3	Observations . . . . .	162
9.3.1	Time profile . . . . .	162
9.3.2	Imaging . . . . .	164
9.3.3	Spectra . . . . .	165
9.3.4	Next steps . . . . .	165
9.4	Conclusions . . . . .	165
<b>10</b>	<b>Future work and conclusions</b>	<b>167</b>
10.1	Future work . . . . .	167
10.1.1	<i>RHESSI</i> studies . . . . .	167
10.1.2	Solar observations with <i>NuSTAR</i> . . . . .	167
10.1.3	<i>FOXSI-1</i> and <i>FOXSI-2</i> . . . . .	168
10.1.4	A spaceborne <i>FOXSI</i> . . . . .	169
10.2	Conclusion . . . . .	170
<b>A</b>	<b>FOXSI optics calibration results</b>	<b>171</b>
<b>B</b>	<b>FOXSI detector calibration results</b>	<b>176</b>
<b>C</b>	<b>FOXSI X-ray alignment results</b>	<b>185</b>
	<b>Bibliography</b>	<b>188</b>

# List of Figures

1.1	Soft X-ray images of the Sun captured by Wolter-I type focusing optics, in (left) 1965 and (right) 2010. (Left) Example of the first resolved X-ray image of the Sun, produced via sounding rocket, from Giacconi et al. (1965). Emission from the corona above the solar limb is visible, as well as an active region on the solar disk. (Right) Image from the X-ray Telescope (XRT) aboard the <i>Hinode</i> spacecraft (Golub et al. 2007). The advances in sensitivity and angular resolution are such that not only active regions but fine structure in the quiet Sun can be observed. . . . .	2
1.2	Diagram showing the main layers of the solar atmosphere. Surrounding the core are the radiative and convection zones. In the upper atmospheric layers, the solar temperature undergoes a decrease moving outward from the solar “surface” in the photosphere and reaches a minimum in the chromosphere before rising to a surprisingly high value (1–2 MK) in the corona. . . . .	3
1.3	The structured corona visible via Thomson scattering during a 1991 solar eclipse. The chromosphere is also visible as a thin pink layer. Photograph by Viatour (2006). . . . .	5
1.4	Temperature (solid) and density (dashed) structure of the upper layers of the solar atmosphere. Heights are measured above the photosphere. Plot is from Withbroe & Noyes (1977). . . . .	6
2.1	(Left) Diagram of the Sweet-Parker model of reconnection, including a thin, long current sheet, inflow (vertical arrows) and outflow (horizontal arrows). (Right) The Petschek model, in which the diffusive region has a finite length and width. Not all particles make it into the diffusive region; many instead are redirected at the standing shocks. Both figures are from Zweibel & Yamada (2009). . . . .	11
2.2	A diagram of collisionless Hall reconnection. On scales smaller than the ion gyroradius, ions are not bound to field lines and Hall effects become important. The ion diffusion region is larger than the electron diffusion region, allowing for reconnection on appropriate time scales. This picture has been well-validated in the Earth’s magnetotail and could also be applicable to solar flares. Figure is from Lin (2011). . . . .	12

2.3	Two-dimensional diagram of the standard flare model. A rising plasmoid (not shown) instigates reconnection with the overlying coronal field, producing the magnetic field drawn here. Particles are accelerated in the shaded central region; energized electrons can then stream down the flare loops (orange), or escape upward into interplanetary space. Image is from Christe (2007), based on Sturrock (1966). . . . .	15
2.4	Two-dimensional diagram of an interchange reconnection geometry, from Shibata et al. (1997). Interchange reconnection has been proposed as an explanation for solar jets observed in the EUV and SXR; the role of energetic electrons in this model will be explored in Chapter 4. . . . .	16
2.5	Distribution of flare energies from nanoflares (left) to microflares (right), as measured in thermal SXR and EUV, with some of the measured power-law indices shown. The distribution at higher flare energies roughly follows a power law with an index of 1.8. Whether nanoflares follow the same distribution has important implications for the role of nanoflares in coronal heating. Figure is from Hannah et al. (2008). . . . .	21
2.6	Illustrations of magnetic fibrils intertwining due to random footpoint motions in the photosphere, from (left) Parker (1972) and (right) Parker (1983). These motions can cause magnetic stress to build, resulting in small reconnection events.	22
2.7	A sample <i>RHESSI</i> X-ray spectrum from the 2002 July 23 class X4.8 solar flare, showing thermal (red) and nonthermal (pink) components, as well as gamma ray lines from nuclear contributions (blue). Image is from Lin (2011). . . . .	26
3.1	Overview of the <i>RHESSI</i> instrument . . . . .	32
3.2	Diagram of <i>RHESSI</i> 's RMC imaging system . . . . .	34
3.3	Modulation curves for simple Gaussian sources . . . . .	35
3.4	The <i>RHESSI</i> detector system . . . . .	37
3.5	Effective area of the <i>RHESSI</i> detectors . . . . .	37
3.6	Comparison of images made using several standard <i>RHESSI</i> imaging algorithms, including (upper left) back projection, (upper right) Clean, (lower left) visibility forward-fit, and (lower right) Maximum Entropy Method images. The double nature of the source is observed clearly with the visibility-based routines (bottom row). All images are from the time interval 2003 August 21 15:16:15–15:18:00 UT, in the energy range 10–25 keV, and made using subcollimators 3–9. . . . .	40
4.1	Black: The interchange reconnection diagram shown in Figure 2.4, from Shibata et al. (1997). Overlaid on this diagram are hypothetical HXR sources (not from the original model), including paths traveled by energetic electrons (light blue), bright HXR footpoints in which electrons lose all energy (dark blue), and dense shock regions where energetic electrons may undergo collisions (purple). With current instrumentation, the coronal sources are unlikely to be observed in the presence of bright footpoints. . . . .	45

- 4.2 Time profiles of the August 21, 2003 limb event. Panel (a): *GOES* lightcurves. Panel (b): *RHESSI* 6–8 keV emission (blue) and 20–50 keV emission (black), log scale. Panel (c): *RHESSI* 20–50 keV emission (black) and Phoenix-2 1600 MHz emission (red), linear scale. Panel (d): Phoenix-2 decimetric bursts. Panel (e): Phoenix-2 Type III bursts. Panel (f): *TRACE* 171Å jet height profile, in Mm above the optical limb. There is a gap in the *TRACE* data before 1518 UT. The jet velocity is the slope of the solid black line fit to three time intervals. In panels (b) and (c), the black bar marks the attenuator motion, while gray shading indicates the image times. . . . . 47
- 4.3 *TRACE* 171 Å images of the 2003 August 21 jet, with a pre-event image at time 15:15:02 UT subtracted. The first six frames show emission that is concurrent with the X-ray and radio observations; the last two frames show the beginning of the next jet. There is a gap in the 171Å data between 15:23:19 UT and 15:26:20 UT. A filament obscures the jet near the limb in this filter; it is in this region that the HXR sources discussed in section 4.2.2 lie. The bottom-right image shows the start of the EUV jet overlaid with source locations from the Nançay Radioheliograph (NRH); this data is discussed in section 4.2.3. Markers indicate NRH source centroids at the time of the second (plus signs) and third (triangles) Type III bursts, around 15:19:37 UT and 15:20:34 UT, respectively. . . . . 49
- 4.4 *RHESSI* X-ray images and spectra of the 2003 August 21 flare, during (left column) the pre-impulsive phase, (middle column) the first nonthermal burst, and (right column) the second nonthermal burst. Top row: thermal contours (red) and nonthermal contours (blue) superimposed on a later *TRACE* 1550Å image of the jet. The *TRACE* image time is 15:23:35 UT in all images. Bottom row: *RHESSI* spectra, assuming a spectral index of 1.7 below the break. In panel (f), the spectrum was fit with two broken power laws (dashed lines) to represent the two nonthermal sources. All *RHESSI* images were produced using the MEM\_NJIT imaging algorithm with subcollimators 3–9. Contour levels are 30, 50, 70, and 90 percent. . . . . 51
- 4.5 Left: *RHESSI* thermal emission from a small post-flare loop in the latter half of the second HXR burst (red). Middle: Overlays of *RHESSI* nonthermal emission from the pre-impulsive phase reconnection outflow (green) and the jet emission (black). Reconnection outflow is correctly positioned to supply energetic electrons to the post-flare loop. Right: These sources are overlaid on a cartoon of interchange reconnection similar to that in Figure 4.1, demonstrating the expected locations of HXR sources. . . . . 55

4.6	Left: The relation between the jet density and temperature in the thin- and thick-target approximations, assuming all energy deposited in the nonthermal source is transferred into thermal energy of the jet (solid lines) or allowing for additional loss to jet kinetic and potential energies (dotted lines). The dashed black line indicates the density ( $1.2 \times 10^{11} \text{cm}^{-3}$ ) separating the two regimes. Right: Simulated flux at 7 keV for a range of temperatures, with densities taken from the left panel. Only values from the left panel are included in the plot. The dashed line marks the flux observed from the bright northern source, while the dash-dotted line marks a conservative observing limit of 10 times fainter. Fluxes below the dash-dotted line probably could not be seen within <i>RHESSI</i> 's dynamic range. . . . .	58
5.1	An example of a CME observation from the <i>Large Angle Spectrometric Coronagraph (LASCO)</i> aboard <i>SOHO</i> . A coronagraph uses an occulting disk to block bright light from the solar disk, allowing faint reflected light from the corona to be measured. This example shows the typical bright front, dark cavity, and bright core often observed in CMEs. Image is from Riley & McComas (2009). . . . .	64
5.2	Time profile of the 2010 November 03 flare, in SXR, HXR, and radio emission. The panels show (top panel) <i>RHESSI</i> HXR emission from 30–50 keV with numbered imaging intervals for Figure 5.7, (second panel) separate lightcurves for the two <i>RHESSI</i> sources discussed in section 5.2.2, (third panel) the <i>RHESSI</i> spectrogram, (fourth panel) a <i>PHOENIX</i> radio light curve at 1600 MHz, and (bottom panel) a spectrogram combining radio data from the <i>PHOENIX</i> and <i>HUMAIN</i> radio observatories. . . . .	66
5.3	Temperature response of the six AIA filters sensitive to hot coronal plasma. Measurement in a single filter is insufficient to infer a temperature. By combining data from multiple filters, temperatures can be obtained. Note that the filters with best sensitivity to $\sim 10$ MK plasma are 131 and 94 Å. Figure is from Lemen et al. (2012). . . . .	67
5.4	View of the ejected plasmoid in four different AIA filters at times around 12:14:44. The 94 and 131 Å filters are sensitive to the hot plasma at the ejecta's core, while the 211 and 335 Å filters show the cooler surrounding sheath. Images are from Bain et al. (2012a). . . . .	69
5.5	Results of forward-fitting <i>dEM</i> curves to AIA data using the technique from Aschwanden & Boerner (2011). The left two columns show the measured emission measure and the right two columns show the temperature. The core of the ejected plasma reaches a temperature of $\sim 11$ MK, while the sheath surrounding the core is cooler. The color scales cover the ranges $\log[EM]=27-31$ and $\log[T]=5.7-7.5$ , with <i>EM</i> in $\text{cm}^{-3}$ and <i>T</i> in MK. . . . .	70

- 5.6 *RHESSI* HXR images at 18–40 keV produced using the (left) Clean, (middle) Two-step Clean, and (right) vis\_fwdfit imaging techniques. The regular Clean image shows artifacts in the corona as it over-resolves the large-area, diffuse, high-altitude source. The Two-step Clean technique is able to reconstruct the diffuse source by first removing components due to the compact, near-limb source; fluxes from each source were then added to make the middle image. The vis\_fwdfit image corroborates the existence and rough location of the high-altitude source but cannot provide detailed morphology. (Only select simple morphologies are available as of yet in the forward-fitting algorithm.) The middle and righthand images are shown on a log scale to display the diffuse and bright sources together. 71
- 5.7 *RHESSI* contours produced using the Two-step Clean method are shown overlaid on AIA 131Å images. Contours are (blue) the diffuse, high-coronal source, and (red) the compact, near-limb source, both at 18–40 keV. The high coronal component is first observed in image 2 and evolves in a very similar way as the AIA plasma ejection does. By the time of image 6, the high-altitude HXR source is no longer observed. . . . . 72
- 5.8 *RHESSI* HXR spectrum computed over 1 minute, including (black) an integrated spectrum with no imaging, spectra for the (blue) near-limb and (red) high-altitude sources, obtained with imaging spectroscopy, and (green) the summed spectra (red + blue), which closely matches the integrated spectrum. . . . . 73
- 5.9 Evolution of thermal and energetic parameters throughout the plasma ejection, including (top panel) the photon spectral index and (second panel) the number of instantaneous electrons. The third panel shows the energy collisionally deposited in a (red) thick-target or (black) thin-target approximation, compared with the (purple) thermal energy estimated in the ejecta. The bottom panel shows the average temperature of the hot core. For times before ~12:14:07 it is difficult to identify the core volume of interest in Figure 5.5 so calculations of the average temperature and total thermal energy were not done for those times. . . . . 75
- 5.10 The collisional stopping time for energetic electrons in a plasma of density  $5 \times 10^9 \text{ cm}^{-3}$ . . . . . 77
- 6.1 Histogram showing peak 30 keV fluxes from flares located on the solar disk (red) or over the limb (black), in which case only coronal sources are visible. Fluxes from disk flares are much brighter than those from partially occulted flares since footpoint fluxes are included in the measurements of those flares. The 44 on-disk flares are those from the statistical study of double footpoints in Saint-Hilaire et al. (2008), while the 55 partially occulted flares are those from Krucker & Lin (2008); all flares are of GOES class C and higher. The Gaussian averages of the on-disk and occulted flare histograms are  $\log[\text{flux}] = 0.5$  and  $-0.8$ , respectively, indicating that footpoint HXR sources are, on average, 1.3 orders of magnitude brighter than coronal sources. . . . . 80

6.2	Schematic of a grazing-incidence focusing X-ray telescope. Incident photons undergo a double reflection before being focused. Typically, mirrors of different diameters are nested together to increase the effective area of the instrument. Image is from Ehle et al. (2001). . . . .	83
6.3	(Left) Point spread function of the <i>FOXSI</i> optics compared with that of other instruments. <i>FOXSI</i> 's PSF (black line) falls by two orders of magnitude within 50 arcsec, a vast improvement over the dynamic range of <i>RHESSI</i> (gray shaded region). (Right) Effective area of the optics alone (dashed lines) and of the entire instrument including the detector response and absorption by blankets (solid lines), for the first <i>FOXSI</i> rocket payload (blue) and the <i>FOXSI</i> 2 upgrade (red). Both figures are from Krucker et al. (2011b) . . . . .	86
6.4	(Left) The parameter space of emission measure (EM) and temperature to which <i>FOXSI</i> is sensitive. Shown here are the values of the EM and temperature that would produce 350 (blue) or 70 (black) total counts in the <i>FOXSI</i> instrument in one minute. The higher the temperature, the lower the emission measured needed to produce this count rate. (Right) Simulated <i>FOXSI</i> counts for one minute for several emission measures and temperatures. . . . .	87
6.5	Simulated <i>FOXSI</i> count rates for the active-region thermal plasmas similar to those reported in Miceli et al. (2012) and Warren et al. (2011), taking into account <i>FOXSI</i> 's effective area and livetime. For each plot the thermal plasma has been approximated by a single temperature and emission measure. The lefthand plot shows the expected counts (solid line) and a simulated <i>FOXSI</i> observation (data points with error bars). In the righthand plot, each count spectrum has been scaled to its maximum, illustrating the difference in peak energies between the two spectra. Miceli et al. (2012) found the active region flux to be dominated by a 7 MK component, so no lower-temperature component was included in the simulation of the 7 MK plasma. Warren et al. (2011) calculated the flux from a small active region core only. For this simulation, the flux was scaled to the active region size of $\sim 100 \times 100$ arcsec <sup>2</sup> . A smaller size (and thus smaller X-ray flux) is appropriate if the emission arises primarily from a core region. . . . .	88
6.6	Simulations of spectra for nonthermal (blue) and 2 MK thermal (red) X-rays from quiet-Sun network flares. On the left, simulated photon flux is shown for various values of the cutoff energy $E_0$ , with a fixed power-law index of 5 above and 1.7 below the break. In the righthand plot, data points and error bars show the expected <i>FOXSI</i> count spectra. Both plots are from (Krucker et al. 2011b) .	89
7.1	Ray-tracing diagram demonstrating Snell's law. $\vec{k}_I$ , $\vec{k}_R$ , and $\vec{k}_T$ are the incident, reflected, and transmitted rays, respectively. . . . .	92
7.2	Reflectance of X-rays from 1 to 80 keV vs grazing incidence angle for a 0.25 mm thick layer of nickel (solid lines) or iridium (dashed lines), computed using the IMD package for IDL (Windt 1998). The interface was modeled as a step function with no roughness. . . . .	95

7.3	X-ray reflectivity for a thin nickel layer with surface roughness included, for 7 keV photons (solid line) and 11 keV photons (dashed line). Surface roughnesses range from 0 to 12Å RMS. Calculations were done using the IMB software (Windt 1998).	97
7.4	Diagram showing paths for a wave entering a thin slab. In addition to a simple reflection (solid line), the wave could reflect once or more within the slab (dashed lines).	98
7.5	Schematic of a Kirkpatrick-Baez configuration; from Aschenbach (1985).	99
7.6	Wolter type I, II, and III geometries; from Aschenbach (1985).	100
7.7	(Left) An electroforming bath at MSFC for plating ENR optics. (Right) Several <i>HERO</i> shells of various diameters. Both images are from Ramsey et al. (2004).	103
7.8	(Left) A <i>FOXSI</i> module seen edge on. The seven nested shells are visible along with the spider support structure and module casing. (Right) A closeup photograph of the clips adhering the mirror shells to the spider.	104
7.9	Theoretical effective area of the <i>FOXSI</i> optics, all shells and all modules combined.	105
7.10	(Upper left) Point spread function for one slice of the focal plane (here, referred to as the horizontal PSF), measured on-axis. The FWHM ranges from 6.7 to 8.3 arcseconds. (Upper right) Point spread function for an on-axis vertical slice, showing FWHM values from 6.9 to 8.2 arcseconds. The on-axis PSF is rotationally symmetric. (Bottom row) PSF measured for horizontal and vertical slices at an off-axis angle of 10 arcmin. The PSF is “squeezed” becoming wider in one dimension and thinner in the other.	108
7.11	The relationship between the measured and actual PSF FWHM. The difference between the two is an effect of the large (50 μm) pinhole used in the measurements.	109
7.12	(Left) On-axis flux measured for all optics using pinholes of various diameter. The x-axis shows the size of the pinhole, while the y-axis shows the measured flux relative to the maximum measured flux (with the largest pinhole of 3.0 mm). A normalized count rate of 0.5 defines the half-power diameter; here it is 25.4–30.1 arcseconds. Right: half-power diameter for all seven optics modules at several off-axis angles. For most of the modules, the HPD is fairly consistent within 5 arcminutes of the central axis; the performance at ±10 arcminutes is severely degraded.	110
7.13	Ray diagram for a single Wolter-I mirror shell, with a closeup showing the annulus that is the collecting area for that mirror. In this drawing, the parabolic and hyperbolic shapes are approximated by straight lines.	111

7.14	(Top left) Theoretical values for the effective area for each <i>FOXSI</i> shell, assuming an infinite source distance and a surface roughness of $7 \text{ \AA}$ , calculated using the XOP software. These curves add together to yield the effective area of a single module. The shells are numbered with odd numbers from 1 (largest diameter) to 13 (smallest). Below $\sim 11 \text{ keV}$ , the largest shells contribute most because of their larger collecting areas, but it is the smaller shells that dominate at higher energies because of their smaller grazing angles. (Top right) The effects of a finite source distance (104 m) and various surface roughnesses are compared. Areas are for a single <i>FOXSI</i> optics module (all shells combined). (Bottom left) The finite-source-distance effective areas at various surface roughnesses are compared with the measured area from a single <i>FOXSI</i> module. (Bottom right) A simulation (blue line) of pileup effects confirms that the discrepancy in the effective area measurement (red line) is due to pileup in the detector. . . . .	113
8.1	Energy bands for three types of solids (not to scale). . . . .	117
8.2	Cross sections of photon interactions in germanium. Up to $\sim 100 \text{ keV}$ , photoabsorption is the most likely interaction. Results are similar for interactions in silicon. Figure from Gao et al. (2007). . . . .	119
8.3	Sketch demonstrating the electrical properties surrounding a p-n junction. Even in the absence of an applied bias voltage there is a built-in potential and depletion region. Applying a reverse bias voltage (positive potential to the n-side) will increase the width of the depletion region. Image from Servagent (2007). . . . .	122
8.4	Occupancy of energy states in a Fermi distribution, for various temperatures. $\mu$ is the Fermi energy. For $kT \ll \mu$ , all states with energy $\epsilon < \mu$ (i.e. valence band) are filled and all those with energy $\epsilon > \mu$ (conduction band) are empty. As $kT$ approaches the Fermi energy, thermal fluctuations allow more electrons into the conduction band. . . . .	124
8.5	Diagram of a double-sided strip detector. Holes and electrons are collected at strips on the p- and n-sides that are oriented orthogonally to each other so that a two-dimensional image can be obtained. Each strip acts as an individual p-n junction. The “p-stops” improve charge collection on the n-side and will be discussed in Section 8.2.1. Figure from Takeda et al. (2008). . . . .	125
8.6	Efficiency as a function of X-ray energy for a $500 \text{ }\mu\text{m}$ thick detector. Silicon, the lowest- $Z$ material considered here, has appreciable efficiency only up to tens of keV. For higher energy HXR and gamma-ray studies, higher- $Z$ materials like germanium and cadmium telluride must be used. . . . .	128
8.7	(Left) A Poisson probability distribution for 10 mean successes. (Right) Poissonian distribution of waiting times between successive events, with waiting times in units of the inverse count rate $r$ , and with the distribution normalized to $r$ . . . . .	130
8.8	Photographs of the <i>FOXSI</i> DSSD. . . . .	133

8.9	Efficiency of the <i>FOXSI</i> detectors for the X-ray energy range of interest. The dashed line includes the effect of the low-energy threshold (LET) of the VATA451 ASIC and is an averaged value from all of the ASICs used for flight. (Details of this measurement will be discussed later in this chapter.) Attenuation length data is from Henke et al. (1993). . . . .	134
8.10	Block diagram of the VATA, showing the charge-sensitive amplifier, slow shaper and sampling circuitry (VA part), ADC, and fast shaper for triggering (TA part). Image from Ishikawa et al. (2011). . . . .	135
8.11	Flowchart for <i>FOXSI</i> data handling. After data is measured, digitized, and read out from each detector by four ASICs, a FPGA performs minor processing and data reduction. The formatter FPGA then packages all the detector data into a telemetry stream, which is transmitted to a ground station at White Sands and fed into the <i>FOXSI</i> DAQ software for live monitoring of flight data. After the flight, data is processed into Level 1 products and analyzed. . . . .	136
8.12	Block diagram of the <i>FOXSI</i> electronics package. Each of the 7 detectors has 4 R/O ASICs and a dedicated FPGA. Data from each FPGA is collected by a formatter FPGA (encoder) and packaged into a data packet inserted into the telemetry stream. Power, telemetry, and uplink commanding are provided by the NASA Sounding Rocket Operations (NSROC) team. . . . .	137
8.13	(Upper left) A photograph of the <i>FOXSI</i> detector board, showing the n-side of the detector and its two readout ASICs. (Upper right) Design showing the focal plane assembly that holds the 7 detector boards, FPGA board, formatter board, and power board. (Bottom) Design showing the attenuator mechanism. By sending a command during the flight, a pin puller is activated, allowing the spring-loaded mechanism to insert thin attenuators in front of 6 out of the 7 detectors. Images are from Krucker et al. (2011b). . . . .	138
8.14	Block diagram of the FPGA functions, including SRAM memory, communication, timing, and processing modules. For simplicity, several FPGA modules are left out of the diagram and several buses are condensed into single lines. Boxes outside the dashed line are external to the FPGA. Each detector has a dedicated FPGA, which is interrogated independently by the formatter. . . . .	140
8.15	The 256-word formatter data packet for <i>FOXSI</i> . The first three rows (light green) contain sync, time, and housekeeping information. This is followed by detector-specific information, shown here in colored blocks. Each detector section includes the trigger time (if any) followed by a 4-word hit channel mask, 3-strip data (10 bits + 6 bits addressing), and the common mode value for each of the four ASICs per detector. The text at the bottom describes the encoding of temperature and voltage information in the housekeeping data. . . . .	142
8.16	Photographs of selected ASICs with visible fractures after the cooling accident. Differential thermal expansion cracked the chips, rendering them inoperable. . .	144

8.17	Uncalibrated Am-241 spectra taken with detector 101, in raw ADC values with the common-mode values subtracted. Spectra for each ASIC is shown; the relatively poor performance of the n-side as compared to the p-side is evident. . . .	147
8.18	Calibrated Am-241 spectra for all ASICs of detector 101. . . . .	148
8.19	Histograms of (left) the energy resolution at the 13.9 keV Am-241 line and (right) the threshold energy at which the system is 50% efficient for all detectors with the <i>FOXSI</i> VATA451 ASIC. The values were measured separately for each p-side ASIC. Some detectors were read out with a different iteration of this ASIC, the VATA450; these detectors were not used for flight and are not included in this histogram. . . . .	149
8.20	Example of the measurement of the detector efficiency near the low energy threshold. (Top) Measured count rates in the Fe-55 5.9 keV peak, with the best fit curve overplotted. Error bars are statistical uncertainties. (Bottom) The corresponding efficiency for a threshold value of 12; this is the value chosen for flight. This measurement is for one p-side ASIC of detector 101. . . . .	150
8.21	An image test for one of the first <i>FOXSI</i> detectors tested at SSL. The mask ('F' plus two lines) made by fine lines of solder is clearly visible. At the top and bottom of the image a checkered pattern indicates the locations of wirebonding pads, which alter the collection properties of the underlying detector volume (Ishikawa et al. 2011). . . . .	151
8.22	(Left) Example of an exponential fit to a distribution of measured livetimes (on an arbitrary y-axis scale). The pseudotrigger rate for this data run (as measured by a counter inserted in the data packet) is 209 counts per second. (Right) Results of pseudotrigger testing of the livetime system. Stars show raw measured count rates with no livetime correction; data points with error bars are the rates determined by fitting exponential curves to the livetime distribution; error bars are those from the fit. Each pseudotrigger rate was tested for 30–60 seconds. . . . .	153
8.23	Count rates measured from a an X-ray generator 20 meters in front of the payload, with X-rays focused by the optics onto detector 6. Black data points are the raw measured count rates, with no livetime correction. Red data points are the rates reconstructed by fitting the livetime distribution. The red line shows a linear fit to the data. . . . .	154
8.24	Results from one thermal vacuum test, with a 65–70°C heat shroud. (Top) Temperatures on the seven detector boards (and one detector itself). Detector 1 tends to reach the coldest temperatures and also heat up the fastest because of its location near the cooling inlet. (Middle) Temperatures from thermistors on the focal plane assembly itself. (Bottom) Temperatures on electronics boards located outside the blanketed focal plane. The hottest components are an oscillator on the formatter board and an aluminum plate serving as a heat sink for the electronics stack. . . . .	156

9.1	(Left) Schematic of the experimental section of the <i>FOXSI</i> payload. (Right) Photograph of the <i>FOXSI</i> rocket on the launch rail at White Sands. The experiment section is enclosed in a styrofoam box for temperature control. Non-flight equipment (liquid nitrogen, a cooling controller, and temperature sensor monitors) was located on the launch rail next to the experiment section. The two rocket stages include Black Brant and Terrier motors. . . . .	158
9.2	Map showing the four targets from the <i>FOXSI</i> observation, overlaid on a $94\text{\AA}$ image from the Atmospheric Imaging Assembly (AIA) aboard the <i>Solar Dynamics Observatory</i> . Targets 0 and 1 contained active regions on the disk; target 2 contained only quiet-Sun regions, and target 3 contained an active region at the limb. The first three targets revealed extremely low count rates. A brighter source was found in the fourth target. . . . .	160
9.3	<i>FOXSI</i> count rate time profiles, integrated over energies 5–15 keV. (Left) <i>FOXSI</i> time profile for the 6.5-minute observation time, with the four successive targets approximately indicated. Little, if any, change in rates is observed among the various targets, until the microflare is observed just after 1800 UT. (Right) <i>FOXSI</i> and <i>RHESSI</i> count rates are compared for the B2.7 microflare. The top panel shows the <i>FOXSI</i> count rate over time. In the second panel, the same curve (now in red) is rescaled and overlaid on a <i>RHESSI</i> time profile (black). The bottom panel shows the <i>RHESSI</i> spectrogram. Comparing panels 1 and 2 shows that the <i>FOXSI</i> count rate was higher than that of <i>RHESSI</i> , which is expected for <i>FOXSI</i> 's superior sensitivity. . . . .	162
9.4	A comparison of (left) a <i>RHESSI</i> Clean image and (right) a <i>FOXSI</i> image of the B2.7 flare observing during <i>FOXSI</i> 's flight. Each image is scaled to the maximum intensity for that image. The <i>RHESSI</i> image shows artifacts that reduce the dynamic range of the instrument even far from the bright source. The <i>FOXSI</i> image is clean of such artifacts, enabling a much higher dynamic range. . . . .	164
9.5	Microflare count spectra from (left) the <i>FOXSI</i> sounding rocket and (right) the <i>RHESSI</i> spacecraft. <i>RHESSI</i> spectral fitting reveal that the flare had a temperature of 9 MK and an emission measure of $5 \times 10^{46} \text{ cm}^{-3}$ . . . . .	166
A.1	The HPD was measured by taking data with various sized pinholes placed over a detector. The extrapolated pinhole size (in arcseconds) that encompasses half the flux measured by the largest pinhole is taken to be the HPD. The top left plot is a summary showing this measurement for all the optics modules (labeled X0–X6) for an on-axis and several off-axis configurations. Detailed plots showing the actual measurements for each module follow in this and the next figure. . . . .	172
A.2	Results of <i>FOXSI</i> optics calibration . . . . .	173

A.3	The PSF was measured by stepping a single-pixel detector across the core of the focused X-ray image. This measurement was performed for an on-axis (top panels) and for one off-axis (10 arcminutes, bottom panels) position. The FWHM in both dimensions is shown for each module. The off-axis PSF is squeezed in the radial direction and elongated in the azimuthal direction, with respect to the center of the field of view. . . . .	174
A.4	Shown here is the “vignette” of the field of view, or the maximum flux recorded for several off-axis angles, for three optics modules. The effective area of the optics decreases with off-axis angle since some X-rays are incident on the mirror at an angle too large to reflect well. These plots show that the optics response falls by a factor of two approximately 600 arcseconds (10 arcminutes) away from the center (on-axis). The edges of the detector field of view are $\sim 480$ arcseconds off-axis, where the response is $\sim 0.6$ times the on-axis response. . . . .	175
B.1	Results of <i>FOXSI</i> detector testing . . . . .	177
B.2	Results of <i>FOXSI</i> detector testing . . . . .	178
B.3	Results of <i>FOXSI</i> detector testing . . . . .	179
B.4	Results of <i>FOXSI</i> detector testing . . . . .	180
B.5	Results of <i>FOXSI</i> detector testing . . . . .	181
B.6	Results of <i>FOXSI</i> detector testing . . . . .	182
B.7	Results of <i>FOXSI</i> detector testing . . . . .	183
B.8	Results of <i>FOXSI</i> detector testing . . . . .	184
C.1	X-ray images for detectors 0–3. Optic 0 (upper left) is the least well-aligned (2 arcmin), while most of the other optics are aligned to $< 1$ arcmin. Problems with a readout ASIC result in poorer quality data for detector 1 (upper right). . . .	186
C.2	X-ray images for detectors 4–6. In the detector 5 (upper right) image, more spokes (corresponding to slats in the spider supports) are apparent because of a phase offset between spider supports on either side of the module. . . . .	187

# List of Tables

- 2.1 Temperatures and energy losses for the corona and chromosphere, from Withbroe & Noyes (1977). Differentiations are between active regions, the quiet Sun, and coronal holes. See Section 1.2 for a description of these different regions. . . . . 19
- 3.1 The *RHESSI* Instrument . . . . . 33
- 4.1 Spectral parameters of the *RHESSI* X-ray sources . . . . . 52
- 5.1 The six AIA filters with the hottest temperature sensitivity. In designing the instrument, filters were chosen that have sensitivity to iron lines so that multifilter analysis results would not be dependent on elemental abundances. Not shown here are the lower-temperature-sensitive filters of 304, 1600, 1700, and 4500 Å . Table is adapted from Lemen et al. (2012). . . . . 68
- 6.1 Figures of merit for the *FOXSI* sounding rocket payload. Table adapted from Krucker et al. (2011b) . . . . . 84
- 6.2 Timeline of the *FOXSI* sounding rocket project. . . . . 85
- 7.1 Characteristics of the *FOXSI* optics, from Krucker et al. (2011b). . . . . 106
- 7.2 Physical parameters of the seven nested mirrors in one *FOXSI* optics module. The geometric area shows the area of the annulus through which X-rays can intersect the paraboloidal mirror. The reduced geometric area shows the annulus area reduced due to the finite source distance of 104 meters at the SLF. The shell numbers reflect an arbitrary naming system. . . . . 112
- 7.3 Measured post-alignment offsets for the *FOXSI* optics . . . . . 112
- 8.1 Physical parameters for selected semiconductor materials. Values are taken from Sellin et al. (2005) and chapters 11 and 13 of Knoll (2000). Values for Si, CdTe, and CdZnTe are at a temperature of 300 K; values for Ge are at 75 K, the usual operating temperature for Ge detectors. . . . . 118
- 8.2 Parameters of the *FOXSI* detectors and readout system, adapted from Krucker et al. (2011b) . . . . . 133

---

8.3	Information on the radioactive sources used for gain calibration. The activity, prominent lines, and approximate number of X-ray events collected for each detector is shown. Closely spaced lines are not resolved; a weighted peak was measured. . . . .	146
9.1	Timeline of some of the key events during the <i>FOXSI</i> flight. . . . .	161

# Acknowledgments

As mentioned in the dedication, my late advisor, Bob Lin, has been an excellent role model, wise instructor, and positive motivator in my entering the field of solar physics and completing my graduate studies. He will always have my gratitude for introducing me to a rich and interesting field of work and for helping me get my start.

I am also indebted to Säm Krucker, who has mentored me and supervised my work for the last four years. His dedication and supporting hard work have been crucial in pushing this dissertation to the finish line. I'd especially like to thank him for making time for me despite living on two continents and for allowing me to speak my mind more freely than would probably be recommended.

I thank the other members of my dissertation committee: Stuart Bale, Gibor Basri, and Steve Boggs, and also Jonathan Wurtele who served on my qualifying exam committee. All have provided a supportive and encouraging environment while at the same time holding me to high standards. Their support in finishing my dissertation after the loss of Bob is especially appreciated.

All the members of the FOXSI team are dear to my heart. Much of the work in this thesis is theirs; I am simply the one writing it down. Steven Christe was the first to introduce me to the project and as project manager has made every effort to ensure I had the resources and advice necessary to bring the instrument to completion. As a former Berkeley student himself he has gone above and beyond the call of duty to help steer me through the difficulties of graduate school. The mechanical engineering expertise of Paul Turin is one of FOXSI's greatest strengths, and his patient instruction is much appreciated. David Glaser is an excellent role model with his attention to detail, calm demeanor, and perseverance. Jose Fermin's friendship and hard work were crucial in getting me through several difficult months of rebuilding FOXSI. Brian Ramsey has been a wonderful mentor and host for me at NASA/Marshall and helped me to get an important fellowship to sustain me through a few years of my program. Shinnosuke Ishikawa is an invaluable friend and colleague; I want to thank him, Shinya Saito, and the rest of the ISAS team (and affiliates) for so often coming to our aid. Many thanks are due to Steve McBride for teaching me about electronics systems and noise reduction; for teaching me that it's better to ask for forgiveness than permission; and for his words of encouragement after the FOXSI accident.

It is not possible to list individually the many wonderful souls at the Space Sciences Laboratory who have influenced me, but the list is long and diverse. Virtually every member

of the RHESSI group has helped me out in some big way, as have many scientists and engineers from other groups, whether it be to loan equipment, provide advice, or simply take a walk with me in Tilden Park. In particular, I'd like to thank Albert Shih for being a great friend and mentor ever since my start at SSL, and Nicole Duncan, who has done a great deal of hand-holding over the last year. I also thank David Smith for useful feedback on the detector chapter of this dissertation.

At Lawrence Berkeley Laboratory, special thanks are due to Marco Battaglia, Devis Contarato, and Piero Giubilato for getting me started on detector work and readout systems.

The Physics Department and the Physics and Astronomy Club at San Francisco State University turned out to be the perfect place for a waitress and former ballerina to begin her quest to learn physics. I met many interesting and inspiring people there. Not the least of these is Carolina Calvo, whose enthusiasm is one of the most positive forces in the universe.

My family played a big part in my interest in experimental physics, though neither they nor I knew it at the time. My dad got me started on BASIC programming and shared with me his curiosity about how things work and his joy in building things. My brother's interest in programming set a great example for his impressionable little sister who wanted to do everything he did. Later on, after choosing a computer-intensive career himself, he helped me through my first programming class in college. My mom taught hard work, determination, and career success by example – many of my strong-minded feminist principles came from her. But she also taught me how to sew, and I am convinced that anybody who has battled a finicky sewing machine and won can work any piece of lab equipment. My family has always supported me despite a long string of impulsive, life-changing decisions that took me progressively farther away from them. They probably do not realize just how much I love them and miss them.

This dissertation certainly never would have come about without the unwavering support of Andy Sybilrud. It takes a special kind of person to marry a professional student, but Andy was born with more patience and compassion than most. The difficult periods of grad school were made a great deal easier by the support and loving home he provided. He has worked hard for many years to support the two of us despite getting so much less of my time than he really deserves. Since I met him twelve years ago he has given me a fun life that is always filled with joy! I look forward to the next several decades that we will spend together.

# Chapter 1

## Introduction

### 1.1 Welcome

On March 17 1965 an Aerobee sounding rocket launched from the White Sands Missile Range in New Mexico carrying focusing X-ray optics into space to produce the first resolved soft X-ray images of the Sun (Giacconi et al. 1965). Pinhole camera images of solar X-rays had previously been made (also via rocket), but this flight was the first to produce resolved, useful images around 1 keV, one of which is shown in Figure 1.1. The innovation that enabled this success was the use of Wolter-I grazing-incidence reflecting optics.

Half a century later we know much more about solar X-rays and the processes on the Sun that produce them: primarily hot plasmas for lower energy (“soft”) X-rays, and at higher energies (“hard”) X-rays, energetic electrons accelerated in giant explosions (solar flares) that emit bremsstrahlung radiation. Thanks to the *Reuven Ramaty High Energy Spectroscopic Imager (RHESSI)* spacecraft, we have hard X-ray observations with sufficient angular and energy resolution to be able to identify thermal and nonthermal plasmas and to separate discrete spatial features of flares. But some fundamental questions still elude us: What processes accelerate these particles? Why is the corona of the Sun so hot? What is the source of the large number of flare-accelerated electrons observed in X-rays?

On November 2 2012 a Black Brant rocket launched from White Sands. Like its ancestor, this rocket carried Wolter-I type optics to image X-rays from the Sun, but this time higher-energy sources were the target. The *Focusing Optics X-ray Solar Imager (FOXSI)* payload successfully demonstrated the use of focusing optics for studying solar X-rays from 5–15 keV. Such optics have the potential to study solar hard X-ray (HXR) sources with better sensitivity and dynamic range than any present solar instrument can. A spaceborne instrument carrying this type of optic offers the best possibility for answering some of the outstanding questions in high-energy solar physics by investigating HXR-emitting energetic electron populations in solar flares.

The motivation, construction, and flight of *FOXSI* will be a major theme of this dissertation, along with the use of *RHESSI* observations to study faint HXR sources in the

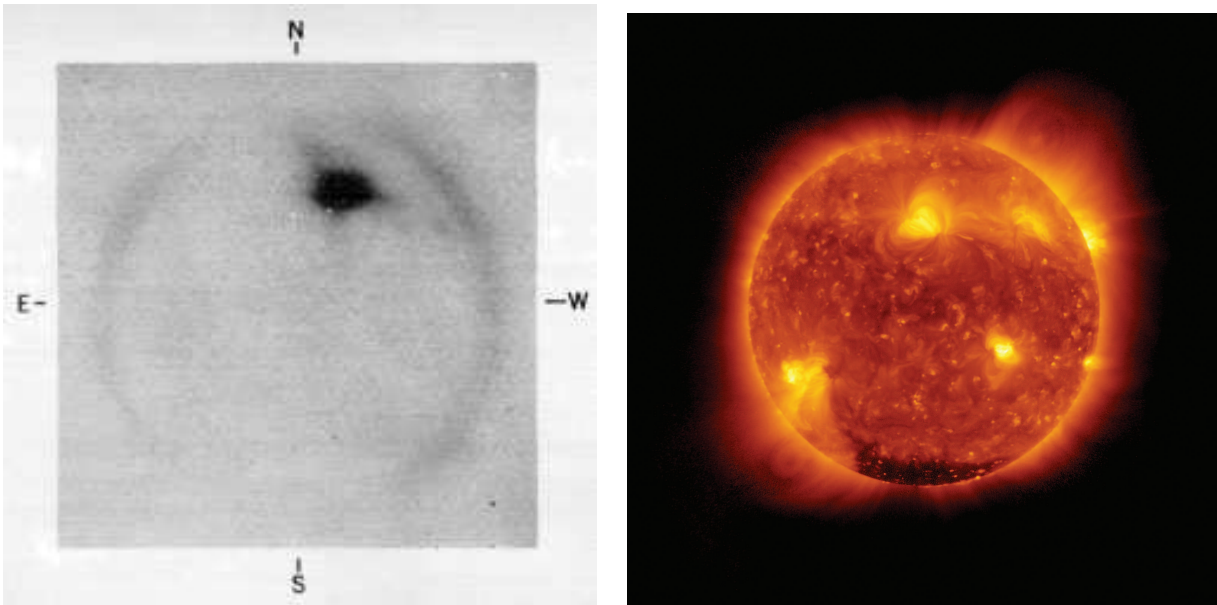


Figure 1.1: Soft X-ray images of the Sun captured by Wolter-I type focusing optics, in (left) 1965 and (right) 2010. (Left) Example of the first resolved X-ray image of the Sun, produced via sounding rocket, from Giacconi et al. (1965). Emission from the corona above the solar limb is visible, as well as an active region on the solar disk. (Right) Image from the X-ray Telescope (XRT) aboard the *Hinode* spacecraft (Golub et al. 2007). The advances in sensitivity and angular resolution are such that not only active regions but fine structure in the quiet Sun can be observed.

solar corona. This chapter will provide an introduction to the Sun and solar flares and will preview the chapters ahead.

## 1.2 Solar structure

An overview of the components of the solar atmosphere can be found in, for example, Phillips (1995) or Gibson (1977).

### Inner layers

The highest steady-state temperature ( $\sim 16$  MK), highest pressure, and the most energetic processes in the Sun are found at its core; it is here where hydrogen is continuously fused into helium via the proton-proton chain. The core extends to about a quarter of a solar radii. Above the core is an atmospheric zone where radiative transfer dominates (called the radiative zone), extending to about two-thirds of the solar radius. Above this

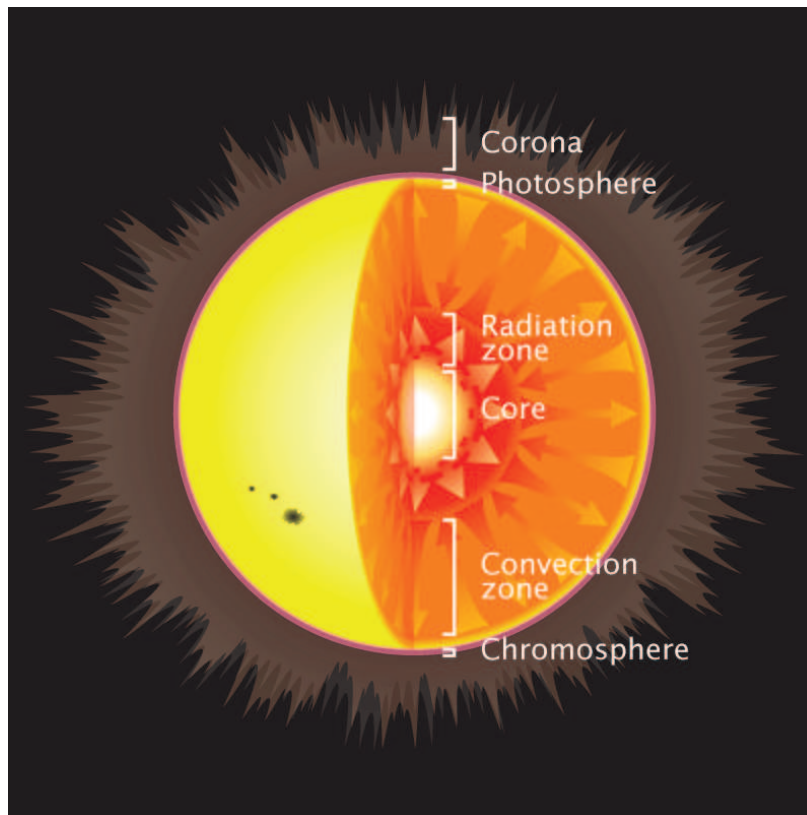


Figure 1.2: Diagram showing the main layers of the solar atmosphere. Surrounding the core are the radiative and convection zones. In the upper atmospheric layers, the solar temperature undergoes a decrease moving outward from the solar “surface” in the photosphere and reaches a minimum in the chromosphere before rising to a surprisingly high value (1–2 MK) in the corona.

zone lies the convection zone, where radiation is not sufficient to transfer energy and large mass convections take place. A complete treatment of solar flares should include a discussion of these inner layers, as it is here that the complex solar magnetic fields that power flares are generated, and it is here that a portion of the flare energy is sometimes dissipated in the form of acoustic waves. This text, however, will focus only on the upper layers of the atmosphere, particularly the corona, which is the immediate environment in which particles are accelerated.

### Photosphere

The photosphere contains the annulus most often thought of as the “surface” of the Sun, where the solar atmosphere becomes optically thick to visible light. It is from this zone that the Sun’s blackbody radiation spectrum is emitted. The temperature at the surface

is  $\sim 5800$  K and the density is  $\sim 10^{17}$  cm $^{-3}$ . In 1859 Kirchhoff correctly proposed that the Fraunhofer absorption lines which had been noticed in the solar spectrum were due to blackbody radiation from the solar surface selectively absorbed by cooler material in the solar atmosphere above it. On a very fine scale the photosphere can be seen to be made up of an ever-changing sea of granules observed down to 175 km in diameter. These granules are convection cells formed by the rising and falling of hot and cool gas in the photosphere.

## Chromosphere

The chromosphere is a 2000–3000 km thick layer lying directly above the photosphere. During the moment of totality in a solar eclipse, the chromosphere often appears reddish or pink due to H $\alpha$  emission (see Figure 1.3); it is for this reason that it is so named. H $\alpha$  observations show a multitude of “spicules” (fine jets or plumes) in the chromosphere extending up into the corona. Moving upwards from the photosphere through the chromosphere, the density decreases by several orders of magnitude. The temperature also initially decreases to a temperature minimum (de Jager 1963), but then turns upward and rises. (See the temperature and density structure in Figure 1.4.) The chromosphere thus encompasses a wide range of temperatures and densities. Just above the chromosphere is a thin layer known as the *transition region*, which contains a transition between the chromosphere and the corona and marks a sharp drop in density and a sudden rise in temperature with height. As shall be seen in Chapter 2, the chromosphere plays a significant role in solar flares as a location where many flare-accelerated electrons deposit their energies, heating the ambient plasma so that it expands upward to fill flare loops with hot material.

## Corona

Much of the flare physics discussed in this dissertation will take place in the mysterious environment of the corona, or outermost layer of the solar atmosphere. In the corona the parameter  $\beta$  (defined as the ratio of plasma pressure to magnetic pressure) is quite low; Densities are small ( $10^{10}$  cm $^{-3}$  and less) and much of the energy is stored in high magnetic fields (10–1000 Gauss). The quiescent (non-flaring) coronal temperature is 1–2 MK, in sharp contrast with the much lower temperatures of the chromosphere and photosphere. As discussed in Chapter 2, a large and unidentified energy input is necessary in order to maintain this high temperature. When solar flares erupt, plasma in the corona typically reaches temperatures of 10–20 MK and occasionally can reach up to twice that value. There is no radial distance at which the corona is said to end; the solar atmosphere extends out into interplanetary space.

## The quiet and active Sun

*Active regions* are groups of sunspots, regions of high magnetic fields and high magnetic complexity. To date, all solar flares identified as such arise from active regions. (This topic will be discussed in detail in Chapter 2.) The *quiet Sun*, on the other hand, is the non-flaring



Figure 1.3: The structured corona visible via Thomson scattering during a 1991 solar eclipse. The chromosphere is also visible as a thin pink layer. Photograph by Viatour (2006).

Sun. The term “quiet” is a misnomer, since the quiet Sun shows rich and dynamic structure (for example, see the righthand panel in Figure 1.1). Magnetic fields are still found to form loops, as in active regions, but no flare-like explosions have been definitively identified. The quiet Sun should not be mistaken for *coronal holes*, which are cooler and less dense. Coronal holes are characterized by magnetic field lines that are open to interplanetary space instead of the closed loop structures ubiquitous in the quiet Sun and active regions. During times of solar minimum, the entire solar disk is made up of quiet Sun and coronal holes.

## 1.3 Solar flares

Sunspots (dark regions on the solar disk with high magnetic fields) were seen by the naked eye as far back as the fourth century B.C., but detailed study could not be done

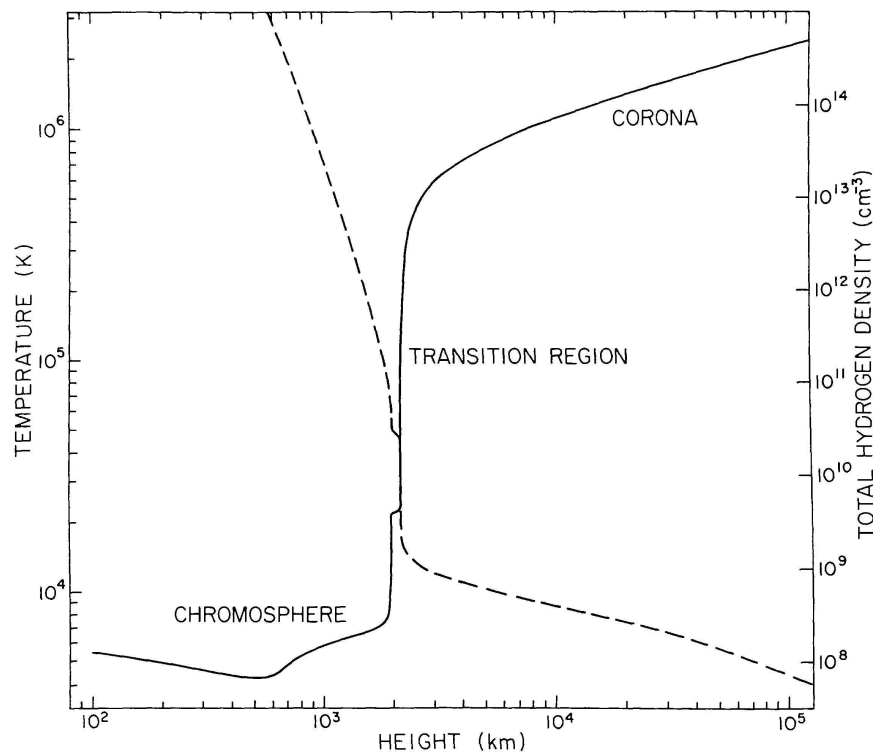


Figure 1.4: Temperature (solid) and density (dashed) structure of the upper layers of the solar atmosphere. Heights are measured above the photosphere. Plot is from Withbroe & Noyes (1977).

until after the invention of the telescope in the 1600s. Galileo used sunspots to correctly deduce that the Sun rotates with a period of a little less than a lunar month. In the 18th century astronomers studying sunspot numbers discovered an  $\sim 11$  year periodicity; the Sun varied between “solar maximum” (in which the maximum number of sunspots is recorded) and a “solar minimum.” In the 1850s Sir Richard Carrington used sunspots to make more exact measurements of the solar rotation period and noted its latitude-dependent nature; equatorial regions rotate faster than polar regions do. He also noticed the tendency of sunspots to originate at higher latitudes early in the solar cycle and then migrate toward the equator.

The solar corona was occasionally observed in ancient times. Solar eclipses were recorded at least back to the 8th century B.C. according to Assyrian and Chinese records. During an eclipse the intense photosphere is obscured and the higher layers of the solar atmosphere can be observed, including the chromosphere (appearing as a pink thin layer at the time of totality) and the corona (see Figure 1.3). The first recorded observation of the corona was in the first century A.D. By the 1800s, solar eclipses were used to make detailed studies of the

corona and the first photograph of the corona was made during the 1851 eclipse. Non-eclipse observations were not made until the coronagraphs of the 20th century – a coronagraph is a device which uses a disk to occult the bright solar disk so that the faint corona can be imaged.

A typical way to record sunspot observations in the 17th through mid-19th centuries was to project a telescope image onto a screen and sketch it. In 1859 Carrington (1859) and Hodgson (1859) were independently observing sunspots in this way when they each noticed a transient brightening within a sunspot group. This event is now known to be a solar flare observed in white light, a rare occurrence. The flare was associated with a huge geomagnetic storm a day later, with bright aurorae (caused by flare-accelerated charged particles interacting with the Earth’s magnetic field and atmosphere) seen from almost all over the Earth. This gave hints of the intimate connection between solar flares and geomagnetic activity. Greater detail on the history of solar observations and the Sun-Earth connection can be found in, for example, Phillips (1995) and an interesting description of the events surrounding the 1859 Carrington flare is found in Clark (2007).

With modern instruments, it is now known that solar flares are the most powerful accelerators in the solar system, accelerating electrons up to hundreds of MeV and ions up to tens of GeV (Benz 2008). Total energy output can be up to  $10^{32}$ – $10^{33}$  ergs in as short a time as 10–1000 seconds. As with the 1859 flare, some of this energy can reach the Earth in the form of high-energy photons and charged particles, interfering with power and communications systems, causing radiation damage to spacecraft, and threatening the health of astronauts or pilots/passengers in high-latitude flight paths.

With 10 years of *RHESSI* observation, high-energy aspects of flares have become far better understood, and the role of the corona as energy source and acceleration site has become well established. The prevalence of coronal sources, the flare frequency distribution, and the relationships in space and time between HXR-producing electrons and gamma-ray-producing ions have been well-studied. Despite these gains, some outstanding questions remain. What particle acceleration mechanisms can transfer energy from the coronal magnetic field to kinetic energy with the required efficiency? What is the source of the huge number of accelerated electrons inferred from HXR flare footpoint observations? What role do flares play in the heating of the corona to its observed high temperature of 1–2 MK?

Answering these questions will not only satisfy our curiosity about our nearest neighbor, but will provide insight into energetic astrophysical processes in faraway stellar systems and galaxies. With spatially resolved, sensitive remote measurements as well as in-situ measurements, the Sun can serve as a laboratory for the study of magnetism and particle acceleration in phenomena across the universe.

As we shall see, further probing of the high-energy aspects of solar flares requires the development of HXR instrumentation with higher sensitivity and dynamic range than is currently available with *RHESSI*.

## 1.4 What's ahead

This dissertation will present some of the relevant problems in high-energy solar physics, demonstrate attempts that are being made to address these problems in minute ways, and suggest future observational tools for further investigation. Chapter 2 will describe our current understanding of solar flare energetics, introduce the problems of flare particle acceleration and coronal heating, and describe the observational methods and tools that are available to study these problems. Chapter 3 will provide detail on *RHESSI*, the most sensitive solar HXR observer to date. Chapters 4 and 5 will display case studies of the investigation of coronal HXR sources using *RHESSI* observations of occulted flares. Chapter 6 will introduce the *FOXSI* sounding rocket payload and describe the scientific motivation for the instrument. Details of the instrument components will be provided in Chapters 7 and 8, and a description of the first rocket flight will be presented in Chapter 9. Chapter 10 will conclude with a preview of potential future work.

Almost all dissertations are the work of teams, not individual students, and this dissertation is no exception. One of the main topics here is the design, building, testing, and flight of the *FOXSI* sounding rocket payload, for which at least a dozen scientists and engineers are responsible. To facilitate the evaluation of my work, I include here a summary of my contributions to the work presented in this dissertation: The topics in Chapters 2 and 3 are summaries of others' work. Chapters 4 and 5 are solar flare case studies for which I am the primary author. The remaining chapters concern the *FOXSI* instrument. As the graduate student on a small payload I have had the privilege to participate in many aspects of the experiment. My main contributions were in the testing and calibration of the *FOXSI* detectors (work for which I was the lead scientist), the design and coding of the FPGA firmware to read out the detectors, simulations of expected *FOXSI* observations of active regions, flight operations, and preparation of the preliminary results of the first flight. I contributed in more minor ways to the calibration of the *FOXSI* optics, the X-ray alignment of the payload, and the display software for monitoring data in-flight.

# Chapter 2

## Solar flare processes

### Abstract

The aim of this chapter is to provide an introduction to the current understanding of high-energy aspects of solar flares, to describe some of the outstanding inconsistencies in high-energy solar astrophysics, and to introduce a few of the observational tools available to address these problems. Topics include a description of the standard solar flare model, theories of reconnection and particle acceleration processes, and the problem of coronal heating. The chapter will finish by demonstrating how hard X-ray (HXR) studies are the most direct method of observing energetic electron populations in the solar corona. Formulae, unless otherwise specified, follow the ‘cgs’ system.

### 2.1 Introduction

Much of our understanding of high-energy aspects of solar flares is often described by a model referred to as the “standard flare model.” This model provides an outline of the mechanisms by which a flare develops and attempts to explain observed features like the locations and time evolution of energetic particles. Particle acceleration in flares is thought to be initially triggered by magnetic reconnection in the corona; unknown acceleration processes then serve to efficiently convert the released energy into energetic particles. Some of the theorized mechanisms by which this acceleration takes place will be described in Section 2.3. The chapter begins with a discussion of the standard model.

### 2.2 The standard flare model

The “standard flare model” usually refers to a two-dimensional model that was progressively developed over many years through work by Carmichael (1964), Sturrock (1966),

Hirayama (1974), and Kopp & Pneuman (1976); for this reason it is also referred to as the CSHKP model, though many other authors have later added to it.

While many aspects of the standard flare model are debated, there is a general agreement that the energy to power solar flares comes from the strong magnetic fields of the solar corona. Prior to the flare, the energy is stored in coronal magnetic fields. Compared to other possible energy sources, coronal magnetic fields win the contest by forfeit; no other source contains (and can transfer) the required energy. As discussed in Tandberg-Hanssen & Emslie (1988), neither thermal nor gravitational energy is sufficient in order to power any but the tiniest flares, and nuclear processes are not applicable in the outer layers of the solar atmosphere. The preflare energy is therefore in the magnetic field and magnetic reconnection is the main driver for energy transfer.

### 2.2.1 Reconnection

Magnetic reconnection can occur when the magnetic fields of the corona become stressed; the fields then reconfigure into a lower-energy configuration. The difference in initial and final energy is available to accelerate particles.

#### Sweet-Parker and Petschek reconnection

The left panel of figure 2.1 shows the most basic geometry, which is commonly called the Sweet–Parker model (Sweet 1958; Parker 1957, 1963). At the top and bottom of the diagram are horizontally-directed magnetic fields. In the center (shaded box), oppositely-directed fields approach; where they meet is a null region of no magnetic field. Far from the null region ideal magnetohydrodynamics (MHD) applies; in the vicinity of the null point is a diffusive region. If there is an electric field pointing out of the page, then the ideal MHD equations allow an inflow  $\vec{v}_{in}$  of charged particles into the reconnection region (vertical gray arrows) so that  $\vec{E} + \vec{v}_{in} \times \vec{B} = 0$ . In order to conserve energy and momentum, there must be a corresponding outflow  $\vec{v}_{out}$  (horizontal gray arrows).

Comparing the energy density in the initial magnetic field  $B_i$  to the kinetic energy density of the outflowing plasma with mass density  $\rho$  shows the maximum velocity that can be attained by the outflow:

$$\frac{B_i^2}{2\mu_0} = \frac{1}{2} \rho v_{out}^2 \quad (2.1)$$

$$v_{out} = \frac{B_i}{\sqrt{\mu_0 \rho}} \equiv v_A \quad (2.2)$$

For a typical solar coronal magnetic field of  $B_i = 10$  Gauss and a coronal density on the order of  $10^9 \text{ cm}^{-3}$ , the kinetic energy per particle is only a few keV, far less than the energies observed in flare-accelerated particles (up to MeV scales for electrons, and GeV scales for protons). The outflow velocity happens to be the Alfvén velocity  $v_A$ .

A careful consideration of the timescales for Sweet-Parker reconnection reveals that reconnection rates are far too low: solar flare reconnection in the corona would occur on a time scale of years rather than minutes or seconds (Shibata & Magara 2011)!

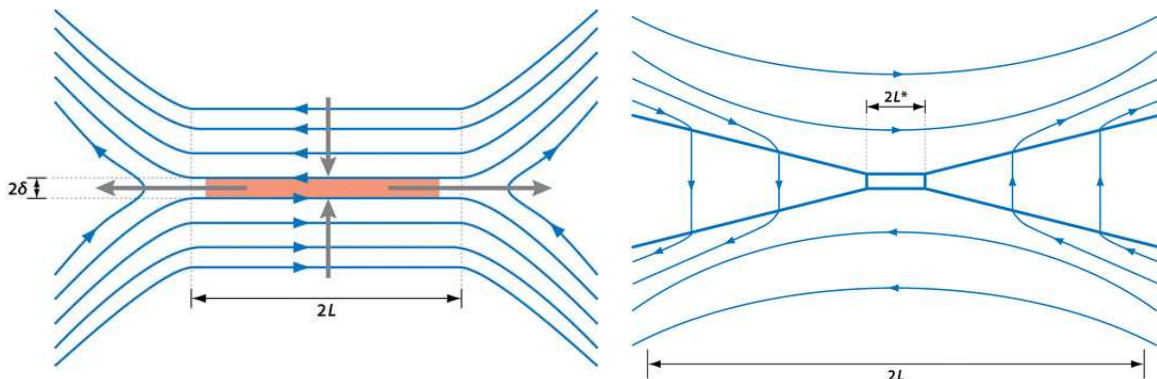


Figure 2.1: (Left) Diagram of the Sweet-Parker model of reconnection, including a thin, long current sheet, inflow (vertical arrows) and outflow (horizontal arrows). (Right) The Petschek model, in which the diffusive region has a finite length and width. Not all particles make it into the diffusive region; many instead are redirected at the standing shocks. Both figures are from Zweibel & Yamada (2009).

Petschek (1964) suggested some upgrades to the Sweet-Parker model (see righthand panel, Figure 2.1). The diffusive region, instead of having a length  $L \gg \delta$ , its thickness, instead has dimensions comparable to each other ( $L \sim \delta$ ). Standing slow MHD shocks separate the inflow from the outflow regions. Most particles do not enter the diffusive region itself but alter their directions at the slow shocks (blue paths in the diagram). This model allowed for much faster reconnection rates than the Sweet-Parker model, on the time scales of flares (Shibata & Magara 2011).

### Collisionless Hall reconnection

The discussion above of Sweet-Parker reconnection stemmed from an ideal MHD perspective, with an anomalous resistivity in the diffusion region requiring the use of resistive MHD in that vicinity. The model can be greatly modified if Hall effects are included. As derived in Chen (1984) and many other texts, the generalized Ohm's Law in MHD is:

$$\vec{E} + \vec{v} \times \vec{B} = \eta \vec{J} + \frac{1}{en_e} (\vec{J} \times \vec{B} - \vec{\nabla} P_e) \quad (2.3)$$

Here,  $\vec{E}$  and  $\vec{B}$  are the electric and magnetic fields,  $\vec{v}$  and  $\vec{J}$  are the plasma velocity and current,  $\eta$  is a resistive term,  $\vec{J} \times \vec{B}$  is a Hall term, and  $\vec{\nabla} P_e$  is a polarization current term. Often, all three of the terms on the right are neglected, leading to the ideal MHD condition mentioned in Section 2.2.1.

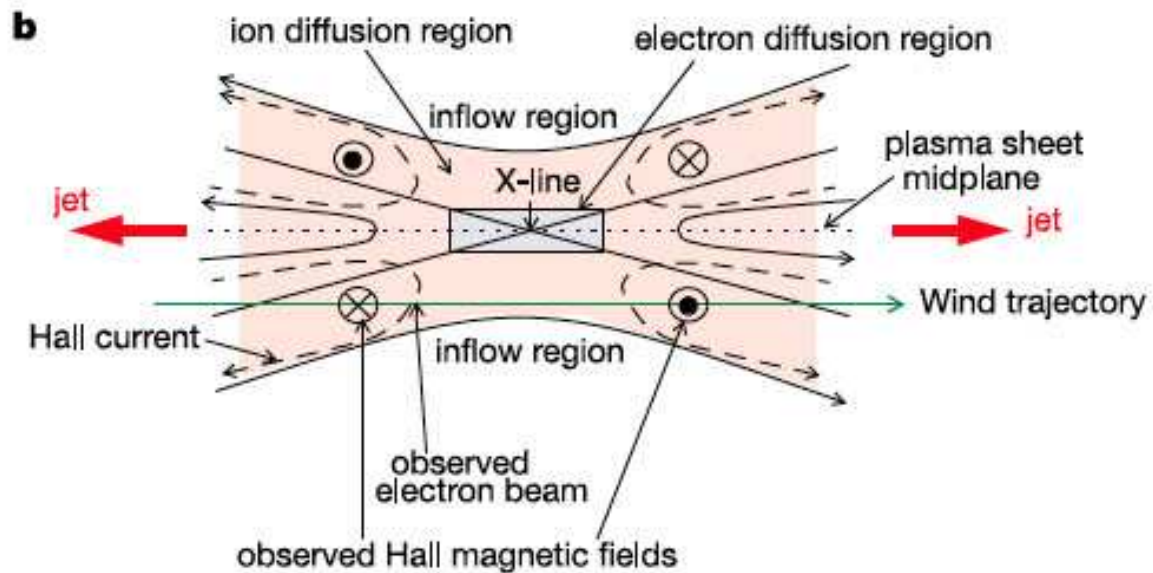


Figure 2.2: A diagram of collisionless Hall reconnection. On scales smaller than the ion gyroradius, ions are not bound to field lines and Hall effects become important. The ion diffusion region is larger than the electron diffusion region, allowing for reconnection on appropriate time scales. This picture has been well-validated in the Earth's magnetotail and could also be applicable to solar flares. Figure is from Lin (2011).

Several commonly used regimes of MHD are:

$$\text{Ideal MHD} \quad \vec{E} + \vec{v} \times \vec{B} = 0 \quad (2.4)$$

$$\text{Resistive MHD} \quad \vec{E} + \vec{v} \times \vec{B} = \eta \vec{J} \quad (2.5)$$

$$\text{Hall MHD} \quad \vec{E} + \vec{v} \times \vec{B} = \frac{1}{en_e} (\vec{J} \times \vec{B}) \quad (2.6)$$

The “frozen-in flux” phenomenon is only a feature of ideal MHD; the Sweet–Parker reconnection model requires an anomalous resistivity to arise in the diffusion region so that collisional effects can tear plasma away from the field lines. Hall MHD, on the other hand, offers a way to decouple particles from the magnetic field without collisions: for length scales smaller than the ion gyroradius the ions can decouple from the magnetic field while the electrons are still tied to field lines. The ion diffusion region is therefore much larger than that of the electrons (see Figure 2.2). The differing motions of ions and electrons produce a current and generate a quadrupolar Hall magnetic field. It can be shown that the reconnection rates expected from this type of reconnection are up to six orders of magnitude faster than those predicted by the Sweet–Parker model (Birn & Hesse 2001).

Lin (2011) reviews examples of the evidence for collisionless Hall reconnection in space plasmas and discusses its potential application to solar flares. Hall reconnection was directly observed by in-situ measurements from the spacecrafts *WIND* and *POLAR* in the magnetotail, finding the characteristic quadrupolar Hall magnetic field (Øieroset et al. 2001) and a fast reconnection rate (Mozer et al. 2002), respectively. Since then, several more direct observations of collisionless Hall reconnection have been recorded, including in laboratory measurements (Zweibel & Yamada 2009). Some observations have noted electrons accelerated up to tens of keV in association with reconnection events (Chen et al. 2008); this acceleration could be due to the collapsing magnetic islands discussed in Section 2.3. Cassak et al. (2006) proposed that steady-state Sweet–Parker reconnection could persist for an extended period before a solar flare while magnetic energy is built up, suddenly transitioning to Hall reconnection at the time when explosive energy release is observed.

### 2.2.2 Standard flare geometry

Reconnection is thought to be the instigator of solar flares. But many of the well-observed aspects of flares happen far from the reconnection and acceleration sites. A diagram of the main features of the most common standard flare geometry is shown in Figure 2.3. The chain of events is started with a volume of plasma that rises from the chromosphere into the corona, lifted by magnetic buoyancy, a phenomenon that occurs when high magnetic field strength within the plasmoid causes it to have a lower density than its surroundings, causing it to rise due to gravitational forces. In two dimensions this plasmoid can be thought of as a discrete cell; in three dimensions the ends of this “flux rope” are actually anchored in the photosphere. Upon rising into the corona and finding its way obstructed by the coronal magnetic field, the plasmoid pushes its way upward, stretching the fields it encounters along

the way, until magnetic stress builds to the point that reconnection becomes favorable. The field lines reconnect, and the resulting field is a flare loop (shown in orange in Figure 2.3) below the reconnection site.

Processes in the reconnection region energize electrons and ions up to MeV and GeV scale energies, respectively. (See section 2.3 for a discussion of acceleration mechanisms.) Accelerated particles are ejected from the reconnection region in one of two directions: (1) Electrons and ions streaming anti-sunward have the opportunity to escape the Sun and stream along field lines in interplanetary space. These electrons sometimes emit radio waves (see Section 2.5.2); the electrons and ions whose paths coincide with the Earth are often detected in-situ. (2) Sunward-streaming particles are injected into the flare loop, where they may be magnetically trapped in the loop due to the strong magnetic fields at the base of the loop. If they are trapped, then eventually pitch-angle scattering drives them into the loss cone and they precipitate into one of the bases of the loop in the chromosphere, referred to as the flare footpoints. The high chromospheric density (as compared to the corona) causes the energetic particles to lose all their nonthermal energy via collisions, and the particles are effectively stopped. This energy goes into (among other processes) heating of the chromosphere. The heated plasma expands in the only direction that pressure will allow – upward, filling the flare loop with hot (10–20 MK) plasma, a process known as chromospheric evaporation (e.g. Fisher et al. 1985). In all moderate-to-large flares the hot loop is observed in soft X-rays (SXR) and the extreme ultraviolet (EUV), which are sensitive to high-temperature plasma, while the flare footpoints, where rapid deceleration of the electron beams taken place, emit in HXRs (Saint-Hilaire et al. 2008; Fletcher & Hudson 2008).

This picture places the acceleration region in the corona, and several observations concur. Aschwanden et al. (1995) studied HXR timing vs energy and found a 20 ms delay between 25-50 keV and 50-100 keV HXR emission; this was interpreted as a time-of-flight difference between faster and slower electrons from the top of the flare loop to the footpoints. Furthermore, a few studies have demonstrated the existence of double HXR sources in the corona (Sui & Holman 2003; Liu et al. 2008; Glesener et al. 2012). These double sources are usually interpreted to be symmetric about the reconnection site.

In order to confirm and complete this flare model, it is necessary to make sensitive observations of the acceleration region itself, as well as of any escaping energized particles from the region. As we shall see, achieving this goal requires more sensitive measurements than are currently available.

### 2.2.3 Interchange reconnection

A scenario closely related to the standard flare model is that of “interchange reconnection. This scenario is very close to the standard model in that reconnection between emerging flux and the overlying coronal magnetic field energizes particles, causing a bright solar flare. However, in the case of interchange reconnection the overlying magnetic field takes the shape of so-called open field lines. The term “open field line” is a misnomer since Maxwell’s equations reassure us that all magnetic field lines must be closed. The reason

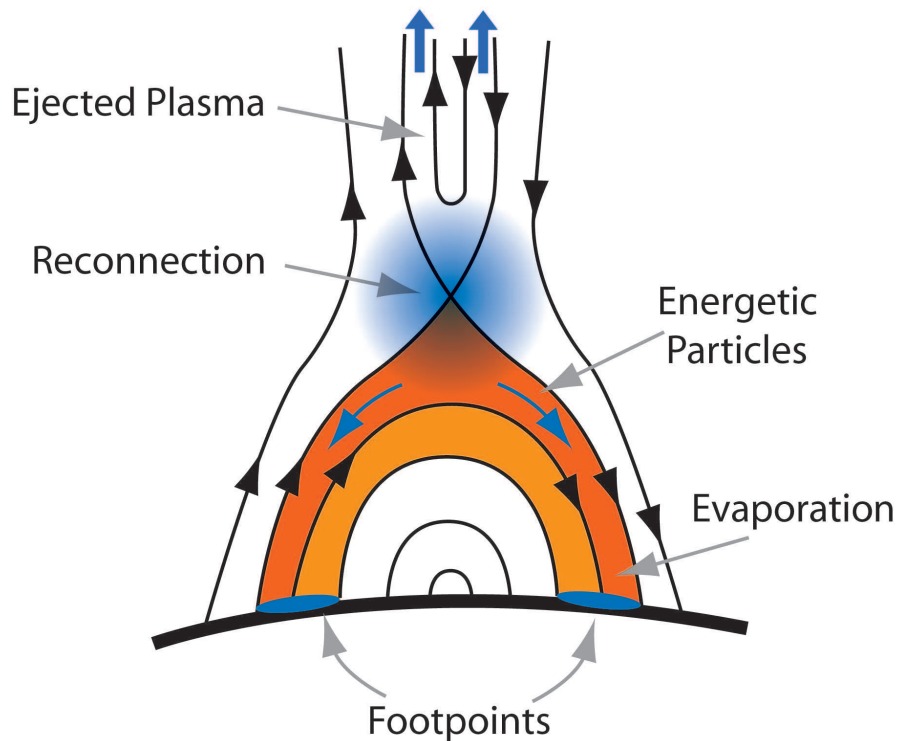


Figure 2.3: Two-dimensional diagram of the standard flare model. A rising plasmoid (not shown) instigates reconnection with the overlying coronal field, producing the magnetic field drawn here. Particles are accelerated in the shaded central region; energized electrons can then stream down the flare loops (orange), or escape upward into interplanetary space. Image is from Christe (2007), based on Sturrock (1966).

some coronal fields are referred to as open is that a field line anchored in the photosphere may extend outward through the solar corona and far out into interplanetary space before eventually bending back on itself and returning to its source at the Sun. For flare studies, in which only a small section of the chromosphere and corona are observed, the field lines can be thought of as open.

Reconnection with emerging flux can cause an open field line to switch the location of its photospheric footpoint. A diagram of such a geometry is shown in Figure 2.4. Post-reconnection field lines take the shape of a small post-flare loop (left side of diagram) and open field lines. As in the standard flare model, accelerated particles can be injected into the flare loop or else can escape to interplanetary space on the open field. As shall be seen in Chapter 4, jets of slower plasma from the chromosphere or the corona can also be generated along the open lines and travel outward along the same paths as the initial energetic particles take.

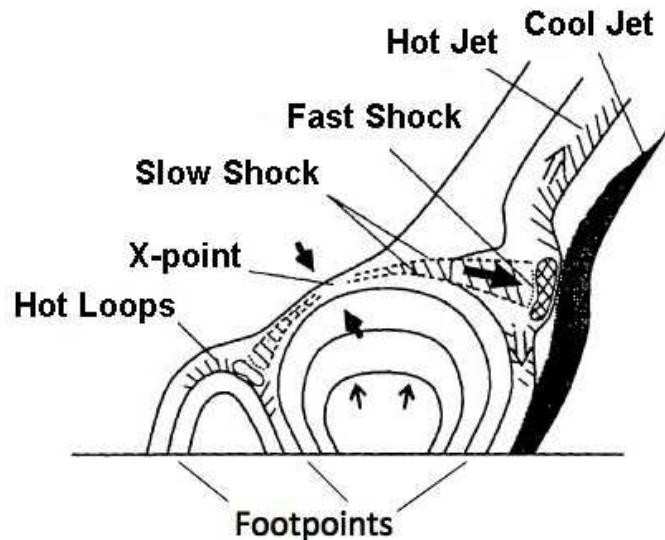


Figure 2.4: Two-dimensional diagram of an interchange reconnection geometry, from Shibata et al. (1997). Interchange reconnection has been proposed as an explanation for solar jets observed in the EUV and SXR; the role of energetic electrons in this model will be explored in Chapter 4.

## 2.3 Flare acceleration mechanisms

The standard flare model does not specify the exact mechanisms by which magnetic energy is efficiently transferred into particle kinetic energy. In fact, Carmichael (1964) had this to say about acceleration mechanisms: “The process by which the particles are accelerated does not have to be identified – all we need say is that the observations seem to require such acceleration.” Much of the characterization of the standard model proceeds assuming a “black box” including the reconnection site and its surroundings from which particles emerge at the observed energies (up to MeV and GeV scales for electrons and ions, respectively). The acceleration site does not need to be exactly the same as the reconnection site; several of the mechanisms discussed here are applicable in the region surrounding the reconnection point.

There are several theories for what processes might occur inside this black box. As discussed in section 2.2.1, traditional reconnection itself cannot accelerate particles up to the observed energies. However, additional processes could take place near the reconnection region. Several of the following processes are discussed in detail in Aschwanden (2006).

### Electric field acceleration

Direct acceleration by steady-state electric fields in the corona could produce a runaway effect, accelerating electrons and ions to very high energies. This can only occur if the

electric force on the particles is greater than the attractive force between negative electrons and positive ions, which are accelerated in opposite directions by the electric field (e.g. Holman 1985). The electric field could be fragmented, producing a large number of small-scale currents. In order for acceleration to persist, this scenario requires a return current, i.e. a current opposite to and canceling the current caused by direct electric field acceleration. The return current can consist of a large number of particles with a smaller velocity than that of the accelerated particles.

### **Turbulent acceleration**

Direct electric field acceleration requires steady-state fields. If the coronal fields are instead time-varying then wave-particle interactions can transfer energy into particles. Particles constantly interact with whichever waves have frequencies in resonance with the particles' gyrofrequencies or harmonics thereof. Stochastic acceleration occurs if these interactions result in a net transfer of energy into particle kinetic energy (e.g. Petrosian & Liu 2004).

The most important waves are (Aschwanden 2006): Alfvén, magnetosonic, and ion sound waves for ions; and Whistler, Langmuir, and electromagnetic waves for electrons. Energy transfer by wave-particle interactions should produce characteristic turbulent power spectra that could be identified. Stochastic acceleration requires a certain degree of pre-acceleration past an energy threshold above which the mentioned waves become resonant, and also requires a degree of wave turbulence to be present in the plasma.

### **Shocks**

Shocks, or boundaries between sub-Alfvénic and super-Alfvénic velocities, are ubiquitous in space plasmas. Shocks can accelerate particles via first-order Fermi processes, wherein a charged particle is accelerated when encountering a magnetic mirror moving towards it in the charged particle's frame of reference (Fermi 1949). If one shock interaction occurs per particle, this is known as shock drift acceleration, while if multiple interactions take place then diffusive shock acceleration is applicable. Fast shocks (in a quasi-perpendicular field) are the most efficient type of shock accelerators.

There is a wide range of evidence for particle acceleration in shocks throughout the solar system, for example in association with Type II radio bursts caused by shocks traveling outward from the Sun into interplanetary space (e.g. Pulupa et al. 2010). Several studies have considered the application of shock acceleration to flares. For example, Bai et al. (1983) proposed shocks propagating upwards from footpoints to explain time differences between ion and electron flare emission. Somov & Kosugi (1997), Tsuneta & Naito (1998) and others applied the fast shocks associated with reconnection to flare particle acceleration.

### **Magnetic islands**

A reconnection current sheet may split into many magnetic islands via a tearing mode instability. Drake et al. (2006a,b) demonstrated via particle-in-cell (PIC) simulations that

many magnetic islands can be produced in a long current sheet and can acceleration particles trapped within them as they contract. This process is effective in a low  $\beta$  environment, i.e. one where the magnetic energy density is much higher than the particle pressure. The process quenches when  $\beta \sim 1$  (when particle pressure and magnetic pressure are roughly the same). An observation by Krucker et al. (2010) appears to support this model, as bulk energization of electrons high in the corona was observed, with  $\beta$  (as determined from coronal magnetic field measurements and particle density estimates) rising from a low value prior to the impulsive phase to  $\sim 1$ .

### Footpoint acceleration

Fletcher & Hudson (2008) proposed that chromospheric footpoints, not the corona, are the location of flare particle acceleration. In this model, Alfvén waves arising from the coronal reconnection site travel down flare loop legs and excite particles in the chromosphere. This model avoids the problem of the large number of electrons required to match the thick-target HXR interpretation; an abundance of electrons is available in the chromosphere (though not in the corona). However, the exact mechanism for particle energization is not identified in this model.

### Observational considerations

Raymond et al. (2012) list some requirements that must be fulfilled by candidates for flare particle acceleration mechanisms, some of which include the ability to accelerate electrons up to MeV scales and ions to tens of GeV, high efficiency (up to  $\sim 50\%$ ), and fast reconnection rates to match the observed X-ray and radio time variations. The preceding discussion of candidate mechanisms shows that better observations could help distinguish between them via: (1) measurement of electron spectra as close to the time and place of reconnection as possible, in order to identify features characteristic of specific mechanisms; and (2) measurement of the acceleration locations, which could be the reconnection site itself, collapsing fields, nearby shocks, or flare footpoints. As we shall see, both of these goals require better sensitivity and more dynamic range than is available in current instruments.

## 2.4 The coronal heating problem

As mentioned in the introduction, the coronal temperature is 1–2 MK at quiescent times. During flares, temperatures of 20–30 MK are typically attained and occasionally “superhot” temperatures of 30–50 MK have been observed (Caspi & Lin 2010). These temperatures are in stark contrast to the photospheric temperature of 5800 K. In addition, the corona must experience several types of energy loss: heat conduction to the cooler chromosphere, radiative losses, and mass losses via the solar wind, which is a steady-state flow of material throughout the solar system and is thought to have its source in the corona and/or chromosphere. Withbroe & Noyes (1977) tabulated these losses (see Table 2.1),

Parameter	Quiet Sun	Coronal hole	Active region
Transition layer pressure (dyn cm <sup>-2</sup> )	$2 \times 10^{-1}$	$7 \times 10^{-2}$	2
Coronal temperature ( $K$ , at $r \approx 1.1R_{Sun}$ )	1.1 to $1.6 \times 10^6$	$10^6$	$2.5 \times 10^6$
Coronal energy losses (erg cm <sup>-2</sup> s <sup>-1</sup> )			
Conduction flux $F_c$	$2 \times 10^5$	$6 \times 10^4$	$10^5$ to $10^7$
Radiative flux $F_r$	$10^5$	$10^4$	$5 \times 10^6$
Solar wind flux $F_w$	$\lesssim 5 \times 10^4$	$7 \times 10^5$	$< 10^5$
Total corona loss $F_c + F_r + F_w$	$3 \times 10^5$	$8 \times 10^5$	$10^7$
Chromospheric radiative losses (erg cm <sup>-2</sup> s <sup>-1</sup> )			
Low chromosphere	$2 \times 10^6$	$2 \times 10^6$	$\gtrsim 10^7$
Middle chromosphere	$2 \times 10^6$	$2 \times 10^6$	$10^7$
Upper chromosphere	$3 \times 10^5$	$3 \times 10^5$	$2 \times 10^6$
Total chromospheric loss	$4 \times 10^6$	$4 \times 10^6$	$2 \times 10^7$
Solar wind mass loss (g cm <sup>-2</sup> s <sup>-1</sup> )	$\lesssim 2 \times 10^{-11}$	$2 \times 10^{-10}$	$< 4 \times 10^{-11}$

Table 2.1: Temperatures and energy losses for the corona and chromosphere, from Withbroe & Noyes (1977). Differentiations are between active regions, the quiet Sun, and coronal holes. See Section 1.2 for a description of these different regions.

finding a total coronal energy loss of  $10^5$  to  $10^7$  erg cm<sup>-2</sup> s<sup>-1</sup> for quiet to active regions, respectively. In order to maintain a steady-state temperature and volume, an energy input into the corona equivalent to these losses is required. As of today, this heating source is unidentified and remains one of the largest problems in solar physics.

It is generally accepted that the needed energy must originate from the photosphere (for example in convective motion of photospheric footpoints) and propagate into the corona. One form of energy transport considered to explain coronal heating is Alfvén waves. These waves can certainly propagate into the corona, but the low coronal density makes it difficult to dissipate these waves there except through fortunate phase mixing of the wave frequencies with local gyrofrequencies (Heyvaerts & Priest 1983).

De Pontieu et al. (2011, 2009) observed mass flow associated with chromospheric spicules (small jets from the chromosphere). Although spicules had been observed for decades, these were the first observations that confirmed their association with mass upflow into the corona. The mass flow from these spicules is calculated to be enough to replace the coronal energy loss; spicule heating is thereby a strong candidate for the role of coronal heating.

### 2.4.1 Flare heating

Another possibility is that the required energy input is supplied by flares. As has been shown in this chapter, flares are thought to be explosive releases of energy from the coronal magnetic field. The role of the photosphere is to manipulate the footpoints of coronal field lines so as to stress the field and trigger reconnection. Flares therefore provide a possible energy input into the corona.

Flares are often categorized by energy, with “large” flares having total thermal energies of  $10^{30}$ – $10^{33}$  ergs. “Microflares” are those having energies down to six orders of magnitude below the largest flares, or  $10^{27}$ – $10^{30}$  ergs. Thermal emission from these flares is observed in HXRs and they are always observed in active regions. Flares below this scale are referred to as “nanoflares” and have energies of  $10^{24}$ – $10^{27}$  ergs. These emit thermal radiation in extreme ultraviolet (EUV) wavelengths. The smallest flares have been statistically studied by Krucker & Benz (1998); Parnell & Jupp (2000); Aschwanden et al. (2000), while microflare frequencies were studied by Christe et al. (2008a); Hannah et al. (2008) and Shimizu (1995).

Figure 2.5, from Hannah et al. (2008), combines many of these results into a flare frequency distribution over total flare energy, from nanoflares to large flares. In general, the number of flares  $N$  with thermal energy  $W$  follows a power law:

$$\frac{dN}{dW} = A W^{-\alpha} \quad (2.7)$$

where  $A$  is a normalization constant and  $\alpha$  is a power-law index of approximately 1.8. As pointed out by Hudson (1991), the exact value of  $\alpha$  has important ramifications, as can be seen by looking at the power in the flare distribution. The power  $P$  released by flares in an energy range  $[W_{min}, W_{max}]$  is:

$$P = \int_{W_{min}}^{W_{max}} \frac{dN}{dW} W dW = \frac{A}{2-\alpha} W^{(2-\alpha)} \Big|_{W_{min}}^{W_{max}} \quad (2.8)$$

Examination of this result shows that if  $\alpha < 2$  then the largest flares contribute most to the total power, while if  $\alpha > 2$  then it is the low-energy side of the flare distribution that determines the total power. Observations of microflares and large flares reveal a power-law index of 1.8, indicating that most of the power is in these flares. However, the actual power observed in micro- and large flares is not enough to provide the necessary energy input to the corona to maintain its high temperature. Furthermore, the implication that the largest flares (which are rare) are the largest contributors of coronal energy input would be troublesome. **Therefore, observations of the flare frequency distribution to date indicate that flare energy is insufficient to heat the corona.**

### 2.4.2 Nanoflare heating

However, subtleties in the lower-energy (the nanoflare) side of the flare frequency distribution may change that conclusion. From Figure 2.5, studies of nanoflare frequencies (in

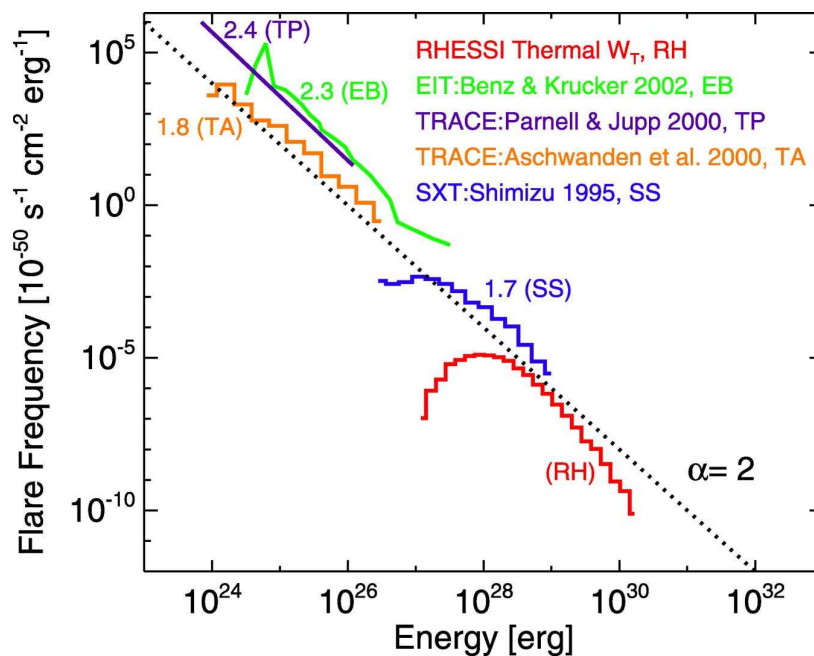


Figure 2.5: Distribution of flare energies from nanoflares (left) to microflares (right), as measured in thermal SXR and EUV, with some of the measured power-law indices shown. The distribution at higher flare energies roughly follows a power law with an index of 1.8. Whether nanoflares follow the same distribution has important implications for the role of nanoflares in coronal heating. Figure is from Hannah et al. (2008).

particular, the studies of Benz & Krucker (2002) and Parnell & Jupp (2000)) have found steeper power-law indices than that observed in larger flares, and in some cases have found that  $\alpha > 2$ . These studies are quite sensitive to systematic influences, for example in flare selection, and so the exact value of  $\alpha$  is uncertain. This would indicate that nanoflares are the more important driver for total flare power. But why would nanoflares display a different behavior than larger flares do?

The term *nanoflare* was first coined by Parker (1988), who throughout the 1970s and 1980s developed a theory of small-scale reconnection events occurring all over the Sun as an energy input to the corona (Parker 1983). In Parker’s view, a nanoflare was essentially a reconnection quantum, the basic unit of energy release, and flares were made up of many of these quanta. These small-scale reconnection events would arise from the random walk of photospheric footpoints of coronal magnetic fibrils, which would become intertwined, as illustrated in Figure 2.6. Tangential discontinuities in the magnetic field would arise, leading to current sheets and reconnection. These small reconnection bursts would not be limited to active regions but would be ubiquitous all over the Sun; Parker (1983) envisioned the Sun as a “swarm” of nanoflares.

The term “nanoflare” has since evolved to refer to flares of a certain size, as defined in

section 2.4.1. Small-scale energy release events occurring frequently all over the Sun are now more commonly referred to as “network flares.” In some contexts, the terms are the same: a search for nanoflares in the quiet Sun is a search for network flares.

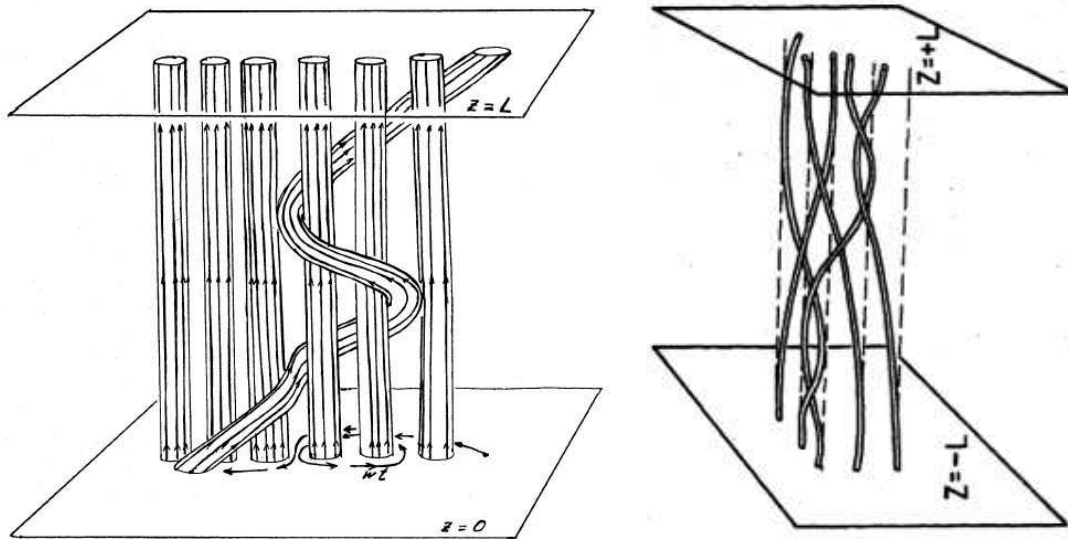


Figure 2.6: Illustrations of magnetic fibrils intertwining due to random footpoint motions in the photosphere, from (left) Parker (1972) and (right) Parker (1983). These motions can cause magnetic stress to build, resulting in small reconnection events.

Several studies have investigated EUV and SXR brightenings in the quiet Sun, which may be nanoflares/network flares; it is these studies that make up the lower-energy side of the flare frequency distribution shown in Figure 2.5. In addition, radio studies hint at nonthermal components to these brightenings (Krucker et al. 1997). If nonthermal components exist, it would lend credence to the argument that these brightenings are proper flares, containing magnetic reconnection and particle acceleration, and could thus serve as an energy input to the corona. So far, it is known that these brightenings are “flarelike,” in that they have impulsive rises and decays, they occur in small loops, and sometimes occur simultaneously with jets. However, a HXR signal, which would allow the nonthermal properties of these brightenings to be assessed, has proved elusive. No HXR instrument has yet recorded a significant signal from quiet-Sun nanoflares. **Greater HXR sensitivity is therefore needed in order to assess nanoflares as a source of significant energy input to the corona.** The ways in which current HXR instrumentation falls short in this respect will be discussed in Chapter 6.

## 2.5 Methods of observation

Every part of the electromagnetic spectrum is used to study the Sun, and a diverse set of observing tools exists, including spacecraft, sounding rockets, high-altitude balloons, and ground observatories. In addition, particles escaping the Sun into interplanetary space can sometimes be detected in-situ by spacecraft. Observations in multiple energy ranges can study different emission mechanisms and thus gather information on a greater number of solar parameters, so X-ray and gamma-ray studies of high-energy solar phenomena are frequently complemented by SXR, EUV, optical, and radio observations for context. This section does not pretend to be comprehensive but presents an overview of the major emission mechanisms important to the solar flare analysis in this dissertation.

### 2.5.1 X-ray emission from the Sun

A charged particle (for example, an electron) scattering off other charged particles (for example, ambient ions) produces bremsstrahlung (“braking,” or “free-free”) radiation. For electrons of energies at the keV scales and higher some emitted radiation is in the X-ray range. The term *soft* X-rays refers to lower energy X-rays, for solar flare studies this term is typically used for radiation on the order of 1 keV ( $\sim 1$  nm wavelength). Higher energies are called *hard* X-rays. There is quite a bit of variation in the usage of these terms in various field and by various observers: sometimes radiation up to 10 keV is called soft; at other times the terms are used to distinguish between thermal and nonthermal emission. Soft X-ray observations from the *Geostationary Operational Environmental Satellites (GOES)* are commonly used to categorize solar flare magnitudes with the classes A, B, C, M, or X. (A-class flares have peak *GOES* fluxes of  $< 10^{-7}$  W m $^{-2}$ ; classes increase logarithmically, with X-class flares having peak fluxes of  $> 10^{-4}$  W m $^{-2}$ .) The X-ray spectrum has a characteristic shape that depends on whether the emitting electron population is thermalized (thermal bremsstrahlung) and if not, how much of the electrons’ energy is lost when interacting with the target plasma volume (nonthermal thin- and thick-target bremsstrahlung). Much of the discussion here is adapted from Aschwanden (2006) and relies on HXR principles and studies documented by Brown (1971), Lin (1974), and Hudson et al. (1978).

A classical description of charged particle scattering is that of Rutherford scattering, in which the differential cross section  $\frac{d\sigma}{d\Omega}$  can be found to be:

$$\frac{d\sigma}{d\Omega} = \frac{Z}{4} \left( \frac{e^2}{m v^2} \right)^2 \frac{1}{\sin^4(\theta/2)} \quad (2.9)$$

It has been assumed that the incident particle is an electron of velocity  $v$  and having electric charge  $-e$ .  $\Omega$  is the solid angle into which the electron is scattered and is related to the deflection angle  $\theta$  by  $d\Omega = 2\pi \sin\theta d\theta$ .  $Z$  is the charge of the scattering nucleus; for an electron scattering off a proton,  $Z = 1$ .

Consideration of the power radiated by the scattered electron and conservation of energy and momentum leads to a total cross section for bremsstrahlung. The details of this

calculation are given in Jackson (1962). For solar flare analysis, the Bethe-Heitler cross section is often used, in the following form:

$$\sigma(E, \epsilon) \approx \frac{8\alpha r_e^2 m_e c^2}{3} \frac{1}{E \epsilon} \ln \left[ \sqrt{\frac{E}{\epsilon}} + \sqrt{\frac{E}{\epsilon} - 1} \right] \quad (2.10)$$

$E$  is the energy of the incident electron and  $\epsilon$  is the energy of the radiated photon.  $\alpha$  is the fine structure constant,  $r_e$  is the classical electron radius,  $m_e$  is the electron mass, and  $c$  is the speed of light. The radiated intensity  $\frac{dN_x}{dt d\epsilon}$  is dependent on the cross section  $\sigma(E, \epsilon)$  and the densities of electrons  $n_e$  and target particles  $n_p$  (here, assumed protons) in the target volume  $V$ :

$$\frac{dN_x}{dt d\epsilon} = \int_{\epsilon}^{\infty} \sigma(E, \epsilon) v(E) \left( \int n_p n_e(E) dV \right) dE \quad (2.11)$$

where  $v$  refers to the incident electron velocity. The limits of integration are chosen as such because all electrons at or above a given photon energy could radiate a photon at that energy.

In other words, to compute intensities, the cross section is convolved with the instantaneous electron distribution  $n_e$  in the source; this relationship implicitly defines that electron distribution. Therefore, if the X-ray distribution is observed then the initial electron distribution can be inferred by inverting this equation. **This relationship makes X-rays the most direct observation method for flare-energized electrons as they move about the coronal and chromospheric plasma.**

### Thermal bremsstrahlung

A plasma containing a Maxwellian distribution of electrons can emit bremsstrahlung in the X-ray range if the temperature is high enough. For a velocity distribution  $f(v)$  of electrons with average thermal velocity  $v_{th}$ ,

$$f(v) = \sqrt{\frac{2}{\pi}} \frac{v^2}{v_{th}^3} e^{-v^2/v_{th}^2} \quad (2.12)$$

The emitted X-ray distribution is:

$$I(\epsilon) \approx 8.1 \times 10^{-39} \int_V \frac{\exp(-\epsilon/k_B T)}{T^{1/2}} n^2 dV \quad (\text{keV s}^{-1} \text{ cm}^{-2} \text{ keV}^{-1}) \quad (2.13)$$

where  $T$  is the plasma temperature and  $k_B$  is Boltzmann's constant. Here, it has been assumed that the plasma is made up of equal densities of electrons and protons:  $n_e = n_p = n$ . This equation can be found by considering the velocity-dependent power lost by the scattering electron and convolving this with the Maxwellian velocity distribution in equation 2.12. See Aschwanden (2006) for a walkthrough of the derivation.

If the assumption is made that the temperature  $T$  is constant over the volume observed, then measurement of the X-ray distribution directly leads to a calculation of the electron temperature of the emitting plasma. The photon distribution is then commonly written as:

$$I(\epsilon) \approx 8.1 \times 10^{-39} \frac{\exp(-\epsilon/k_B T)}{T^{1/2}} EM \quad (\text{keV s}^{-1} \text{ cm}^{-2} \text{ keV}^{-1}) \quad (2.14)$$

where  $EM$  is the emission measure, defined as  $EM = \int n^2 dV$  (here in  $\text{cm}^{-3}$ ), and often approximated as  $n^2 V$ . The emission measure is a measure of the “brightness” of the X-ray source, and depends directly on the density of scattering electrons and number of target ions in the volume. (Here, the two densities are assumed to be the same.)

In the case that the emitting source is not isothermal, the emission measure may be composed of temperature-dependent components:

$$EM = \int dEM = \int \frac{dEM}{dT} dT \quad (2.15)$$

In solar flares, thermal X-ray emission is common from hot (10–20 MK) plasma filling up flare loops. It should be noted that a thermal X-ray spectrum generally includes more components than the bremsstrahlung (free-free) emission discussed here. Other components include recombination (free-bound) emission and spectral lines.

### Nonthermal bremsstrahlung

A second common emitter of bremsstrahlung X-rays is a nonthermal electron beam traveling through ambient plasma. It is usually assumed that the density  $n_e$  in the nonthermal beam is small compared to the ambient plasma density  $n_p$ . In solar flares, these beams could be outflow electrons leaving the acceleration region or beams of energized electrons streaming down flare loop legs or magnetically trapped in flare loops. (Beams of energized electrons ejected into interplanetary space could also emit bremsstrahlung, but to date this emission has been too faint to detect.)

Flare-accelerated electrons frequently follow a power-law energy distribution  $f(E)$  with power-law index  $\delta$ :

$$f(E) \propto E^{-\delta} \quad (2.16)$$

Brown (1971) demonstrated that for a power-law electron distribution the resulting X-ray distribution  $I(\epsilon)$  is also a power law. The index for this power law is usually called  $\gamma$ :

$$I(\epsilon) = A\epsilon^{-\gamma} \quad (2.17)$$

$A$  is a normalization factor. The next section will discuss the relationship between the photon and electron power-law indices  $\gamma$  and  $\delta$ . Brown (1971) also showed that equation (2.11) can

be inverted in this case, allowing the electron distribution to be directly inferred from the photon distribution, if some approximations about the target plasma are made.

It has been empirically determined that solar flare energetic electron populations do not extend to arbitrarily low energies; instead an apparent cutoff in the electron distribution happens at a cutoff energy. This cutoff produces a break in the emitted X-ray power-law. This a key parameter in many observations since the total energy in energetic electrons depends strongly on how low in energy the distribution extends.

Figure 2.7 shows an example *RHESSI* X-ray spectrum demonstrating thermal components (red), a nonthermal power-law (magenta), and nuclear contributions at the highest (gamma-ray) energies (blue). Gamma-ray observations will not be discussed in this work.

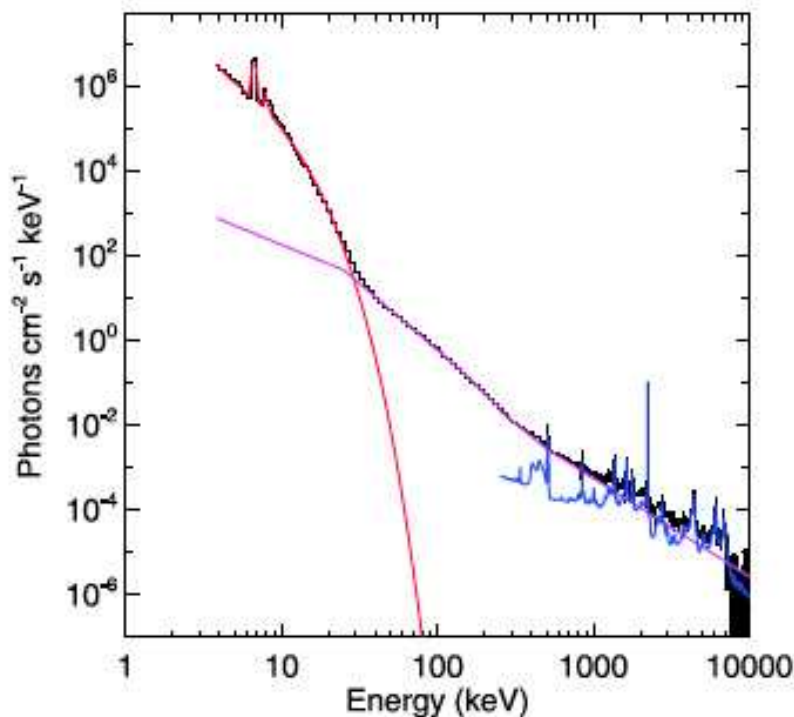


Figure 2.7: A sample *RHESSI* X-ray spectrum from the 2002 July 23 class X4.8 solar flare, showing thermal (red) and nonthermal (pink) components, as well as gamma ray lines from nuclear contributions (blue). Image is from Lin (2011).

### Thin and thick targets

Two approximations are frequently used in order to simplify the relationship between the electron and photon distributions. In a “thin target,” plasma densities are so small that the incident electrons pass through the target volume with their energies essentially unchanged. This scenario is unfeasible, since the electrons must lose some energy in order

for X-ray emission to be observed, but it provides a useful approximation for emission from the tenuous solar corona. A “thick target,” on the other hand, is dense enough that the incident electrons lose all their energy through collisions in the target volume. This is often an accurate description for electron beams that impinge on the dense chromospheric footpoints of a flare loop.

Brown (1971) and Lin (1974) give simple relationships between the electron and photon power-law indices in this approximation:

$$\gamma = \delta + 1 \quad \text{Thin target} \quad (2.18)$$

$$\gamma = \delta - 1 \quad \text{Thick target} \quad (2.19)$$

The power deposited by incident electron beams in the thin or thick target model approximations can be calculated directly from photon spectrum parameters (see Brown (1971) and Lin (1974) for the derivation of these formulas).  $E_0$  is the energy at which a break is observed in the photon spectrum.  $\beta(x, y)$  refers to the  $\beta$  function.

$$P_{thin>(> E_0) = 9.5 \times 10^{24} \gamma(\gamma - 1) \beta\left(\gamma - \frac{1}{2}, \frac{3}{2}\right) A E_0^{-(\gamma-1)} \quad \text{erg s}^{-1} \quad (2.20)$$

$$P_{thick>(> E_0) = \gamma P_{thin} \quad (2.21)$$

The instantaneous electron distribution  $n_e$  can be calculated directly from the photon spectrum without needing to resort to assumptions about the thin or thick nature of the target if the ambient plasma density  $n_p$  is known (Lin 1974):

$$\frac{dn_e}{dE} = 1.21 \times 10^{42} \gamma(\gamma - 1)^2 \beta\left(\gamma - \frac{1}{2}, \frac{3}{2}\right) \frac{A E^{(-\gamma+\frac{1}{2})}}{n_p V} \quad (2.22)$$

Strictly speaking, this equation is a thin-target equation, since it refers to the emitting electron population at any given instant in time and thus does not consider a changing distribution. The time spent by the electrons in the target volume (i.e. whether they are replenished) must be known in order to compute the total distribution of energetic electrons over the observation interval.

## 2.5.2 Radio emission

Radio instruments have proven to be useful tools to complement SXR and HXR studies, since they can give additional information about energetic electron processes. Comprehensive reviews of the emission processes and relevant observations can be found in Dulk (1985) and Bastian et al. (1998).

### Coherent emission

Energetic electron beams traveling through ambient plasma give rise to a bump-on-tail instability. The onset of this instability occurs when there is a significant positive gradient

in the electron velocity distribution. Wave-particle interactions quickly generate Langmuir waves at the characteristic plasma frequency  $\nu_p$ :

$$\nu_p = \sqrt{\frac{e^2 n_e}{\pi m_e}} \approx 9000 \sqrt{n_e} \quad (Hz) \quad (2.23)$$

Wave-wave interactions subsequently convert Langmuir waves into electromagnetic waves of the same frequency. (These nonlinear processes are not yet fully understood.) For electron beams moving through the tenuous solar corona near flares, ambient densities are on the order of  $10^8$ – $10^9$ , corresponding to radio frequencies on the order of 100 MHz. Electron beams escaping outward to interplanetary space emit at even lower frequencies characteristic of the low density plasma through which they travel.

Often associated with flares are radio bursts falling quickly in frequency; these are referred to as Type III radio bursts and are thought to be emitted from energetic electron beams accelerated in flares as the beams travel radially outward and encounter plasma of decreasing density. Occasionally series of Type III bursts will contain features drifting upward in frequency – these signatures indicate electron beams propagating sunward into denser regions (Bastian et al. 1998).

### Incoherent emission

One of the most significant contributors to incoherent radio emission is gyrosynchrotron emission from mildly relativistic (tens of keV to MeV) electrons gyrating around the coronal magnetic field lines. This emission is usually at high harmonics of the electron gyrofrequency  $\nu_c = eB/m_e$ . This type of emission could arise, for example, from flare-accelerated electrons magnetically trapped in flare loops. As the electrons traverse the loop they encounter varying magnetic field strengths, leading to broadband emission, usually in the centimeter wavelength range.

### 2.5.3 Time evolution of flares

Flare time profiles often display two phases commonly referred to as the impulsive and gradual phases. The impulsive phase of a flare is the phase in which energy is released, usually characterized by a sudden onset of intense HXR emission. Nonthermal HXR emission is most commonly seen in this phase and appears in bursts with one or more peaks. This is followed by a gradual phase of thermal emission from flare-heated plasma, which then slowly decays as the plasma cools.

Many, though by no means all, flares exhibit a behavior known as the Neupert effect (Neupert 1968), in which the integral of emission from energetic electrons (i.e. HXRs or microwave) matches the profile of thermal emission (EUV or SXR). This is expected in the

standard model; as the flare energy is initially carried in energetic electrons which then collisionally deposit energy and thermalize, so that thermal emission from the ambient plasma dominates the decay phase.

## Chapter 3

# The Reuven Ramaty High Energy Solar Spectroscopic Imager (RHESSI)

### Abstract

The *Reuven Ramaty High Energy Solar Spectroscopic Imager (RHESSI)* is a NASA Small Explorer spacecraft launched in 2002 to study high-energy X-ray and gamma-ray emission from solar flares. *RHESSI* improved on its predecessors by offering superior sensitivity, energy range (3 keV–17 MeV), energy resolution, and spatial resolution (down to 2.3 arcseconds) in a single instrument, making it an ideal tool for studying HXR and gamma-ray signatures of particle acceleration in the corona. In this chapter, the scientific goals, main hardware components, and basic data analysis principles of *RHESSI* will be discussed.

### 3.1 Introduction

The stated goal of *RHESSI* (Lin et al. 2002) is to “understand particle acceleration and explosive energy release in the magnetized plasmas at the Sun.” Solar flares release a tremendous amount of energy, up to  $10^{33}$  ergs, in a short amount of time (100–1000 seconds). The preflare energy is stored in the coronal magnetic field, and  $\sim 10$ –50% of this energy goes into accelerated electrons and ions. An extraordinarily efficient acceleration mechanism is needed, but the details of the mechanism have been relatively unknown. Through imaging spectroscopy of the HXR and gamma-ray emission from solar flares, the behavior of the accelerated electrons and ions can be studied.

Such lofty goals give rise to a demanding set of requirements for the instrument. The energy range must be large enough to enable study of both thermal and nonthermal X-ray bremsstrahlung spectra as well as high-energy nuclear gamma-ray lines. The energy resolution must be fine enough to resolve nuclear lines, resolve steep thermal spectra, and ascertain the energy cutoff between thermal and nonthermal spectra, important for determining the

energy content in energetic electrons. The mass and cost of the payload also need to be appropriate for a NASA Small Explorer mission.

*RHESSI* met these requirements by implementing an indirect Fourier-based imaging system and cooled, high-purity germanium (Ge) detectors, achieving high sensitivity over almost four orders of magnitude in energy (from 3 keV to 17 MeV). The bulk Ge detectors are segmented into thinner front segments that measure X-rays up to 100 keV and large rear segments that can stop gamma-rays without being restricted by the front-segment dead time. Insertable attenuators reduce flux at lower energies when count rates are above a certain threshold, reserving detector livetime for higher energies. An overview of the *RHESSI* instrument is given in Lin et al. (2002) and its accompanying papers.

*RHESSI* was originally designed as a 2–3 year mission but with capabilities appropriate for longer-term operation. As a result *RHESSI* remains highly functional after almost eleven years, allowing it to observe maxima of solar cycles 23 and 24. The instrument was built with the capability to temporarily warm the detectors from their nominal temperature of 75K (maintained by a mechanical cooler) to 100 degrees Celsius in order to repair damage suffered from their high-radiation environment; annealing has been performed three times over the course of the mission and has been critical in maintaining detector performance.

As intended, *RHESSI* has provided a wealth of information on particle acceleration and energy transfer in solar flares. A review of *RHESSI*'s scientific achievements can be found in a dedicated issue of the *Space Sciences Review* (Emslie et al. 2011). A short list of some of the major accomplishments was compiled by Brian Dennis and can be found in the *RHESSI* Nuggets<sup>1</sup>. *RHESSI* produced the first imaging of gamma-ray flare footpoints, finding a displacement between the locations of energetic ions and electrons (Hurford et al. 2003, 2006). Rich coronal HXR structure and dynamics were discovered, including several cases of double coronal sources (Sui & Holman 2003; Liu et al. 2008; Glesener et al. 2012), and it was found that coronal HXR sources (and therefore the presence of energetic electrons in the corona) are probably present in most flares (Krucker & Lin 2008). For the first time, microflares could be studied in detail; they were found to occur only in active regions and behave similarly to larger flares (Hannah et al. 2008; Christe et al. 2008a). *RHESSI*'s fine energy resolution enabled investigation of the low-energy cutoffs of nonthermal electron spectra, resulting in more accurate estimates of nonthermal electron energy content (Holman et al. 2003, and others).

Figure 3.1 shows the components of the *RHESSI* instrument, with examples of its capabilities. Table 3.1 gives some of the figures of merit for the instrument. The following sections will briefly describe *RHESSI*'s main components.

## 3.2 Imaging system

At the time *RHESSI* was proposed, focusing optics were not available in the HXR or gamma-ray ranges due to the small grazing angles and highly polished surfaces necessary

---

<sup>1</sup>[http://sprg.ssl.berkeley.edu/~tohban/wiki/index.php/RHESSI's\\_Tenth\\_Anniversary](http://sprg.ssl.berkeley.edu/~tohban/wiki/index.php/RHESSI's_Tenth_Anniversary)

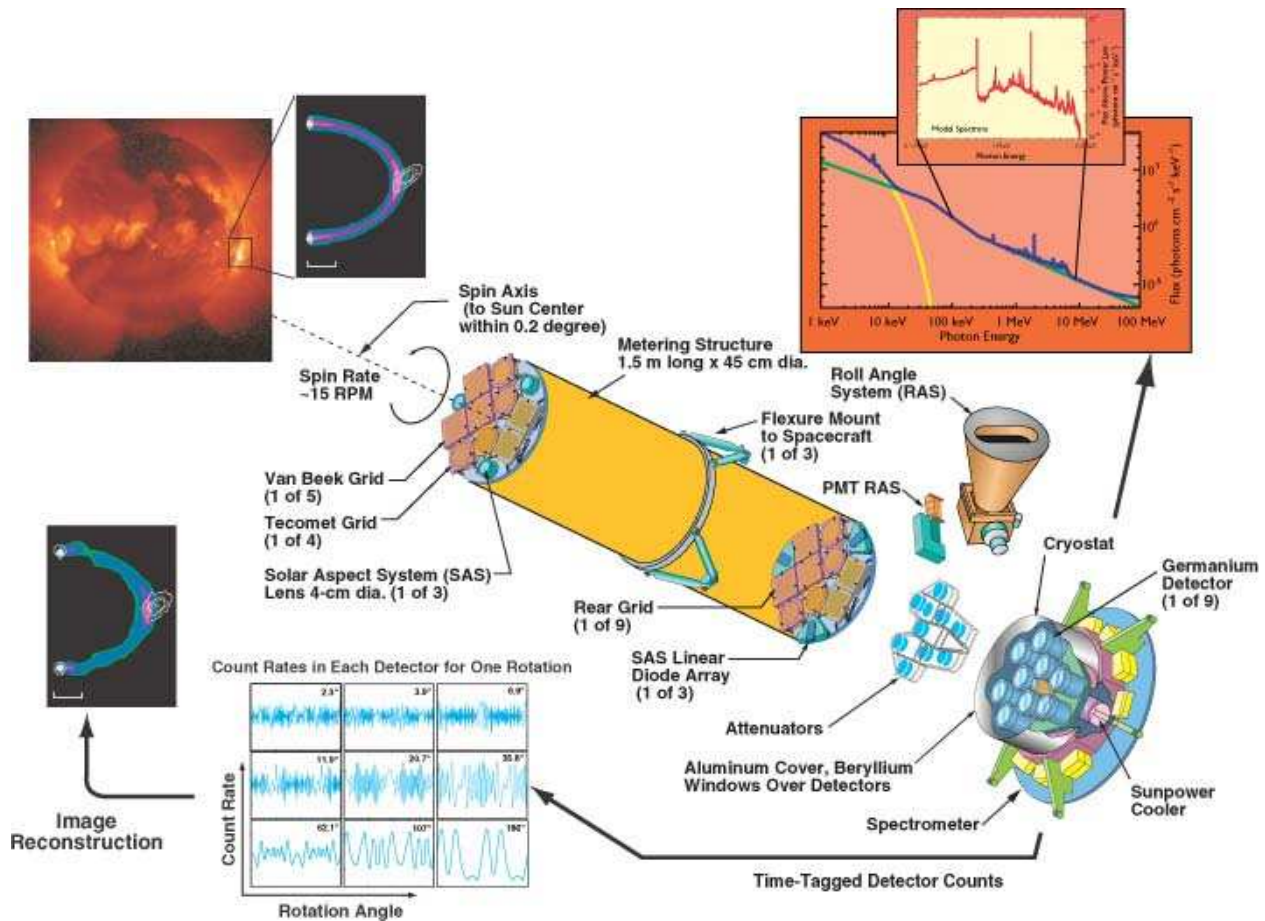


Figure 3.1: Illustration showing the components and capabilities of the *RHESSI* instrument; image from Lin et al. (2002). The imaging system consists of nine pairs of grids separated by 1.55 m and works by modulating source flux as the spacecraft spins. This Fourier-based method of imaging can resolve sources down to 2.3 arcseconds. The detector system is composed of nine identical coaxial high-purity germanium detectors, offering good energy resolution and sensitivity up to 17 MeV.

Table 3.1. The *RHESSI* Instrument

---

Energy range	3 keV to 17 MeV
Energy resolution (FWHM)	$\lesssim 1$ keV at 3 keV, increasing to $\sim 5$ keV at 5 MeV
Angular resolution	2.3 arsec to 100 keV, 7 arcsec to 400 keV, 36 arcsec to 15 MeV
Field of view	Full Sun
Detectors	9 Ge detectors (7.1-cm diameter by 8.5 cm length)
Imager	Rotation modulation collimator system: 9 pairs of grids with pitches from $34 \mu\text{m}$ to 2.75 mm
Launch date	2002 February 5
Anneals	November 2007 March 2010 February 2012

---

to reflect photons at these energies. (A decade and a half later, such technology *does* exist for HXR energies—this topic will be explored in the later chapters—but not for gamma ray energies.) Because of this, an indirect imaging system was chosen, similar to that used on predecessors such as Hinotori and the *Yohkoh* Hard X-ray Telescope (HXT). *RHESSI*'s imaging system is described in detail in Hurford et al. (2002).

Rotation modulation collimators (RMCs) operate by selectively blocking portions of incoming flux. The collimator pattern is chosen such that the flux transmitted to the detector depends on the source position within the field of view. By moving the pattern with respect to the source and measuring the transmitted flux as a function of time, spatial information can be reconstructed. *RHESSI* has nine RMCs, usually referred to as its subcollimators, each with two grids separated by length  $L = 1.55$  m. Each subcollimator has a different grid pitch, which is identical for both grids in the pair. The grid material is opaque to all but the highest energy photons.

Imagine that an X-ray source illuminates a two-grid collimator on-axis with grid pitch  $p$  and grid separation  $L$ . (See the diagram in Figure 3.2.) If the grids are quite thin and the slits and slats are of equal width and exactly coaligned among the grids (an ideal case), then 50% of the intensity is transmitted to the detector. As the source moves off-axis, some of the flux passing through the first grid is blocked by the second grid, so the transmitted intensity is reduced. Moving further off-axis, when the off-axis angle reaches  $p/(2L)$ , no intensity is transmitted. Continuing on, the intensity grows until at an angle of  $p/L$ , the original transmitted intensity of 50% is attained. The quantity  $p/(2L)$  defines the spatial resolution of the imaging system. For *RHESSI*, the nine collimators have spatial resolutions ranging from 2.3 to 183 arcseconds (FWHM).

In order for this technique to work, the collimating pattern must be moved with respect

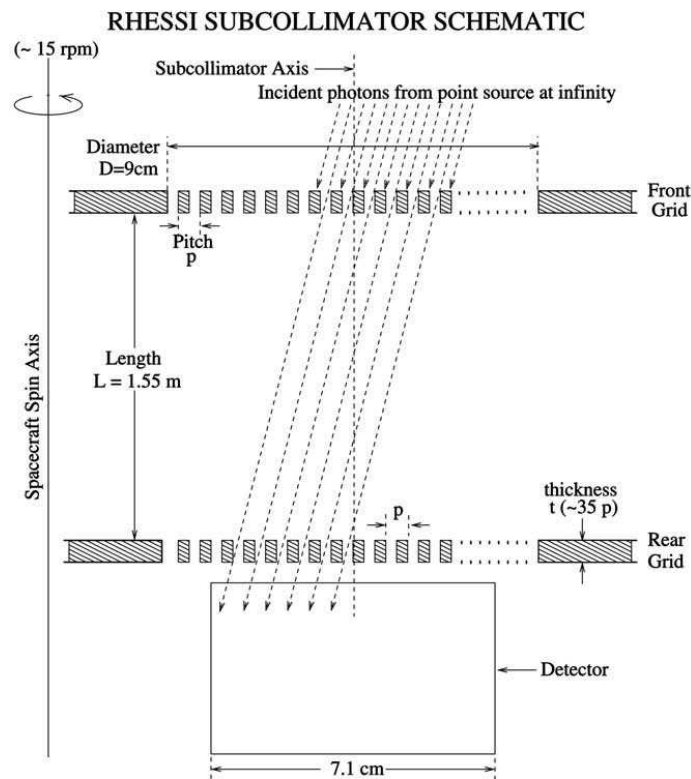


Figure 3.2: Diagram of the RMC imaging system, image from Hurford et al. (2002). Each subcollimator has two identical-pitch grids widely spaced apart. Transmission of X-ray flux through the grids depends on the orientation of the source with respect to the grids. As the spacecraft rotates, this orientation changes and the transmitted flux is modulated in a way that captures two-dimensional spatial information.

to the source. RHESSI modulates the source flux by spinning the spacecraft with a rotation rate of  $\sim 15$  rpm. Because the spatial information is encoded in the measured flux modulation curve, the detector itself does not need to have spatial resolution (for example, multiple electrodes, pixels, or strips). The detector can then be optimized for sensitivity and energy resolution. The detector records the time and energy of each photon. With knowledge of the spacecraft roll provided by *RHESSI's* Roll Aspect System (Fivian et al. 2002), this timing information can be translated into angular information.

The measured intensity curve is quasi-triangular for the ideal case of thin grids with equally sized slits and slats. The amplitude of the modulation curve is proportional to the source intensity, and the frequency and phase of the curve depend on the source location. This principle is illustrated in Figure 3.3, in which theoretical modulation curves of simple Gaussian sources of various locations and sizes are compared. The source location is encoded in the frequency and phase of the modulation curve, while the spatial extent and flux of the source determines the waveform's peak-to-peak amplitude and mean value. RHESSI differs

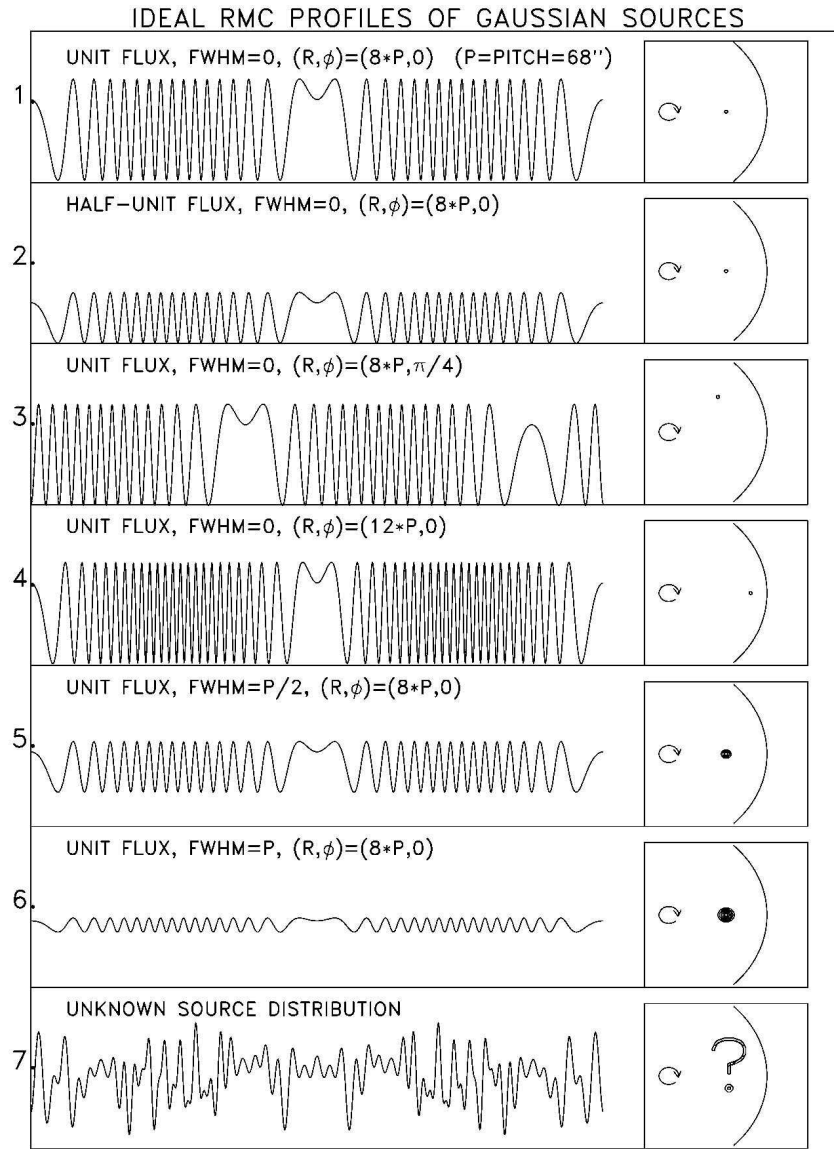


Figure 3.3: Illustration comparing modulation curves for several simple Gaussian sources, image from Hurford et al. (2002). Compared to the reference panel (1), the panels show (2) a reduced amplitude from a fainter source; (3) a phase shift due to angular displacement of the source; (4) a higher frequency from a source located radially distant from the spin axis; (5) and (6) reduced modulation due to an extended source size, and (7) a complicated modulation curve resulting from a more intricate source structure.

from the ideal case with effects due to grid shadowing caused by the non-negligible grid thickness, incomplete photon absorption by the grid at higher energies, and diffraction at the lowest energies. Factoring in these complications, a sinusoidal wave is found to better fit the modulation curve (Hurford et al. 2002).

Sources more complex than those in the first few panels of Figure 3.3 will add together to produce a complicated modulation curve such as that in the bottom panel. The task is then to extract the two-dimensional spatial information of the source(s) on the Sun from this curve. This is a computationally intensive process for which many approaches exist. An overview of the main considerations and some of the more popular methods is found in Hurford et al. (2002). Different Fourier components are sampled as the spacecraft rotates, for a total of up to 1000 independent components. Future instruments could improve on this system with collimators that sample a larger range of spatial frequencies. One such imaging system, with grids selected to measure an almost continuous range of spatial frequencies, will be tested on the Gamma-Ray Imager/Polarimeter for Solar flares (GRIPS) (Shih et al. 2012), a balloon payload slated to fly during the maximum of solar cycle 24.

### 3.3 Spectrometer

*RHESSI*'s science goals require a detector responsive to energies from thermal X-rays to high-energy nuclear gamma rays (3 keV–17 MeV). The detector's energy resolution must be fine enough to separate thermal and nonthermal spectra ( $\sim 1$  keV resolution needed) and also to separate and resolve nuclear de-excitation lines to investigate line broadening. Previous gamma-ray spectrometers were scintillators with insufficient resolution to accomplish these goals.

*RHESSI* met these challenges by utilizing high-purity germanium (semiconductor) detectors, which have good efficiency well into gamma-ray energies and have a small bandgap for fine energy resolution. A full description of the spectrometer is given in Smith et al. (2002). The physics of photon energy deposition and measurement in a solid-state detector will be discussed further in chapter 8 of this dissertation.

Because *RHESSI*'s imaging information is encoded in the modulation produced by the imaging system, the detector system does not need to be pixelized. Instead, a bulk germanium (Ge) detector can be used to maximize sensitivity. *RHESSI* has nine identical detectors corresponding to the nine subcollimators of the imaging system. Each detector has a coaxial, cylindrically symmetric geometry (Figure 3.4, left). The bulk Ge is slightly n-type with a thin boron implant on the outer surface and a layer of diffused lithium ions implanted on the inner core. This inner electrode is broken in such a way that each detector is electrically segmented into two sections. The front segment stops most photons up to  $\sim 100$  keV and has a lower background due to its smaller volume. The rear segment has a volume large enough to measure gamma rays with high efficiency. Because the rear segment is read out through a different channel than the front segment, it is not burdened by the high dead time associated with the high count rate from the front segment. A bias voltage of 2000–4000V

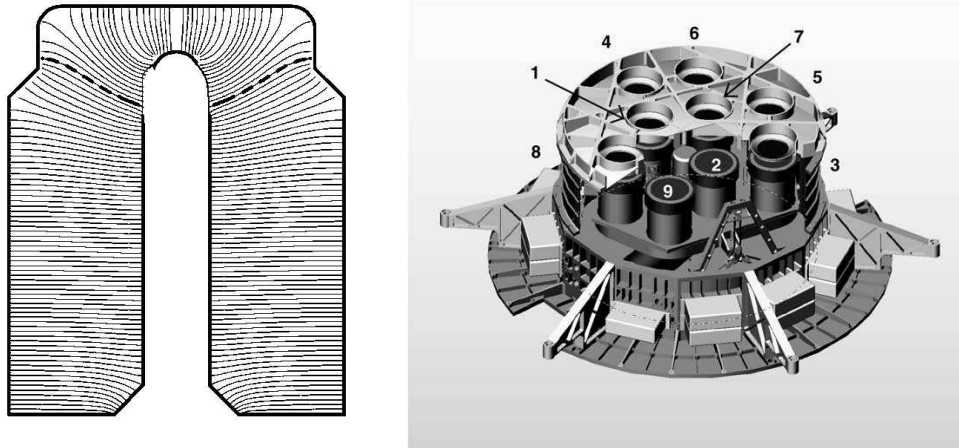


Figure 3.4: The *RHESSI* detector system, images from Smith et al. (2002). (Left) Cross-section of a single coaxial Ge detector, showing example field lines and segmentation. (Right) Model of the full set of nine Ge detectors. Each detector has a corresponding subcollimator in the imaging system.

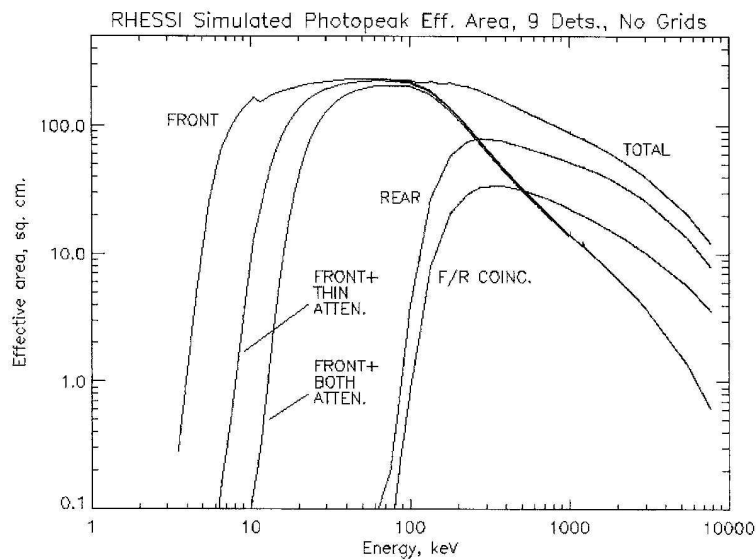


Figure 3.5: Effective area for the *RHESSI* detectors for photopeak absorption, image from Smith et al. (2002). The effective area is shown for the front and rear segments separately and for multiple attenuator states. The total area includes the front- and rear-segments with no attenuators and the F/R coincidence curve shows the area for events measured in both front and rear segments.

is applied to fully deplete the detector. A passive graded-Z shield surrounds the sides of the front segments.

Separate circuitry reads out the front and the rear segments of each detector. This circuitry includes a fast shaper for pileup rejection and a slow shaper (with 8  $\mu$ s peaking time) for energy measurement. An analog to digital converter (ADC) converts the slow shaper signal into a 13-bit digital value.

Low-noise operation of a germanium detector requires cooling to  $\sim 75$  K. To accomplish this, the detectors are mounted on a cold plate housed in a cryostat. The temperature is controlled by a Stirling-cycle mechanical cooler, chosen for its efficiency, low weight, and cost-effectiveness.

In high-count-rate situations, the front segment dead time will be so high that low fluxes at higher HXR energies will not be well-measured. Because of this, *RHESSI* was designed with a set of lightweight aluminum attenuators (or “shutters”) that are automatically inserted when the front segment livetime reaches a low threshold. Either a thick, thin, or both attenuators can be inserted just over each detector. After a specified length of time, the attenuators are removed and the livetime is rechecked. This enables good flux measurements from microflares (attenuators are left out) all the way up to the brightest flares (attenuators are inserted to suppress low-energy counts). The attenuators are moved by applying current to heat shape-memory alloy wires.

## 3.4 Software

RHESSI telemetry data returns a stream of events with 32 bits of data for each photon, including energy information, the detector ID, arrival time, and livetime information. Initial data processing stores this data as Level 0 FITS files. RHESSI analysis software needs to be able to manipulate this data to produce images, spectra, and lightcurves. For imaging, the software must decode the time modulation curves into spatial information. For spectra, the software must subtract a background and deconvolve the energy spectrum with the detector response. The software must be able to process a large data volume (up to a few gigabytes for large flares). A primary goal was to make RHESSI data products widely available in a short amount of time. Details of this software, including the overall structure and design considerations, are given in Schwartz et al. (2002). Several guides to RHESSI analysis are available on the software page of the RHESSI wiki<sup>1</sup>.

Software tools were crafted prior to launch and continually expanded throughout the mission by a dedicated team of scientists. The tools use the Interactive Data Language (IDL) with the SolarSoftWare (SSW) package. RHESSI analysis tools make use of object orientation, a feature new to IDL at the time of the mission planning. Since RHESSI delivers quasi-single-photon data, any user can choose a field of view, pixel size, time integration, energy range, and spatial resolution that suit their particular analysis. This leads to a great deal of analytical flexibility, but requires the user to make many careful decisions along the

---

<sup>1</sup>[http://sprg.ssl.berkeley.edu/~tohban/wiki/index.php/RHESSI\\_Software](http://sprg.ssl.berkeley.edu/~tohban/wiki/index.php/RHESSI_Software)

way. Users can choose to use either a graphical user interface (GUI) or a command line interface, both of which use the same underlying objects and procedures. The GUI guides the user through the choices inherent in producing an image, spectrum, or lightcurve, thus allowing each access for the non-expert, while the command line approach is more useful for large batch processing and repeatable, easily-documented analysis.

### 3.4.1 Image reconstruction methods

Several methods exist of transforming Fourier components measured by *RHESSI*'s rotation modulation system into two-dimensional images; those used to obtain the results in the next two chapters will be discussed here. Most of these algorithms are included in the *RHESSI* software. All of them share the feature that the user can choose the field of view, pixel size, energy range, time interval, and the set of subcollimators for the image. Since each subcollimator has a different spatial scale, this choice affects the resolution of the final image.

#### Back projection

The most straightforward method of *RHESSI* image reconstruction is that of back-projection (Hurford et al. 2002). Here, knowledge of the grid orientation is used to trace back the possible photon paths through the grid to produce a probability map on the Sun. The probability map for a single photon resembles a striped grid. As the spacecraft rotates and multiple photons are accumulated, the cumulative probability map isolates the true location of the X-ray source. At least a half spacecraft rotation ( $\sim 2$  seconds) is necessary to locate the source.

A back projection image gives accurate locations but is subject to large distortions (“side lobes”) caused by sparse sampling of the Fourier plane (Hurford et al. 2002). The other methods are all, to some degree, efforts to reduce these side lobes and produce more detailed and clear images, but each introduces its own uncertainties. A back projection image can also include a “ghost” image on the other side of the spin axis from the true source because the modulation curve is symmetric under a 180 degree source rotation; in practice, the true source is more intense than the ghost because the instrument is not an ideal imager. In Figure 3.6, an image made using back projection (upper left) is compared with other algorithms.

#### Clean

One of the most widely-used *RHESSI* imaging techniques is borrowed from radio astronomy and referred to as the “Clean” method (Hurford et al. 2002). This algorithm assumes the image consists of a superposition of point sources. Even extended source structure can be recovered in this way, by modeling the extended source as a group of closely-spaced point sources.

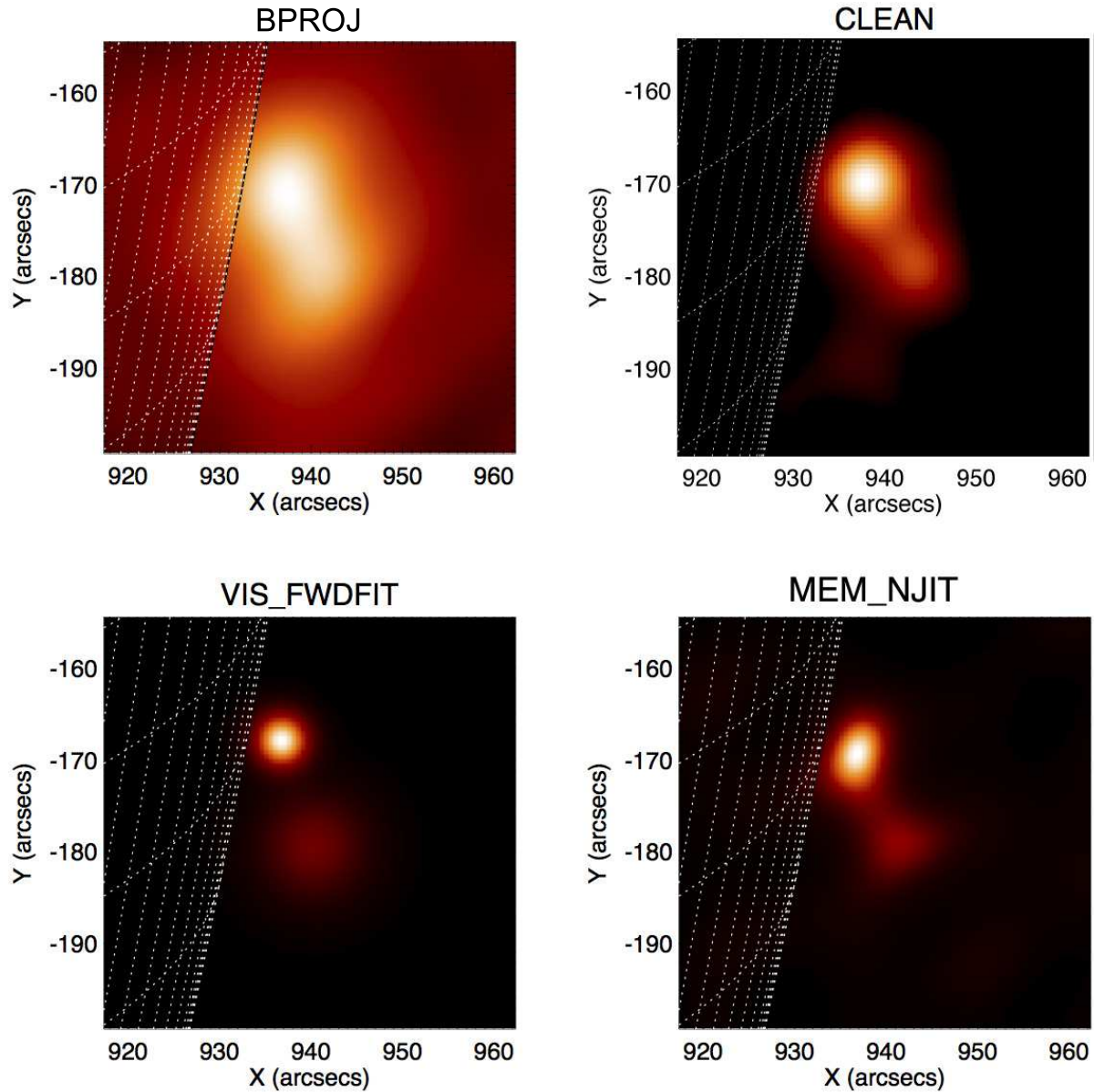


Figure 3.6: Comparison of images made using several standard RHESSI imaging algorithms, including (upper left) back projection, (upper right) Clean, (lower left) visibility forward-fit, and (lower right) Maximum Entropy Method images. The double nature of the source is observed clearly with the visibility-based routines (bottom row). All images are from the time interval 2003 August 21 15:16:15–15:18:00 UT, in the energy range 10–25 keV, and made using subcollimators 3–9.

Beginning with a back projection map (a “dirty” map), this algorithm cleans the map via an iterative process: first, the highest-intensity point in the map is selected and saved to a list of Clean components. The point spread function (PSF) of the imaging system is computed for a point source at this location and with a fraction (default 10%) of the measured intensity. This PSF (which includes the side lobes) is then subtracted from the back projection map, essentially removing that source. The process is repeated until a certain number of iterations is reached or a sufficiently negative value is reached in the residual map. At this point a list of Clean components (point sources) has been accumulated. A new PSF with a Gaussian profile and width corresponding to the resolution of the chosen grids is computed for each source. These PSFs are added together to produce a “Clean” image map. An example is shown in Figure 3.6, upper right. The Clean algorithm is thought to give accurate flux values and reliable source structure (i.e. for flares with good statistics, spurious sources are not produced), but Clean source sizes are somewhat larger than those found using other techniques and fine structure is sometimes not resolved.

### Visibilities

It is often convenient to organize the modulation data into “visibilities,” which are Fourier components of the image (Hurford et al. 2002). To produce a visibility, the modulation curve over a small roll angle is plotted. A sinusoid is fit to this data, giving the amplitude and phase of the visibility for that roll angle. An array of visibilities for all detectors and all roll angles serves as an excellent starting point for several of the *RHESSI* imaging algorithms. A convenience of this method is that data for a particular roll angle can be added up over several rotations in order to produce the modulation curve. In addition, any static offset to the modulation curve does not affect the visibility calculation, so an unmodulated background is automatically subtracted.

The `vis_fwdfit` imaging algorithm in the *RHESSI* software uses a forward-fitting technique to turn visibilities into an image. One must assume a functional form for the source; a single or double Gaussian source, a single elliptical source, or a loop source are current options (Hurford 2006). An example of is shown in Figure 3.6, lower left.

### Maximum Entropy Method

Like the concept of visibilities, the Maximum Entropy Method (MEM) is borrowed from radio astronomy; it is described in Schmahl et al. (2007). The goal of MEM is to maximize the information entropy of the image while minimizing the chi-squared value (as a measure of the goodness of fit). A full mathematical treatment is given in Cornwell & Evans (1985). For *RHESSI*, the most commonly used MEM technique was developed by the New Jersey Institute of Technology and is known as MEM\_NJIT. This algorithm implements the MEM technique on a set of precomputed *RHESSI* visibilities. MEM\_NJIT images are quick to compute and are thought to have accurate flux values and better resolution of fine source structure as compared with Clean, but poorer accuracy in source position (Schmahl et al.

2007). An example of an MEM image is shown in Figure 3.6, lower right.

### Two-step Clean

A variation of the Clean algorithm is used to image a faint, extended source in the presence of a compact, brighter one. This novel method, which is not yet included in the *RHESSI* software, is referred to as “Two-step Clean” (Krucker et al. 2011a). Usually this method is turned to when one of the previous algorithms has produced hints of a faint source nearby a brighter, more compact one. Since the regular Clean method chooses components based on maximum flux, a faint source might not survive the map cleaning. However, if this faint source is extended over a large area, it may encompass a substantial intensity and deserve further investigation.

The first step in the process is to produce a Clean component list as previously described, using the finer subcollimators (for example, grids 1–4). Small grids see reduced modulation for larger sources (see panels 5 and 6 in Figure 3.3) and sources much larger than the spatial resolution of the chosen subcollimators are essentially invisible. The smaller subcollimators, then, will produce an image *only* of the compact source and *not* of the extended source. The result of the first step is thus a list of the Clean components for the compact source only.

Since investigation of the faint, large-area source is the goal, the next step is to make a Clean image using only the larger subcollimators (for example, grids 5–9). At the beginning of this step, the previous list of Clean components with their appropriate PSFs are subtracted from the image, essentially removing the compact source. The Clean process is then continued as usual, with the effect that a detailed map of the extended source is obtained. An example comparing the results of regular Clean, Two-step Clean, and `vis_fwdfit` will be shown in chapter 5.

### 3.4.2 Spectroscopy

RHESSI event data contain the ADC values of all measured photons. Transforming measured count rates binned by ADC value into energy spectra requires knowledge of the detector response for the given detectors at a given time. (The detector responses change over the lifetime of the mission as radiation damage alters detector properties and as detectors are annealed to repair that damage.) The detector response matrix is not, in general, diagonal, since the detector energy resolution is not perfect and because photons may scatter out of the detector without depositing all their energy. Spectral analysis is therefore usually done by forward-fitting a hypothesized spectral shape with an initial guess for each parameter. The guessed spectrum is convolved with the detector response, producing a theoretical count spectrum. This count spectrum is compared with the actual measured counts and a chi-squared value is computed. The process is continued iteratively for different parameter values until the choice with the best chi-squared value is found.

RHESSI spectra are usually computed using the OSPEX<sup>1</sup>, an object-oriented spectral

---

<sup>1</sup>[http://hesperia.gsfc.nasa.gov/ssw/packages/spex/doc/ospex\\_explanation.htm](http://hesperia.gsfc.nasa.gov/ssw/packages/spex/doc/ospex_explanation.htm)

analysis framework. First, a spectral response matrix is computed in the main RHESSI software, specifying the desired detectors, time interval, and energy range. These are exported as FITS files, which serve as an input to OSPEX or other spectral analysis tools. OSPEX has many built-in spectral shapes that can be fit. Those used for the work in this thesis include a Maxwellian thermal spectrum, a nonthermal power law, and combinations of these.

The spectroscopic and imaging properties of RHESSI are not exclusive functions. Since energy information is stored for each photon, spectra can be produced for isolated regions of an image. To make use of this “imaging spectroscopy” capability, a series of images are produced for different energy intervals, with all other parameters (field of view, imaging technique, etc.) kept fixed. The energy intervals should be chosen to obtain the maximum number of energy bins with sufficient statistics in each bin to produce reliable images. A particular spatial region of this imaging cube is then selected and the count rates are computed in that region for each energy bin. This count spectrum can then be fed into the OSPEX (or any other) software to implement spectroscopy for the isolated region. Repeating the procedure, one can produce spectra for several isolated sources in a flare. Examples of *RHESSI* imaging spectroscopy can be found in Krucker & Lin (2002) and Glesener et al. (2012).

## Chapter 4

# Hard X-ray Observations of a Jet and Accelerated Electrons in the Corona

### Abstract

This chapter will demonstrate the use of *RHESSI* observations to study energetic electron populations in a particular case study. This event on 2003 August 21 is a unique HXR observation of a solar jet on the limb in which the flare footpoints were occulted, allowing faint emission from accelerated electrons in the corona to be studied in detail. *RHESSI* observed a double coronal hard X-ray source in the pre-impulsive phase at both thermal and nonthermal energies. In the impulsive phase, the first of two hard X-ray bursts consists of a single thermal/nonthermal source coinciding with the lower of the two earlier sources; the second burst shows an additional nonthermal, elongated source, spatially and temporally coincident with the coronal jet. Analysis of the jet hard X-ray source shows that collisional losses by accelerated electrons can deposit enough energy to generate the jet. The hard X-ray time profile above 20 keV matches that of the accompanying Type III and broadband gyrosynchrotron radio emission, indicating both accelerated electrons escaping outward along the jet path and electrons trapped in the flare loop. The double coronal hard X-ray source, the open field lines indicated by Type III bursts, and the presence of a small post-flare loop are consistent with significant electron acceleration in an interchange reconnection geometry. This analysis has been published in Glesener et al. (2012).

### 4.1 Introduction

The emerging flux reconnection model for flares presented in 2.2.3 was first proposed by Heyvaerts et al. (1977) and later expanded upon by Shibata and others (Shibata et al. 1989, 1992b; Yokoyama & Shibata 1996) to both predict and explain flare-related jets. As discussed in Section 2.2.3, magnetic buoyancy causes magnetic flux to emerge from the

chromosphere into the corona, where reconnection occurs between the emerging field and the overlying coronal field. This is referred to as “interchange reconnection” if a field line that is open to interplanetary space switches the location of its photospheric footpoint. As with the standard flare model discussed in Section 2.2.2, this model places the reconnection site in the corona. Post-reconnection field lines take the shape of a small, hot loop and field lines that are open to interplanetary space.

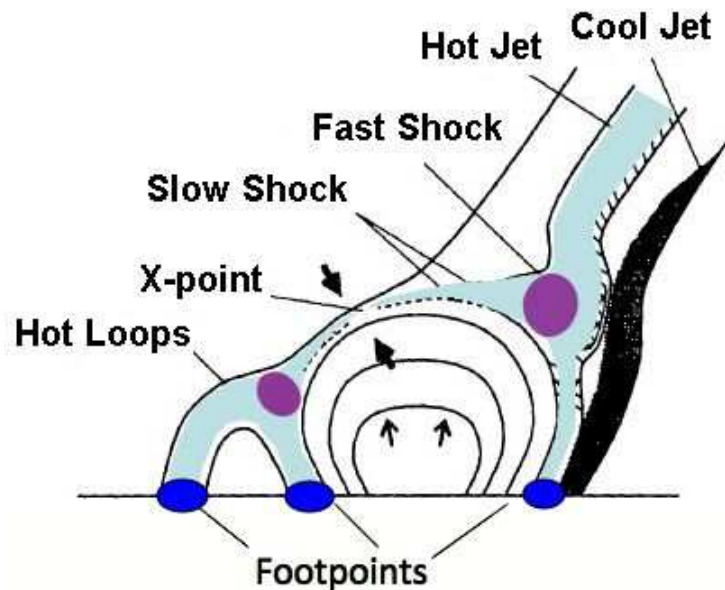


Figure 4.1: Black: The interchange reconnection diagram shown in Figure 2.4, from Shibata et al. (1997). Overlaid on this diagram are hypothetical HXR sources (not from the original model), including paths traveled by energetic electrons (light blue), bright HXR footpoints in which electrons lose all energy (dark blue), and dense shock regions where energetic electrons may undergo collisions (purple). With current instrumentation, the coronal sources are unlikely to be observed in the presence of bright footpoints.

Simulations suggest that a fast shock can arise in regions where the reconnection outflow reaches a strong perpendicular magnetic field. Gas pressure behind this shock could drive a jet along these field lines with a speed on the order of the Alfvén speed. Another jet could arise from chromospheric evaporation; this comparatively cooler jet should have as its characteristic velocity the local sound speed, and could be present concurrently with the former jet (Yokoyama & Shibata 1996).

The soft X-ray jets predicted by this model were first observed by the Soft X-ray Telescope (SXT) aboard *Yohkoh* (Shibata et al. 1992a). Hundreds of jets were observed over *Yohkoh*'s lifetime. Shimojo et al. (1996) performed a statistical study of *Yohkoh* jets, measuring the lengths, lifetimes, and velocities of 100 jets. Apparent velocities were determined to be 10 to 1000 km s<sup>-1</sup>, with 200 km s<sup>-1</sup> the average value.

More recently, Kim et al. (2007) performed a study of three Hinode jets with overlapping *TRACE* coverage, finding velocities from 90–310 km s<sup>-1</sup>. Hinode observations of the polar coronal holes (Savcheva et al. 2007; Cirtain et al. 2007) have found tens to hundreds of X-ray jets per day, with multiple jet velocity components of  $\sim 200$  and  $\sim 800$  km s<sup>-1</sup>. Chifor et al. (2008) determined that a repeated extreme EUV/X-ray jet arose from chromospheric evaporation. H $\alpha$  surges (Roy 1973) have been found to represent cooler counterparts to many hot X-ray jets (Chae et al. 1999; Jiang et al. 2007).

Jets are strongly correlated with Type III radio bursts (e.g. Raulin et al. 1996) and are sometimes associated with impulsive, electron/He<sup>3</sup>-rich solar energetic particle (SEP) events observed in the interplanetary medium (Nitta et al. 2008; Wang et al. 2006), indicating that accelerated electrons have access to open field lines. Any accelerated electrons traveling downward would lose their energies to collisions, producing three HXR footpoints as shown (dark blue) in the diagram in Figure 4.1. Krucker et al. (2011a) studied the HXR emission for 16 flares associated with prompt solar impulsive electron events observed at 1 AU to energies above 50 keV and found that seven of these show three-footpoint configurations consistent with interchange reconnection. Seven of the remaining events show two footpoints (four with an elongated source that may be hiding a third source) and two are unresolved. All 6 events with coverage by the *TRACE* spacecraft show EUV jets with onsets at the time of the HXR emission (within the tens of seconds cadence). This suggests that prompt impulsive electron events are often instigated by interchange reconnection.

Fainter HXR sources should also exist in the corona along nonthermal electron paths and will be brightest where the density is enhanced, for example, in the vicinity of the hypothesized fast shocks (purple regions, Figure 4.1). Compared with footpoints, however, coronal sources are expected to be fainter by  $\gtrsim 1$ –2 orders of magnitude, which is at or beyond the dynamic range of current instrumentation. Furthermore, any coronal HXR emission from jets emitted along the observer’s line of sight will be difficult to disentangle from footpoint emission. Despite these obstacles, Bain & Fletcher (2009) found an example of HXR emission from a large two-ribbon flare on the disk that coincided with an EUV jet. HXR and radio data suggested the presence of nonthermal electrons in the jet itself. In summary, several HXR and radio observations have indicated that interchange reconnection is an important driver for solar jets.

Here, we present *RHESSI* observations of HXR emission from a coronal jet at the limb. The base of the jet (and the accompanying flare) was occulted, so that HXR coronal sources can be studied without the presence of bright footpoint emission. Much of the jet’s motion occurs in a direction transverse to the line of sight, so that elements of the two-dimensional model shown in Figure 4.1 can be clearly seen. We find coronal HXR sources at three distinct times: (1) a double source in the pre-impulsive phase; (2) a near-limb source during the first impulsive burst, coinciding with the lower of the two earlier sources; and (3) an additional, elongated nonthermal source occurring co-temporally and co-spatially with the jet, in the second impulsive burst. This observation is the first to see multiple coronal HXR sources in conjunction with a coronal jet.

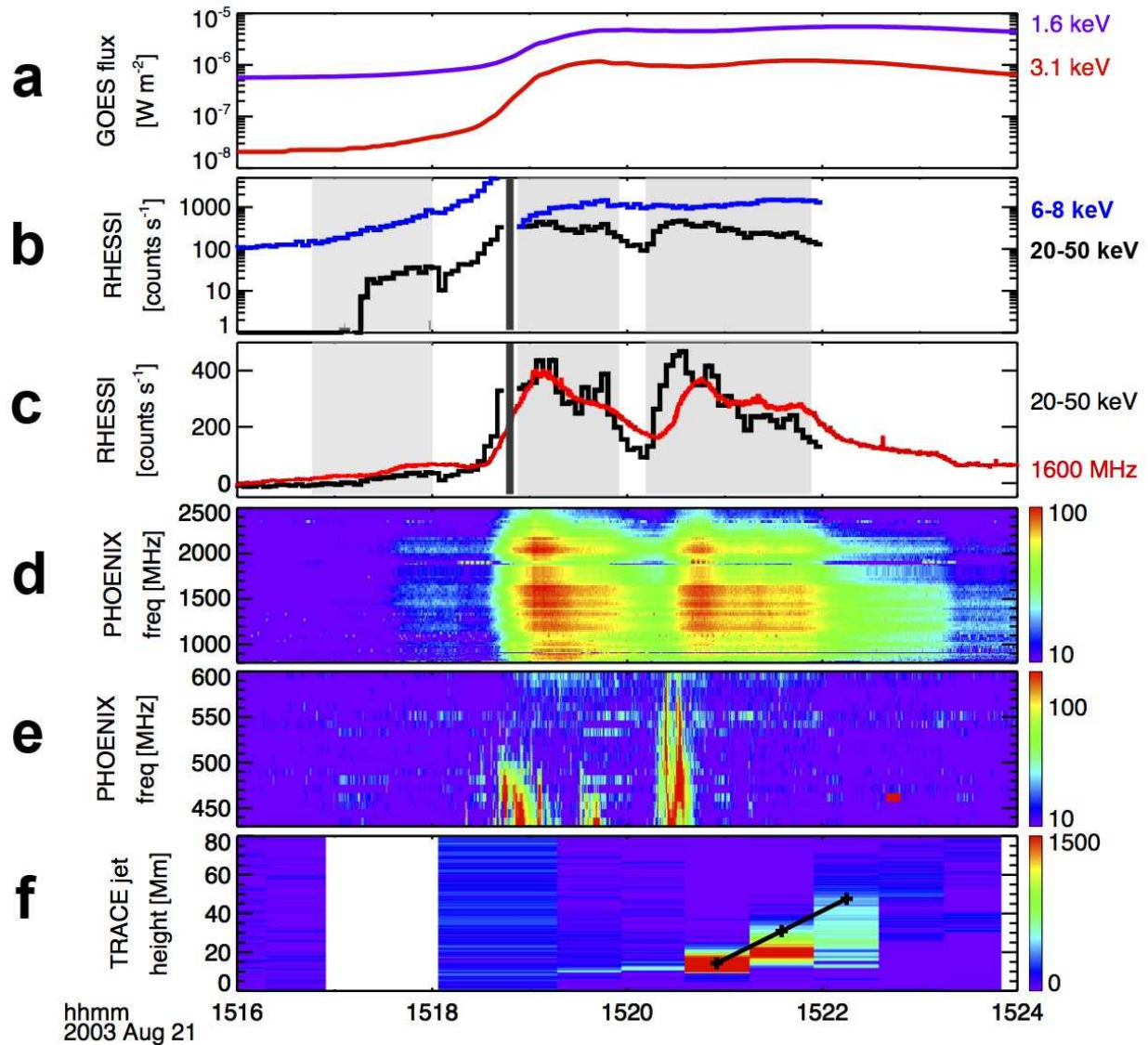


Figure 4.2: Time profiles of the August 21, 2003 limb event. Panel (a): *GOES* lightcurves. Panel (b): *RHESSI* 6–8 keV emission (blue) and 20–50 keV emission (black), log scale. Panel (c): *RHESSI* 20–50 keV emission (black) and Phoenix-2 1600 MHz emission (red), linear scale. Panel (d): Phoenix-2 decimetric bursts. Panel (e): Phoenix-2 Type III bursts. Panel (f): *TRACE* 171Å jet height profile, in Mm above the optical limb. There is a gap in the *TRACE* data before 1518 UT. The jet velocity is the slope of the solid black line fit to three time intervals. In panels (b) and (c), the black bar marks the attenuator motion, while gray shading indicates the image times.

## 4.2 Observations

On 2003 August 21, *RHESSI* observed a flare just over the western solar limb with a pre-impulsive phase and two HXR bursts. This flare began at  $\sim 15:18$  UT and was a *GOES* class C4.9 flare (top panel, Fig. 4.2). To find the most likely heliocentric location of the flare, its active region (10431) was tracked across the solar disk using locations of *GOES* X-ray flares (from the *GOES* event database) and *RHESSI* flares (from the *RHESSI* microflare list). Using actual flare locations was necessary in order to isolate the flaring section(s) of this rather large, complex active region. The flare longitudes were plotted vs time and fit with a linear function, which was extrapolated to locations beyond the limb. Uncertainty in the calculated occultation is taken from the uncertainty in the linear fit parameters (caused by variation in the flare locations). The average flaring location of the active region was thus determined to be disk-occulted by  $1.6 \pm 2.5$  degrees at the time of this flare. It is therefore likely that the event was occulted by between 0 and 4.1 degrees (corresponding to an occultation height of 0 to 1.8 Mm), based on locations of previous flares. The occultation could be even greater if the flare came from a different section of the active region than the one that produced the on-disk flares. Based on this analysis alone, it is impossible to conclude whether the flare was occulted. However, no footpoints are apparent in *RHESSI* X-ray images; only coronal sources are observed (see the discussion at the end of section 4.3.1), leading us to conclude that the event was partially occulted.

### 4.2.1 *TRACE* EUV observations

The *Transition Region and Coronal Explorer* (*TRACE*) (Handy et al. 1999) was observing the limb in the vicinity of the flare. Around 15:20 UT, *TRACE* observed a UV/EUV jet emerging from the region. Figure 4.3 shows a *TRACE* 171Å time sequence of the jet, with a pre-jet image from 15:15:02 UT subtracted from each frame. (Note that a gap exists between 15:23:19 UT and 15:26:20 UT.) The base of the jet is not visible in this filter because a filament obscures the near-limb region. (A filament, or prominence, is a loop of cool chromospheric material that rises into the corona, often persisting for days or weeks before erupting.) The jet begins as an emergence along multiple channels (times 15:20:39 UT and 15:21:19 UT). As the event proceeds, the brightening develops finer structure, with more northern field lines also brightening (times 15:21:59 UT and 15:22:39 UT). Later, after the events discussed here, the jet becomes stronger and more collimated (last two panels).

In order to measure the jet velocity, the jet height was tracked over time. The *TRACE* 171 Å filter was chosen for this measurement because of its higher cadence (usually 40 seconds), though the jet cannot be tracked below  $\sim 10$  Mm because of the obscuring filament. Using running difference maps (in which the preceding frame is subtracted from each frame), emission was integrated across the width of the jet and the resulting height profile tracked over time. (See Figure 4.2, bottom panel.) A line was fit to the 50% intensity level for the three most intense time intervals, with the midpoint of the time interval as the independent variable. The jet velocity, given by the slope of this line, is  $417 \pm 73$  km s<sup>-1</sup>. This is a

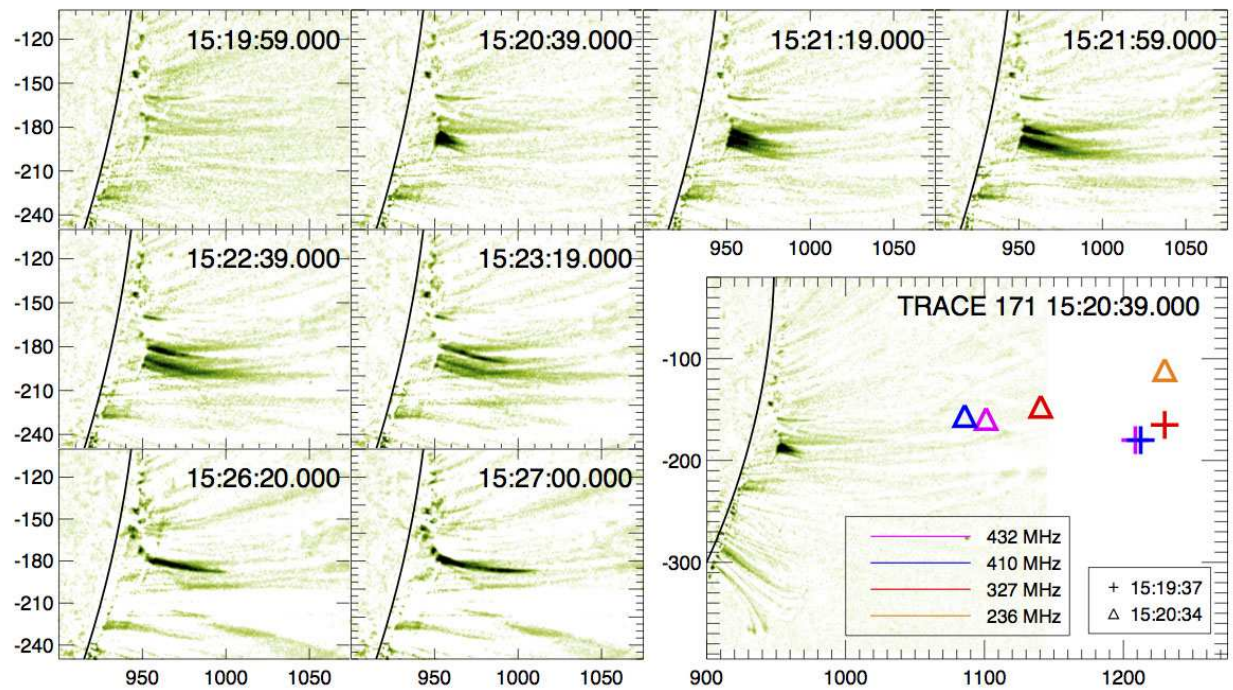


Figure 4.3: *TRACE* 171 Å images of the 2003 August 21 jet, with a pre-event image at time 15:15:02 UT subtracted. The first six frames show emission that is concurrent with the X-ray and radio observations; the last two frames show the beginning of the next jet. There is a gap in the 171 Å data between 15:23:19 UT and 15:26:20 UT. A filament obscures the jet near the limb in this filter; it is in this region that the HXR sources discussed in section 4.2.2 lie. The bottom-right image shows the start of the EUV jet overlaid with source locations from the Nançay Radioheliograph (NRH); this data is discussed in section 4.2.3. Markers indicate NRH source centroids at the time of the second (plus signs) and third (triangles) Type III bursts, around 15:19:37 UT and 15:20:34 UT, respectively.

lower limit since the line-of-sight motion is unknown. The uncertainty was determined by randomly varying the time within each interval and recomputing the slope. The jet is first visible in a 40-second *TRACE* image centered at 15:20:39 UT; extrapolation of the height profile back to the solar limb shows that the jet could have originated up to 47 seconds earlier than this.

The jet temperature cannot be determined from *TRACE* data because of the lack of simultaneous multiwavelength images. The jet is visible in the 171Å filter, which is most sensitive to plasma of  $\sim 1$  MK but also has a smaller sensitivity peak at 10 MK (Phillips et al. 2005). Jets are commonly observed across a wide frequency range, being simultaneously observed in UV, EUV, and X-ray images (Alexander & Fletcher 1999; Kim et al. 2007), suggesting a multithermal nature.

#### 4.2.2 *RHESSI* HXR observations

For the 2003 August 21 event, *RHESSI* observed a pre-impulsive phase (15:16:44–15:18:01 UT) and two HXR bursts (15:18:53–15:19:49 UT and 15:20:18–15:21:55 UT) (Figure 4.2), before the spacecraft entered the South Atlantic Anomaly, a high-radiation region in which *RHESSI* does not collect data. Figure 4.4 shows *RHESSI* images and spectra from three time intervals, overlaid on a *TRACE* 1550Å image at 15:23:35 UT that shows the UV jet. Although none of the *RHESSI* images occur simultaneously with this image (*RHESSI* images are from 2 to 7 minutes earlier), the overall geometry can be studied. *RHESSI* images were produced using the MEM imaging technique described in Section 3.2; all images were checked for consistency with Clean images. The images were coaligned by adjusting the *TRACE* roll angle until a *TRACE* 195 Å image matched an image from the Extreme ultraviolet Imaging Telescope (EIT) aboard the *Solar and Heliospheric Observatory (SOHO)* spacecraft. The coalignment of the *TRACE* and *RHESSI* images is expected to be good to 5 arcseconds.

A summary of source parameters for all three time periods is presented in Table 4.1.

##### **Pre-impulsive phase: double coronal source**

Panel (a) in Figure 4.4 shows *RHESSI* thermal (red) and nonthermal (blue) sources during the pre-impulsive phase (15:16:44 to 15:18:01 UT), before the attenuator insertion. Two coronal sources are visible: a source near the limb and a high coronal source  $\sim 10$  arcseconds above the limb, both emitting at thermal and nonthermal energies. This time period is 2–4 minutes before the EUV jet first appears.

Panel (d) shows a spatially integrated HXR spectrum during this time interval. Due to low statistics, detailed imaging spectroscopy cannot be performed. However, fluxes in each source were compared in two energy bands (10–15 and 15–25 keV) to obtain approximate spectral exponents for assumed power-law distributions, with the result that the high-altitude source shows a softer spectrum (Table 4.1). Assuming a cutoff energy of 16 keV for each,

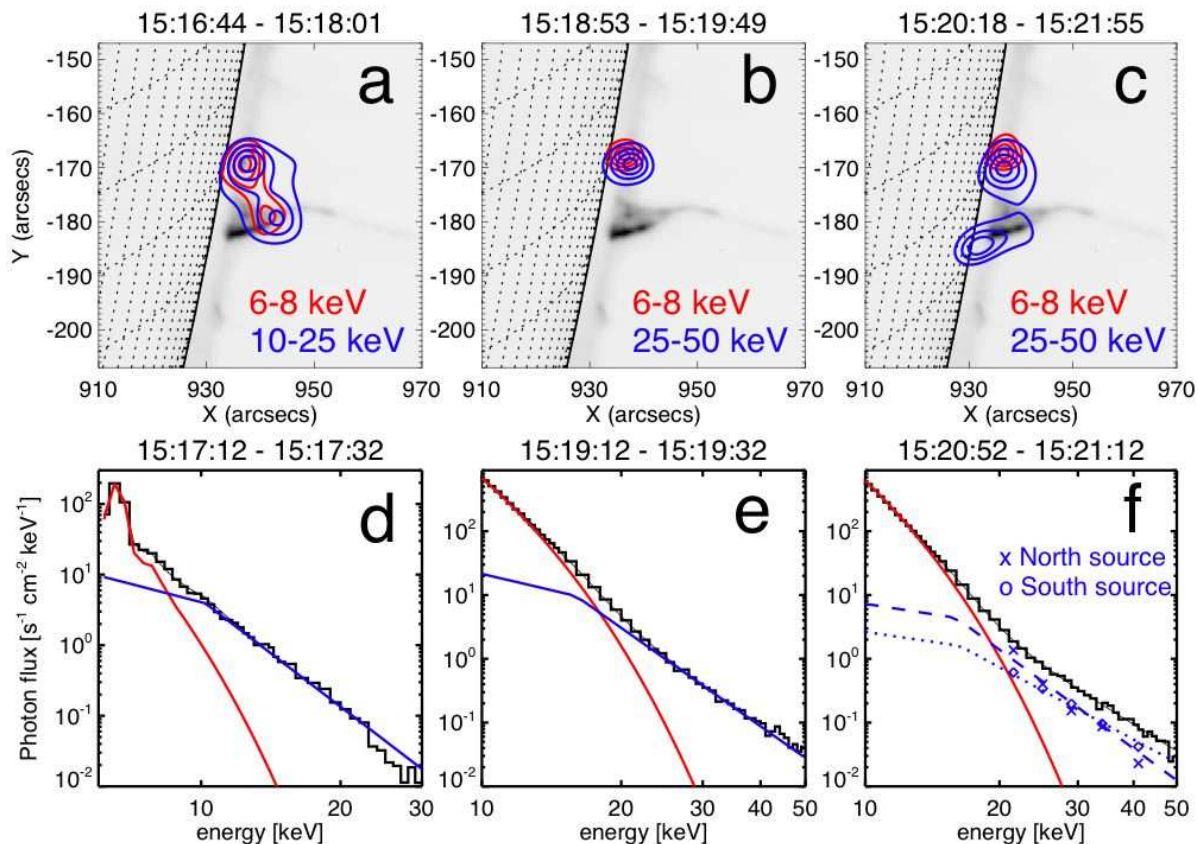


Figure 4.4: *RHESSI* X-ray images and spectra of the 2003 August 21 flare, during (left column) the pre-impulsive phase, (middle column) the first nonthermal burst, and (right column) the second nonthermal burst. Top row: thermal contours (red) and nonthermal contours (blue) superimposed on a later *TRACE* 1550Å image of the jet. The *TRACE* image time is 15:23:35 UT in all images. Bottom row: *RHESSI* spectra, assuming a spectral index of 1.7 below the break. In panel (f), the spectrum was fit with two broken power laws (dashed lines) to represent the two nonthermal sources. All *RHESSI* images were produced using the MEM\_NJIT imaging algorithm with subcollimators 3–9. Contour levels are 30, 50, 70, and 90 percent.

Table 4.1. Spectral parameters of the *RHESSI* X-ray sources

Time	Location	Area <sup>a</sup>	T[MK]	EM[cm <sup>-3</sup> ]	n[cm <sup>-3</sup> ]	$\gamma$	$\epsilon_0$ [keV] <sup>b</sup>	$E_{thin}$ [erg] <sup>c</sup>	$E_{thick}$ [erg] <sup>d</sup>
Pre-impulsive phase (15:16:44–15:18:01)	Near-limb	6" $\times$ 8"	13 <sup>e</sup>	$6.7 \times 10^{46}$ <sup>e</sup>		2.7–4.2	16 <sup>e</sup>	$5\text{--}9 \times 10^{26}$	$1\text{--}4 \times 10^{27}$
	High-altitude	3" $\times$ 4"							
First HXR burst (15:18:53–15:19:49)	Near-limb	5" $\times$ 4"	24	$8.5 \times 10^{47}$	$1.6 \times 10^{11}$	5.1	16	$1 \times 10^{29}$	$7 \times 10^{29}$
Second HXR burst (15:20:18–15:21:55)	Near-limb north	5" $\times$ 5"	22	$1.1 \times 10^{48}$	$1.5 \times 10^{11}$	5.7	16	$5 \times 10^{28}$	$3 \times 10^{29}$
	Near-limb south (jet) <sup>f</sup>	8" $\times$ 4"				3.8	16	$1 \times 10^{28}$	$4 \times 10^{28}$

<sup>a</sup>Areas are taken from MEM images of thermal sources, except for the last source. Since no thermal source is seen from the jet location the nonthermal source area is listed instead.

<sup>b</sup>Break energy of the photon spectrum.

<sup>c</sup>Energy deposited in ambient plasma in a thin-target regime.

<sup>d</sup>Energy deposited in ambient plasma in a thick-target regime.

<sup>e</sup>The low count rates in this time interval do not allow for detailed imaging spectroscopy of the individual sources. The temperature and emission measure given here are from the integrated spectrum, not individual sources. Spectral indices are estimated from comparison of flux measured in two energy bands, and a cutoff energy of 16 keV is assumed for the computation of deposited energy.

<sup>f</sup>There is no observable thermal emission from the jet X-ray source. See section 4.3.2 for discussion.

the energy deposited for both thin- and thick-target models was calculated, using formulas in Lin (1974), and was found to be on the order of  $10^{27}$ – $10^{28}$  erg, respectively.

### First HXR burst: Near-limb source

The image shown in panel (b) of Figure 4.4 covers the first nonthermal burst of the flare from 15:18:53 UT to 15:19:49 UT, with a primary peak at 15:19:10 UT and a secondary peak at 15:19:45 UT. The higher coronal source detected in the pre-impulsive phase is no longer detectable, possibly due to dynamic range limitations, since the remaining, near-limb source is about two orders of magnitude more intense than the pre-impulsive phase sources. The near-limb source has both a hot (24 MK) thermal component and a nonthermal component significantly steeper ( $\gamma = 5.1$ ) than in the pre-impulsive phase (Figure 4.4, panel (e); Table 4.1). The centroids of the thermal and nonthermal sources differ by  $\sim 2$  arcseconds. (Centroids were obtained using `vis_fwdfit`, described in Section 3.2.)

### Second HXR burst: X-ray emission from the EUV jet

Panel (c) of Figure 4.4 shows an X-ray image at the time of the second nonthermal burst, from 15:20:18 to 15:21:55 UT. The northern, near-limb coronal source is still visible, but now a new, elongated, southern source appears. Comparison with the UV background image shows that this source originates from the location of the *TRACE* jet, and the HXR burst occurs at the same time as the jet (see Figure 4.2), indicating that the HXR originate from the jet itself. The jet is not seen in thermal X-rays ( $\sim 6$ – $10$  keV), possibly due to dynamic range limitations since the northern thermal source is very bright. (See discussion in section 4.3.2.)

Since this HXR image contains two spatially distinct sources, a nonthermal spectrum was computed for each source individually using imaging spectroscopy, as in Krucker & Lin (2002), and two power-law indices were obtained. To obtain cutoff energies and thermal parameters, these results were then used as initial parameters to fit the integrated spectrum with one thermal component and two broken power laws to represent the separate nonthermal sources. These spectra are shown in panel (f) of Figure 4.4 and parameters are given in Table 4.1. The northern source is at the same location as the near-limb source of the first HXR burst, with similar thermal (22 MK) and nonthermal ( $\gamma = 5.7$ ) components. The southern nonthermal jet source is weaker but has a significantly harder spectrum ( $\gamma = 3.8$ ). Its elongated shape points toward the high coronal source of the pre-impulsive phase.

## 4.2.3 Radio observations

Radio emission from the August 21 event was observed by the Phoenix-2 solar radio spectrometer in Bleien, Switzerland, which records in frequencies from 0.1 to 4 GHz (Messmer et al. 1999) (Figure 4.2, panels d and e). Type III radio bursts occur in three bunches, while gyrosynchrotron bursts occur at higher frequencies. Together, these two components

produce radio emission that closely mimics the *RHESSI* HXR profile above  $\sim 20$  keV. The first two Type III bursts start at  $\sim 500$  MHz and coincide with the primary and secondary peaks of the first HXR burst, respectively. The third Type III burst starts at  $\gtrsim 600$  MHz, simultaneous with the peak of the second HXR burst. These are followed by longer bursts of gyrosynchrotron emission that coincide with the duration of each HXR burst (Figure 4.2, panel c).

The Nançay Radioheliograph (NRH) (Kerdran & Delouis 1997) provides images at 432, 410, 327, and 236 MHz. The source locations at the time of the last two Type III bursts are shown in Figure 4.3, overlaid on a *TRACE* image of the beginning jet. The radio sources are located at higher altitudes with decreasing frequency, characteristic of electron beams moving radially outward through progressively less dense plasma. The field lines along which the jet emerges point toward the NRH sources, suggesting that the jet takes the same path as the Type III-generating electron beams. Raulin et al. (1996) also found that solar jets and Type III-emitting electrons follow similar paths. Compared with the second burst, the path of the last burst is translated to the north by  $\sim 50$  arcseconds. As discussed in section 4.2.1, the jet displays the same behavior.

Christe et al. (2008b) studied an unusual series of six Type III bursts, each simultaneous with a HXR microflare, but found that the HXR were thermal, not nonthermal bremsstrahlung from the Type III-emitting electron beams. Krucker et al. (2008a) found a partially occulted event in which the nonthermal HXR and Type III emission were temporally correlated. In the event presented here, the HXR emission appears to be temporally correlated with the combined Type III and gyrosynchrotron emission. (See Figure 4.2, panel c.)

## 4.3 Discussion

### 4.3.1 Evidence for interchange reconnection

In the righthand panel of Figure 4.5, a diagram of the Heyvaerts/Shibata model is shown with the observed X-ray sources overplotted. The pre-impulsive double source (shown in green, middle and right panels) appears to correspond to the locations of the hypothesized fast shocks formed by reconnection outflow. One outflow jet is aimed downward towards the limb and the other is projected laterally, higher in the corona. The non-thermal HXR emission in the corona indicates the presence of accelerated electrons up to  $>30$  keV. This is consistent with the reconnection and acceleration regions being located between the two coronal sources. Studies of flares on 2002 April 15 (Sui & Holman 2003), 2002 April 30 (Liu et al. 2008), and 2003 November 3 (Chen & Petrosian 2012) also found double sources in the corona and in each case inferred a reconnection site between the two sources. Pre-impulsive thermal and nonthermal HXR emission was also detected in the corona in the 23 July 2002 X4.3 flare, and attributed to the reconnection process (Caspi & Lin 2010).

In the first intense HXR burst ( $\sim 15:19$  UT), the emission from the near-limb source

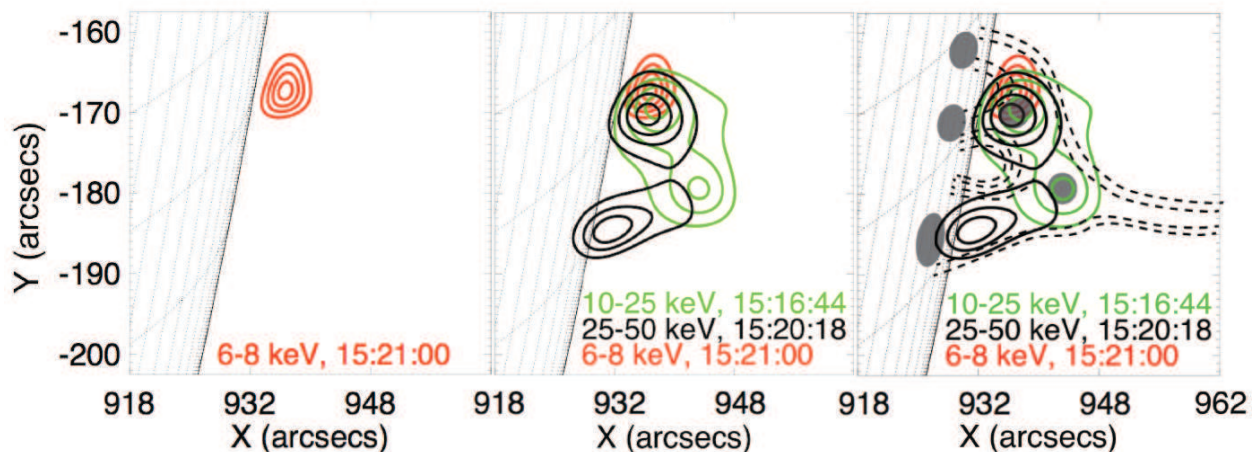


Figure 4.5: Left: *RHESSI* thermal emission from a small post-flare loop in the latter half of the second HXR burst (red). Middle: Overlays of *RHESSI* nonthermal emission from the pre-impulsive phase reconnection outflow (green) and the jet emission (black). Reconnection outflow is correctly positioned to supply energetic electrons to the post-flare loop. Right: These sources are overlaid on a cartoon of interchange reconnection similar to that in Figure 4.1, demonstrating the expected locations of HXR sources.

becomes brighter by two orders of magnitude. A high-corona source could still be present, as in the pre-impulsive phase, but only if it is  $\gtrsim 10$  times fainter than the near-limb source, in order to be undetected. Two Type III radio bursts are observed simultaneously with the primary and secondary peaks of the HXR burst. This indicates accelerated electrons escaping on open field lines and is consistent with interchange reconnection. Longer-duration broadband gyrosynchrotron emission mimics the time profile of the HXRs above 20 keV, suggesting the presence of trapped electrons in a post-reconnection loop.

The second impulsive HXR burst ( $\sim 15:21$  UT) is coincident with a third Type III radio burst that extends up to 600 MHz and occurs close to the onset of the jet, along with another long burst of gyrosynchrotron emission. A new HXR source shown in black contours in Figure 4.5, middle and right panels) is spatially coincident with and elongated along the jet, pointing towards the high coronal source observed in the pre-impulsive phase. Scenarios for producing HXRs from the jet will be discussed in the next section.

The jet velocity of  $417 \pm 73$  km s $^{-1}$  is faster than most of the *Yohkoh* jets studied by Shimojo et al. (1996) (average 200 km s $^{-1}$ ) and the *Hinode* jets studied by Kim et al. (2007) (90–310 km s $^{-1}$ ). Bain & Fletcher (2009) found a similar velocity ( $\sim 500$  km s $^{-1}$ ) for a *TRACE* jet which also showed *RHESSI* nonthermal HXR emission. The velocity is on the order of the Alfvén speed, for example for a coronal density of  $\sim 10^{10}$  cm $^{-3}$  and a magnetic field of  $\sim 20$  G. However, the velocity is also consistent with the local sound speed for temperatures of  $\sim 12$  MK. (Possible temperatures will be considered in the next

section.) Therefore, the jet cannot be distinguished by its velocity as either Shibata’s “hot” (gas pressure) or “cool” (chromospheric evaporation) jet. However, in the *TRACE* 1550Å filter (see panel (a) of Figure 4.4), the jet is visible below the higher coronal HXR source, suggesting a chromospheric or low coronal origin.

Late in the event (in the latter half of the second HXR burst), the northern thermal source becomes elongated parallel to the limb (left panel, Figure 4.5). This is consistent with the heating and filling of a small post-reconnection loop at the far northern side of the flare, as predicted by the Heyvaerts/Shibata model. Comparison with the earlier double coronal sources (Figure 4.5, middle and right panels, green contours) confirms that this loop is in the correct location for energized electrons from the reconnection region to be injected into it..

One other magnetic geometry for this flare was considered: that of the standard flare model (see Section 2.2.2), in which electrons accelerated in the corona are injected radially downward into a single flare loop and stream down the loop legs until they reach chromospheric footpoints. In this geometry the three observed HXR sources would correspond to a looptop (or above-the-looptop) source and two footpoints. However, the near-limb HXR source locations, timing, and spectra are inconsistent with flare footpoints. The northern source displays thermal emission slightly below the nonthermal source (see panel (b) of Figure 4.4), while for a flare footpoint higher-energy emission should be located at lower altitudes. The 6-8 keV emission observed late in the event from the northern source (see Figure 4.5, left panel) is indicative of a thermal post-flare loop, not a footpoint, which should emit primarily at nonthermal energies and which should be closer to the limb. The southern source (see panel (c) of Figure 4.4) starts at the limb but is too elongated (8 arcseconds) to be a footpoint. Furthermore, the timing of the near-limb sources, in which the northern source appears 2–4 minutes before the southern source, is inconsistent with a looptop injection followed by precipitation in the two footpoints, which would result in a high coronal source appearing just before, or simultaneously with, the footpoints. When the two near-limb sources are observed together (in the last time interval) their spectral indices differ by 1.9. Saint-Hilaire et al. (2008) studied 53 on-disk flare footpoint pairs and found that none had a difference in spectral index of  $>0.8$ . The simple loop model is thus ruled out for this flare.

### 4.3.2 HXR emission from the jet

HXRs from the jet itself could be produced by accelerated electrons traveling either upward or downward through the source, which could be approximated as either a thin or thick target for energetic electrons. Here, we will consider both regimes and first assume the electrons are traveling downward toward the chromosphere. Formulas for calculating accelerated electron energy deposition from HXR spectra are found in Lin (1974) and summarized in Section 2.5.1.

### Thick-target HXR emission from the jet

If electrons are accelerated in the corona, travel downward, and lose all their energy in the jet source, then the jet HXR emission can be considered a coronal thick target. In this scenario the electrons never reach the chromosphere. Coronal thick-target emission, while extremely rare, is occasionally observed (Veronig & Brown 2004). With the observed HXR source parameters (photon spectral index  $\gamma \sim 3.8$ , cutoff energy  $\sim 16$  keV, and length  $\sim 8$  arcseconds), the average electron energy is  $\sim 22$  keV. The column density necessary to stop a beam of energetic electrons is  $N = 1.5 \times 10^{17} \text{ cm}^{-2} (E/\text{keV})^2$  (Krucker et al. 2008b), so the ambient density averaged over the source must be  $> 1.2 \times 10^{11} \text{ cm}^{-3}$ . The energy deposited by accelerated electrons in a thick-target jet volume is  $4 \times 10^{28}$  erg (see Table 1, lower-right cell).

Can energetic electrons deposit enough energy in this thick target source to supply the energy necessary for the jet? A cylinder with dimensions of the jet HXR source (8" by 4") has a volume of  $5 \times 10^{25} \text{ cm}^3$ . The average density is  $> 1.2 \times 10^{11} \text{ cm}^{-3}$  (for a thick target), so the total number of atoms is  $> 6 \times 10^{36}$ . The jet is visible at least up to 50 Mm and the measured jet velocity is  $417 \text{ km s}^{-1}$ , so the kinetic and gravitational potential energies are  $\gtrsim 8 \times 10^{27}$  and  $\gtrsim 1 \times 10^{27}$  erg, respectively, using the proton mass for each atom. The total jet energy is thus  $\gtrsim 1 \times 10^{28}$  erg, which is less than the energy deposited by accelerated electrons in the jet volume.

The difference between the deposited energy and the jet kinetic and potential energies goes into heating of the jet, neglecting any energy escaping downward. The jet's temperature cannot be measured from observations by either *TRACE* (no overlapping multiwavelength images) or *RHESSI* (no observed thermal source), but constraints can be obtained. The thermal energy is  $U = 3k_B T n V$ , where  $k_B$  is Boltzmann's constant and  $U$ ,  $n$ ,  $T$ , and  $V$  are the jet's thermal energy, density, temperature, and volume, so the jet density and temperature are related by  $nT = U/(3k_B V)$ . If *all* the energy deposited by nonthermal electrons goes into thermal heating, then  $nT \approx 2 \times 10^{18} \text{ K cm}^{-3}$ ; this relation is shown in the left panel of Figure 4.6 (solid red line). If a portion of the energy goes into jet kinetic and potential energy, as discussed above, then the relation is modified (dotted red line). The necessary density for a thick-target approximation ( $> 1.2 \times 10^{11} \text{ cm}^{-3}$ ) thus allows a range of temperatures below  $\sim 12$  MK (according to the dotted red line).

This constraint is confirmed by the lack of a *RHESSI* thermal source. The jet travels on field lines open to interplanetary space, so it is possible that plasma does not remain in the region long enough to be heated to a high enough temperature to be observed. Thermal sources detected by *RHESSI* are usually found in closed loops. Moreover, if a thermal source at the location of the jet is  $\gtrsim 10$  times fainter than the bright northern source, it might not be detectable within *RHESSI*'s dynamic range. In the right panel of Figure 4.6, SXR fluxes at 7 keV are calculated for a range of temperatures (solid and dotted red lines) and compared with the observed flux from the northern source (dashed line) and the estimated observing limit (dash-dotted line). It can be seen that a jet thermal source with temperature below  $\sim 11 - 15$  MK likely would not be detected within the dynamic range of the instrument.

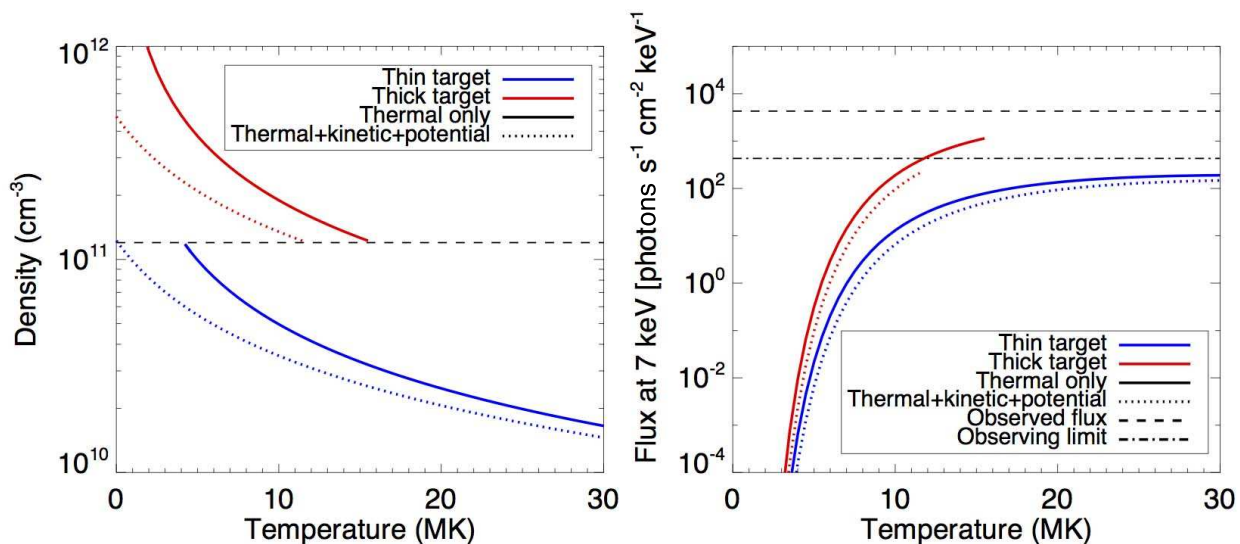


Figure 4.6: Left: The relation between the jet density and temperature in the thin- and thick-target approximations, assuming all energy deposited in the nonthermal source is transferred into thermal energy of the jet (solid lines) or allowing for additional loss to jet kinetic and potential energies (dotted lines). The dashed black line indicates the density ( $1.2 \times 10^{11} \text{cm}^{-3}$ ) separating the two regimes. Right: Simulated flux at 7 keV for a range of temperatures, with densities taken from the left panel. Only values from the left panel are included in the plot. The dashed line marks the flux observed from the bright northern source, while the dash-dotted line marks a conservative observing limit of 10 times fainter. Fluxes below the dash-dotted line probably could not be seen within *RHESSST*'s dynamic range.

### Thin-target HXR emission from the jet

For jet densities lower than  $\sim 10^{11} \text{ cm}^{-3}$ , the downward-traveling energetic electrons would not lose all their energy in the HXR source. In this case the electrons pass through the region and instead deposit most of their energy in an occulted chromospheric footpoint (the southernmost gray footpoint shown in the right panel of Figure 4.5). Then the energy deposited in the jet HXR source is given by the thin-target formula (Lin 1974). Compared with the thick-target model, thin-target energy deposition for a given photon spectrum is reduced by a factor of  $\gamma$ , in this case to  $1 \times 10^{28}$  erg (see Table 1). In this scenario the electrons deposit most of their energy in an unseen footpoint below; the jet thus originates from the chromosphere (through chromospheric evaporation by the accelerated electrons) and is only further heated in the corona. In this scenario the HXR-producing energetic electrons will still collisionally deposit enough energy to generate the jet, but now this occurs in the unseen footpoint.

The thin-target density-temperature relation is plotted in blue in the left panel of Figures 4.6; estimated flux at 7 keV is plotted in blue in the right panel. None of the allowed density-temperature pairs would produce a thermal source observable by *RHESSI*. However, this calculation neglects heating by energetic electrons in the chromosphere, which would presumably heat the evaporating plasma before it emerges into the corona. Fisher et al. (1984) showed that at least half the energy of evaporating material is thermal and that velocities of a few times the sound speed can be attained, so that the jet should be heated to  $>2$  MK before reaching the corona if it is produced by chromospheric evaporation.

In either the thick- or thin-target scenarios it is clear that the HXR-producing energetic electrons can collisionally deposit enough energy to generate the jet. It is unclear why a jet is generated in the second, but not the first, impulsive HXR burst. Comparison of the more northern source in the two bursts indicates that the first burst exhibited twice as much energy deposition as the second burst (see Table 4.1) and thus presumably contained enough energy to generate a jet. A possible explanation is that the reconnection process is not symmetric, and so the northern source is not a good point of comparison for the two bursts. It is also possible that there is a time lag between the energy deposition and the jet emergence, so that it is the first burst that generates the jet. (The precise jet start time cannot be derived from *TRACE* observations; also, if the jet initially accelerated then the start time would be earlier than that obtained from the linear extrapolation indicated in Figure 4.2.) In this scenario, the downward-traveling accelerated electrons only become detectable in HXRs when the high-density jet is present. An extended injection or coronal trapping would be necessary so that the first energetic electrons to reach the chromosphere generate the jet, while later energetic electrons interact with the emerging jet and produce HXRs.

### Upward-traveling electron beams

An alternative interpretation to those just presented is that the jet HXR source is produced by upward-moving nonthermal electrons. These electrons must be accelerated in the base of the jet and travel upwards along the jet path. Fletcher & Hudson (2008) proposed a flare model in which energy is transported from the reconnection site to footpoints by Alfvén waves, not particle beams, and reviewed various mechanisms for acceleration in the footpoints. In this case the role of the double coronal source, which indicates pre-impulsive electron acceleration in the corona, would need to be explained. The jet and accelerated electrons can emerge simultaneously, agreeing well with the timing of the EUV and HXR observations.

If the jet HXR source could be split into a lower and an upper source, the beam direction could be determined by comparing the spectral indices of the two sources. For a downward-traveling beam, the lower part of the source would have a harder spectrum since collisions preferentially deplete lower-energy electrons from the beam. Conversely, for an upward-traveling beam, the upper part of the source would have the harder spectrum. Alternatively, the direction of the beam could be determined by comparing source locations at different energies; Saint-Hilaire et al. (2010) showed that the HXR source height decreases with energy only for electron beams traveling downward into the chromosphere (encountering a positive density gradient). Statistics in this event do not allow us to distinguish between these cases.

## 4.4 Summary

The observation presented here is the first to see several HXR coronal sources in an interchange reconnection type jet event. Key aspects include:

- A double coronal HXR source at both thermal and nonthermal energies in the flare pre-impulsive phase, indicating early electron acceleration to tens of keV and heating to 13 MK even before the impulsive flare. These sources may indicate locations of reconnection outflows in the Shibata model.
- Nonthermal HXR emission spatially and temporally coincident with the EUV jet. Energy deposition by nonthermal electrons is sufficient to provide the thermal, kinetic, and potential energies of the jet.
- Two intense HXR bursts in the impulsive phase, accompanied by radio emission that closely follows the time profile of *RHESSI* HXRs above 20 keV. This includes Type III emitting beams (suggestive of interchange reconnection) that travel similar paths to that taken by the EUV jet, and gyrosynchrotron emission from electrons trapped in flare loops.
- A small post-flare loop in the correct position to be heated by energetic electrons from the reconnection region.

---

To detect weak coronal sources in the presence of stronger sources, instruments with higher sensitivity and dynamic range are needed. Focusing optics such as those flown on the *Focusing Optics X-ray Solar Imager* sounding rocket, which will be described in later chapters, or those included on the astronomy telescope *NuSTAR* (Harrison et al. 2010) could be used to observe HXR components, while The Atmospheric Imaging Assembly aboard the *Solar Dynamics Observatory* (Lemen et al. 2012) can provide density and temperature estimates of the EUV jets. In addition, images from the proposed *Frequency Agile Solar Radiotelescope* (Bastian 2003) could study Type III-emitting electron beams and could provide local density information.

## Chapter 5

# Energetics and Heating in a Solar Plasma Ejection Observed By RHESSI and AIA

### Abstract

As discussed in the previous two chapters, *RHESSI* has provided remarkable insight into the locations and spectra of energetic flare particles. With the advent of high-cadence, multiwavelength extreme ultraviolet (EUV) observations by the Atmospheric Imaging Assembly (AIA) aboard the *Solar Dynamics Observatory*, it is now more possible to study the dynamic structures among which these energetic particles move. On November 3, 2010, a C4.9 solar flare occurred just behind the eastern limb of the Sun, accompanied by a coronal mass ejection. The flare footpoints were occulted by the solar disk by about 6 degrees, allowing a detailed study of the faint coronal X-ray sources. EUV images from AIA show a mass of plasma ejected from the solar surface. Isothermal analysis using multiple EUV filters shows that this erupting plasma reaches a high temperature of  $\sim 10$  MK. Meanwhile, RHESSI X-ray images reveal a large, diffuse hard X-ray source matching the location, shape, and evolution of the ejecting plasma, suggesting the presence of nonthermal electrons that may be magnetically trapped in the region. In this chapter, *RHESSI* spectroscopy and AIA temperature analysis are combined in order to examine the relationship between the populations of thermal and nonthermal electrons in the ejecta plasma. Electron spectra, locations, and temporal evolution are examined in order to test the hypothesis that nonthermal electrons collisionally heat the erupting plasma to this high temperature.

## 5.1 Introduction

Earlier chapters detailed how HXR's can be used to trace out paths of energetic electrons and determine their energies. HXR's are thus a good diagnostic of high-energy aspects of flares and are so far the most direct observable of flare particle acceleration. UV and EUV wavelengths, on the other hand, can provide thermal plasma diagnostics. This is important not only for outlining the structure of the plasma among which the energetic electrons travel, but also for tracing the evolution of the flare energy, which is eventually transferred from energetic particles to thermal plasma.

Typically, heating by energetic electrons takes place primarily at the flare footpoints, where the high chromospheric density causes electron beams to collisionally lose all their nonthermal energy. Occasionally, as discussed in Chapter 2, nonthermal and thermal sources are observed in the corona (most easily observed in partially occulted flares), indicating collisional heating at or above the flare looptop.

On rare occasions, energetic electrons are observed in large bubbles high above flare sites. Kane et al. (1992) studied a flare with impulsive HXR and SXR emission at an altitude of  $>200$  Mm above the limb. Unocculted observations from the *Pioneer Venus Orbiter* suggest that this flare was probably 1000 times more intense than its (occulted) GOES class of C indicated. Hudson et al. (2001) also studied a HXR source at an altitude of up to 200 Mm in a flare occulted by 26 degrees and found an upward motion of  $\sim 1000$  km s $^{-1}$ . The location and motion of energetic electrons were confirmed by incoherent microwave emission (see Section 2.5.2) observed in images by the Nobeyama radioheliograph; the source of both emissions was assumed to be electrons trapped in expanding loops as part of a related CME. Krucker et al. (2007) studied a flare that was highly occulted from Earth by 40 degrees and was observed with no occultation by the Gamma Ray Spectrometer on the *Mars Odyssey* spacecraft. At this level of occultation, the entire flare loop was occulted and only above-the-looptop sources were observed from Earth. A large HXR source expanded and moved upward with a radial velocity of 750 km s $^{-1}$ , much more slowly than the front of the related CME (2300 s $^{-1}$ ). Again, the location of nonthermal electrons inferred from the HXR's were confirmed by Nobeyama microwave images.

It is possible that these rising HXR sources could be related to the flares' accompanying coronal mass ejections (CMEs). CMEs are large-scale ejections of plasma from the low solar corona. Often,  $10^{14}$ – $10^{16}$  grams of material are ejected, reaching velocities of over 2000 km s $^{-1}$ . Traditionally, CMEs are observed in optical and UV wavelengths, where they consist of a fast-moving outer shell, a cavity just behind the shell, and a core volume (Klimchuk 2001; Landi et al. 2010). See Figure 5.1 for an example of an observation showing these components. In the absence of heating, one would expect the exploding material to have a temperature not hotter than that of the corona ( $\sim 1$  MK), or perhaps even that of the chromosphere ( $< 50,000$ K), depending on the mass source. Kumar & Rust (1996) proposed a model in which magnetic energy is transferred roughly equally into kinetic, potential, and thermal energy of the rising plasmoid. However, several observations have observed a surprising degree of heating within the core as the plasmoid rises. Akmal et al. (2001)

studied a CME that occurred on 1999 April 23 out to 3.5 solar radii. From UV observations, the heating rate as the CME moved outwards was estimated and found to be comparable to the kinetic and gravitational energies. Lee et al. (2009) considered a CME observed on 2001 December 13 and found, using techniques similar to that of Akmal, that continuous heating was required, the maximum temperature was due to heating, not an initial temperature state, and that the heating made up  $\sim 75\%$  of the energy transfer. Landi et al. (2010) studied a CME that occurred on 2008 April 8 in which the ejected material was hot enough to emit in soft X-rays. In this case the calculated heating rate was much larger than the kinetic energy and the processes of wave heating, conduction, and internal shock heating were ruled out as viable heating mechanisms; magnetic heating and heating by energetic particles were considered plausible.

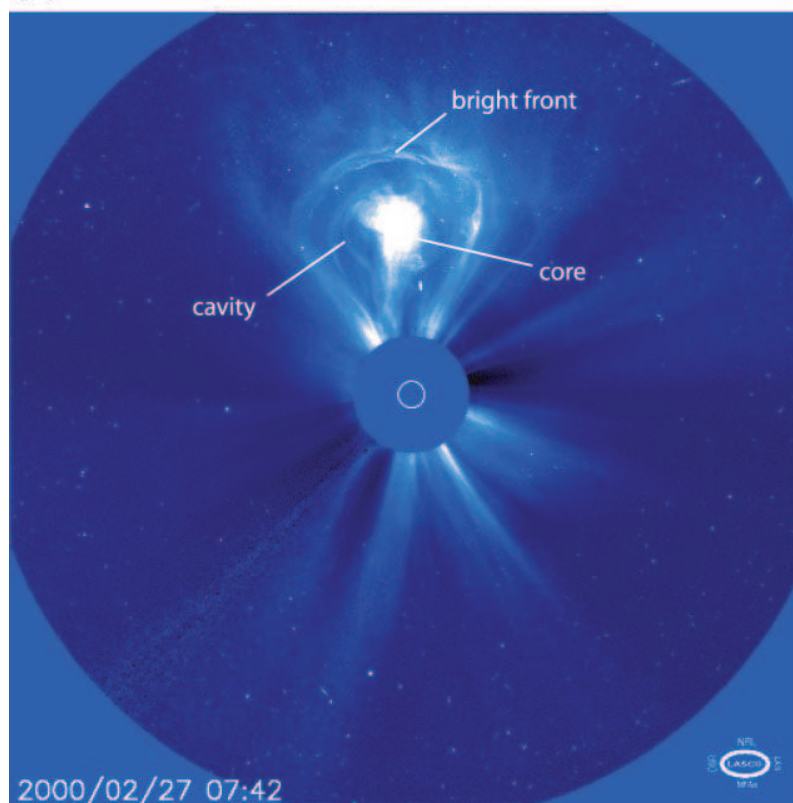


Figure 5.1: An example of a CME observation from the *Large Angle Spectrometric Coronagraph (LASCO)* aboard *SOHO*. A coronagraph uses an occulting disk to block bright light from the solar disk, allowing faint reflected light from the corona to be measured. This example shows the typical bright front, dark cavity, and bright core often observed in CMEs. Image is from Riley & McComas (2009).

Recently available observational tools and techniques now allow us to investigate high-temperature and high-energy aspects of CMEs. The *Solar Dynamics Observatory (SDO)* was

launched in March 2010. One of the instruments onboard SDO is the Atmospheric Imaging Assembly (AIA), a telescope that images in narrow-band extreme ultraviolet filters (Lemen et al. 2012). Several filters have sensitivity to hot coronal plasma; by combining data from multiple filters, temperatures of hot coronal plasma can be determined on a per-pixel basis. Meanwhile, *RHESSI* gives information on the locations and spectra of energetic electrons, so the collisional losses in energetic electrons can be compared with any rise in the thermal energy of the plasma.

On 2010 November 03 *RHESSI* and AIA observed a partially occulted eruptive event on the eastern limb. AIA data capture the rising plasmoid that is the start of the CME and find that it contains temperatures of up to 10 MK. *RHESSI* observations, using an imaging technique designed to accentuate faint, diffuse coronal sources, show that this plasmoid is filled with energetic electrons that contain enough energy to collisionally heat the plasmoid to the observed high temperature. These observations show that energetic electron heating is a possible explanation for the anomalous heating observed in CMEs propagation.

## 5.2 Observations

This solar eruptive event was a *GOES* C4.9 class flare that occurred on 2010 November 03, with a *RHESSI* peak time of 12:17:14. Data from the Extreme Ultraviolet Imager (EUVI) aboard the *STEREO-B* spacecraft (Howard et al. 2008) were used to determine the level of occultation as seen from the Earth. *STEREO-B* trails the Earth in its orbit and can thus observe regions of the Sun that are occulted from the Earth's point of view. The EUVI flare image was saturated, so the center of the saturated pixels was taken to be the flare location and the uncertainty was determined by the extent of the saturated region. Comparison of the orbital locations of *STEREO-B* and the Earth, which were 82 degrees apart, revealed that the flare site was occulted by 5–7 degrees from the Earth's point of view. The CME associated with the flare had an angular width of 66 degrees and an apparent velocity of 241 km s<sup>-1</sup> according to the LASCO CME catalog (Gopalswamy et al. 2009).

Figure 5.2 shows a time profile of fluxes for this event, including *rhessi* HXR lightcurves, a *RHESSI* spectrogram, and a radio spectrogram from the *PHOENIX* and *HUMAIN* instruments.

### 5.2.1 AIA observations of ejected plasma

AIA takes full-solar-disk images in seven narrow EUV filters and three UV filters with 1.5 arcsecond resolution on a cadence of 12 seconds. The six EUV filters with peak temperature sensitivity above 1 MK were chosen to respond to iron lines of various formation temperatures in order to facilitate multifilter analysis. By choosing primarily Fe lines, multifilter calculations are not dependent on the elemental abundance in the solar atmosphere (Lemen et al. 2012). Figure 5.3 shows temperature responses for the six filters with responses to the hottest plasma of the solar corona, and the primary ion and temperature sensitivity

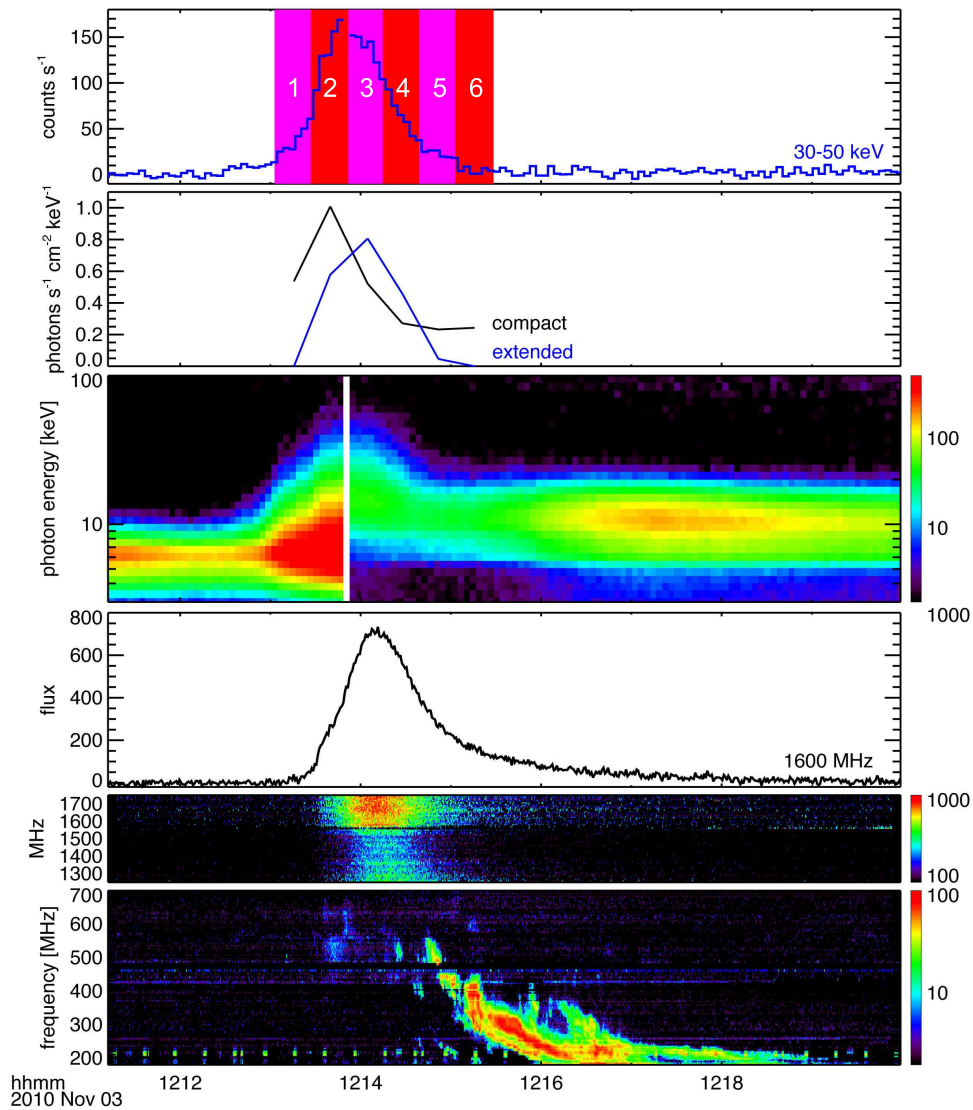


Figure 5.2: Time profile of the 2010 November 03 flare, in SXR, HXR, and radio emission. The panels show (top panel) *RHESSI* HXR emission from 30–50 keV with numbered imaging intervals for Figure 5.7, (second panel) separate lightcurves for the two *RHESSI* sources discussed in section 5.2.2, (third panel) the *RHESSI* spectrogram, (fourth panel) a *PHOENIX* radio light curve at 1600 MHz, and (bottom panel) a spectrogram combining radio data from the *PHOENIX* and *HUMAIN* radio observatories.

of these six filters is shown in Table 5.1. A single filter generally contains response to more than one temperature and may have a broadly peaked response; multiple filters must be used to extract temperatures from AIA images.

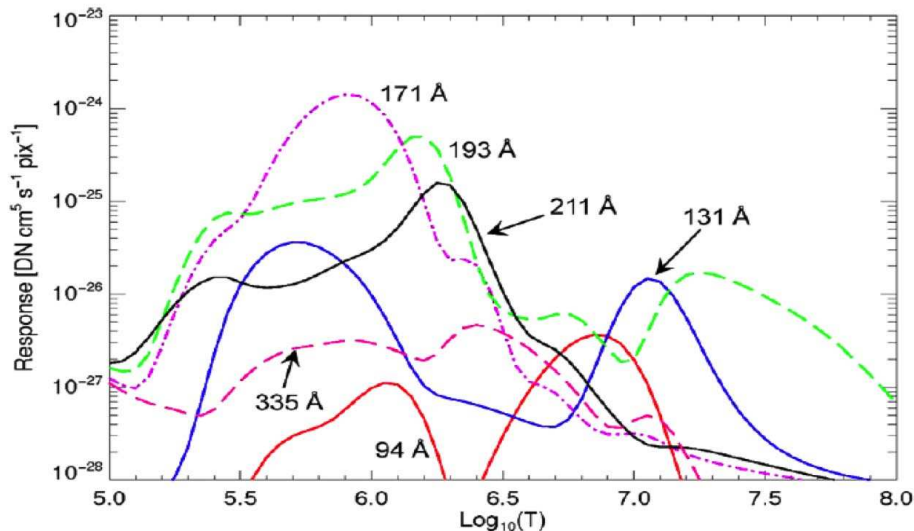


Figure 5.3: Temperature response of the six AIA filters sensitive to hot coronal plasma. Measurement in a single filter is insufficient to infer a temperature. By combining data from multiple filters, temperatures can be obtained. Note that the filters with best sensitivity to  $\sim 10$  MK plasma are 131 and 94 Å. Figure is from Lemen et al. (2012).

Figure 5.4 shows the 2010 November 3 plasma ejection in four AIA filters around 12:14:44. Since each filter has a different temperature sensitivity (see Figure 5.3), different regions of the ejecta are visible in the various filters. The core region of the ejected plasma is best seen in the 131 Å filter (second from the left) and is noticeable in the 94 Å filter, while the 211 and 335 Å filters show only the outer sheath.

Several studies have focused on this particular event because it displays a diverse set of rarely observed phenomena. Reeves & Golub (2011) found that the ejected plasma is full of hot plasma, while Cheng et al. (2011) interpreted a feature in the ejected plasma as an observation of a rising flux rope. Meanwhile, on the northern edge of the plasmoid, vortices appeared which were interpreted as Kelvin-Helmholtz instabilities by Foullon et al. (2011). Associated with this event was radio emission at frequencies observable by the Nancay Radioheliograph (NRH) of 200–400 MHz, so that locations of emission could be determined. With these (rarely observed) images, Bain et al. (2012b) and Zimovets et al. (2012) found that a shock wave typical of CMEs moved ahead at a faster speed than the sheath of ejected plasma visible in AIA.

The multifilter analysis method of Aschwanden & Boerner (2011) was used to find the temperatures and emission measures of the ejected plasma. This method is a forward-fitting

Channel	Primary ion(s)	Region of atmosphere	Char. $\log(T)$
171 $\text{\AA}$	Fe IX	quiet corona, upper transition region	5.8
193 $\text{\AA}$	Fe XII, XXIV	corona and hot flare plasma	6.2, 7.3
211 $\text{\AA}$	Fe XIV	active-region corona	6.3
335 $\text{\AA}$	Fe XVI	active-region corona	6.4
94 $\text{\AA}$	Fe XVIII	flaring corona	6.8
131 $\text{\AA}$	Fe VIII, XXI	transition region, flaring corona	5.6, 7.0

Table 5.1: The six AIA filters with the hottest temperature sensitivity. In designing the instrument, filters were chosen that have sensitivity to iron lines so that multifilter analysis results would not be dependent on elemental abundances. Not shown here are the lower-temperature-sensitive filters of 304, 1600, 1700, and 4500  $\text{\AA}$ . Table is adapted from Lemen et al. (2012).

method that assumes a differential emission measure ( $dEM$ ) that is a Gaussian in  $\log T$  space:

$$\frac{dEM(T)}{dT} = EM_P \exp\left(-\frac{[\log(T) - \log(T_P)]^2}{2\sigma_T^2}\right) \quad (5.1)$$

Here,  $EM_P$  and  $T_P$  are the peak emission measure and its respective temperature and  $\sigma_T$  is the Gaussian width. All variables are functions of  $(x, y)$  coordinates of the image. The flux  $F_\lambda$  measured by an AIA filter  $\lambda$  is a convolution of the dEM with the temperature response  $R_\lambda(T)$  of that filter:

$$F_\lambda = \int \frac{dEM(T)}{dT} R_\lambda(T) dT \quad (5.2)$$

Again, the fluxes and  $dEMS$  are functions of  $(x, y)$  coordinate. The method of Aschwanden & Boerner (2011) creates a 3-dimensional table of expected fluxes over a parameter space of peak temperatures  $T$  and Gaussian  $dEM$  widths  $\sigma_T$  for each filter. It then compares the observed fluxes to the values in this table and selects the  $T, \sigma_T$  pair with the lowest  $\chi^2$  value. Isothermal plasma is characterized by a narrow fit  $dEM$ , while multithermal plasma would be better fit by a broad  $dEM$ . The fit can be done with angular resolution down to the size of one AIA pixel (0.6 arcse), or pixels can be binned together for better statistics (assuming that nearby pixels view plasma of similar  $dEM$ s).

To apply the technique to this flare, the filters 94, 131, 193, 211, and 335  $\text{\AA}$  (those sensitive to the hottest plasma) were used. The 171  $\text{\AA}$  filter was left out of the analysis because bright loops in the vicinity of the flare (and persisting throughout the event) dominated the

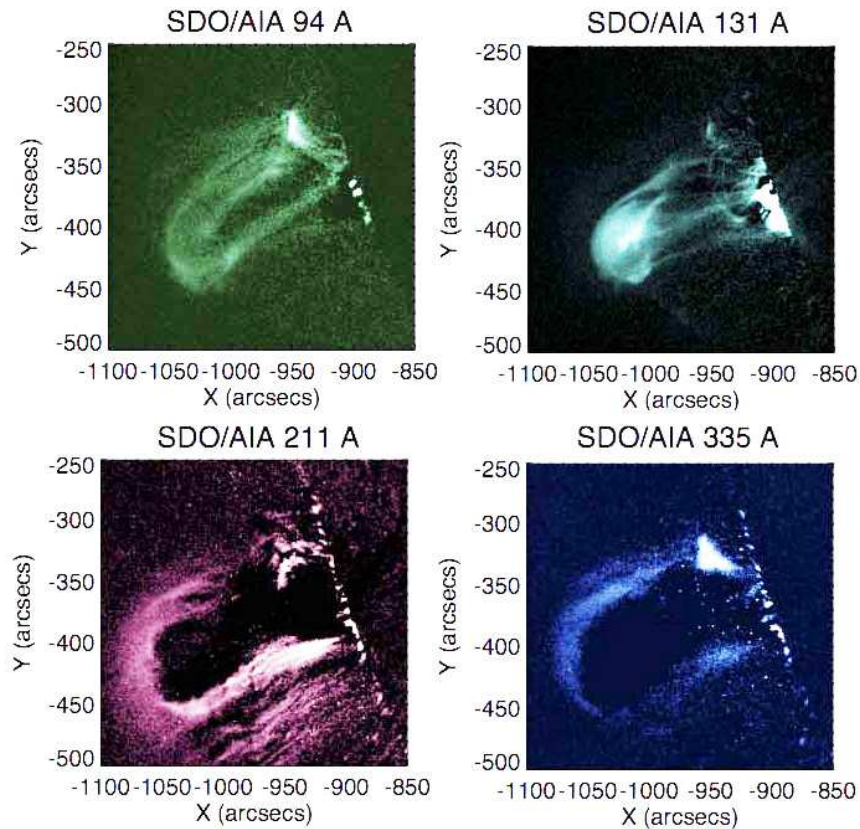


Figure 5.4: View of the ejected plasmoid in four different AIA filters at times around 12:14:44. The 94 and 131Å filters are sensitive to the hot plasma at the ejecta’s core, while the 211 and 335Å filters show the cooler surrounding sheath. Images are from Bain et al. (2012a).

emission. The image was binned into 2x2 pixels for improved statistics in each bin; this resolution should be close to the FWHM of the AIA telescope point spread function. A pre-eruption image from  $\sim 12:00$  was subtracted from each image; this ensures that only emission from the ejection is included in the analysis. It should be noted that this assumes a time-invariant background; brightening or dimming of the background loops could introduce contamination into the analysis.

The forward-fit results are shown in Figure 5.5. The lefthand columns show total emission measure ( $EM = \int dEM$ ) maps, in which the fine structure of the plasma can be seen. Note that all the features from the various filters shown in Figure 5.4 are clearly visible in the same image since the temperature dependence has been removed. The righthand columns show temperature maps illustrating temperatures of up to  $\sim 10$  MK in the core of the ejected plasma, surrounded by lower temperatures of a few MK in the sheath.

Other methods of obtaining temperatures using multifilter AIA analysis exist, for ex-

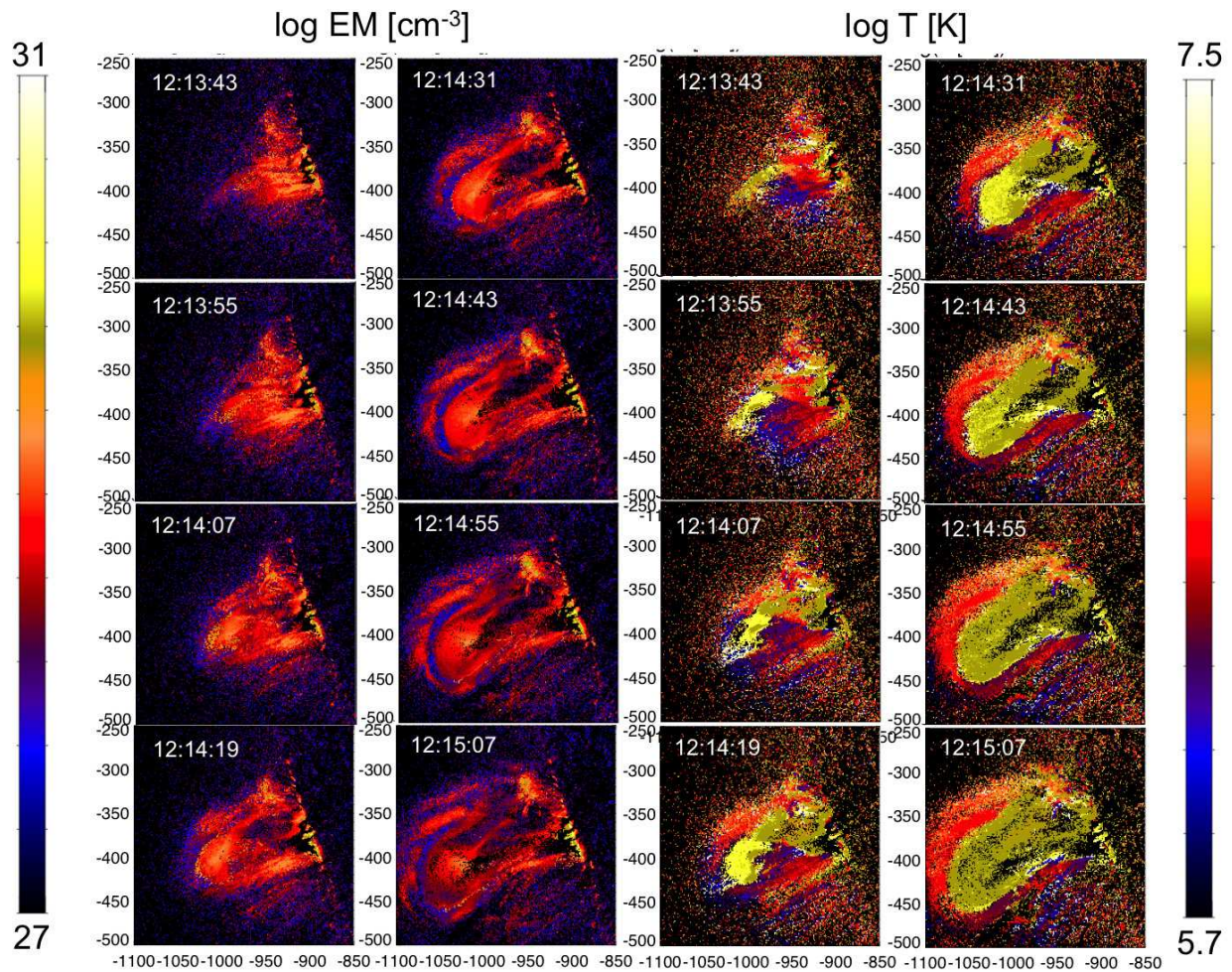


Figure 5.5: Results of forward-fitting  $dEM$  curves to AIA data using the technique from Aschwanden & Boerner (2011). The left two columns show the measured emission measure and the right two columns show the temperature. The core of the ejected plasma reaches a temperature of  $\sim 11$  MK, while the sheath surrounding the core is cooler. The color scales cover the ranges  $\log[EM]=27-31$  and  $\log[T]=5.7-7.5$ , with  $EM$  in  $\text{cm}^{-3}$  and  $T$  in MK.

ample the isothermal filter-ratio method of Schmelz et al. (2011) as well as multithermal  $dEM$ -fitting routines described therein. Hannah & Kontar (2012) have developed a regularized inversion method of calculating  $dEM$ s from multifilter data and find temperatures of up to 11–14 MK when applying this analysis to the 2010 November 03 event (Hannah et al. 2012), in agreement with the analysis presented here.

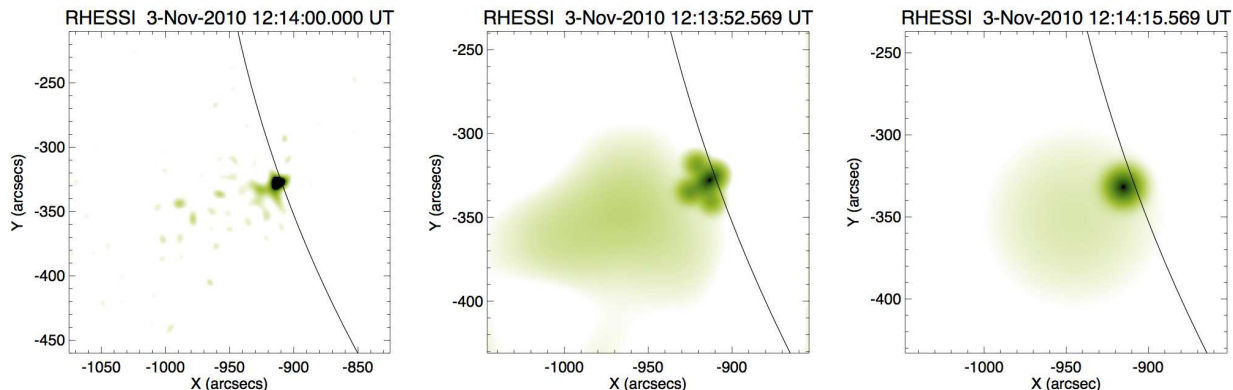


Figure 5.6: *RHESSI* HXR images at 18–40 keV produced using the (left) Clean, (middle) Two-step Clean, and (right) `vis_fwdfit` imaging techniques. The regular Clean image shows artifacts in the corona as it over-resolves the large-area, diffuse, high-altitude source. The Two-step Clean technique is able to reconstruct the diffuse source by first removing components due to the compact, near-limb source; fluxes from each source were then added to make the middle image. The `vis_fwdfit` image corroborates the existence and rough location of the high-altitude source but cannot provide detailed morphology. (Only select simple morphologies are available as of yet in the forward-fitting algorithm.) The middle and righthand images are shown on a log scale to display the diffuse and bright sources together.

### 5.2.2 *RHESSI* HXR from the ejecta

*RHESSI* observed the entire duration of the flare, finding HXR emission in the impulsive phase from 12:13 to 12:15 UT followed by gradual thermal emission throughout the *GOES* peak (see Figure 5.2). *RHESSI* images made using the Clean technique described in section 3.4.1 show a compact source near the limb, shown in the left panel of Figure 5.6. Since the flare footpoints are occulted this is likely upper part of the flare loop. The Clean image hints at emission from a high coronal source at 18–40 keV, but any emission from this source is near the level of noise in the image. To draw out emission from any large-area, diffuse source higher in the corona, the Two-Step Clean method described in section 3.4.1 was used to remove emission from the compact near-limb source; the result is shown in the middle panel of Figure 5.6. This image shows that the *RHESSI* HXR are emitted not only from the near-limb source but also from a high-altitude source higher in the corona. An image

made using the `vis_fwdfit` method (also described in section 3.4.1) was used to corroborate the existence of a high coronal source; this image is shown in the right panel.

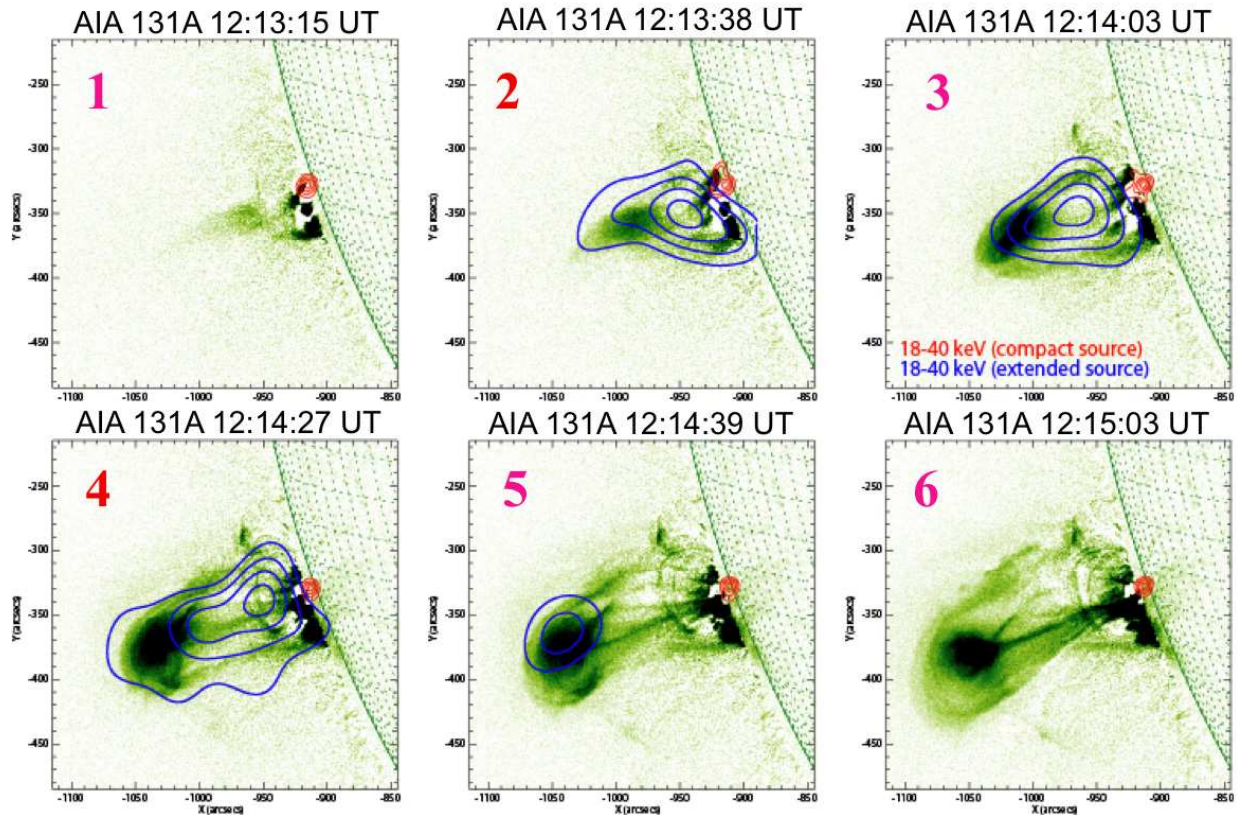


Figure 5.7: *RHESSI* contours produced using the Two-step Clean method are shown overlaid on AIA 131Å images. Contours are (blue) the diffuse, high-coronal source, and (red) the compact, near-limb source, both at 18–40 keV. The high coronal component is first observed in image 2 and evolves in a very similar way as the AIA plasma ejection does. By the time of image 6, the high-altitude HXR source is no longer observed.

Two-step Clean images were made using grids 3–5 for the compact source and grid 5–9 for the diffuse source (with the compact source subtracted) for six time intervals to examine the time evolution of the 18–40 keV HXR source locations. These images are shown in Figure 5.7, overlaid in blue on background images from the AIA 131Å filter. Red contours show the compact HXR source near the limb. Each *RHESSI* image shows high coronal emission (blue) closely matching the location and extent of the AIA plasma, until 12:15:03, when no more *RHESSI* high coronal emission is observed.

The time profiles of the compact (near-limb) and diffuse (high-altitude) HXR sources are shown in the the second panel of Figure 5.2. The profile of the high-altitude source matches that of the 1600 MHz radio source, indicating that HXR and radio emission likely

have the same source of energetic electrons.

To obtain spectra for the two *RHESSI* sources, imaging spectroscopy was performed using `vis_fwhdfit` imaging. A photon power-law spectrum was fit to each of the two sources; these spectra over the time interval 12:14:00–12:15:00 UT are shown in Figure 5.8. The high coronal spectrum has a harder spectrum, with a spectral index of 4.5 vs 5.9 for the near-limb source. The high-altitude source contributes most of the emission above 25 keV.

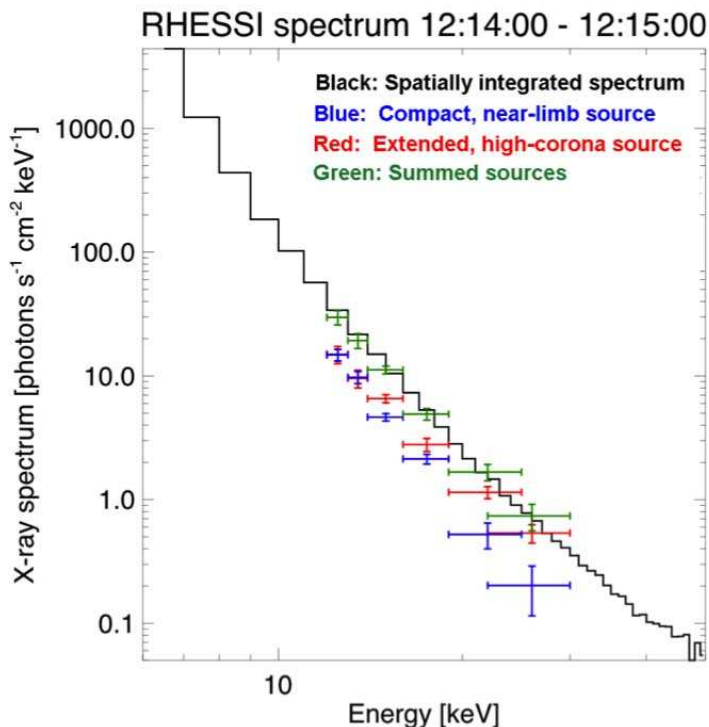


Figure 5.8: *RHESSI* HXR spectrum computed over 1 minute, including (black) an integrated spectrum with no imaging, spectra for the (blue) near-limb and (red) high-altitude sources, obtained with imaging spectroscopy, and (green) the summed spectra (red + blue), which closely matches the integrated spectrum.

### 5.3 Discussion

As shown in Figure 5.7, the diffuse, high-corona source observed by *RHESSI* corresponds (in both location and shape) to the core of the ejected plasma observed by AIA. The spectrum of the HXR source is nonthermal, indicating that the ejected plasma is filled with energetic electrons. With assumptions about the plasma density and cutoff energy of

the X-ray spectrum, the energy in this energetic electron population can be estimated. The thermal energy in the plasma can also be estimated using the multifilter AIA measurements.

### 5.3.1 Thermal energy

AIA does not give information about the line-of-sight extent of the ejected plasma, so we make the assumption that the ejecta is cylindrically symmetric about the axis of its motion (approximately radial). Approximate volumes are selected by eye to include the core of the ejected plasma; since the true volume cannot be determined (but should not be incorrect by a factor of 10) the results presented here should be considered accurate to within an order of magnitude. The total emission measure (see Section 2.5.1)  $EM$  is defined as

$$EM = \int n^2 dV \approx n^2 V \quad (5.3)$$

where the last approximation assumes a constant density over the selected volume. The flux in each image pixel is due to plasma in a volume equal to the pixel area times the assumed line-of-sight length, so a density  $n = \sqrt{EM/V}$  can be computed for each pixel. The average density over the selected region was found to be  $\sim 5 \times 10^9 \text{ cm}^{-3}$  from AIA multifilter measurements of  $EM$ .

The thermal energy is

$$U = nV k_B T \approx \sqrt{EM \cdot V} k_B T \quad (5.4)$$

Here, the temperature  $T$  is taken to be the average temperature in the selected volume as measured from AIA images. Figure 5.9 shows the evolution of the total thermal energy (third panel, purple) and the average temperature in the plasma core (bottom panel) as the ejecta rises. The maximum thermal energy attained is  $5 \times 10^{29} \text{ cm}^{-3}$ .

### 5.3.2 Collisional energy loss

The thermal energy can be compared with the energy in energetic electrons observed by *RHESSI*. In order to isolate emission from the high-altitude HXR source and not the near-limb source, power-law spectra were fit to the HXR emission above 30 keV in each of the time intervals. As discussed in section 5.2.2, emission above this energy comes from the harder, high-altitude source. The top panel of Figure 5.9 shows the evolution of the HXR spectral index over time. The number of instantaneous electrons (second panel) and thick- and thin-target collisional energy losses (third panel) were calculated using formulas in Lin (1974) and detailed in Section 2.5.1. The assumed volumes and inferred density of  $5 \times 10^9 \text{ cm}^{-3}$  were used in calculating the electron parameters. The values are quite sensitive to the cutoff energy of the HXR spectrum, which cannot be obtained from *RHESSI* data for this event due to contamination from the near-limb source below  $\sim 20$  keV. Figure 5.8 implies that the power-law may extend to 12 keV or lower as no obvious cutoff is observed

in the spectrum produced using imaging spectroscopy for the high-altitude source. We take a conservative value of 15 keV for this parameter; if the cutoff energy is lower then the energetic electrons are greater in number and contain more energy than reported here.

As shown in the third panel of Figure 5.9, the thermal energy of the plasma core (purple) is comparable to the collisional energy loss by nonthermal electrons. The thermal energy lies between the curves showing the thick-target (red) and thin-target (black) approximations, indicating that the energetic electrons could provide the required energy to heat the plasma to high temperatures as it rises.

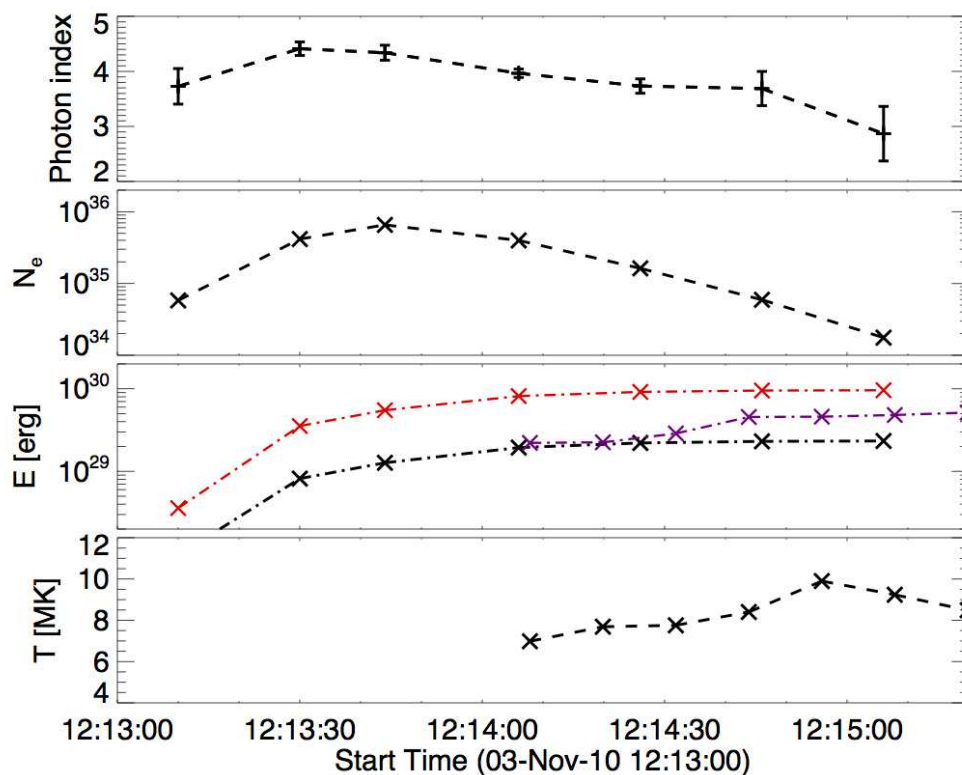


Figure 5.9: Evolution of thermal and energetic parameters throughout the plasma ejection, including (top panel) the photon spectral index and (second panel) the number of instantaneous electrons. The third panel shows the energy collisionally deposited in a (red) thick-target or (black) thin-target approximation, compared with the (purple) thermal energy estimated in the ejecta. The bottom panel shows the average temperature of the hot core. For times before  $\sim 12:14:07$  it is difficult to identify the core volume of interest in Figure 5.5 so calculations of the average temperature and total thermal energy were not done for those times.

### 5.3.3 Electron injection profile

The first two panels of Figure 5.9 show that the photon spectral index decreases with the number of energetic electrons in the plasma core. This is consistent with a scenario in which electrons are injected into the plasma near the beginning of the event and gradually lose energy due to collisions. Because the collisional cross-sections fall with energy, the lower-energy electrons lose energy and disappear from the HXR-emitting distribution more quickly than the higher-energy electrons do, causing a hardening of the spectrum.

However, the collisional loss time is not consistent with this picture. The column length  $N_s$  necessary to effectively stop electrons of energy  $E$  is (Krucker et al. 2008b):

$$N_s(E) = 1.5 \times 10^{17} \text{ cm}^{-2} \left( \frac{E}{\text{keV}} \right)^2 \quad (5.5)$$

With the column depth  $N_s = nvt$ , where  $n$  is the plasma density,  $v$  the electron velocity, and  $t$  the collisional stopping time, the relationship between  $t$  and  $E$  is shown in Figure 5.10 for the measured core density of  $5 \times 10^9 \text{ cm}^{-3}$ . The stopping times are smaller than the time bins in Figure 5.9, so electrons accelerated only by an initial injection would quickly thermalize. The injection must be ongoing, lasting to within a few seconds of the end of the HXR emission, and the injection profile must be similar to the electron population curve in the second panel of Figure 5.9. This implies that the thick-target approximation (red line in Figure 5.9) is more accurate and there is sufficient energy in the nonthermal electrons to supply the observed thermal energy. If the plasma density measurement is off by an order of magnitude, then the collisional stopping times would be similar to the observed HXR decay time and a thin-target or thin-thick approximation would be more appropriate.

## 5.4 Summary

The ejected plasma observed by AIA in the 2010 November event includes the core and sheath morphology typical of a CME and is likely the initial stage of the CME. Multifilter AIA analysis shows that the core of this plasma is heated after its ejection and reaches a surprisingly high temperature of  $\sim 10$  MK. This is consistent with the studies of Akmal et al. (2001); Lee et al. (2009); Landi et al. (2010) that show significant heating in CMEs, much greater than their kinetic energy.

The diffuse, high-corona HXR source observed by RHESSI corresponds (in both location and shape) to the core of the ejected plasma observed by AIA, indicating that the ejecta is filled with energetic electrons containing enough energy to collisionally heat the plasma to the observed high temperatures. A continuous, or extended, injection of electrons is needed in order to maintain the energetic population over the observed time intervals. This injection could be provided by reconnection in a current sheet associated with the CME.

Further studies combining AIA and *RHESSI* data are necessary to determine if accelerated electrons are common in erupting CMEs and if they are the main contributor to the

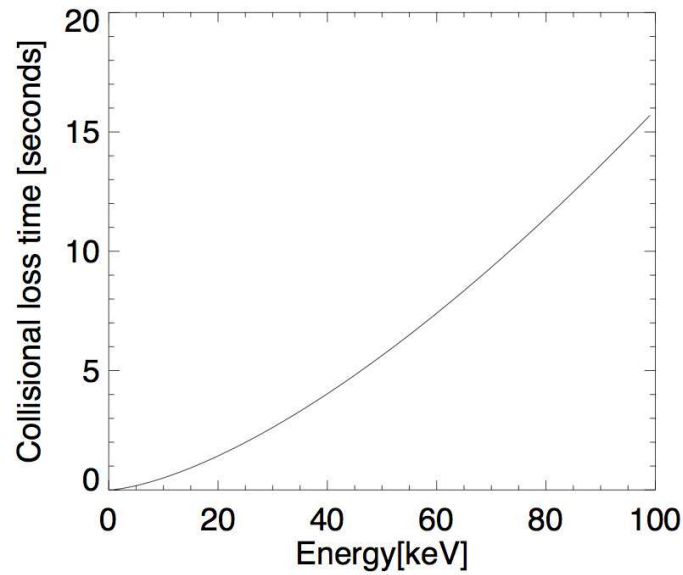


Figure 5.10: The collisional stopping time for energetic electrons in a plasma of density  $5 \times 10^9 \text{ cm}^{-3}$ .

surprisingly high thermal energy contained therein. Instrumentation with more sensitivity and a higher dynamic range such as that on *FOXSI* could study HXRs from CMEs in more detail. For such an instrument it would not be necessary for the main flare site to be occulted, and it could be determined if accelerated electrons are a common CME feature.

## Chapter 6

# Introduction to the Focusing Optics X-ray Solar Imager (FOXSI)

### Abstract

*RHESSI* observations of solar flares over the last 10 years have illuminated many characteristics of flare geometry and energetics due to *RHESSI*'s wide energy range, fine energy and spatial resolutions, and ability to do imaging spectroscopy of distinct regions in the same flare. However, answers to some important questions elude *RHESSI* because of its limited sensitivity and dynamic range. In particular, it is difficult to study coronal sources in the presence of bright footpoints using *RHESSI* data, and *RHESSI* has failed to find any signature of HXRs from the quiet Sun, though it has set the most stringent upper limits on this flux to date. A solution to these difficulties is to build an instrument using HXR focusing optics, which can be coupled with pixelated or strip detectors to drastically reduce the background, producing better sensitivity. The dynamic range of such an instrument would also be improved over that of *RHESSI* due to a narrower point spread function. The *Focusing Optics X-ray Solar Imager (FOXSI)* is a Low Cost Access to Space sounding rocket payload that flew from the White Sands Missile Range on November 2, 2012. Targets during the six-minute observing interval included three active regions and portions of the quiet Sun. This chapter will discuss the scientific motivation of *FOXSI*, give a brief introduction to the instrument, and state the goals of the mission. The following two chapters will provide detail on the theory, heritage, fabrication, and calibration of the instrument components. Preliminary results of the flight will be presented in chapter 9.

### 6.1 Scientific Motivation

In the decade since its launch, *RHESSI* has added a great deal to our understanding of the standard flare model (see Chapters 2 and 3). However, some lines of inquiry are

inconclusive due to *RHESSI*'s limitations in sensitivity and dynamic range. In envisioning the next generation of high-energy solar observers, it is necessary to consider (1) which remaining questions have the greatest scientific importance, and (2) which observational capabilities may be technologically accessible within the next several years.

The 2012 heliophysics decadal survey compiled by the Committee on a Decadal Strategy for Solar and Space Physics listed four key scientific challenges for the study of the Sun and the heliosphere (SH) (Space Studies Board et al. 2012):

- SH-1: Understand how the Sun generates the quasi-cyclical magnetic field that extends throughout the heliosphere.
- SH-2: Determine how the Sun's magnetism creates its hot, dynamic atmosphere.
- SH-3: Determine how magnetic energy is stored and explosively released and how the resultant disturbances propagate through the heliosphere.
- SH-4: Discover how the Sun interacts with the local interstellar medium.

Improved solar HXR observations are essential in meeting two of these challenges, SH-2 and SH-3. For example, the mechanisms producing the hot corona are still unknown. Some heating candidates have been identified (for example, flares and spicules; see Section 2.4), and identifying which, if any, of these candidates can supply and maintain the solar corona's high temperature of  $>10^6$  K is a fundamental part of challenge SH-2. More sensitive HXR observations of nonthermal electrons in nanoflares can contribute toward meeting this challenge, either by establishing flare heating as a capable contributor to coronal heating or by ruling out its role entirely.

The survey also underscores the importance of understanding how and when solar flares release energy, identified in challenge SH-3. Prior to a flare, magnetic energy is stored in the coronal magnetic field. The exact mechanisms by which energy is transferred into kinetic energy is unknown, although several mechanisms have been theorized (see Section 2.3). Direct observations of the acceleration region and its immediate surroundings via HXR measurements will resolve debates about basic flare structures, which acceleration mechanisms are at work, and which are the most important.

### 6.1.1 Coronal sources

*RHESSI* has investigated these questions to the best of its abilities. As discussed in chapter 3, *RHESSI* has made remarkable progress in exploring flare acceleration and geometries, with much of the evidence supporting the standard model. For the first time, *RHESSI* was able to use imaging spectroscopy to study coronal and footpoints separately (e.g. Krucker & Lin 2002) and also found examples of double sources in the corona, suggesting an acceleration site between them (e.g. Sui & Holman 2003; Liu et al. 2008; Glesener et al. 2012). In at least one case, *RHESSI* observations suggest that a high coronal source is the acceleration region itself (Krucker et al. 2010).

But *RHESSI* has typically only been able to study coronal sources in detail in rare cases, usually when the flare is partially occulted, because of its limited dynamic range. And even then, statistics are usually quite low, especially in the case of multiple sources. Bremsstrahlung intensity varies with the densities of both the scattering electrons and the target ions. Since the chromosphere is orders of magnitude denser than the corona, chromospheric footpoints should be vastly brighter than looptop or above-the-looptop coronal sources. Figure 6.1 compares the flux at 30 keV from flares located on the solar disk to that from flares observed over the limb. On-disk flares, including footpoints, are 10–100 times brighter than flares displaying only coronal sources.

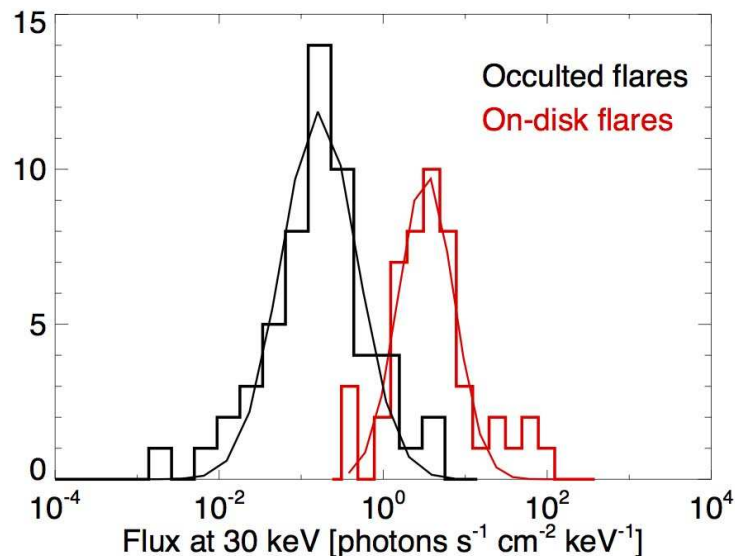


Figure 6.1: Histogram showing peak 30 keV fluxes from flares located on the solar disk (red) or over the limb (black), in which case only coronal sources are visible. Fluxes from disk flares are much brighter than those from partially occulted flares since footpoint fluxes are included in the measurements of those flares. The 44 on-disk flares are those from the statistical study of double footpoints in Saint-Hilaire et al. (2008), while the 55 partially occulted flares are those from Krucker & Lin (2008); all flares are of GOES class C and higher. The Gaussian averages of the on-disk and occulted flare histograms are  $\log[\text{flux}] = 0.5$  and  $-0.8$ , respectively, indicating that footpoint HXR sources are, on average, 1.3 orders of magnitude brighter than coronal sources.

However, it is thought that coronal HXR sources are ubiquitous. Krucker & Lin (2008) found that nearly all (50 out of 55 studied) partially occulted flares have coronal sources that are visible by *RHESSI*. Therefore, the reason coronal sources are not usually observed is due to *RHESSI*'s limited dynamic range; its ability to image faint sources in the presence of bright ones is limited by the rotation modulation technique as the modulation curve is

dominated by the brightest source. Each source acts as a background for every other source in the image. Typically, a source will not be imaged by *RHESSI* if there also exists a source on the Sun  $\sim 10$  times brighter. Figure 6.1 shows that footpoints together are on average  $\sim 20$  times brighter than coronal sources, or separately  $\sim 10$  times brighter, putting coronal sources on the very edge of the detection limit for *RHESSI*. *RHESSI* images of multiple sources typically show a dynamic range of  $\lesssim 5$ , while Figure 6.1 indicates that a dynamic range better than  $\sim 20$  is required in order to reliably image the two features (footpoints and coronal sources) together.

*RHESSI* is also limited in its imaging of faint coronal sources by its sensitivity in relation to its background. *RHESSI* utilizes cylindrical germanium detectors (7.1 cm diameter by 8.5 cm), allowing for good efficiency over a wide energy range (see Chapter 3). However this large volume also results in a large background, which scales directly with volume (though it should be noted that for HXR observations the background comes only from the front segments). *RHESSI*'s high-background orbit and lack of shielding (in order to minimize weight and cost) compound this issue. This deficiency in sensitivity is illustrated by the failure of *RHESSI* to image HXRs from electron jets associated with Type III radio bursts (and which later are observed in-situ at 1 A.U.). This limitation is discussed in Saint-Hilaire et al. (2009), who conclude that *RHESSI* could only observe an upward-traveling Type III-emitting beam if it were to contain  $> 10^{35}$  electrons above 10 keV, i.e. comparable to the number of electrons thought to be contained in the downward-moving electron beam. To date, *RHESSI* has only found one potential example of HXRs from Type III-emitting populations (Krucker et al. 2008a).

### 6.1.2 Nanoflares and coronal heating

*RHESSI* made important headway in investigating the flare frequency distribution by measuring the thermal and nonthermal energies of microflares, or flares with energies between  $10^{27}$  to  $10^{30}$  ergs, and found that microflare occurrence follows a power law with index 1.7 (Christe et al. 2008a; Hannah et al. 2008), which is too flat to adequately heat the corona; these observations were discussed in Section 2.4.1. These were found to occur only in active regions and to be similar to large flares in that a nonthermal power-law distribution of accelerated electrons (observed in HXRs) collisionally transfers energy into thermal energy. The power in microflares in this fairly flat distribution was found to be insufficient to heat the corona, especially since at solar minimum no active regions are observed on the disk (yet coronal heating persists).

At the lower-energy side of the flare frequency distribution, it is unclear if the distribution continues or if it breaks upward. The contribution from nanoflares (see Section 2.4.2 for a definition) is thus important in evaluating the ability of flares to heat the corona. If nanoflares occur not only in active regions but across the entire solar surface (in which case they are usually termed “network flares”), then it is conceivable that they do not follow the same power-law distribution as that of larger flares. As discussed in Section 2.4.2, quiet-Sun brightenings have already been observed as thermal sources in the EUV and SXR, while ra-

dio observations suggest nonthermal counterparts (Krucker et al. 1997). HXR measurement of the nonthermal components would establish whether they are, in fact, flares and thus whether they are a potential source of energy input to the corona.

Several studies have looked for HXR emission from the quiet Sun (Peterson et al. 1966; Edwards & McCracken 1967; Feffer et al. 1997), with an attempt by Hannah et al. (2010) using *RHESSI* data being the most recent and most sensitive. It is necessary to use imaging for this measurement in order to separate the faint signal from the extrasolar background. But *RHESSI*'s modulation technique is not sensitive to faint sources well-distributed across the entire disk. Instead, a coarse modulation feature of the *RHESSI* grids (due to the grid thickness) was used that modulates the entire Sun as a source. Hannah et al. (2007) describes this “fan-beam modulation” technique. The instrument is off-pointed from the solar center by 0.4–1.0 degrees during some quiet times to take advantage of this method. Hannah et al. (2010) found that nonthermal HXR spectra of nanoflares capable of heating the corona must be steep ( $\gamma > 5$ ) and have a low cutoff energy ( $\sim 0.1$ – $1$  keV) in order to fall below the *RHESSI* upper limits.

More sensitive HXR measurements of the quiet Sun would either (1) make the first measurements of nonthermal emission from nanoflares and determine whether they are capable of heating the corona; or (2) set much deeper upper limits on quiet Sun HXR emission, possibly ruling out nanoflares as coronal heating candidates. A more sensitive instrument would measure individual nanoflares, instead of spatially and temporally averaged emission.

In conclusion, *RHESSI*'s sensitivity and method of imaging are not appropriate for identifying and measuring nanoflares, and its sensitivity and dynamic range are not sufficient for fully understanding particle acceleration in regular flares.

## 6.2 Advantages of focusing optics

A potential solution to these observational difficulties is to develop a direct-imaging instrument using focusing HXR optics. These optics focus HXRs at small angles of incidence ( $< 0.5$  degrees in the *FOXSI* energy range) with a double reflection off superpolished and finely figured mirrors. Since each mirror has a small geometric area, several mirrors are usually nested together to form a telescope, as in Figure 6.2. Focusing, grazing-incidence optics have been the standard in SXR astronomy for over a decade, having flown on the Chandra X-ray Observatory and the XMM-Newton spacecrafts. More recently, technological advancements have extended the available energy range of grazing-incidence optics to the HXR regime.

In addition to being a direct imaging technique and therefore offering easier image reconstruction, focusing optics can offer better sensitivity and dynamic range. By focusing HXRs onto a position-sensitive detector that is divided into small volumes (strips or pixels), the background is reduced, leading to increased sensitivity. (In principle the smaller detectors could also be more easily shielded, potentially reducing the background even further.) The dynamic range of the image is constrained by the point spread function (PSF) of the optics,

which is dependent on the figuring accuracy and smoothness of the mirrors. Technological advances in the last 10–15 years have resulted in the ability to fabricate optics accurate and smooth enough to achieve appreciable effective area and narrow PSFs in the HXR energy range, as we shall see in section 7. This imaging technique will work well even in the case of multiple sources spread out over the entire field of view, unlike in the case of *RHESSI*.

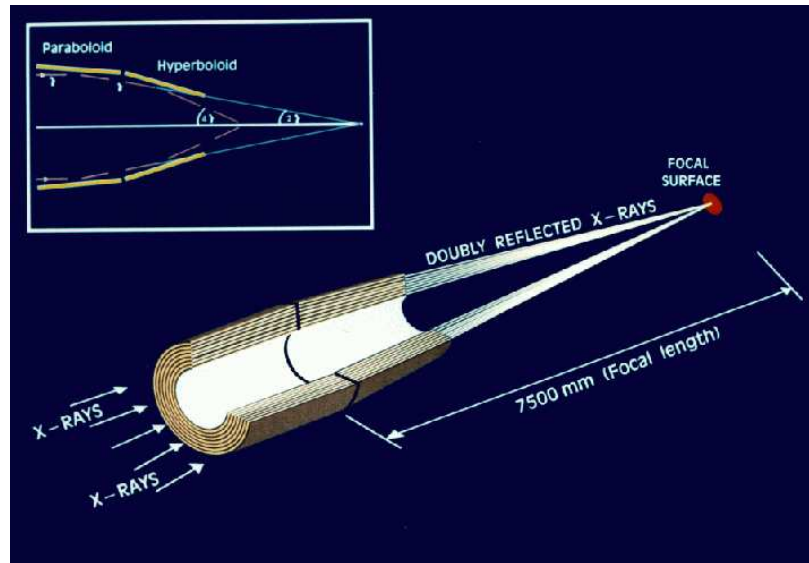


Figure 6.2: Schematic of a grazing-incidence focusing X-ray telescope. Incident photons undergo a double reflection before being focused. Typically, mirrors of different diameters are nested together to increase the effective area of the instrument. Image is from Ehle et al. (2001).

### 6.3 The *FOXSI* sounding rocket

In 2007, the *Focusing Optics X-ray Solar Imager (FOXSI)* proposed by UC Berkeley’s Space Sciences Laboratory (SSL) was selected for funding as a sounding rocket payload in NASA’s Low Cost Access to Space (LCAS) program. *FOXSI*’s scientific goal is to make the first HXR observations of nonthermal electrons in quiet-Sun nanoflares, or else to set new upper limits. As a sounding rocket payload, *FOXSI* can achieve sufficient altitude ( $\gtrsim 120$  km) to observe HXR in the 4–15 keV range, appropriate for studying nanoflares. *FOXSI* utilizes focusing HXR optics and silicon strip detectors to achieve a sensitivity  $\sim 50$  times that of *RHESSI* at 10 keV. A technological goal of *FOXSI* is to demonstrate the viability of these optics for solar flare observations, an important foundation for a potential future spacecraft proposal; see Chapter 10 for some discussion of a spaceborne *FOXSI* concept.

Energy range	$\sim 4$ to 15 keV
Field of view	16 x 16 arcmin <sup>2</sup>
Sensitivity (at 8 keV)	$\sim 0.004$ ph cm <sup>-2</sup> s <sup>-1</sup> keV <sup>-1</sup> , approx. 50 times that of <i>RHESSI</i>
Dynamic range	100 for source separation $>30$ arcsec
Optics angular resolution (FWHM)	7 arcsec
Detector angular resolution	7.7 arcsec
System effective angular resolution (FWHM)	10 arcsec
Optics effective area	150 cm <sup>-2</sup> at 8 keV, 14 cm <sup>-2</sup> at 15 keV
Overall effective area	120 cm <sup>-2</sup> at 8 keV, 8 cm <sup>-2</sup> at 15 keV

Table 6.1: Figures of merit for the *FOXSI* sounding rocket payload. Table adapted from Krucker et al. (2011b)

*FOXSI* is the first project to apply the technical advantages of HXR focusing optics to solar observations. Many of the technical advances made by astrophysics experiments (like high sensitivity and small half power diameters) can be borrowed, but solar observing requires narrower point spread functions for high-quality imaging of extended and nearby sources. At minimum, a solar HXR imager needs to be able to separate flare footpoints from each other and from coronal sources, requiring an angular resolution of  $\lesssim 10$  arcseconds. Ideally, with even better resolution more details of coronal sources (and potentially the acceleration region itself) could be studied. *FOXSI* demonstrates that these qualities can be achieved by focusing optics with a dynamic range of 100–1000 and a point spread function with FWHM of 7 arcseconds, appropriate for solar flare studies. Table 6.1 lists some of the key parameters of the project and Table 6.2 shows a project timeline.

*FOXSI*'s detectors and optics are supplied by team members at JAXA/ISAS (Japan) and NASA/MSFC, respectively, and SSL is responsible for the payload design, mechanical structure fabrication, detector readout electronics system, payload assembly, science planning, and flight monitoring/commanding.

### 6.3.1 *FOXSI* optics

The heart of the *FOXSI* rocket payload is a set of seven focusing HXR optics. These optics were fabricated at NASA's Marshall Space Flight Center (MSFC) by a team led by Dr. Brian Ramsey, and draw heavily from the optics development by the High Energy Replicated Optics (HERO) balloon program at MSFC (Ramsey et al. 2002; Ramsey 2005). Each of *FOXSI*'s seven optics modules consists of seven nested mirrors with a Wolter I figure, produced via MSFC's electroformed nickel replication process (Gubarev et al. 2006) in order to keep costs and fabrication time low. The theory, heritage, fabrication process, and measured abilities of these optics is the subject of chapter 7. The optics achieve a spatial resolution of better than 7 arcseconds and an effective area of 140 cm<sup>2</sup> at 10 keV (see Fig. 6.3, right panel, for a plot of the optics effective area).

---

Fall 2007	Selection of <i>FOXSI</i> as an LCAS sounding rocket payload
Spring 2008	Start of <i>FOXSI</i> design work
2008–2011	Optics fabrication
Fall 2010	Selection of <i>FOXSI</i> for a second LCAS flight
2010–2011	Calibration of <i>FOXSI</i> optics
2010–2012	Detector and R/O system testing at SSL
2011–2012	Calibration of <i>FOXSI</i> detectors
February–March 2012	<i>FOXSI</i> 's first launch campaign, cut short by cooling accident
Summer 2012	Rebuild of the <i>FOXSI</i> detector system
August 2012	Calibration of new <i>FOXSI</i> detectors
October–November 2012	<i>FOXSI</i> launch campaign at White Sands
November 2 2012	First launch
2013–2014	Upgrades for <i>FOXSI</i> 2
Fall 2014	Second launch

---

Table 6.2: Timeline of the *FOXSI* sounding rocket project.

### 6.3.2 *FOXSI* detectors

The use of focusing optics requires a position-sensitive detector for reconstructing images. *FOXSI*'s science goals also require fine energy resolution and appreciable efficiency in the 4–15 keV range to be able to separate thermal and nonthermal HXR components. These requirements are fulfilled through the use of double-sided silicon strip detectors (DSSDs) with 75  $\mu\text{m}$  pitch strips. The *FOXSI* DSSDs (Ishikawa et al. 2011; Saito et al. 2010) are provided by Professor Tadayuki Takahashi's group at ISAS/JAXA in Sagamihara, Japan. The detector concept arose from detector development for the Hard X-ray Imager (HXI) on the planned Astro-H spacecraft (Kokubun et al. 2010). A readout ASIC (the VATA451) was also developed by the ISAS team especially for *FOXSI* with collaboration from IDEAS/Gamma Medica and Stanford University, again drawing on previous iterations for HXI. The detector and ASIC combination were selected and designed to provide the spatial resolution (7 arcseconds), energy resolution (500 eV) and energy cutoff ( $\sim 4$  keV) required by *FOXSI*. Chapter 8 will describe the detectors in detail as well as the electronics system constructed at Berkeley for the detector readout.

## 6.4 *FOXSI*'s science goals

*FOXSI*'s 6 minute observation time is dedicated to two measurements: (1) thermal X-rays from active regions and (2) nonthermal X-rays from the quiet Sun.

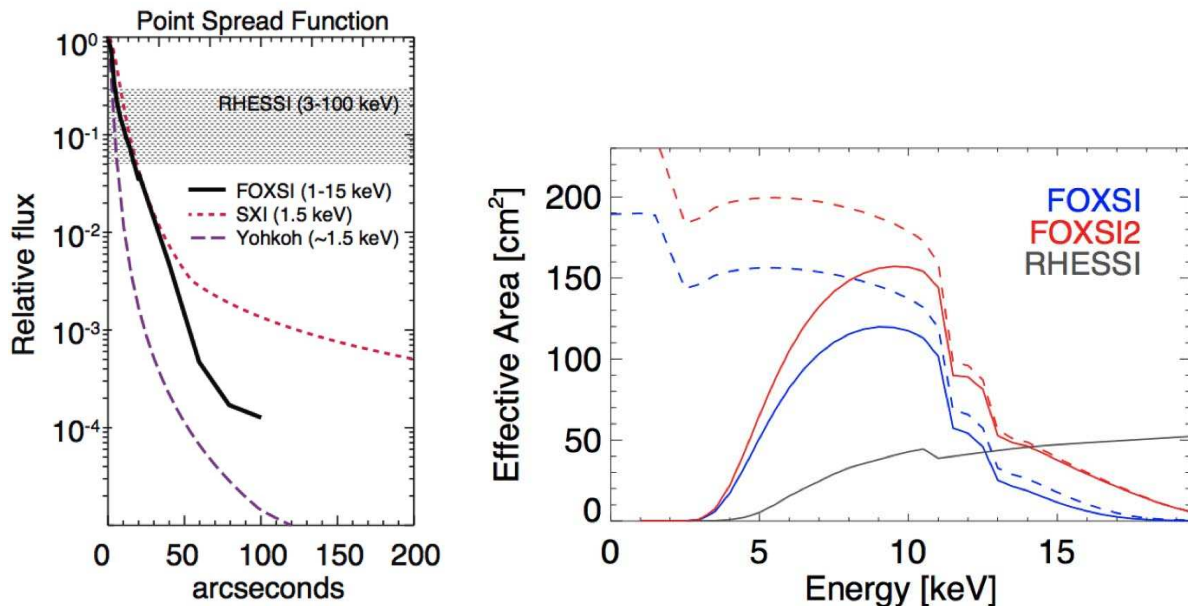


Figure 6.3: (Left) Point spread function of the *FOXSI* optics compared with that of other instruments. *FOXSI*'s PSF (black line) falls by two orders of magnitude within 50 arcsec, a vast improvement over the dynamic range of *RHESSI* (gray shaded region). (Right) Effective area of the optics alone (dashed lines) and of the entire instrument including the detector response and absorption by blankets (solid lines), for the first *FOXSI* rocket payload (blue) and the *FOXSI* 2 upgrade (red). Both figures are from Krucker et al. (2011b)

### 6.4.1 Active region temperatures

An unanswered question surrounding the thermal nature of active regions is whether a high-temperature component exists and is common. It is generally accepted that active regions have temperatures of 2–3 MK even when quiescent (i.e. not flaring). However, several recent studies have suggested the additional presence of a hotter component. McTiernan (2009) examined quiescent active region temperatures over the duration of the *RHESSI* mission and found a persistent component at 7–8 MK. Schmelz et al. (2009) combined *Hinode* XRT and *RHESSI* data to produce an active region differential emission measure (DEM) with a very hot component at  $T \sim 10$  MK. Most recently, Miceli et al. (2012) used data from the SphinX instrument ( $\sim 1$ –7 keV, similar to *GOES* but with better sensitivity) and found a hot component with a temperature of 7 MK and an emission measure of  $\sim 2.7 \times 10^{44} \text{ cm}^{-3}$ . Warren et al. (2011), on the other hand, found a peak temperature at 4 MK and no noticeable hot component when examining a quiescent active region using *Hinode* EIS and AIA data.

*FOXSI*'s energy range and sensitivity are ideal for studying this problem. If a hot component exists, it should produce measurable count rates in *FOXSI*'s energy range of

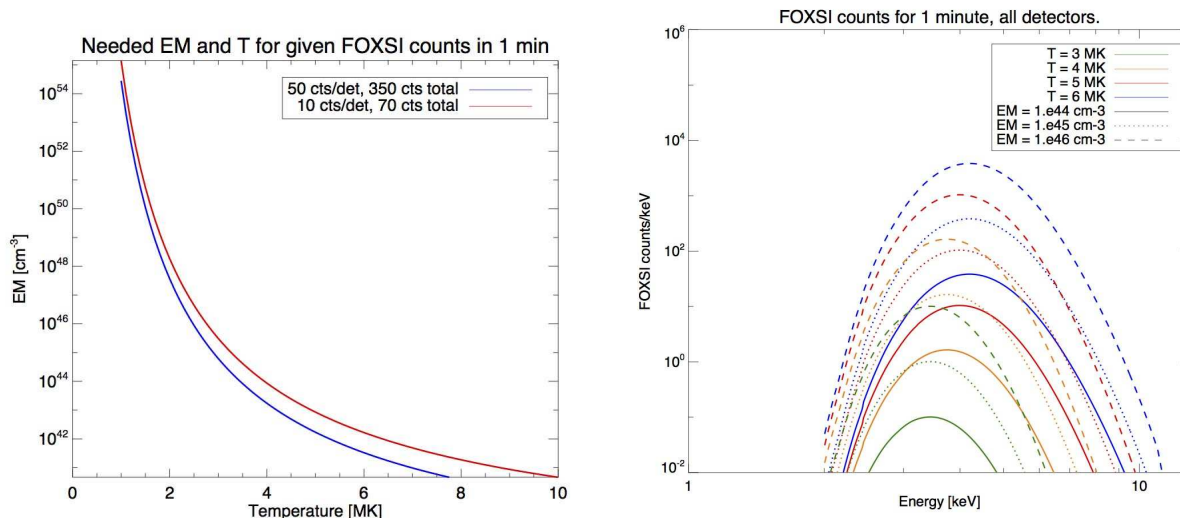


Figure 6.4: (Left) The parameter space of emission measure (EM) and temperature to which *FOXSI* is sensitive. Shown here are the values of the EM and temperature that would produce 350 (blue) or 70 (black) total counts in the *FOXSI* instrument in one minute. The higher the temperature, the lower the emission measured needed to produce this count rate. (Right) Simulated *FOXSI* counts for one minute for several emission measures and temperatures.

4–15 keV unless it is extremely faint. *FOXSI* also has sensitivity to lower temperatures of 2–5 MK depending on the emission measure; figure 6.4 shows the emission measures and temperatures to which *FOXSI* is sensitive. The lefthand panel shows the emission measure (EM) necessary to produce a given *FOXSI* count value for a range of temperatures. Simulated *FOXSI* count spectra for several choices of temperatures and EM are shown in the righthand panel. Figure 6.5 shows simulated *FOXSI* spectra for a one-minute observation of the thermal plasma reported in two of the previous studies (one containing a hot component and one not). Unlike some of the previous studies, *FOXSI* has high enough sensitivity that it does not need to accumulate data over a long time interval or concatenate several data sets in order to adequately measure an active region thermal spectrum.

It was intended that one minute of solar observations by the sounding rocket payload would be devoted to active region study. This would serve as an important check of the instrument, since thermal fluxes from active regions were expected to be measurable. In practice (see Chapter 9), fluxes from active regions were extremely low during the first flight and most of the observation time included an active region within the field of view.

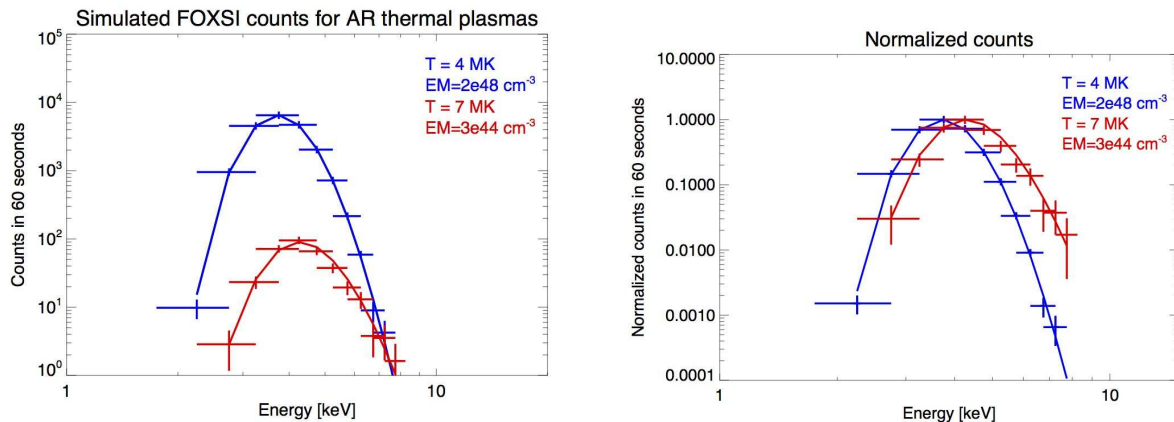


Figure 6.5: Simulated *FOXSI* count rates for the active-region thermal plasmas similar to those reported in Miceli et al. (2012) and Warren et al. (2011), taking into account *FOXSI's* effective area and livetime. For each plot the thermal plasma has been approximated by a single temperature and emission measure. The lefthand plot shows the expected counts (solid line) and a simulated *FOXSI* observation (data points with error bars). In the righthand plot, each count spectrum has been scaled to its maximum, illustrating the difference in peak energies between the two spectra. Miceli et al. (2012) found the active region flux to be dominated by a 7 MK component, so no lower-temperature component was included in the simulation of the 7 MK plasma. Warren et al. (2011) calculated the flux from a small active region core only. For this simulation, the flux was scaled to the active region size of  $\sim 100 \times 100 \text{ arcsec}^2$ . A smaller size (and thus smaller X-ray flux) is appropriate if the emission arises primarily from a core region.

### 6.4.2 Nonthermal emission from quiet Sun nanoflares

Recent studies of the quiet Sun have found temperatures of 1–2 MK, for example Sylwester et al. (2012), using the SphinX instrument, and Brooks et al. (2009), using EIS. Even during transient events (network flares), the temperatures remains less than 2 MK (Krucker & Benz 1998). These temperatures are below *FOXSI's* sensitivity range, so any quiet-Sun emission in the *FOXSI* energy range of 4–15 keV should be nonthermal HXR emission.

Radio studies have found a nonthermal component to quiet-Sun network flares (Krucker et al. 1997), suggesting that they may be similar processes to more commonly observed active-region flares. Assuming the thermal energy of these network flares is deposited by nonthermal electrons in a thick target (i.e. the energy of the initial nonthermal electron population is the same as the ultimate thermal energy), the nonthermal HXR spectrum can be simulated for various values of the spectral index and cutoff energy. These simulations are shown in Figure 6.6, showing that any nonthermal quiet-Sun nanoflare spectrum should be measurable by *FOXSI*.

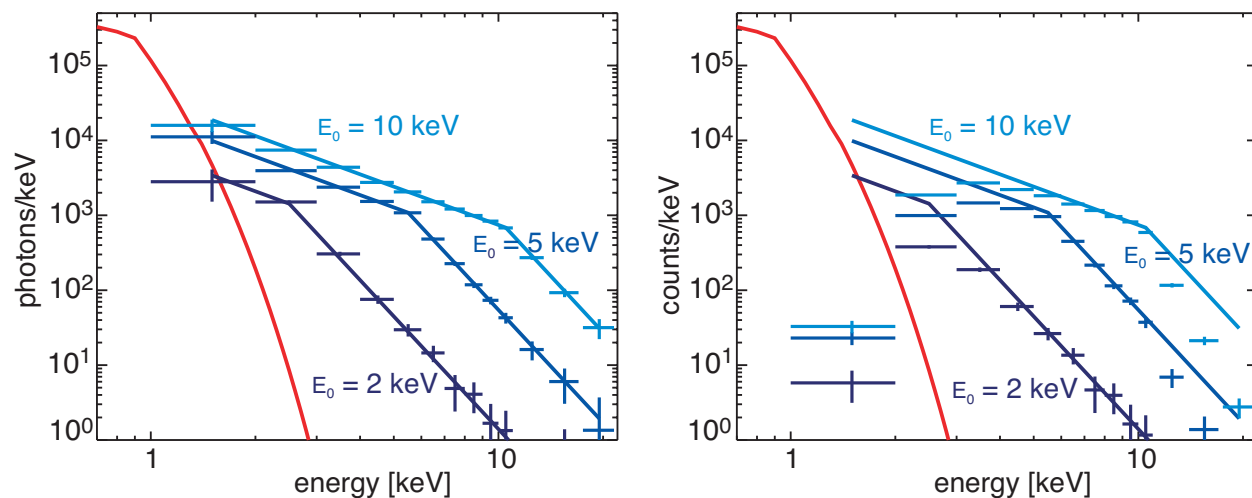


Figure 6.6: Simulations of spectra for nonthermal (blue) and 2 MK thermal (red) X-rays from quiet-Sun network flares. On the left, simulated photon flux is shown for various values of the cutoff energy  $E_0$ , with a fixed power-law index of 5 above and 1.7 below the break. In the righthand plot, data points and error bars show the expected *FOXSI* count spectra. Both plots are from (Krucker et al. 2011b)

The absence of nonthermal HXR emission would suggest that the flaring process for network flares (if they are indeed flares) is different than that for regular flares. This would provide an opportunity for new theories to explain how network flares are powered, and would allow for the possibility that the quiet-Sun network flare distribution is different (and possibly steeper) than the active-region flare distribution.

The majority of the observing time was intended to be devoted to this science goal. In the unlikely case that quiet-Sun HXR fluxes were higher than the rates for which the instrument was optimized (count rates of  $\sim 500$  per second), aluminum attenuators could be inserted in front of the detectors to reduce fluxes, especially at low energies (see Section 8.2.4). As it turned out, these attenuators were not needed during the first flight.

Occurrence rates of EUV network flares predict 10–1000 flares in the *FOXSI* field of view in five minutes (Krucker et al. 2011b). EUV brightenings are on the order of minutes, comparable to *FOXSI*'s observation time.

## 6.5 Chapter summary

In 2009, *FOXSI* was funded by LCAS for a second rocket flight, which is expected to take place two years after the first. Upgrades to the instrument will include three smaller-diameter mirrors added to each optics module and the replacement of the silicon detectors with cadmium telluride detectors; both improvements are intended to improve the high-

energy response of the instrument.

The following chapters will describe in detail the elements of the *FOXSI* instrument, their purposes, pre-flight testing and calibration results, and preliminary results from the first flight.

# Chapter 7

## Focusing Hard X-ray Optics for FOXSI

### Abstract

The core of the *FOXSI* instrument concept is a set of focusing hard X-ray optics. The performance of these optics demonstrates that fabrication technology has progressed to the point where HXR focusing optics are feasible within a low-cost mission budget. In order to be useful for high-energy solar flare observations, these optics need to have angular resolutions of 10 arcseconds or less (in order to separate footpoints and coronal sources) and a dynamic range better than that of *RHESSI*. This chapter will describe the physics of X-ray reflectivity, the history and heritage of HXR focusing optics design, and present results from the calibration of the *FOXSI* optics modules.

### 7.1 Introduction to X-ray Focusing Telescopes

A description of the reflection of X-rays is intuitively different than a description of visible light reflection. As shall be shown in this chapter, the index of refraction of materials for X-rays is slightly less than unity, with two consequences: (1) when reflection occurs it is total external reflection as opposed to internal; and (2) the angles of incidence as measured from the surface must be extremely small in order to obtain appreciable reflectivity. Much of the discussion here will follow that in Als-Nielsen & McMorrow (2011).

#### 7.1.1 X-ray reflectivity

When an electromagnetic wave enters a medium with index of refraction  $n$ , three wave components are typically used to describe the interaction: the incident, transmitted, and reflected waves. Figure 7.1 shows these three components, marked by the wavevectors  $\vec{k}_I, \vec{k}_T,$

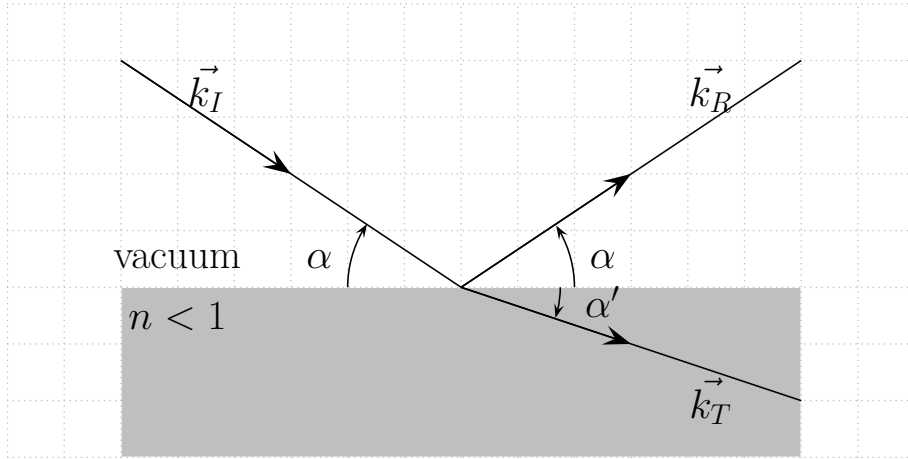


Figure 7.1: Ray-tracing diagram demonstrating Snell's law.  $\vec{k}_I$ ,  $\vec{k}_R$ , and  $\vec{k}_T$  are the incident, reflected, and transmitted rays, respectively.

and  $\vec{k}_R$ , respectively. The incident and reflected waves have the same wavevector magnitude ( $k_I = k_R \equiv k$ ), while the transmitted and incident wavevectors are related by  $k_T = nk$ . Figure 7.1 also illustrates the relationship between the angles of the incident and transmitted beams, known as Snell's Law. (Here, it is assumed that the ray enters from a medium with a refractive index of 1.)

$$\cos \alpha = n \cos \alpha' \quad (7.1)$$

The interaction could instead be described in terms of scattering and absorption. If the incident wave has intensity  $I_0$ , then we expect that after traveling a distance  $z$  within the medium, the intensity  $I$  is reduced due to absorption:

$$I = I_0 e^{-\mu z} \quad (7.2)$$

Here,  $\mu$  is the absorption coefficient of the material; values can be found in the NIST table of X-ray Mass Attenuation Coefficients (Hubbell & Seltzer 2004).

In the classical description of scattering between an electromagnetic wave and a free electron, the wave exerts a force on the electron, causing it to oscillate. The oscillating electron radiates another electromagnetic field, producing the scattered wave. If the scattered and incident waves have identical frequencies then the scattering is elastic and the process is Thomson scattering. The differential cross section  $\frac{d\sigma}{d\Omega}$  is related to the scattering length  $r_0$ .

$$\frac{d\sigma}{d\Omega} = r_0^2 |\hat{\epsilon} \cdot \hat{\epsilon}'|^2 \quad (7.3)$$

where the magnitude is determined by the scattering length and the incident and scattered direction vectors  $\hat{\epsilon}$  and  $\hat{\epsilon}'$  determine the wave polarization. The scattering length here is the

Thomson scattering length (also known as the classical electron radius):

$$r_0 = \frac{e^2}{4\pi\epsilon_0 m_e c^2} = 2.82 \times 10^{-5} \text{ \AA} \quad (7.4)$$

X-ray energies are well above most electronic transitions in atoms (with the exception of, for example, K and L shell transitions). As a result, bound electrons react much like free electrons do to the electromagnetic field and Thomson scattering is a good approximation. Each electron contributes to the scattering with the Thomson scattering length and each scatter produces a phase shift of  $\pi$ . The index of refraction,  $n$ , is slightly less than unity:

$$n = 1 - \delta + i\beta \quad (7.5)$$

Here,  $\delta$  and  $\beta$  are defined by the material:

$$\delta = \frac{n_e r_0 \lambda^2}{2\pi}; \quad \beta = \frac{\mu \lambda}{4\pi} \quad (7.6)$$

where  $n_e$  is the electron density of the material. Both parameters depend heavily on the wavelength and are thus small for high-energy X-rays. A complete derivation of  $\delta$  is given in chapter 3 of Als-Nielsen & McMorrow (2011). The relation can be seen most easily by comparing two descriptions of the interaction: (1) the refractive description, where an electromagnetic wave passing through a thin sheath of material undergoes a phase shift of  $(n-1)k\Delta$ , where  $\Delta$  is the thickness of the sheath; and (2) the scattering description, where the wave is scattered by each electron in the sheath. Adding up the scattered waves and using the Thomson scattering length produces a phase shift of  $(2\pi\rho r_0\Delta)/k$ . Equating these two expressions for the phase shift results in the definition for  $\delta$  above.

The definition for  $\beta$  can be found by considering the effect of an imaginary part of  $n$  on a normal-incidence wave with initial field amplitude  $A_0$  as it enters a medium:

$$A_0 e^{ik_T z} = A_0 e^{inkz} = A_0 e^{i(1-\delta)kz} e^{-\beta kz} \quad (7.7)$$

This last factor produces an attenuation of the field, reducing the beam amplitude by  $e^{-\mu z/2}$  and the intensity by  $e^{-\mu z}$ .  $\beta$  is thus defined as  $\mu/(2k)$ .

Since the refractive index is less than unity for X-rays, total external reflection can occur for angles of incidence  $\alpha$  less than the critical angle  $\alpha_c$ , with  $\alpha$  measured from the surface. (See Figure 7.1.) Angles tend to be quite small, so small-angle approximations can be used in Snell's law. For the critical angle  $\alpha = \alpha_c$  the transmitted ray angle  $\alpha' = 0$ :

$$\cos \alpha_c = n \quad (7.8)$$

$$1 - \frac{\alpha_c^2}{2} \approx 1 - \delta \quad (7.9)$$

$$\alpha_c = \sqrt{2\delta} \quad (7.10)$$

For the X-ray range,  $\delta$  and  $\alpha_c$  are very small. For a 4 keV photon (wavelength  $3.1\text{\AA}$ ),  $\delta = 4.4 \times 10^{-5}$  and  $\alpha_c = 9.4$  milliradians (0.54 degrees), assuming an electron density of  $\sim 1\text{\AA}^{-3}$ . For a 15 keV photon (wavelength  $0.8\text{\AA}$ ),  $\delta = 3.1 \times 10^{-6}$  and  $\alpha_c = 2.5$  milliradians (0.14 degrees). Very small angles of incidence are thus needed in order to reflect X-rays.

If the X-rays enter a thin sheath of atoms instead of a layer of free electrons, the scattering length is modified by a factor  $f_1$  reflecting the form factor of the atom. This factor accounts for the phase differences of the wave as it interacts with the various electrons of the atom. In this case  $\delta$  becomes

$$\delta = \frac{n_{\text{atom}} r_0 \lambda^2}{2\pi} f_1 \quad (7.11)$$

The relevant density ( $n_{\text{atom}}$ ) is now the number density of atoms. The form factor  $f_1$  is in general complex, but at X-ray energies far from absorption edges can be approximated by  $Z/A$ , the ratio of atomic number to atomic weight, to account for the multiple scatterers within an atom.

At the interface, the wave amplitude and its derivative must be continuous. Let  $a_I$ ,  $a_R$ , and  $a_T$  be the amplitudes of the incident, reflected, and transmitted waves, respectively. The boundary conditions require:

$$a_I + a_R = a_T \quad (7.12)$$

$$a_I \vec{k}_I + a_R \vec{k}_R = a_T \vec{k}_T \quad (7.13)$$

The component of the last equation perpendicular to the surface is:

$$a_I k \sin \alpha - a_R k \sin \alpha = a_T (nk) \sin \alpha' \quad (7.14)$$

Using this and the continuity in amplitude,

$$\frac{a_I - a_R}{a_I + a_R} = n \frac{\sin \alpha'}{\sin \alpha} \approx \frac{\alpha'}{\alpha} \quad (7.15)$$

Finally, these relations can be rearranged to give the **Fresnel equations**, ratios of the reflected and transmitted amplitudes to the incident amplitude.

$$r \equiv \frac{a_R}{a_I} \approx \frac{\alpha - \alpha'}{\alpha + \alpha'} \quad (\text{reflectivity coefficient}) \quad (7.16)$$

$$t \equiv \frac{a_T}{a_I} \approx \frac{2\alpha}{\alpha + \alpha'} \quad (\text{transmitivity coefficient}) \quad (7.17)$$

Here, the polarization of the incident wave has been ignored. The angle in the medium  $\alpha'$  is related to the angle of incidence (grazing angle) by Snell's Law:  $\cos \alpha = n \cos \alpha'$ . The reflectivity and transmitivity thus depend only on the incidence angle and the refractive index, given by equation 7.5, and reflectivity is highest when  $\delta$  is large. From the discussion concerning Equation 7.11 it is clear that reflectivity is higher for heavier elements. It should

be emphasized that the presence of  $\beta$  in the definition of  $n$  means that a small degree of absorption occurs; for this reason reflection below the critical angle is usually not total, and some reflection can take place even above  $\alpha_c$ .

The intensity of the reflected and transmitted waves are given by  $R = r^2$  and  $T = t^2$ . The reflectance is plotted for X-rays incident on two materials in Figure 7.2.

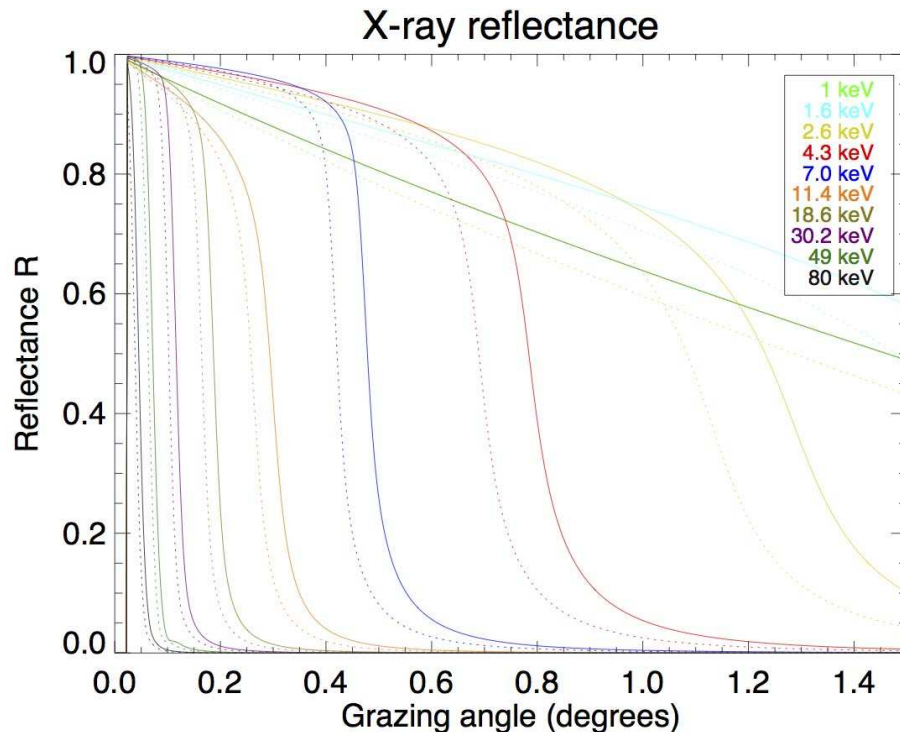


Figure 7.2: Reflectance of X-rays from 1 to 80 keV vs grazing incidence angle for a 0.25 mm thick layer of nickel (solid lines) or iridium (dashed lines), computed using the IMD package for IDL (Windt 1998). The interface was modeled as a step function with no roughness.

### Surface roughness

So far a perfectly smooth surface has been assumed. However, in working with X-ray imaging systems, Ehrenberg (1949) noticed stray flux outside the focus. It was guessed that this was due to unwanted scattering because of surface roughness; this hypothesis was confirmed by producing a mirror with sinusoidally shaped gold strips on the surface and measuring the stray flux. Therefore, an extremely well-polished surface is necessary for X-ray imaging using reflection. For example, at a grazing angle of 2 degrees, surface roughness on the order of the X-ray wavelength will deflect 20% of the incoming photons away from the focus (Aschenbach 1985).

To analyze the effect of surface roughness, it is necessary to look at the theory of wave scattering on statistically rough surfaces. Detailed treatments are given in Aschenbach (1985) using either vector perturbation techniques or a Kirchhoff approximation. Both techniques can describe either a statistically or randomly uneven surface. The surface is usually described with a function  $z = f(x, y)$ , with  $z$  being the height above a level  $x - y$  plane. Often this function is assumed to be a Gaussian distribution of surface heights with width  $\sigma$ . In this case, the result for intensity  $I_s$  scattered away from the focus is:

$$I_s/I_0 = 1 - \exp [-(2k\sigma \sin \alpha)^2] \quad (7.18)$$

This last term is a Debye-Waller factor, originally derived to explain scattering due to thermal fluctuations, but which can also be used to describe stray flux due to statistical surface fluctuations (Del Río & Dejus 2004). For small  $\sigma$ ,

$$I_s/I_0 \approx (2k\sigma \sin \alpha)^2 \quad (7.19)$$

In principle, the surface roughness can be deduced by measuring the intensity scattered away from the focus, integrated over solid angle.

Figure 7.3 shows examples of calculated reflectivity taking into account the effect of surface roughness. At small graze angles there is little change with roughness, while for larger angles reflectivity is decreased by 50% or more. The effect of roughness on a real telescope system will be discussed further in section 7.4.4.

### Thin slabs and multilayers

In the first section, a wavefront was incident on a medium of infinite thickness. If the medium has a finite thickness  $\Delta$ , there are more scattering components to include. Figure 7.4 shows a wave entering a thin slab of refractive index  $n_2$  from a medium with refractive index  $n_1$ . For simplicity, let's suppose the medium is the same on either side of the slab.

At the interface from  $n_1$  to  $n_2$ , the wave reflects with reflection coefficient  $r_{12}$  and transmits with transmission coefficient  $t_{12}$ . The transmitted portion of the wave is then scattered at the lower interface with coefficients  $r_{21}$  and  $t_{21}$ . Since  $r$  is antisymmetric under exchange of angles  $\alpha$  and  $\alpha'$  (see equation 7.17),  $r_{12} = -r_{21} \equiv r$ .

A wave transmitted through the upper surface, reflected off the lower surface, and transmitted again through the upper surface will interfere with a wave that has simply reflected off the upper surface. Whether this interference is constructive or destructive depends on the phase difference between the two waves. To keep track of phase differences, a phase factor  $p = e^{ik_1\Delta \sin \alpha}$  will be included for each traverse of the thin slab. Adding up the various reflections and transmissions for waves that emerge back into the first medium gives an infinite series:

$$r_{slab} = r + t_{12}(-r)t_{21}p^2 + t_{12}(-r)^3t_{21}p^4 + t_{12}(-r)^5t_{21}p^6 + \dots \quad (7.20)$$

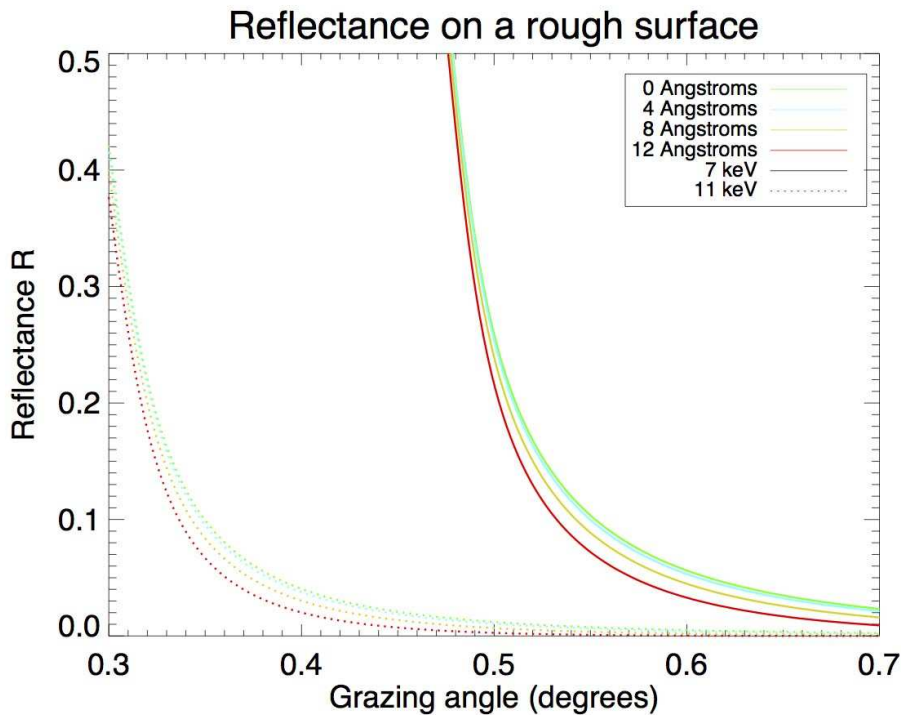


Figure 7.3: X-ray reflectivity for a thin nickel layer with surface roughness included, for 7 keV photons (solid line) and 11 keV photons (dashed line). Surface roughnesses range from 0 to 12 Å RMS. Calculations were done using the IMB software (Windt 1998).

This is a geometric series that can be evaluated to be (Als-Nielsen & McMorrow 2011):

$$r_{slab} = r - t_{12}t_{21} r p^2 \frac{1}{1 - r^2 p^2} \quad (7.21)$$

It can be further shown that  $t_{12}t_{21} = 1 - r^2$ , allowing the expression to be simplified:

$$r_{slab} = \frac{r(1 - p^2)}{1 - r^2 p^2} \quad (7.22)$$

A technique that builds on this principle is to alternate layers of high and low  $Z$  materials, known as **multilayers**, to enhance reflectivity. The pairs of layers are called bilayers. The difference in refractive indices between the layers produces reflection at each interface. Though each reflection is weak, waves reflected off hundreds of multilayers can add constructively to produce appreciable reflectivity even above the critical angle. This is especially important for higher energies, where the critical angle is exceedingly small.

A thorough description of multilayer refraction is given in chapter 3 of Als-Nielsen & McMorrow (2011). The condition for constructive interference of reflected waves is essentially

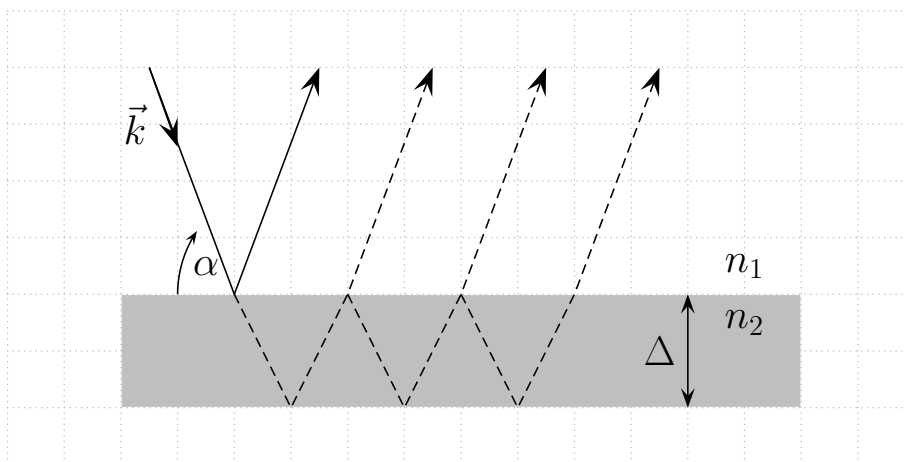


Figure 7.4: Diagram showing paths for a wave entering a thin slab. In addition to a simple reflection (solid line), the wave could reflect once or more within the slab (dashed lines).

the Bragg diffraction condition:

$$2\Delta \sin \theta = m\lambda \quad (7.23)$$

where  $m$  is the diffraction order and  $\Delta$  is the layer thickness. By varying the thickness of the multilayers throughout the stack (“depth-graded” multilayers), reflectivity can be improved over a wider spectral range.

### 7.1.2 Focusing optics geometries

Traditional refractive lenses as used for visible light are not feasible for the X-ray range, because the index of refraction is close to unity. The focal length for such a system would be unfeasibly long. However, it is possible to focus X-rays using a chain of lenses, for example, silicon compound refractive lenses (CRL) (Aristov et al. 2000).

The other imaging option is X-ray reflection. From the discussion so far, it is apparent that angles of incidence (or “grazing angles”) must be extremely small. Aschenbach (1985) gives a thorough history of developments in X-ray reflecting geometries. The principle of X-ray reflection off a smooth surface was shown by Compton in 1922, but the first spherical geometries considered had strong aberrations.

Kirkpatrick & Baez (1948) developed a geometry making use of a double reflection. In this configuration a parallel X-ray beam reflects off a curved parabolic or spherical plate, creating a focused line (one-dimensional imaging). By adding a second reflection off a second plate oriented orthogonally to the first, the line is corrected to a focused point (Figure 7.5).

Wolter (1951a,b) put forth the idea to use double bounces off of parabolic and hyperbolic sections, reducing off-axis distortions. The mirrors could be complete figures of revolution and could be nested together for better collecting area. In a Wolter Type I system, rays first reflect at a grazing incidence angle off the inner side of a paraboloid and then reflect off the

inner side of a hyperboloid, both mirrors having a common focus. For a Type II system, the second reflection occurs on the outer side of the hyperboloid. Drawings of these geometries are shown in Figure 7.6.

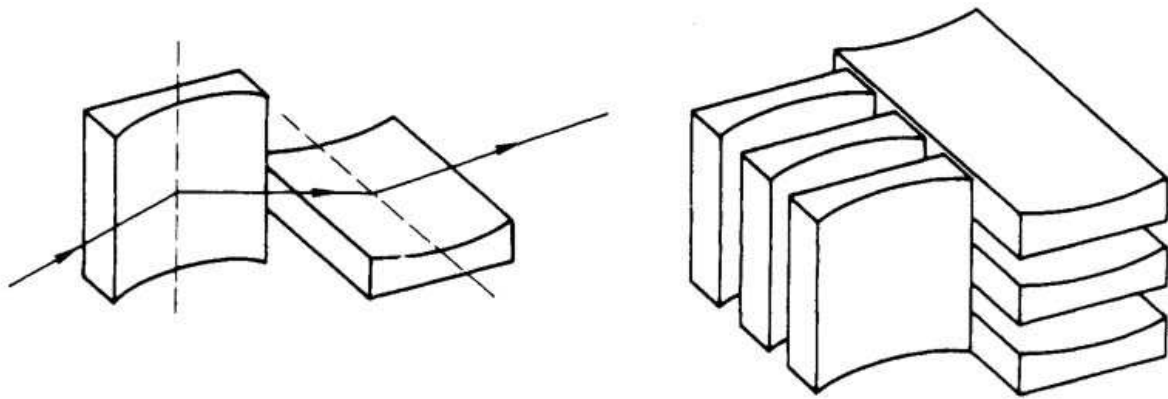


Figure 7.5: Schematic of a Kirkpatrick-Baez configuration; from Aschenbach (1985).

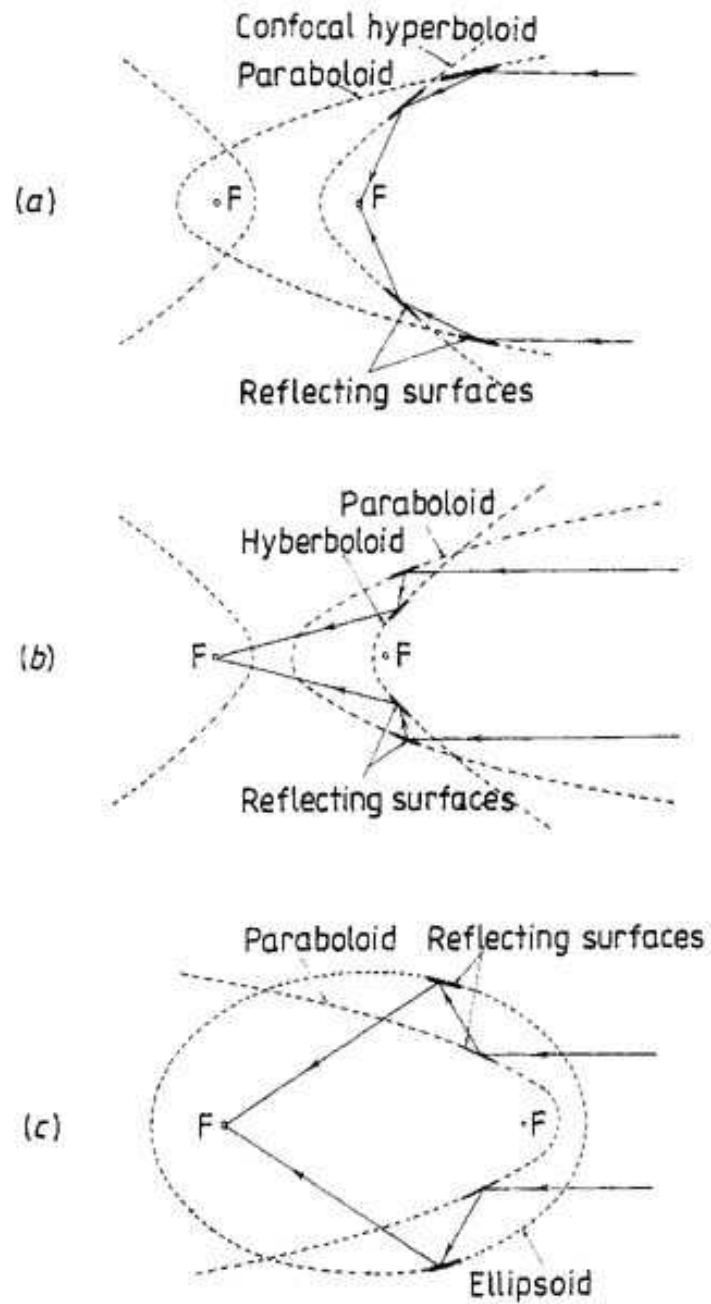


Figure 7.6: Wolter type I, II, and III geometries; from Aschenbach (1985).

## 7.2 Heritage of the *FOXSI* optics

Focusing optics offer clear advantages for HXR studies of astrophysical and solar sources. Since photons are focused onto a small area, a pixellated or strip detector can be used, greatly reducing background (which scales with detector area). A point spread function (PSF) with a narrow width can be achieved, increasing the dynamic range for the study of multiple sources of different intensities.

Giacconi & Rossi (1960) first recognized and suggested the value of Wolter optics for astronomical observation. Throughout the 1960s, X-ray telescopes were flown on sounding rockets to image the Sun; the first focused X-ray images of the Sun were taken in 1965 with Wolter optics on a sounding rocket (Giacconi et al. 1965), imaging in the 8–12 Å wavelength range (see Figure 1.1). In 1973, telescopes on Skylab measured the solar corona, and from 1978–1981 the HEAO-2/Einstein observatory looked at nonsolar astronomical objects, using four Wolter-Schwarzschild Type I nested mirrors. Since X-ray reflectivity is generally higher for heavier elements, the obvious configuration for astronomical observers (for which weight is usually a concern) is to produce lightweight optics with high-Z coatings.

The high sensitivity offered by grazing incidence HXR optics has revolutionized the field of soft X-ray (SXR) astronomy. Chandra, a NASA astrophysics X-ray observatory launched in 1999, uses a nested set of four iridium-coated glass mirrors with response up to 10 keV (Schwartz et al. 2000). XMM-Newton, an ESA astrophysics mission launched in 1999, contains three modules of 68 gold-coated nickel shells each, observing up to 12 keV (Aschenbach et al. 2000). Until now, use of grazing-incidence optics in the HXR range has been lacking. The critical angle for total external reflection goes approximately with wavelength, so smaller angles are necessary to focus higher energy X-rays, requiring precise figuring and a surface roughness of a few Angstroms RMS. This poses the problem of a limited effective area since only photons incident in a small annulus on each mirror can be focused. To compensate for this, mirrors can be made very thin (< 0.5 mm thick) and densely nested.

Recent advances in mirror fabrication techniques now allow for the production of focusing optics in the HXR range. The High Energy Replicated Optics (*HERO*) project is an astrophysics balloon program at NASA’s Marshall Space Flight Center (MSFC) for the purpose of testing HXR focusing optics fabrication methods and demonstrating their use with new science results. This project is a precursor to *FOXSI* and will be described in detail in the next section. The *Nuclear Spectroscopic Telescope Array (NuSTAR)* (Harrison et al. 2010) is a NASA small explorer launched in June of 2012. *NuSTAR* features slumped-glass optics in a conical approximation to a Wolter I geometry, with multilayer coatings to achieve an energy range of 6–80 keV.

### 7.2.1 The *HERO* balloon program

The *HERO* balloon payload features grazing incidence HXR optics, gas scintillation proportional counters, a gondola, and pointing system all designed and fabricated at MSFC.

The fabrication of the *HERO* optics is detailed in Gubarev et al. (2005, 2006); Ramsey et al. (2002, 2004); Ramsey (2005) and is summarized here. Most of these fabrication techniques were later used for *FOXSI*'s optics.

The *HERO* mirrors were produced at MSFC using an electroformed nickel replication (ENR) technique. To start, an aluminum mandrel with electroless nickel plating is machined to the correct figure. *HERO* used a conical approximation to Wolter I optics to reduce costs, since machining this form requires only two straight cuts instead of the detailed work necessary to produce parabolic and hyperbolic segments. The mandrel is then superpolished to the required smoothness ( $<10$  angstroms RMS).

Next, a nickel-cobalt alloy is electrodeposited onto the mandrel in a plating bath to form a thin shell (0.25 mm thick). A cold bath is then used to release the shell by differential thermal contraction. The daughter shell retains the figure and smoothness of the mandrel and does not require individual polishing, significantly reducing the cost and time needed to fabricate multiple mirrors. Several shells are produced from different diameter mandrels and the interiors of the shells are coated with a 50 nm thick layer of iridium via a sputtering process to increase reflectivity at higher energies.

Since the effective area of a single mirror is small, several mirrors from different mandrels are nested together into a single module with a common focus. A method is needed to co-align the shells when nesting so that resolution is not degraded. To accomplish this, the module is held by two spider support structures on either side and encased in a stainless steel tube. The steel of the spiders and the tube has a thermal expansion coefficient matched to that of the mirror alloy. Early testing indicated that the spider fixtures were stressing and deforming the mirrors, so the following technique was developed: First, an individual shell is held vertically and the spider is attached from the bottom so that the shell enters grooves in the spider. Without allowing contact between the shell and the spider, an RTV compound or glue is injected to fill the grooves. Each shell is consecutively added in this fashion. Once all the shells are in place, a spider fixture is placed on the rear side of the module and its grooves filled with RTV. Further details of the nesting/alignment process can be found in Gubarev et al. (2005, 2006).

The ENR technique was first developed in Italy and first used for astrophysical purposes on XMM-Newton. An alternative is the use of slumped glass, in which glass is heated and shaped over a smooth mandrel; slumped glass can achieve an extremely smooth figure and is lightweight. However, slumped glass optics cannot be produced monolithically. ENR mirror shells are monolithic and thus do not suffer degradations to the angular resolution caused by misalignments when attaching multiple sections. However, the high density of nickel requires that ENR mirrors be made thin, while still strong enough to avoid distortions. Since much of the cost of the process is in fabricating the mandrel, costs can be reduced by utilizing a large mirror length-to-diameter ratio, as the same collecting area can be achieved with a smaller number of diameters.

*HERO* performed its first flight in 2001 in a compact arrangement for testing purposes (Ramsey et al. 2002). For this flight, ENR optics with a 3 meter focal length focused X-rays on gas scintillation proportional counters. The measured half power diameter (HPD) of these

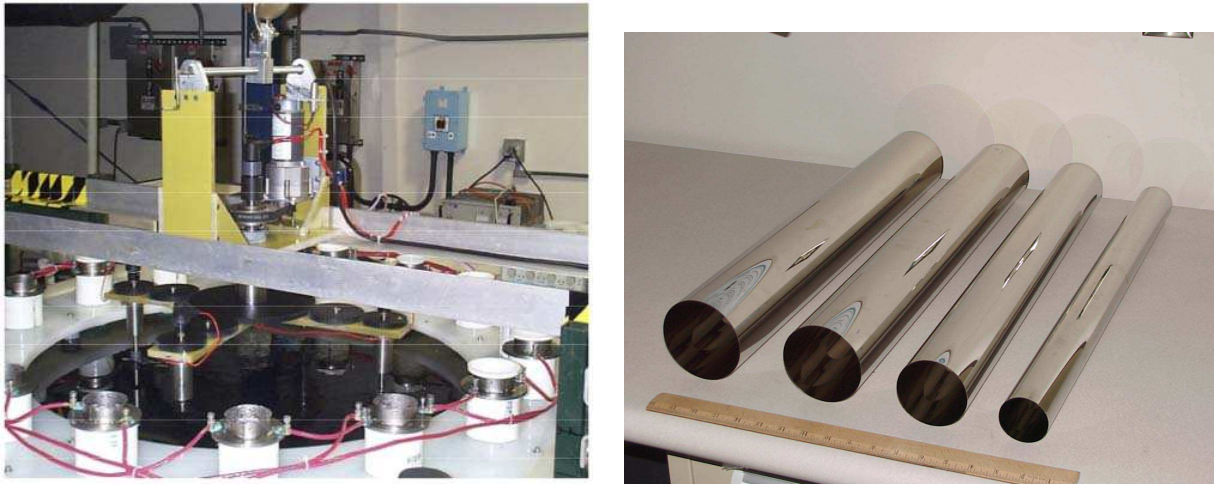


Figure 7.7: (Left) An electroforming bath at MSFC for plating ENR optics. (Right) Several *HERO* shells of various diameters. Both images are from Ramsey et al. (2004).

optics was 45" and the balloon produced the first focused HXR images of galactic sources. *HERO* has since been updated, with 8 optics modules of 12 shells each and an extendable optical bench added to accommodate a longer (6 meter) focal length. The measured HPD is 13–15 arcseconds for the individual shells and 20–25 arcseconds for a completed module.

In fabricating, aligning, and testing the *HERO* optics, MSFC has made several advances in ENR fabrication; a few of these are summarized here: (1) Mirror alloy: a high-strength nickel-cobalt alloy was developed (Engelhaupt et al. 2000). With this, alloy shells can be made quite thin (250  $\mu\text{m}$  for *HERO*, and possibly as low as 100  $\mu\text{m}$ ). (2) Mandrel surface preparation: a degree of adhesion is needed in order to grow the shells on the mandrel but not so much that the shell cannot be released from the mandrel without overstressing the mirror; also, it is necessary that the plating process does not overly degrade the mandrel. For this purpose, MSFC uses an electrolytic process with a strongly alkaline solution. For one mandrel, 18 replications were achieved without degrading the mandrel's smoothness (Ramsey et al. 2004). (3) Stress control: plating bath stresses should be minimized, but some tensile stress is necessary to allow adhesion of the nickel on the mandrel. To accommodate this, the bath chemistry was fine-tuned and the electrode placement in the bath was optimized to produce a uniform current density along the length of the mandrel. Furthermore, it was found that thermal conditioning of the mandrel after fabrication can prevent stresses caused by axial variations in the thermal expansion coefficient. Without this, mm- to cm-scale variations are found in the axial figure of the shells.

With all of these factors optimized, a test mirror was produced with a measured HPD of 11.5 arcseconds at 40 keV. Part of this error was due to the use of a conical approximation instead of true Wolter I optics. Removing this factor, it is expected that an HPD of 8.5 could be achieved for a true Wolter I shape (Ramsey 2005). For future *HERO* missions, multilayer

coatings could be added to obtain increased effective area at higher energies.

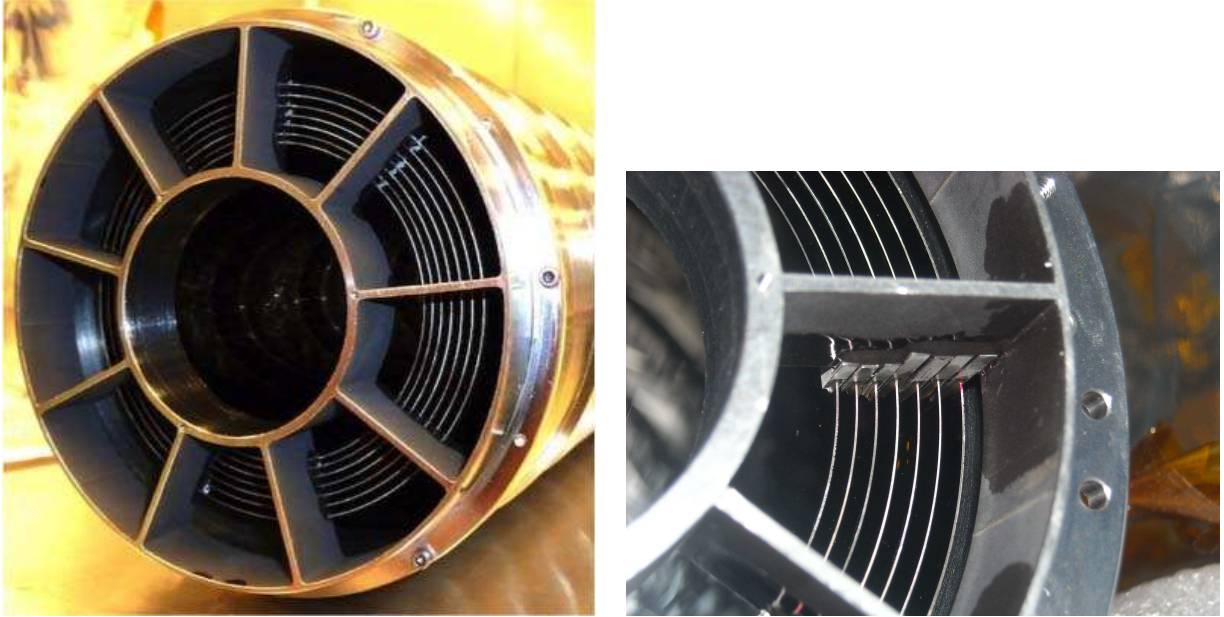


Figure 7.8: (Left) A *FOXSI* module seen edge on. The seven nested shells are visible along with the spider support structure and module casing. (Right) A closeup photograph of the clips adhering the mirror shells to the spider.

### 7.3 Description of the *FOXSI* optics

The *FOXSI* optics (Krucker et al. 2011b) were fabricated in a similar fashion to the *HERO* optics just described. However, for *FOXSI* a true Wolter I figure is used instead of a conic approximation, so that each monolithic mirror contains parabolic and hyperbolic segments. Each segment is 30 cm long, for a total shell length of 60 cm. The shells are 0.25 mm thick and have a 30 nm coating of iridium to improve reflectivity at higher energies. Shell radii range from 3.8 to 5.2 cm. The choice of shell diameters was made in order to maximize the effective area from 5–10 keV within the project budget. Smaller-diameter shells would improve the higher-energy response ( $>11$  keV) due to better reflectivity but would have lower area below 11 keV due to decreased geometrical area of the shells. The focal length of these mirrors is 2 meters, the longest that can be accommodated in a sounding rocket payload, and mirror diameters are chosen so that the grazing angle will be sufficiently small as to focus X-rays up to 15 keV. Seven optics modules were produced altogether, each containing seven mirror shells. The theoretical effective area vs energy for the mirrors is shown in Figure 7.9.

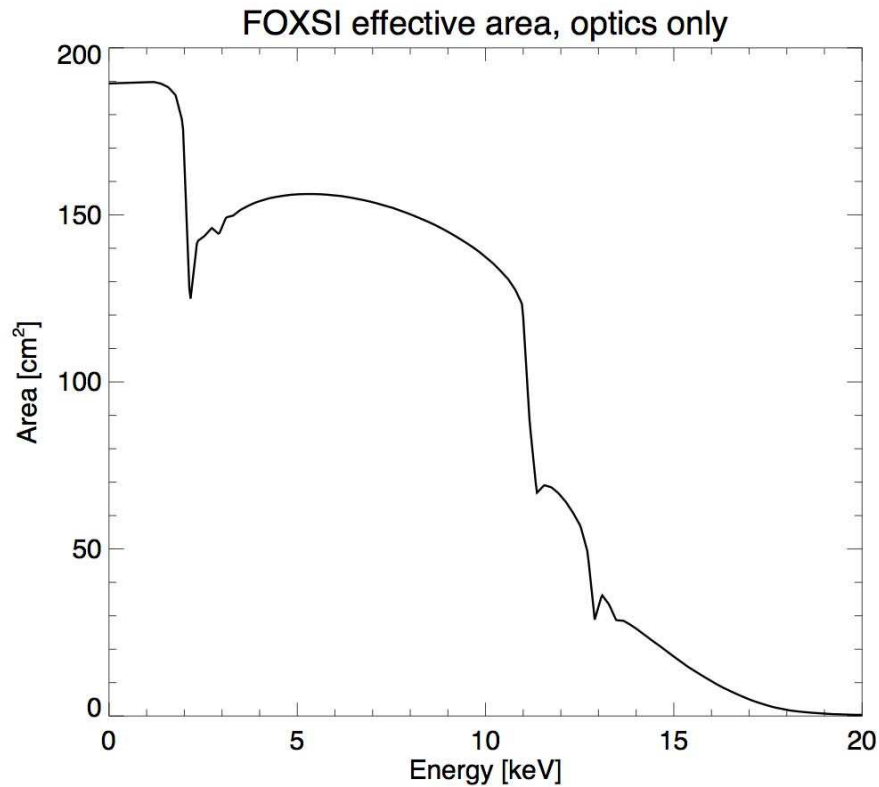


Figure 7.9: Theoretical effective area of the *FOXSI* optics, all shells and all modules combined.

For *FOXSI*, the methods of mandrel fabrication, figuring, polishing, plating, and shell release were the same as those for the *HERO* optics. Early tests indicated a spatial resolution (FWHM of the PSF) of  $\sim 7$  arcseconds for the individual shells. For previous projects, the resolution of a nested module had been degraded from that of a single mirror by the nesting/alignment process. In addition, it is necessary that the attachment of the shells to the support structures is robust enough to withstand vibration loads during the rocket launch. Mirror shell resonances during launch can greatly increase bond-joint loads. These considerations prompted efforts to design and attach the module casings and end pieces in the most careful and robust way.

As with the *HERO* mirrors, the *FOXSI* shells were integrated into the module one at a time and held vertically, fixed, during the process. To avoid stresses induced by the spider end supports, clips were added between the shells and the front spider. First the clips were epoxied to the mirror and then the spider was raised into place and epoxied to the clips. The clips straddled the spokes so that any transmitted stress would act azimuthally and not radially on the mirror. Proximity sensors monitored the circularity of each mirror as it

---

Angular resolution (FWHM)	$\sim 7$ arcsec
Number of modules	7
Number of shells per module	7
Focal length	2 m
Optics type	Wolter I
FWHM field of view	16.6 x 16.6 arcmin <sup>2</sup>

---

Table 7.1: Characteristics of the *FOXSI* optics, from Krucker et al. (2011b).

was epoxied into place, and the epoxy was UV cured in order to reduce any slipping during curing. After all the shells were set in place another spider was adhered on the rear side. The spider was held so that the shells were in its grooves and an RTV compound was injected to fill the grooves. By using this nesting/alignment technique, the complete modules retained the angular resolution of their individual mirrors (Krucker et al. 2011b).

## 7.4 *FOXSI* optics testing and results

### 7.4.1 Calibration setup

The *FOXSI* optics were calibrated at the Stray Light Facility at NASA/Marshall Space Flight Center (MSFC) in Huntsville, AL. The calibration was overseen by Dr. Brian Ramsey of MSFC, and participants were Dr. Mikhael Gubarev (MSFC), Dr. Steven Christe (Godard Space Flight Center), Dr. Säm Krucker (SSL / FHNW), Dr. Shin-nosuke Ishikawa (SSL) and myself.

The Stray Light Facility contains a 100-meter evacuated beam pipe. A single *FOXSI* optics module was placed in a bell chamber at one end. To properly align the optical axis with the evacuated beam pipe, a laser was first placed at the source end of the pipe. The laser illuminated the optic, which produced a focused spot. The optic was mounted on tip-tilt and pan-yaw stages with stepping motors in order to change its off-axis angle; these motors were first used to bring the optic into alignment with the beamline.

After this alignment was finished, a Trufocus X-ray source (model TFS-6051L) was placed at the source end of the beam pipe where the laser had been. Typically, operating parameters of 20 kV and 0.2 mA were used for the X-ray source, producing a continuous X-ray spectrum up to 20 keV with a peak at 4.511 keV due to the  $K\alpha$  line of the Ti target.

A single-pixel cadmium zinc telluride (CdZnTe) detector was placed at a focal distance of 2 meters beyond the optics, outside the evacuated chamber. The X-ray beam passed through a beryllium window and  $\sim 2$  mm of air between the optics and the detector. This single-pixel detector was mounted on a translation stage with stepping motors to move it

across the focal plane.

Each of the seven optics modules was tested individually.

### 7.4.2 Point spread function

The point spread function of a focusing telescope is the image intensity pattern that results from the measurement of a point source. In the most simple case this is a 2-dimensional Gaussian function. The width of the point spread function (PSF) is an important figure of merit as sources smaller than this value cannot be resolved and two sources spaced at this value are difficult to separate. The study of solar flares includes the study of at least three separate sources: two footpoints and a looptop source. For many flares, the footpoint separation is 10–100 arcseconds (Saint-Hilaire et al. 2008; Fletcher & Hudson 2002). Christe et al. (2011) found that the microflare height distribution has a typical height of 6.1–6.9 Mm (8.4–9.5 arcseconds), so a PSF smaller than these values is desirable for a spaceborne *FOXSI* in order to image flare substructure.

The PSF of the *FOXSI* Wolter-I optics has a core region that is approximately a two-dimensional Gaussian and wings (regions far from the core) that fall off roughly linearly with distance from the center of the focal plane. The flux in the wings is important because it contributes to a background for any other sources in the image, reducing the dynamic range of the instrument. To measure these two properties of the *FOXSI* PSF, two separate measurements were performed. First, the detector was stepped across the core region of the PSF on the focal plane in 20  $\mu\text{m}$  steps, using a 50  $\mu\text{m}$  diameter pinhole. Then a coarse scan across a larger field of view was performed (also with a 50  $\mu\text{m}$  pinhole) in 200  $\mu\text{m}$  steps to measure the flux in the wings compared with that in the center of the focal plane. This measurement was repeated for several off-axis angles, as the focusing performance is degraded as the object moves off-axis.

Figure 7.10 shows the core scans in two directions for all the modules, with the full width at half maximum (FWHM) of the PSF being 6.7 to 8.3 arcseconds. It should be noted that the true PSF is even narrower than that measured here, because the smallest pinhole available was 0.05 mm, or 5.2 arcseconds, in diameter. This diameter is large compared to the FWHM being measured and also encompasses a larger size than each of our steps (20  $\mu\text{m}$ , or 2.1 arcseconds); the effect is a smearing of the PSF. An analysis was performed by Dr. Kiranmayee Kilaru of MSFC to deconvolve the real PSF and the pinhole diameter; this result is shown in Figure 7.11, with the result that a measured FWHM of 6.7–8.3 arcseconds corresponds to an actual FWHM of 4.0–6.5 arcseconds. We therefore use the value of 7 arcseconds as an upper limit on the optics on-axis angular resolution; the true value is most likely smaller.

### 7.4.3 Half power diameter

The half-power diameter is the diameter on the focal plane within which half the flux from a point source is contained. For small values of the half-power diameter (HPD), flux

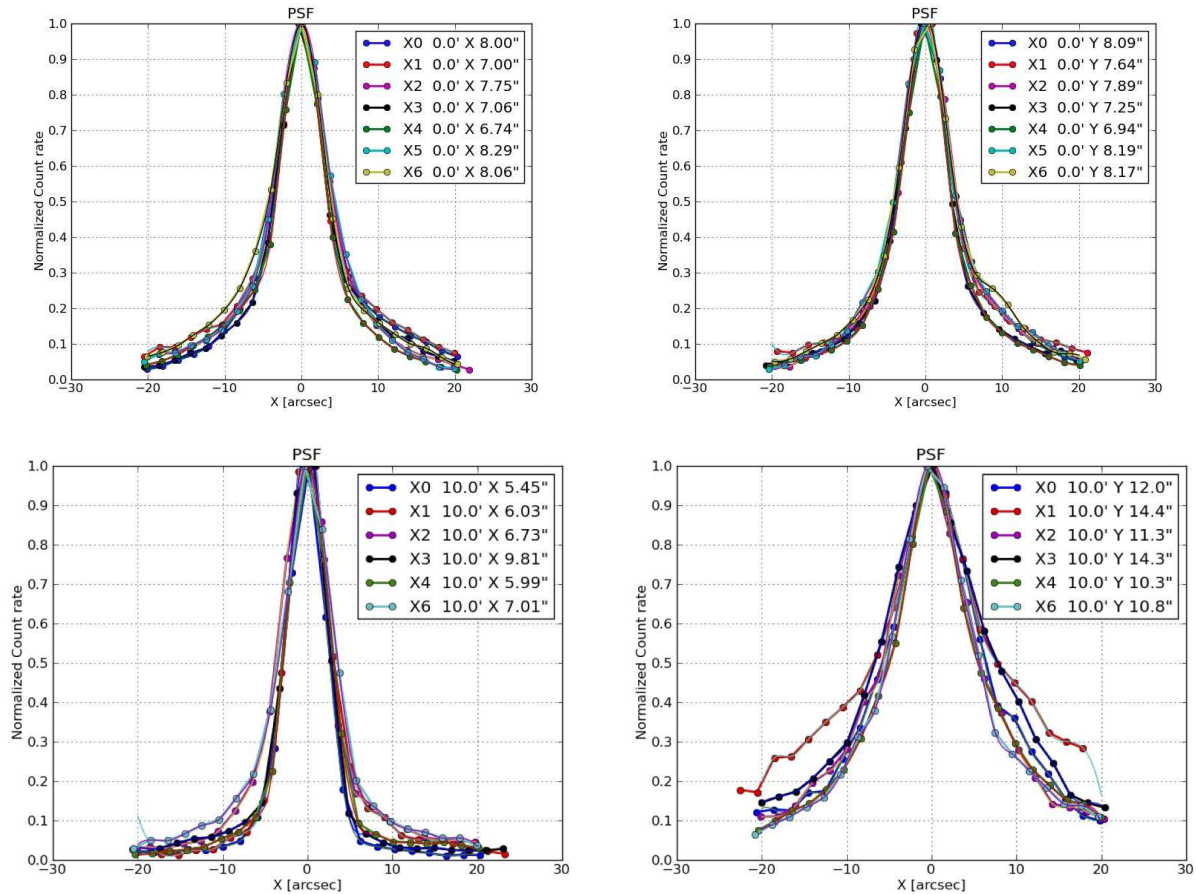


Figure 7.10: (Upper left) Point spread function for one slice of the focal plane (here, referred to as the horizontal PSF), measured on-axis. The FWHM ranges from 6.7 to 8.3 arcseconds. (Upper right) Point spread function for an on-axis vertical slice, showing FWHM values from 6.9 to 8.2 arcseconds. The on-axis PSF is rotationally symmetric. (Bottom row) PSF measured for horizontal and vertical slices at an off-axis angle of 10 arcmin. The PSF is “squeezed” becoming wider in one dimension and thinner in the other.

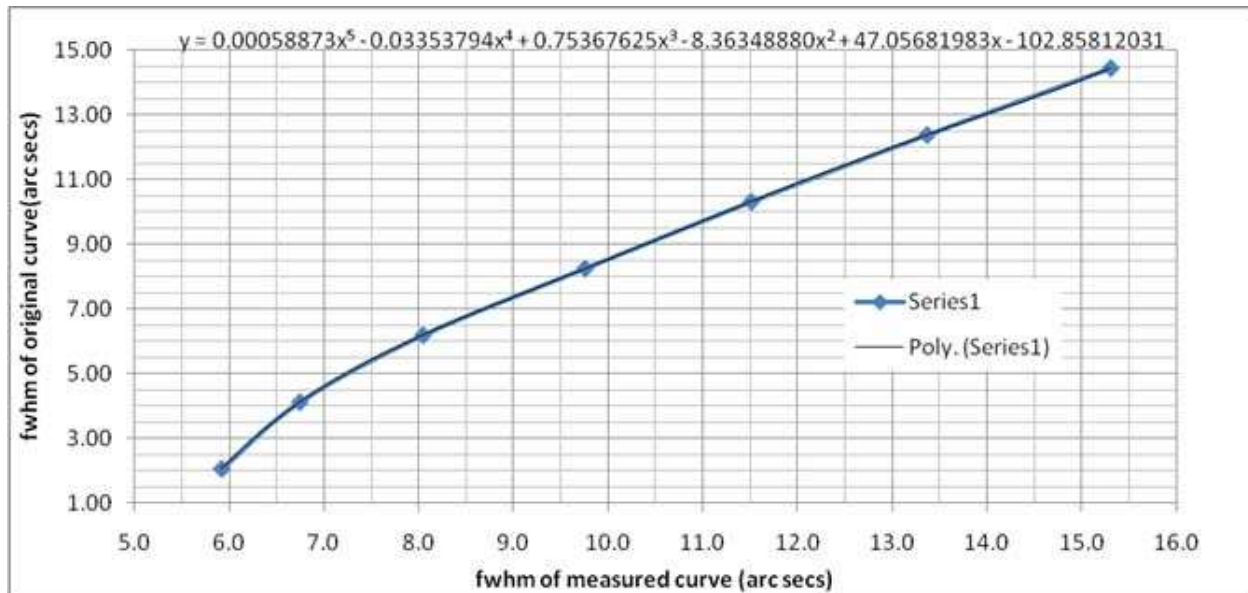


Figure 7.11: The relationship between the measured and actual PSF FWHM. The difference between the two is an effect of the large ( $50 \mu\text{m}$ ) pinhole used in the measurements.

is well concentrated within a small region of the focal plane, while for large HPD values, the flux is spread out across a large region. For pixellated or strip detectors, a small HPD produces better sensitivity because the background scales with number of pixels. The HPD of the *FOXSI* optics was determined by measuring the energy in the focused X-ray beam with various size pinholes placed in front of the detector. Pinhole sizes ranged from  $50 \mu\text{m}$  to  $3.00 \text{ mm}$  ( $5.2 \text{ arcsec}$  to  $5.2 \text{ arcmin}$ ). A plot of the encircled flux is shown in Figure 7.12, left panel, with HPD values ranging from  $25.4$  to  $30.1 \text{ arcseconds}$ . This measurement was repeated at several off-axis angles, as the HPD degrades as the source moves off-axis. (See Fig. 7.12, right panel.)

#### 7.4.4 Effective area

The effective area of each *FOXSI* module was measured using a large ( $3.0 \text{ mm}$ ) pinhole over the detector and measuring long exposures with and without the optic. If  $F_1$  photons are counted with the optic present over time  $t_1$  and  $F_2$  photons are counted without the optic over time  $t_2$ , using a pinhole of area  $A_{pin}$ , then the effective area  $A$  is given by:

$$A = A_{pin} \cdot \frac{F_1}{F_2} \cdot \frac{t_2}{t_1} \quad (7.24)$$

Because the X-ray generator at the Stray Light Facility was not located infinitely far away from the telescope under test, a correction to the effective area needed to be made

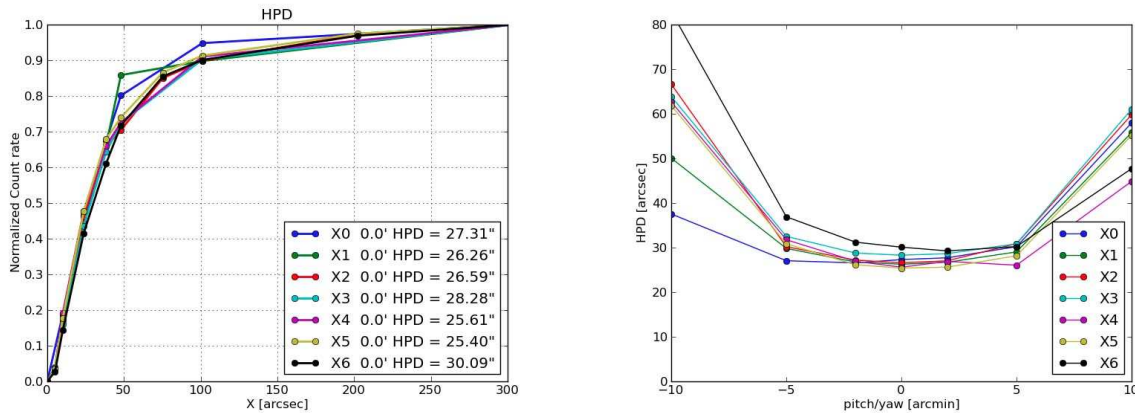


Figure 7.12: (Left) On-axis flux measured for all optics using pinholes of various diameter. The x-axis shows the size of the pinhole, while the y-axis shows the measured flux relative to the maximum measured flux (with the largest pinhole of 3.0 mm). A normalized count rate of 0.5 defines the half-power diameter; here it is 25.4–30.1 arcseconds. Right: half-power diameter for all seven optics modules at several off-axis angles. For most of the modules, the HPD is fairly consistent within 5 arcminutes of the central axis; the performance at  $\pm 10$  arcminutes is severely degraded.

for the finite source distance (104 m). The X-rays did not enter the system parallel to the axis of the optics, and so reflected off the parabolic mirrors at an angle greater than the intended grazing angle. This caused a portion of the incident rays to miss the hyperbolic sections completely, reducing the effective area. The effective area measured at the SLF was therefore less than the true effective area for a source infinitely far away.

To model the expected effective area, the X-ray Oriented Programs (XOP) software was used. XOP includes a database of cross sections and scattering factors used to model, among other things, the interaction of X-rays with reflecting elements (Del Río & Dejus 2004). XOP returns the reflectivity coefficient given the grazing angle, surface roughness, and element and density of the reflector. The reflectivity coefficient is then multiplied by the geometric area of the mirror (the area of the annulus through which an X-ray can enter and intersect the paraboloidal mirror, shown in Figure 7.13) to obtain an expected effective area for each mirror. These areas are added together to obtain a combined effective area of a single nested optics module. The expected effective areas for an infinite vs finite source distance are shown in Fig. 7.14, as well as those for various surface roughnesses of the mirrors. Surface roughness is included by incorporating the Debye-Waller factor mentioned in section 7.1.1.

From Figure 7.14 it can be seen that the measured area for an optics module does not match the predicted curve, for any value of the surface roughness. In fact, the measured value is *higher* than predicted for some energies ( $\sim 7$ – $11$  keV). Since this is physically unrealistic, it

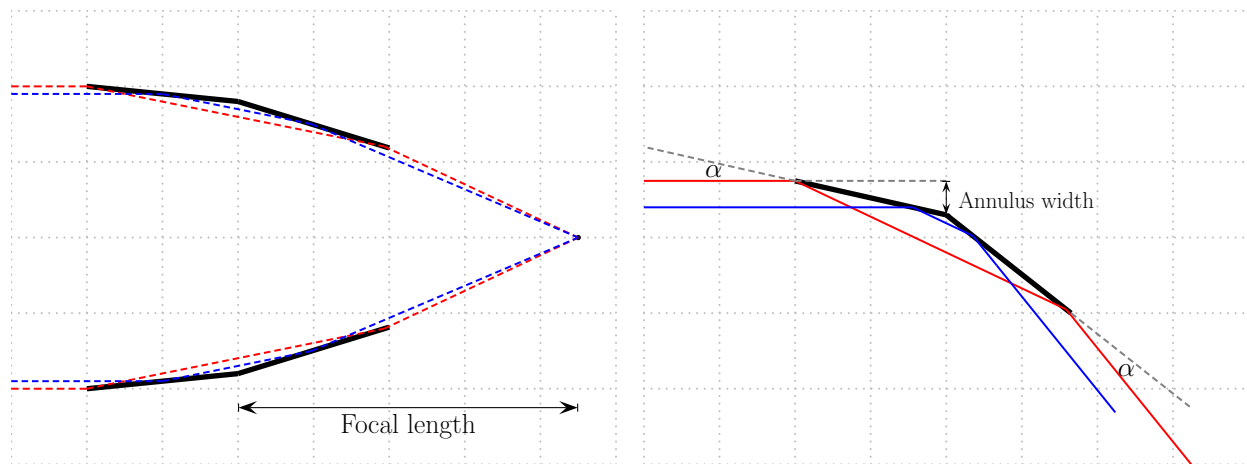


Figure 7.13: Ray diagram for a single Wolter-I mirror shell, with a closeup showing the annulus that is the collecting area for that mirror. In this drawing, the parabolic and hyperbolic shapes are approximated by straight lines.

is thought that the departure from the predicted curve is due to pulse pileup in the readout system of the CdZnTe detector used for this measurement. The optics focus the X-rays to a high intensity on the detector so that the count rates are extremely high ( $\sim 10,000$  per second) for the measurement with (but not without) the optic. At such high count rates, a photon may trigger the system before the previous signal has decayed in the measurement system, leading to an incorrect measurement of the photon energy. Pileup occurs most often around the 4.5 keV Ti line of the source spectrum, showing up as reduced area in Figure 7.14. Because of this issue, the post-flight *FOXSI* analysis will rely heavily on the theoretical values.

A simulation was performed to test the hypothesis that the discrepancy between expected and measured effective areas was due to pileup effects. First, the expected source spectrum after the optics response was calculated using data with no optic present (a “straight through” measurement) and the theoretical effective area curve of the optic. That expected source spectrum was adjusted using a Monte Carlo simulation of pileup effects. The effective area was then recalculated and compared to the measured values. The lower-right panel of Figure 7.14 shows this comparison in blue for the simulated results and red for the measured results, while the black curve shows the theoretical prediction. The closeness of the red and blue plots indicates that pileup is indeed the cause of the effective area discrepancy, though some individual features (excesses in the blue line) are not yet understood.

#### 7.4.5 X-ray alignment with *FOXSI* detectors

Once all experiment components were tested and assembled into the payload, a careful alignment of the optics and detectors needed to be done. (The operation and performance

Shell #	Radius [cm]	Grazing angle [arcmin]	Geometric area [cm <sup>2</sup> ]	Reduced geometric area [cm <sup>2</sup> ]
13	3.799	16.323	2.944	2.714
11	4.000	17.186	3.264	3.009
9	4.210	18.088	3.616	3.333
7	4.429	19.029	4.002	3.689
5	4.659	20.017	4.428	4.081
3	4.900	21.052	4.898	4.515
1	5.151	22.130	5.412	4.989

Table 7.2: Physical parameters of the seven nested mirrors in one *FOXSI* optics module. The geometric area shows the area of the annulus through which X-rays can intersect the paraboloidal mirror. The reduced geometric area shows the annulus area reduced due to the finite source distance of 104 meters at the SLF. The shell numbers reflect an arbitrary naming system.

Optic #	Offset (arcmin)
0	2.2
1	0.5
2	1.1
3	0.1
4	0.5
5	0.7
6	0.7

Table 7.3: Measured post-alignment offsets for the *FOXSI* optics

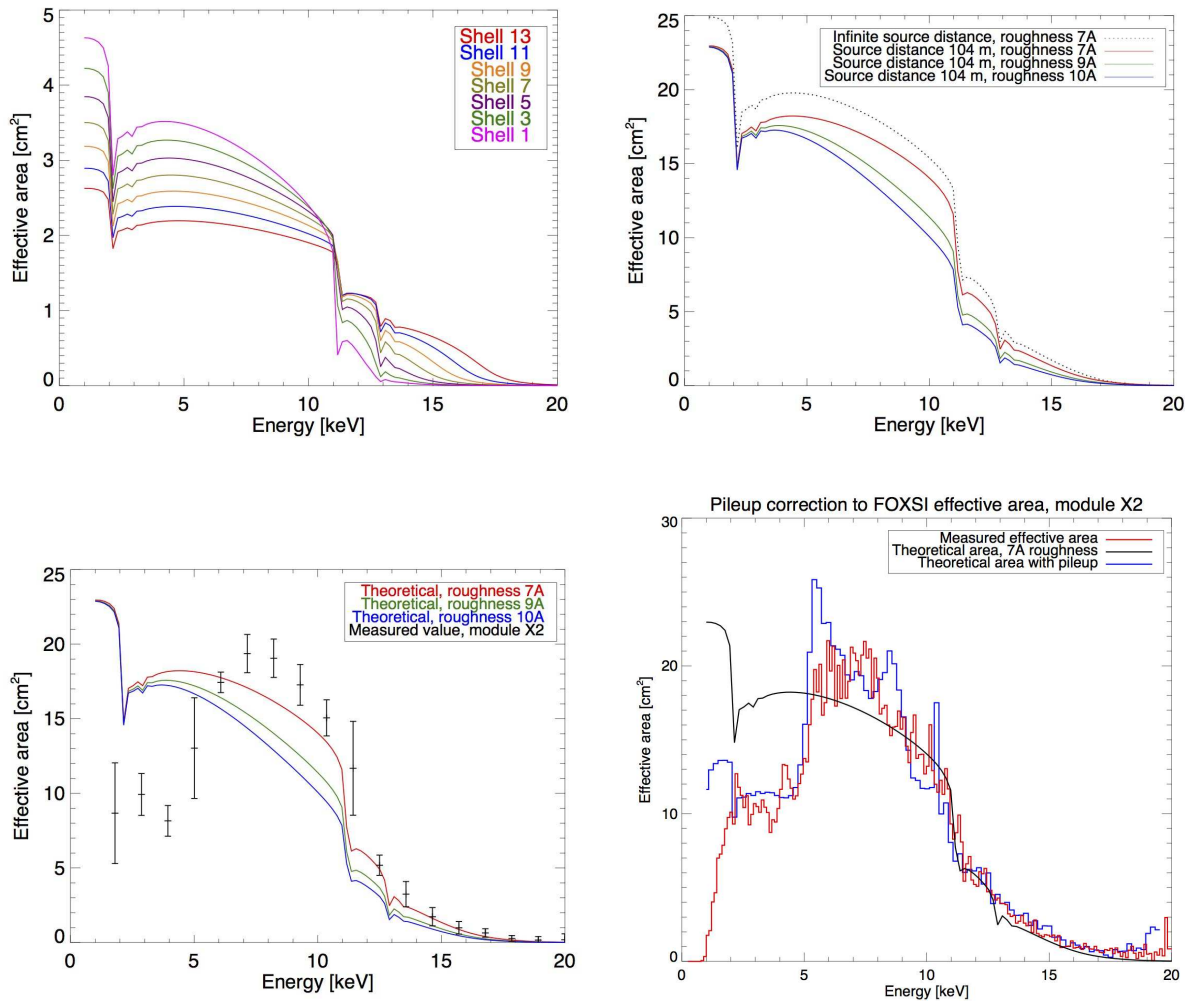


Figure 7.14: (Top left) Theoretical values for the effective area for each *FOXSI* shell, assuming an infinite source distance and a surface roughness of  $7 \text{ \AA}$ , calculated using the XOP software. These curves add together to yield the effective area of a single module. The shells are numbered with odd numbers from 1 (largest diameter) to 13 (smallest). Below  $\sim 11$  keV, the largest shells contribute most because of their larger collecting areas, but it is the smaller shells that dominate at higher energies because of their smaller grazing angles. (Top right) The effects of a finite source distance (104 m) and various surface roughnesses are compared. Areas are for a single *FOXSI* optics module (all shells combined). (Bottom left) The finite-source-distance effective areas at various surface roughnesses are compared with the measured area from a single *FOXSI* module. (Bottom right) A simulation (blue line) of pileup effects confirms that the discrepancy in the effective area measurement (red line) is due to pileup in the detector.

of the detectors will be the subject of the next chapter.) This alignment was carried out in the field at the White Sands Missile Range before integration of the experiment with the rest of the rocket payload. Following is a list of the important components of the alignment procedure:

- **Source holding plate** including 7 source positions and a reference laser position. Each plate position can hold either the X-ray source or a laser. Fine adjustments to plate angles can be made using alignment knobs on the plate stand. The source plate was located 20 meters in front of the payload.
- **Trufocus TFS-3007-HP X-ray generator** with a tungsten target. The source was most commonly operated at 30 kV and 1–4 mA. The source was shielded and all personnel were cleared from the room before operation due to safety concerns.
- **Two low-power collimated lasers.** One (a reference laser) was used to align the source plate and the payload. The other laser could be placed in each source position to illuminate each optic with visible light for an initial alignment.
- **Optics modules**, installed in payload. For use with visible light (laser) the optics had to be installed without thermal blanketing. After all laser tests were finished the optics were reinstalled with blanketing.
- **Detector and electronics assembly**, installed in payload. For optical (laser) tests the detector plane was removed and replaced with a paper target.
- **Pinhole in optics plate**, for alignment of the source plate and payload.
- **Quad photocell.** Laser light through the pinhole was measured on a 4-quadrant photosensor and used to align the source plate and the payload. When the laser beam shining through the pinhole was incident on the center of the photocell, all system components were aligned. One such cell was permanently installed within the detector package; another was located outside the package and could be placed at the focal distance without the detectors present.

Lasers were first used for the initial alignment of the optics with the detectors. The reference laser was positioned so that its beam passed through the pinhole on the optics plate and illuminated the center of the quad photocell on the focal plane. A sheet of paper with printed targets was placed at the focal plane (with no detector package present). Another laser was placed in the source position for the first optic. The laser beam illuminated the entire optic and the focused image pattern could be seen on the paper target.

At this point the alignment of the optic was adjusted by adding shims at the bolts holding the optic into the optics plate. This was a time-consuming procedure since the optic needed to be removed for each shimming attempt. By comparing the focal plane pattern to results of ray-tracing simulations, the angular misalignment of the optic and detector

could be measured; these results are shown in Table 7.3. The process was concluded once an alignment of the optic to the detector was achieved within 1–2 arcmin. This procedure was done for each optic individually.

After laser/shimming alignments were finished, the detector package was replaced onto the payload and X-ray tests were performed. The X-ray generator was placed in position to illuminate one optic and turned on. The detector image was recorded. The test was repeated for each optic.

X-ray images for all detectors are shown in Appendix C. Because the source distance (20 meters) was finite, the image on the detector is a ring instead of a focused point. (This ring was expected from ray-tracing simulations.) The optic is angularly and translationally aligned with the detector if the circle is centered in the middle of the detector and the circle is concentric and uniform. As can be seen from Appendix C and Table 7.3, perfect alignment was not achieved, though almost all optics are aligned to  $<1$  arcminute.

## 7.5 Conclusion

In conclusion, the ENR optics produced at MSFC were found to meet the energy range and dynamic range requirements of *FOXSI*. The on-axis angular resolution achieved by these optics ( $\sim 7$  arcseconds) is better than that dictated in the *FOXSI* proposal (12 arcseconds).

## Chapter 8

# Double-sided Silicon Strip Detectors for FOXSI

### Abstract

To measure energies and positions of quiet Sun nanoflares, *FOXSI's* detector system should have a good low-energy response ( $\lesssim 5$  keV), fine energy ( $< 1$  keV) and angular resolutions ( $\lesssim 10$  arcseconds), and a fast enough readout time to measure count rates of up to hundreds per second. These requirements are met by employing double-sided silicon strip detectors developed by the ISAS Astro-H team. These detectors and their readout systems are compact and low-power and can be precooled before the flight, eliminating the need for an onboard cooler. In this chapter, the physics of semiconductor radiation detector systems as well as common detector choices are briefly summarized. The *FOXSI* detectors and their readout system are described and the results of calibration with radioactive sources is presented.

### 8.1 Introduction to semiconductor radiation detectors

Semiconductor detectors are now the most popular choice for X-ray imagers both on the ground and in space. In comparison to the previous standard, gas proportional counters, semiconductor detectors are smaller due to their higher densities, have faster collection times, and can achieve superior energy resolution due to a greater number of charge carriers for each interaction. Silicon and germanium are commonly chosen materials, with cadmium telluride and cadmium-zinc-telluride becoming more popular as fabrication processes begin to achieve greater purity in these crystals. This chapter starts with a description of how a signal is generated in a semiconductor detector. Much of this description follows that in textbooks by Knoll (2000) and Spieler (2005).

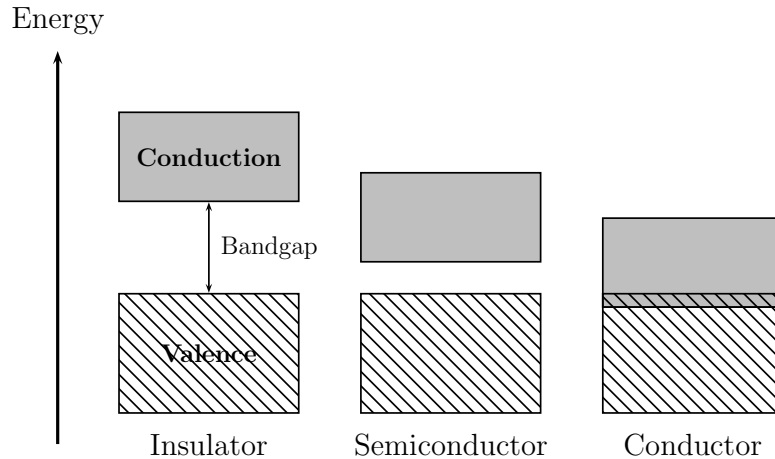


Figure 8.1: Energy bands for three types of solids (not to scale).

### 8.1.1 Signal formation in a semiconductor

A crystalline material is organized in a periodic lattice with a characteristic energy band structure. The valence band contains outer-shell electrons that are bound to specific sites in the lattice, often in the form of covalent bonds with neighboring atoms. Electrons in the conduction band, on the other hand, are not bound to a specific site and are able to migrate throughout the material, causing conductivity in the material. At absolute zero all valence sites would be occupied and the conduction band would be empty. The difference between these two energy bands, known as the energy bandgap, determines the electrical properties of the material; three types are demonstrated in Figure 8.1. The material is a conductor if the valence band overlaps the conduction band (no bandgap). In this case electrons can move easily between free and bound states, and are thus essentially free to migrate. On the opposite extreme, an insulator has a large bandgap (typically  $> 5$  eV), so that a large amount of additional energy needs to be added to the system to free an electron from its valence site. A semiconductor has a smaller, but nonzero, bandgap (typically a few eV). Electrons in a semiconductor can gain enough energy to reach the conduction band if energy is added to the system on the order of a few eV (per electron), whether by thermal fluctuations or by the effect of ionizing radiation. As will be shown in this chapter, this quality makes semiconductors excellent radiation detectors. Bandgap values for some common semiconductors are given in Table 8.1.

When an electron is energized into the conduction band, it leaves behind its place in a covalent bond, creating a vacancy, or hole. The vacancy provides an opportunity for another electron to fill this spot. Since there is now a hole where that electron originated,

	Si	Ge	CdTe	CdZnTe
Atomic number	14	32	48/52	48/30/52
Bandgap energy [eV]	1.12	0.67	1.52	1.53–1.64
Ionization energy [eV]	3.62	2.96	4.43	5.0
Electron mobility [ $\text{cm}^2 \text{V}^{-1} \text{s}^{-1}$ ]	1350	36,000	800–1100	1350
Hole mobility [ $\text{cm}^2 \text{V}^{-1} \text{s}^{-1}$ ]	480	42,000	60–90	120
Fano factor	$\sim 0.1$	$\sim 0.1$	$\sim 0.1$	$\sim 0.1$

Table 8.1: Physical parameters for selected semiconductor materials. Values are taken from Sellin et al. (2005) and chapters 11 and 13 of Knoll (2000). Values for Si, CdTe, and CdZnTe are at a temperature of 300 K; values for Ge are at 75 K, the usual operating temperature for Ge detectors.

the hole has effectively moved position. In this way holes can act as charge carriers with the opposite charge from an electron. The movement of holes is slightly different than that of electrons because hole motion depends on two events: the initial electron energization and the subsequent de-excitation. The effect of added energy (or thermal fluctuations) is therefore to create electron-hole pairs; these are the charge carriers in the semiconductor device.

One way electron-hole pairs can be mobilized is by ionizing radiation interactions. When a beam of photons (or charged particles) is incident on the detector, it may interact with atoms and transfer energy to valence-band electrons, energizing them into the conduction band. Much of the following discussion will assume that the relevant interaction is photoabsorption, appropriate for the  $< 20$  keV energy range of *FOXSI*. (See Figure 8.2 for relevant cross sections.) In this case each photon interacts only once, depositing its full energy in the semiconductor and producing one photoelectron. If this energized electron has an energy greater than the ionization energy, will then ionize other atoms to produce more charge carriers, and the total number of electron-hole pairs produced is proportional to the initial photon energy. At higher X-ray and gamma-ray energies, Compton scattering also has an appreciable cross-section, so that the photon may leave tracks of interactions in the detector, or scatter out of it completely. If the incident radiation is in the form of charged particles, they will also Coulomb scatter in the detector, depositing all or some of their energies. In these two cases the number of charge carriers generated is proportional to the deposited energy, which is generally smaller than the incident energy of the gamma ray or charged particle.

The charge  $Q$  generated in a detector by photoabsorption of a photon with energy  $E$  is (Spieler 2005):

$$Q = \frac{E}{E_i} e \quad (8.1)$$

Here,  $e$  is the electronic charge and  $E_i$  is the ionization energy: the energy needed to create

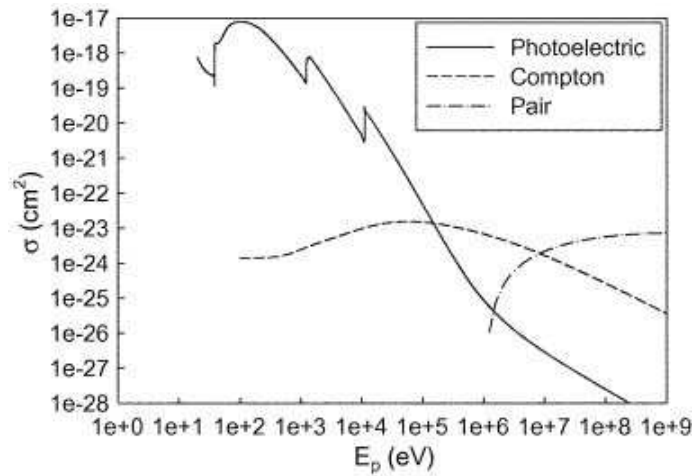


Figure 8.2: Cross sections of photon interactions in germanium. Up to  $\sim 100$  keV, photoabsorption is the most likely interaction. Results are similar for interactions in silicon. Figure from Gao et al. (2007).

one electron-hole pair.  $E_i$  is significantly larger than the bandgap energy  $E_b$ , because some energy is lost to thermal excitation of the semiconductor lattice (Spieler 2005):

$$E_i \approx 2.8 E_b + 0.6 \text{ eV} \quad (8.2)$$

For most input energy ranges, the ionization energy is independent of photon energy, although there is some dependence below  $\sim 1$  keV, where the ionization slightly increases with decreasing photon energy (Knoll 2000). This is one effect (among many others) that may lead to a nonlinear gain of the detector and is a reason why calibration must be performed across the entire energy range of the detector.

If an electric field is applied across the detector, the charge carriers will move preferentially along the field lines. Electrons, having negative charge, move against the field direction. Holes also migrate, but with a perceived motion in the opposite direction from the electrons; the holes can be thought of as particles with positive charges. Electron and hole migration form currents in the same direction across the detector. For low-to-moderate electric field values, the drift velocities  $v_e$  and  $v_h$  of the charge carriers is proportional to the applied field, defining the electron and hole mobilities  $\mu_e$  and  $\mu_h$ :

$$v_h = \mu_h E \quad (8.3)$$

$$v_e = \mu_e E \quad (8.4)$$

Subscripts  $e$  and  $h$  refer to the electron and hole quantities, respectively, and  $E$  is the electric field strength. For stronger electric fields, the drift velocity reaches a saturation value. Many detectors operate in the regime of a saturated velocity to take advantage of fast collection

times. The total time for charge carriers to drift to collecting electrodes at the edges of the detector is often  $< 10$  ns, making semiconductor detectors one of the fastest-responding radiation detection devices.

By collecting the charge carriers (more accurately, by measuring their induced currents) at electrodes placed at the edges of the detector, the deposited energy can be measured and the incident photon energy reconstructed. A current flows in the detector during the entire charge collection time. Integrating the current at the electrode over this time yields a measure of the charge generated by energy deposition. The initial photon energy (in the case of photoabsorption) is given by Equation 8.1.1. Since each interaction liberates the same number of electrons and holes, measurement of either number is sufficient to calculate the initial photon energy. The time profile of integrated charge at the collection point depends on the location of charge pair generation and the mobilities of the carriers, but after sufficient time the full charge generated by photon interactions is collected (assuming full depletion of the detector and neglecting the presence of charge traps).

### 8.1.2 The effect of impurities

An “intrinsic” semiconductor is one with no, or very few, impurities. In this case the number of electrons in the conduction band is always equal to the number of holes present. Extra charge carriers can be introduced into the material by adding intentional impurities known as dopants. Dopants can be added by means of vapor diffusion, deposition, or ion implantation (e.g. Knoll 2000).

#### N-type doping

As an example, in the case of silicon, each atom in the crystal has four covalent bonds. If a small concentration of atoms of an element with one extra valence electron (such as phosphorus) is added into the silicon crystal, each of these atoms will have one weakly bound electron after the four covalent bonds are formed. These are called donor impurities because each atom donates an electron that can be very easily energized into the conduction band. The energy states for these electrons lie within the bandgap (a forbidden region in the intrinsic material), very close to the conduction band. (It is important to note that the bandgap value as it relates to the ionization energy is unchanged from that of the intrinsic material, because the number density of dopants is tiny compared to the number density of the main semiconductor element.) This n-type material has extra mobile charge carriers (and, therefore, a higher conductivity) than the intrinsic material. Charge is primarily carried by electrons, which are referred to as majority carriers; minority carriers are the holes.

## P-type doping

If impurities are added of an element having one fewer valence electron than silicon (for example, boron), then one covalent bond is left vacant. An electron from the conduction band can be captured in this extra vacancy, but it is slightly less bound than a typical valence electron. With impurities in a p-type material, energy states are added within the bandgap very close to the valence band. The extra covalent bond acts as a vacancy, or hole, that can accept an electron, and so these impurities are called acceptors. Here, the holes are the majority charge carrier; electrons, the minority. A material that is heavily doped is labeled either n+ or p+ and has a higher conductivity.

### 8.1.3 Semiconductor junctions

Detector geometries often rely heavily on p-n junctions, adjacent volumes of p- and n-doped materials. Figure 8.3 shows the behavior of the charge distribution, electric field, and potential in the vicinity of such a junction. The n-doped region has a high concentration of mobile electrons in the conduction band, while the p-doped region has a high concentration of holes. Diffusion causes some electrons from the n-side to drift across the junction, and vice versa for the holes (which drift from the p-side to the n-side). These drifts cause thin regions on either side of the junction to become uniformly charged: positively charged on the n-side due to drifted holes, and negatively charged on the p-side due to drifted electrons. This charge distribution forms an electric field opposing further diffusion. Diffused electrons and holes recombine, producing a region spanning the junction that is depleted of charge carriers. This depletion region is present even without an external electric field, and the potential drop across the depletion region due to the diffused charge distribution is known as the built-in potential. This potential forms a barrier, making it difficult for charge carriers to cross the junction.

If a bias voltage is applied across the detector, the depletion region width and potential drop are changed. If a positive bias voltage is applied to the p-side surface with respect to the n-side surface, then holes (the majority carriers in the p-doped region) will be repelled from the anode and pushed toward the depletion region, thinning it. The same effect occurs on the n-side as electrons are repelled from the cathode. The result is a thinner depletion region and a lower barrier for charge carrier motion (i.e. current) across the junction. This is known as a forward-biased P-N junction. Alternatively, if a positive bias voltage is applied to the n-side surface with respect to the p-side, then electrons and holes in the n- and p-sides, respectively, are attracted to the outer surfaces of the detector. This causes the depletion region to widen and its potential drop to increase, raising the potential barrier to current flow across the junction. This bias is known as a reverse bias.

For uniform donor and acceptor dopant concentrations ( $N_D$  and  $N_A$ ) on either side of

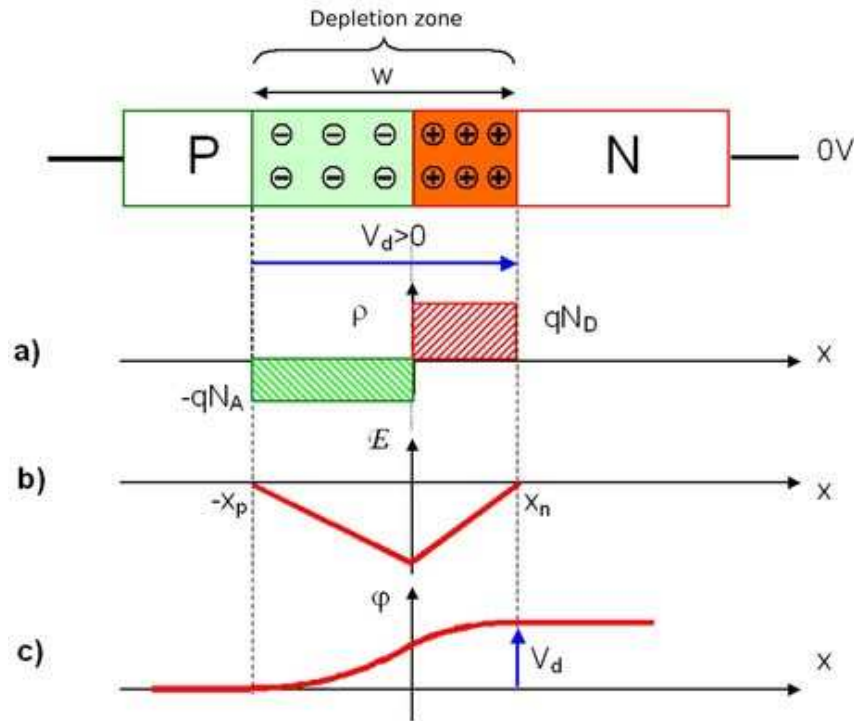


Figure 8.3: Sketch demonstrating the electrical properties surrounding a p-n junction. Even in the absence of an applied bias voltage there is a built-in potential and depletion region. Applying a reverse bias voltage (positive potential to the n-side) will increase the width of the depletion region. Image from Servagent (2007).

the junction (as in panel (a) of Figure 8.3), the potential (panel (c)) is

$$\frac{d^2\phi}{dx^2} = \frac{\rho(x)}{\epsilon} = \begin{cases} -e N_D/\epsilon & \text{donor region} \\ e N_A/\epsilon & \text{acceptor region} \end{cases} \quad (8.5)$$

By integrating this equation twice and taking into account appropriate boundary conditions, the relationship between the depletion width  $d$  and the potential drop  $V$  across the depletion region can be derived. (See Knoll (2000) or Spieler (2005) for details.)

$$d = \sqrt{\frac{2\epsilon V}{e N}} \quad (8.6)$$

Here,  $N$  is the lower of the two dopant concentrations. The depletion thickness thus depends on the square root of the applied bias voltage (or built-in voltage if no bias voltage is applied). If the depletion region width is less than the thickness  $\tau$  of the detector, the detector is partially depleted. If the bias voltage is increased to  $\tau^2 e N / 2\epsilon$  then the entire volume of the detector is depleted of charge carriers.

The conductivity of a reverse-biased p-n junction is low, reducing leakage current (see section 8.1.4). This produces the ideal conditions for radiation detection: the leakage current is kept low, limiting noise. However, charge carriers generated by X-ray interactions are easily swept out of the depletion region by the applied electric field, producing fast and efficient charge collection. The collection time needs to be short compared to the recombination time of electrons and/or holes; otherwise, recombination of charge carriers will reduce the collected signal and worsen the energy resolution of the detector. For this reason, detectors are often “overdepleted” with a bias voltage higher than that necessary to fully deplete the detector in order to achieve electric field uniformity and a short charge collection time. It is desirable to raise the bias voltage to a high value in order to fully deplete or overdeplete the detector, but the voltage must be kept lower than the breakdown voltage, where electrical fields are so high that electrons are accelerated to energies where they ionize atoms in a runaway avalanche process.

### 8.1.4 Leakage current

Normally, a current is present in the detector even in the absence of ionizing radiation. It is desirable to reduce this “leakage current” because it forms a background for currents produced due to ionizing radiation (on the order of  $\mu\text{A}$ ). Here, some of the ways in which leakage current arises are discussed.

Leakage current can be caused by thermal fluctuations that randomly generate charge pairs. In equilibrium, the occupancy  $n$  of a charge carrier for a given energy state (valence or conduction band) with energy  $\epsilon$  is described by the Fermi-Dirac distribution:

$$n = \frac{1}{e^{(\epsilon-\mu)/kT} + 1} \quad (8.7)$$

where  $\mu$  is the Fermi energy, which lies within the bandgap. The occupancy of energy states in a Fermi distribution is shown in Figure 8.4. At  $T = 0$ , no electrons occupy the conduction band and all valence states are filled. With increasing temperature, there is a greater likelihood that electrons will be found in the conduction band, creating a current in the absence of incident radiation. Leakage current  $I_L$  varies with temperature as (Spieler 2005):

$$I_L \propto T^2 \exp\left(-\frac{E_b}{2kT}\right) \quad (8.8)$$

Semiconductor detectors are often cooled to reduce this leakage current. Silicon and cadmium-telluride detectors are usually cooled to  $\sim -25$  degrees Celsius. Germanium, on the other hand, is often cooled to  $\sim 75$  K because of its small bandgap ( $E_b = 0.67$  eV); thermal fluctuations can easily propel electrons to the conduction band.

Leakage currents can also be enhanced by an improper choice of electrodes. A simple metal electrode placed at the edge of the semiconductor would inject charge carriers into

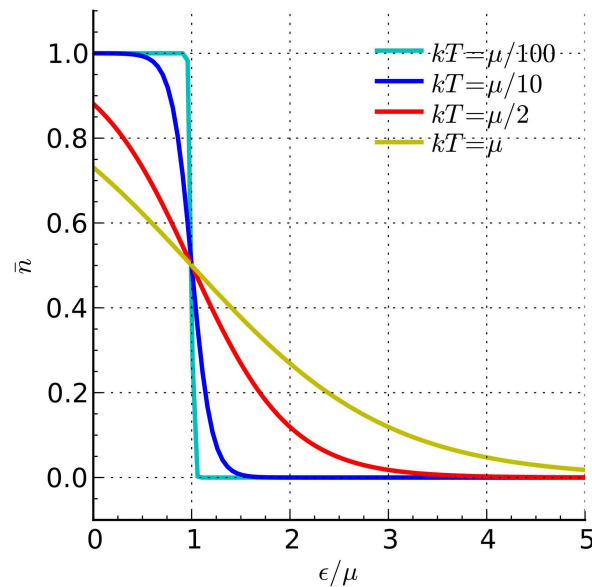


Figure 8.4: Occupancy of energy states in a Fermi distribution, for various temperatures.  $\mu$  is the Fermi energy. For  $kT \ll \mu$ , all states with energy  $\epsilon < \mu$  (i.e. valence band) are filled and all those with energy  $\epsilon > \mu$  (conduction band) are empty. As  $kT$  approaches the Fermi energy, thermal fluctuations allow more electrons into the conduction band.

the material to maintain the carrier concentration at the same time as charge carriers are swept out of the depleted region by the electric field, producing a large quiescent current. For this reason, the charge-collecting electrodes in a detector are usually made up of the p-n junctions discussed earlier. The p-n junction acts as a diode, reducing current except in the cases of radiation interaction or thermal fluctuations. The depletion region has a lower conductivity than that of the intrinsic material, but electron-hole pairs generated by photon interactions are easily swept out of the depletion region by the electric field, producing a measurable signal. P-n junction diodes thus serve as noninjecting electrodes.

### 8.1.5 Semiconductor detector geometries

Many semiconductor detectors use p-n junction charge-collecting diodes, but several geometries are commonly used.

#### Bulk detectors

The least complicated geometry is a bulk wafer of a semiconductor with no spatial differentiation. The detector is depleted and charge collected at junctions on one or both sides of the detector, but no information about where the photon interacted within the

detector is obtained. Such a configuration has minimal readout channels, reducing the complexity of the readout system, and can be used if no positional information is required.

In order to obtain a low capacitance and a large volume within a limit for the distance between electrodes, a coaxial configuration is sometimes used, in which a core is bored into cylindrical symmetric doped bulk material and an electrode implanted on the inside of this core. The *RHESSI* detectors, discussed in Chapter 3 have such a geometry (See figure 3.4). Bulk detectors have high backgrounds (i.e. measured counts that do not originate from the desired source) because the large volume provides a high cross section for background photons or particles.

### Strip detectors

Alternatively, the doped junctions at the detector surfaces can be segmented along the surface to form electrodes in the shape of strips (or pixels, discussed next). If electrodes are segmented on one side of the detector only, then a one-dimensional position of the photon interaction can be measured. Strips of the opposite doping type can also be implanted orthogonally on the other side of the detector to measure a second dimension. A diagram of this geometry is shown in Figure 8.5. In this case, the two types of charge carriers (electrons and holes) are collected on opposite sides of the detector. If 3D knowledge of the interaction location is required (useful for tracking scattering paths of gamma rays or charged particles), strip detectors can be stacked in thin layers, or else fine timing information from charge collection can reveal the depth at which the interaction took place. An example is the 3D-sensitive Ge detectors for the GRIPS high-altitude balloon experiment (Shih et al. 2012).

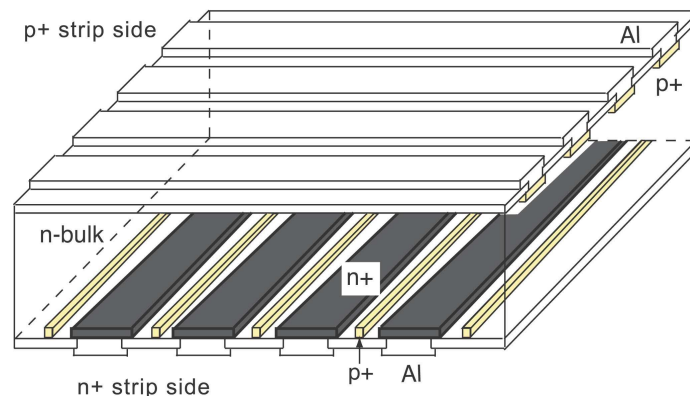


Figure 8.5: Diagram of a double-sided strip detector. Holes and electrons are collected at strips on the p- and n-sides that are oriented orthogonally to each other so that a two-dimensional image can be obtained. Each strip acts as an individual p-n junction. The “p-stops” improve charge collection on the n-side and will be discussed in Section 8.2.1. Figure from Takeda et al. (2008).

But how well can the strip readout pinpoint the location of the photon interaction? As the charge carriers travel, thermal diffusion causes the charge cloud to spread, producing an uncertainty in position of  $\sigma = \sqrt{2Dt}$ , where  $t$  is the travel time and  $D$  is the diffusion constant  $D = \frac{kT}{e} \mu$ . Assuming a uniform electric field, this makes the transverse drift error (Spieler 2005):

$$\sigma \approx \sqrt{\frac{2kT\tau^2}{eV}} \quad (8.9)$$

where  $\tau$  is the thickness of the detector. For a thickness of  $500 \mu\text{m}$  and applied bias voltage  $V = 200V$ , this error is  $\sim 8\mu\text{m}$  even at room temperature, far less than a typical strip or pixel size. In practice, the field is not uniform in the vicinity of the junctions and there can be significantly greater drift error. It can actually be advantageous for the charge cloud to encompass more than one strip, since multiple strips can provide a weighted measurement of the true location, providing greater accuracy than is possible in the case of full charge collection on a single strip.

Strip detectors can be used in conjunction with focusing optics to drastically improve sensitivity by reducing the collecting volume. Large monolithic detectors have high backgrounds due to their large collecting areas and high efficiency (determined by thickness) for background radiation. Focusing optics (such as *FOXSTs*) divert photons onto a smaller area so that the detector volume can be made smaller.

A problem unique to strip detectors is that of “ghosting” at high flux rates. If two photons interact in a 2D strip detector within the time resolution of the measurement system, then two strips on either side of the detector will measure a signal. There are four intersection points between these strips: the two actual photon interaction locations and two ghost locations. For a single measurement it is not possible to distinguish real from ghost hits unless energy information is obtained. Over many events the true source becomes apparent.

### Pixelated detectors

A semiconductor detector that is electrically segmented into pixels offers an even smaller collecting volume for background reduction, lower capacitance (advantageous for noise purposes) and is not subject to ghosting effects. A common type of pixelated detector is the charge-coupled device (CCD), in which pixels are serially read out by transferring charge from pixel to pixel along each row and column.

Complementary metal-oxide semiconductor (CMOS) detectors can, in principle, offer great improvements over CCDs in terms of fast readout and noise reduction (Janesick & Putnam 2003). “Monolithic” CMOS detectors have transistors implanted into each pixel so that pixels can be directly read out by applying timed voltage pulses. The Battaglia group at Lawrence Berkeley Laboratory designed and tested CMOS sensors with  $10\text{--}40\mu\text{m}$  pixel pitches, with correlated double-sampling (dark current removal for each frame) done in-pixel, and also built silicon-on-insulator (SOI) sensors which allow more extensive circuitry to be implemented on-pixel (Arai et al. 2010; Battaglia et al. 2008, 2009). Readout circuitry up to

and including digitization can be implemented on-chip, reducing analog noise and providing greater ease in interfacing.

Alternatively, pixelated detectors can be fabricated in a similar way to strip detectors and read out via an additional chip containing readout electronics, which can be bump-bonded to the back of the detector.

### 8.1.6 Semiconductor detector materials

Several semiconductors are commonly used as radiation detectors; those that are most relevant to the applications in this dissertation are silicon (Si), germanium (Ge), and cadmium-telluride (CdTe). Here, a few relative strengths and weaknesses of these choices are considered.

One of the most important criteria for a detector is the material's efficiency in the energy range of interest. The efficiency is defined as the fraction of photons incident on a detector that interact (and thus generate a signal) in the detector. This depends on the cross-section of X-ray interaction with the semiconductor material as well as the thickness of the detector; if the interaction rate is low (or the detector thin), a photon may traverse the detector without interacting. Since photoabsorption cross-sections fall with energy in the X-ray regime (see Figure 8.2), thicker or higher-Z detectors are needed for appreciable efficiency at higher energies. See Figure 8.6 for a comparison of the efficiencies of Si, Ge, and CdTe. Silicon is the most common detector choice for SXR (1–10 keV) or low-energy HXRs up to 20 or 30 keV, but at higher energies Ge and CdTe must be used. In order to reconstruct a photon flux from a measured flux, the detector's efficiency as a function of energy must be measured or calculated.

The semiconductor bandgap is an important consideration in selecting a detector material. Germanium has a smaller bandgap compared to silicon (See Table 8.1), so more electron-hole pairs are generated for each photon interaction. This is advantageous because of the lower relative statistical error due to collection of a larger number of charge carriers. However, the smaller bandgap allows thermal fluctuations to easily carry electrons into the conduction band, producing a high leakage current. For this reason, Ge detectors must be cooled in order to measure photon interactions; typically, temperatures of  $\sim 75$  K are used. Si and CdTe detectors are also commonly cooled in the range of  $-30$  to  $0^\circ\text{C}$  to reduce leakage current and its resultant noise, but often can be operated at room temperature, albeit with poorer energy resolution.

CdTe is a promising material for X-ray applications in that it provides good efficiency into high energy ranges and is starting to be fabricated in large quantities with high purity. However, CdTe has a low hole mobility and has typically been used for one-sided, not double-sided strip detectors. Recently, though, double-sided CdTe detectors have been fabricated for the Hard X-ray Imager (HXI) on Astro-H (Kokubun et al. 2010); this is accomplished by means of thin strips and a high bias voltage so that hole collection time is less than the average hole lifetime (Ishikawa et al. 2008).

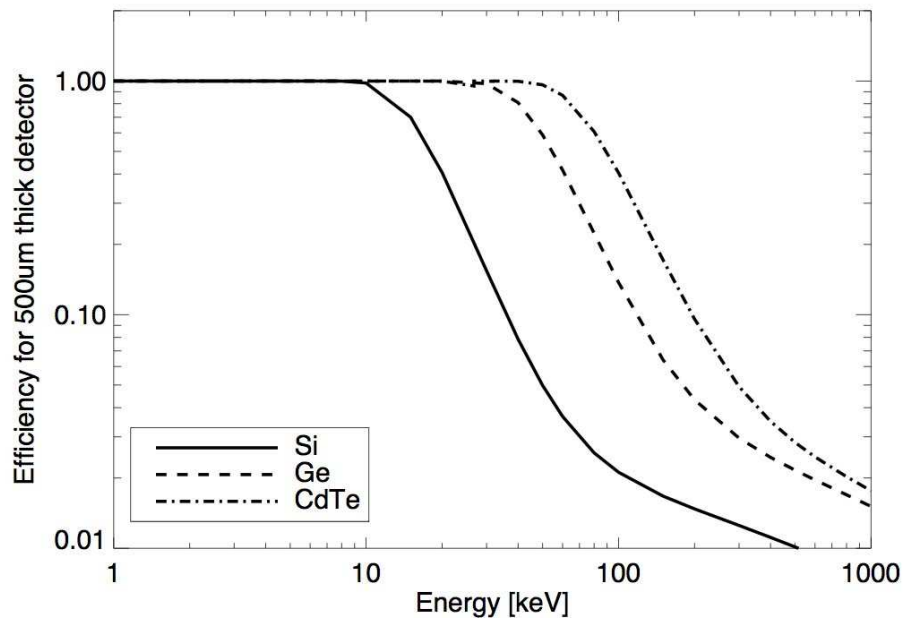


Figure 8.6: Efficiency as a function of X-ray energy for a 500  $\mu\text{m}$  thick detector. Silicon, the lowest-Z material considered here, has appreciable efficiency only up to tens of keV. For higher energy HXR and gamma-ray studies, higher-Z materials like germanium and cadmium telluride must be used.

### 8.1.7 Producing an energy spectrum

Many X-ray detectors for solar observations employ “single photon counting.” This assumes the incident X-ray flux and/or interaction rate is small enough compared to the readout rate that individual photons can be measured independently of each other. Semiconductor interaction and collection times are fast (on the order of picoseconds and nanoseconds, respectively) so the extent to which single photon counting applies is often driven by the time constants in the measuring circuitry (often microseconds). At high count rates, pulses may arrive in quick enough succession that one pulse arrives before the previous pulse has fully decayed, referred to as pulse pileup. Pileup can be ameliorated by employing fast readout circuitry, more readout channels, or by post-measurement corrections. After many photons have been measured, a differential distribution of their energies is produced.

#### Signal processing

Since the collected charge in a detector is small ( $< 1$  fC for low-energy X-rays) (Spieler 2005), the first step in a signal processing chain is usually to amplify the signal with a preamplifier. In some detectors, and for some energy ranges, input capacitance can vary with

collected charge. A “charge-sensitive amplifier” uses feedback to adjust for any variance in capacitance, ensuring that the output of the preamp is proportional to the collected charge (Knoll 2000). Next, the pulse is shaped in order to be sampled. The pulse shape depends on the input resistance and equivalent capacitance and extends the short detector signal ( $\sim 10$  ns) into a longer pulse for measurement. Usually, the maximum (peak) output voltage of the shaper is sampled. Since the signal and noise often have different power spectra, the pulse shaper should be optimized to boost the signal-to-noise (SNR) ratio.

The shaped signal is sampled as closely to the peak as possible and digitized via an analog-to-digital converter (ADC), which outputs a digital value proportional to the analog input. There are several schemes for performing this digitization. One choice is a Wilkinson-style ADC (Wilkinson 1950), which includes a comparator that compares the input analog voltage and a steadily rising (ramped) voltage. The size of the analog input signal is proportional to the time needed for the ramp to reach that value. The digital value can be produced by, for example, latching a clock value when the two signals are equal; this clock value is then proportional to the input pulse. While this style ADC requires appreciable conversion time (up to 6.5 ms for a 16-bit ADC on a 10 MHz clock, for example), the conversion is efficient in that only one comparator is needed for each input channel. Other types of ADCs can perform the conversion in a much shorter period of time but require a large number of comparators that rises with the resolution (number of bits) desired of the ADC.

### Counting statistics

Counting statistics will prove important in this chapter for measuring spectral resolution and for measuring livetime. Statistical noise in a measurement system is due to random fluctuations at each step of the process. If the events occur randomly but independently of each other, the result is a Poisson distribution:

$$P(x) = \frac{(\bar{x})^x e^{-\bar{x}}}{x!} \quad (8.10)$$

$P(x)$  is the probability of  $x$  number of events occurring, in a distribution with mean value  $\bar{x}$ . The Poisson distribution is a specialization of the binomial distribution and is well approximated by a Gaussian distribution for a large expected value ( $\bar{x} \gtrsim 30$ ).

The time  $t$  between successive events with mean count rate  $r$  follows an exponential distribution  $I(t)$  (Knoll 2000):

$$I(t) dt = r e^{-rt} dt \quad (8.11)$$

This distribution also holds for event times measured from random start times (Knoll 2000). The probability of a photon arrival within a given time interval is found by integrating over that interval and normalizing properly. The most likely time interval is 0, and the expected value is found to be  $1/r$  (Knoll 2000). This principle will be useful in calculating count rates using livetimes.

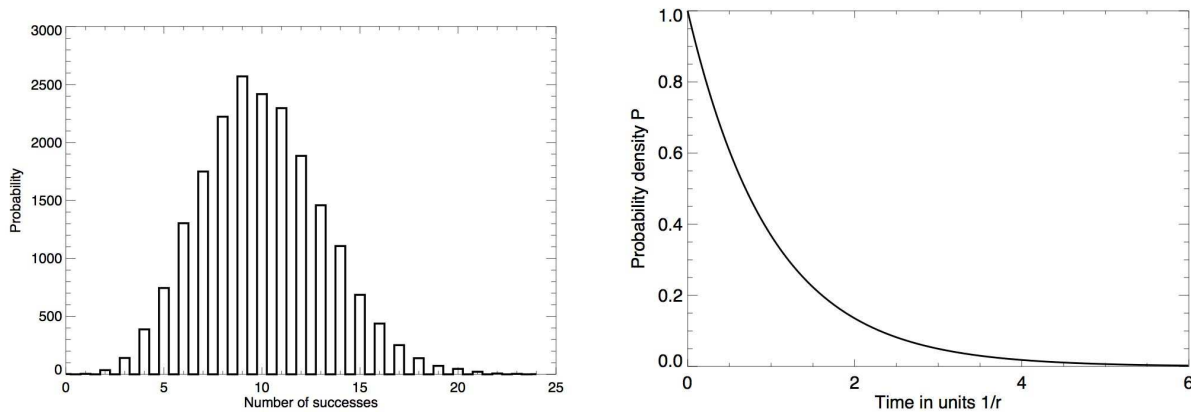


Figure 8.7: (Left) A Poisson probability distribution for 10 mean successes. (Right) Poissonian distribution of waiting times between successive events, with waiting times in units of the inverse count rate  $r$ , and with the distribution normalized to  $r$ .

If  $\bar{x}$  is the mean number of charge carriers produced in an interaction, the standard deviation of this number is  $\sigma_x = \sqrt{\bar{x}}$ . For a random process, Poisson statistics thus limits the energy resolution to  $\sqrt{\bar{x}}$ ; a smaller value cannot be obtained.

Many processes inherent in radiation measurement follow Poisson statistics, for example, the number of photon interactions in a given time interval given a fixed photon flux. But it turns out that in semiconductor detectors (as well as in other types of radiation detectors), the generation of charge carriers is not a Poisson process, and so the obtained energy resolution is not limited by Poisson statistics of charge carrier generation. It has been empirically observed that a smaller resolution can be obtained. (See Spieler (2005) for discussion of the causes of this phenomenon.) The Fano factor adjusts the statistical limit to account for this:

$$F = \frac{\text{Actual variance}}{\text{Poisson variance}} \quad (8.12)$$

Fano factors for semiconductors are typically  $\sim 0.1$ .

## Energy resolution

The energy resolution of a detector is usually defined as the width of the peak in an energy distribution measured for a monoenergetic photon beam (Knoll 2000). Perfect resolution, impossible to attain, would produce a delta function in the differential energy spectrum. The width of the peak is often measured as a Gaussian width or as a full-width at half-max (FWHM) and is due to fluctuations in the measured value due characteristics of the detector and its readout circuitry. Uncertainties can be roughly divided into statistical noise (due to counting statistics and including a Fano factor) and noise due to instrumental factors, which

add in quadrature:

$$\sigma^2 = \sigma_{\text{stat}}^2 + \sigma_{\text{noise}}^2 \quad (8.13)$$

Often, this value is reported as the width of a Gaussian peak divided by the mean value, a relative resolution. Radioactive sources producing X-rays of known energies are used as inputs; measured spectra of these sources are used to measure the gain and resolution of the detector. These radioactive sources can mimic a monoenergetic source if the line width is small compared to the resolution of the detector. The smaller the energy resolution, the finer the structure that can be observed. Two fine features can usually be distinguished from each other if they differ by more than the energy resolution.

### Livetime / Deadtime

Deadtime is the time needed for a measurement system to measure and record one pulse before a second pulse can be measured. (An alternative term is livetime, the time during which the system is ready for a new measurement.) A photon interacting within the deadtime following a previous photon will either be lost or else will contaminate the previous measurement (pileup). Because the photon interaction time and charge collection time are small in semiconductor detectors, deadtime is dominated by the characteristics of the measuring circuitry and the readout system. In order to reconstruct an accurate incident flux rate from a measured count rate, the deadtime of the detector must be accounted for.

In the following discussion (adapted from Knoll (2000)),  $T_D$  and  $T_L$  are the average deadtime and livetime, respectively, measured in seconds while  $\tau_D$  and  $\tau_L$  are the unit-less deadtime and livetime expressed as a fraction of the total collection time. The true count rate  $R_T$  can be found from the measured count rate  $R_M$  by correcting for the time the detector is dead:

$$R_T = \frac{R_M}{1 - R_M T_D} \quad (8.14)$$

The quantity in the denominator is just the fraction of the time the detector is live, so the equation can be expressed in terms of livetime instead:

$$R_T = \frac{R_M}{\tau_L} = \frac{1}{T_L} \quad (8.15)$$

This should be expected from the properties of Poisson statistics discussed earlier. The livetime is the arrival time of an event measured from an arbitrary point in time. The expected value of the livetime is therefore  $1/R_T$ , and calculation of an average livetime is a good measure of the true count rate.

Deadtime can be either paralyzable or nonparalyzable (Knoll 2000). In a (highly preferred) nonparalyzable system, photon-detector interactions that occur during the deadtime are simply lost and have no effect on the system's behavior. In a paralyzable system, each interaction restarts the deadtime, essentially extending it. The systems discussed in this chapter are nonparalyzable systems.

## 8.2 The *FOXSI* detector system

The *FOXSI* mission requires good detector efficiency up to 20 keV,  $< 1$  keV energy resolution, and a  $\lesssim 5$  keV low-energy threshold in order to measure nonthermal HXR emission quiet Sun (Krucker et al. 2011b). The angular resolution should be as good as or better than that of the optics system. At the time of the *FOXSI* proposal, the angular resolution of a *FOXSI* optics module (FWHM of the PSF) was expected to be 12 arcseconds; improvements in the optics assembly since then have lowered this value to  $< 7$  arcseconds. The detector also needs to have a low background in order to achieve a high sensitivity. The readout system must be low-power and must be capable of measuring a few hundred counts  $\text{s}^{-1}$  detector $^{-1}$ . CCD cameras (which have long readout times) are therefore not adequate for *FOXSI*'s purposes.

To meet these challenges, *FOXSI* utilizes double-sided silicon strip detectors (DSSDs) and low-noise, low-power application-specific integrated circuits (ASICs) for detector readout. Both the detector and the ASIC were designed by a group at ISAS/JAXA directed by Prof. Tadayuki Takahashi, with collaboration from Stanford University and Gamma Medica-Ideas (Norway) in the design and fabrication of the ASIC. The detector was manufactured by Hamamatsu Photonics. The detector and ASIC were designed especially for this mission but grew out of a detector development program for the Hard X-ray Imager (HXI) on ASTRO-H, a Japanese astrophysics spacecraft scheduled to launch in 2014. The HXI detector system is layered, with 4 thin Si layers and a CdTe layer. This allows better efficiency than a single thin Si detector alone, with the CdTe layer extending the energy range up to 80 keV (Kokubun et al. 2010). The HXI DSSDs have a 400  $\mu\text{m}$  pitch at a focal length of 12 meters, producing an angular resolution of  $\sim 7$  arcseconds. By using strips instead of pixels, the readout complexity and power consumption are kept low.

### 8.2.1 The *FOXSI* DSSD

The *FOXSI* proposal called for a detector system that could resolve to  $\sim 12$  arcseconds at a focal length of 2 m, so the strip pitch required was  $< 116\mu\text{m}$ . Detectors with 75 and 60  $\mu\text{m}$  pitches were designed for *FOXSI*, with the 75  $\mu\text{m}$  pitch chosen for the final product because of its larger field of view. This resulted in an angular resolution of 7.7 arcseconds. The optics resolution attained also proved to be smaller ( $\lesssim 7$  arcseconds) than that originally required, so the total resolution of the system is  $\sim 10$  arcseconds. The DSSD consists of an n-doped bulk wafer with p+ and n+ doped strips (referred to as the p-side and n-side throughout much of this chapter). See Figure 8.5 for a diagram and the discussion in section 8.1.5 for a description of a DSSD geometry. More details on the detector can be found in Ishikawa et al. (2011) and Saito et al. (2010). Between the n-side strips are additional p+ doped implants (p-stops) for electrical insulation of the strips. Each side of the detector contains 128 strips, for a total of 256 readout channels and an active area of 9.6 x 9.6  $\text{mm}^2$ ; this active area is surrounded by a 100  $\mu\text{m}$  wide guard ring to reduce leakage current due to edge effects. Bonding pads at the edge of the detector allow the detector to be wirebonded

---

*FOXSI* detector system characteristics

---

Detector type	Double-sided Si strip (DSSD)
Readout ASIC	VATA451
Strip pitch	75 $\mu\text{m}$
Number of strips	128 x 128
Active area	9.6 x 9.6 mm <sup>2</sup>
Thickness	500 $\mu\text{m}$
Power	1 mW per channel, 0.26 W per detector
angular resolution	7.7 arcseconds at a focal length of 2 m
Energy resolution	0.5 keV

---

Table 8.2: Parameters of the *FOXSI* detectors and readout system, adapted from Krucker et al. (2011b)

to the readout ASIC. The detector thickness is 500  $\mu\text{m}$ ; a plot of the theoretical efficiency of such a detector is shown in Figure 8.9.



Figure 8.8: Photographs of the *FOXSI* DSSD.

### 8.2.2 The *FOXSI* VATA451 readout ASIC

The *FOXSI* 64-channel ASIC builds on previous iterations of ASICs designed for the HXI project (Tajima et al. 2004) and is known as the VATA451; see Ishikawa et al. (2011) and Saito et al. (2010) for a description. Since *FOXSI* is a lower-energy instrument than HXI, the ASIC was optimized to increase the signal-to-noise value at low energies by increasing

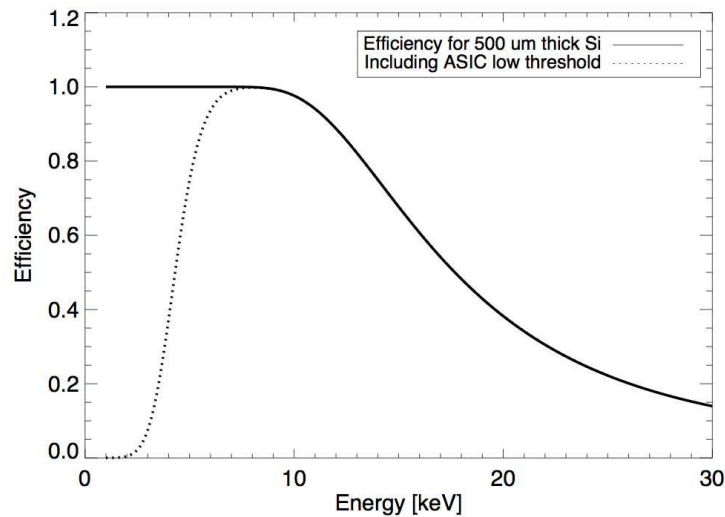


Figure 8.9: Efficiency of the *FOXSI* detectors for the X-ray energy range of interest. The dashed line includes the effect of the low-energy threshold (LET) of the VATA451 ASIC and is an averaged value from all of the ASICs used for flight. (Details of this measurement will be discussed later in this chapter.) Attenuation length data is from Henke et al. (1993).

the preamplifier gain and using a lower feedback capacitance. The VATA451 is optimized for an input capacitance of 5 pF and a leakage current of 10 pA per strip. Power consumption is 1 mW per channel. For each channel, the ASIC contains a charge-sensitive amplifier followed by two shaping amplifiers. One of these is a fast shaper (shaping time  $0.6 \mu\text{s}$ ) followed by a discriminator that provides triggering; the discriminator outputs of all channels meet in a logical OR gate so that an event above the threshold in any strip will produce an ASIC trigger. The other shaper is a slow shaper (shaping time  $3 \mu\text{s}$ ) that shapes the signal for sampling. The sampled analog signal is converted to a digital signal by a Wilkinson-style ADC (see section 8.1.7): the sampled signal on each channel is compared to a reference signal that is ramped up on an external 1–10 MHz clock until it equals the sampled signal, at which point the clock counter is latched for that channel. Digitization of all channels occurs in parallel. The ADC has a maximum of 1023 clock periods; higher-value signals will be registered in an overflow bin. The ramp speed and starting ramp voltage are adjustable by setting bits in a serial register clocked into and latched in the ASIC prior to beginning data acquisition. The 867-bit serial register can also tune values for the fast and slow shapers and the preamp, set thresholds, select the charge polarity to be measured, and disable specified channel triggers, among many other functions.

Data for all channels are clocked out of the ASIC in a serial data stream. Two additional channels are included in addition to the 64 input channels. A “dummy” pedestal channel without an external input monitors shifts in the ASIC due to temperature fluctuations or other drifts. The ADC ramp begins at the dummy channel value (with an adjustable offset)

so that such drifts are not reflected in the measured data values. The pedestal is included in the readout data for reference. A common-mode noise value is calculated by selecting the 32nd channel to finish conversion, which is close to the median value of all strips. In a single acquisition, X-ray data is only found in a few strips (almost always  $< 3$ ) out of the 64 ASIC channels, so the median value well represents a baseline value with no X-ray data. The common-mode noise value is included in the data stream; by subtracting this value from the other channels, any noise component common to all channels (for example, due to shifts in the detector bias voltage) is removed.

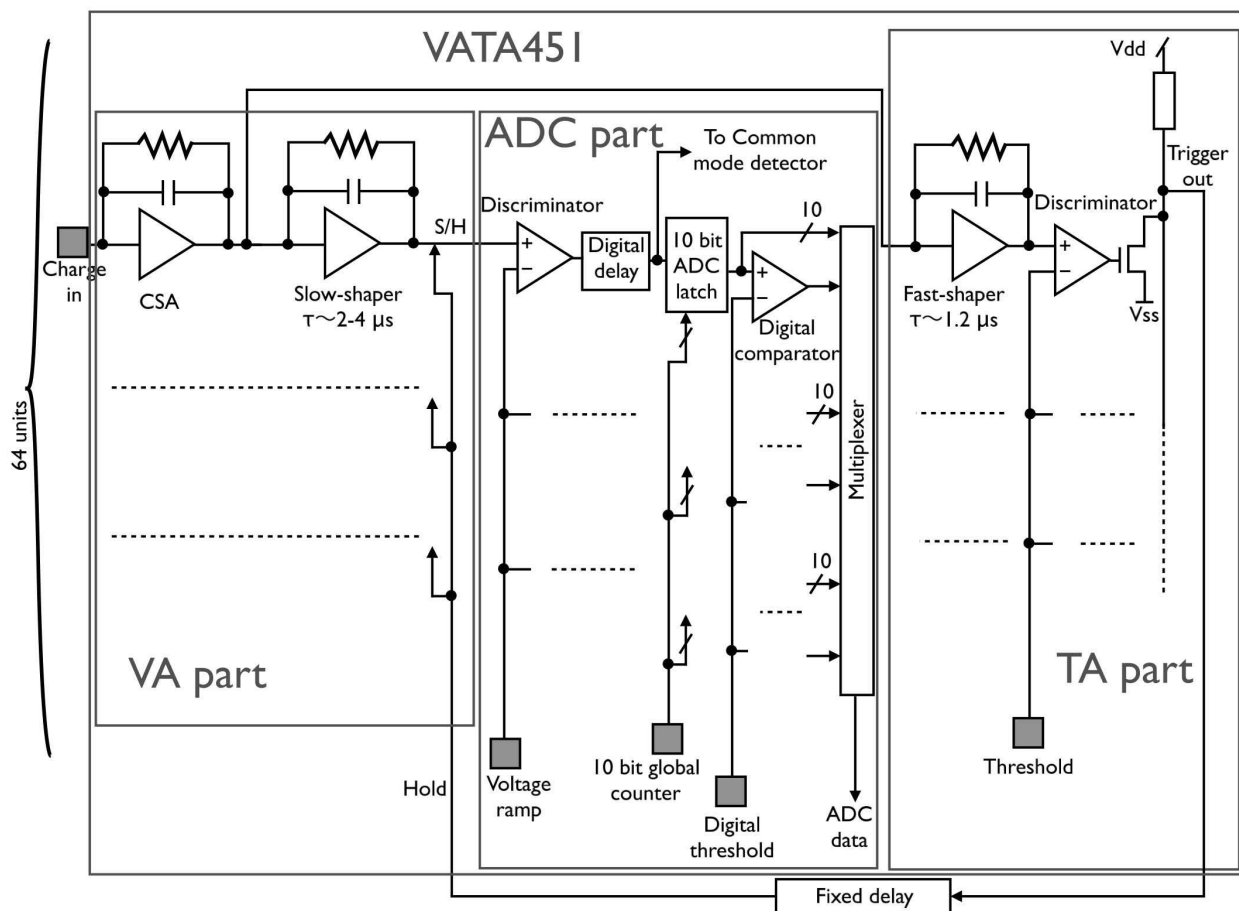


Figure 8.10: Block diagram of the VATA, showing the charge-sensitive amplifier, slow shaper and sampling circuitry (VA part), ADC, and fast shaper for triggering (TA part). Image from Ishikawa et al. (2011).

### 8.2.3 Prototype testing at ISAS/JAXA

Prior to delivery to SSL, a prototype detector/ASIC system was tested at ISAS using hardware and software adapted from tests of prior detector and ASIC iterations. Results of these tests are described in Ishikawa et al. (2011) and Saito et al. (2010). Measurements of the body and interstrip capacitance show that the detector is fully depleted at a bias voltage of 200 V. For the prototyped testing, the detector was operated at a bias voltage of 300 V (for overdepletion) and a temperature of -20 degrees Celsius. Spectra from a radioactive Am-241 source, after calibration, demonstrated an energy resolution of 430 eV and 1.6 keV (FWHM) for the p- and n-sides, respectively, at the 13.9 keV line. The cause of the considerably worse resolution on the n-side is not fully understood although it may be related to properties of the p-stops; this issue is explored in Ishikawa et al. (2011).

Since the p-side energy resolution was found to be three times better than that of the n-side, only the p-side data is used to measure photon energies. The n-side data, however, are necessary for imaging. For accurate image reconstruction the n-side data values must be greater than the width of the pedestal for any strip; otherwise random noise may be mistaken for data and give an incorrect photon position. Measurements of the pedestal were conducted at ISAS and it was found that for a 5 keV photon, the probability of a position error due to detector noise is  $< 10^{-7}$ , while for a 2 keV photon the probability is 6% (Saito et al. 2010). Thus the *FOXSI* DSSD and VATA451 system are capable of meeting the science requirements for energy resolution ( $< 1$  keV) and low-energy threshold ( $< 5$  keV).

### 8.2.4 The *FOXSI* readout system

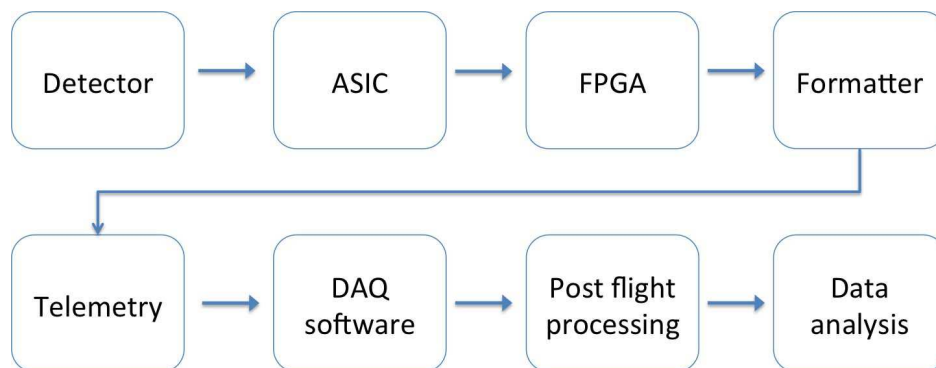


Figure 8.11: Flowchart for *FOXSI* data handling. After data is measured, digitized, and read out from each detector by four ASICs, a FPGA performs minor processing and data reduction. The formatter FPGA then packages all the detector data into a telemetry stream, which is transmitted to a ground station at White Sands and fed into the *FOXSI* DAQ software for live monitoring of flight data. After the flight, data is processed into Level 1 products and analyzed.

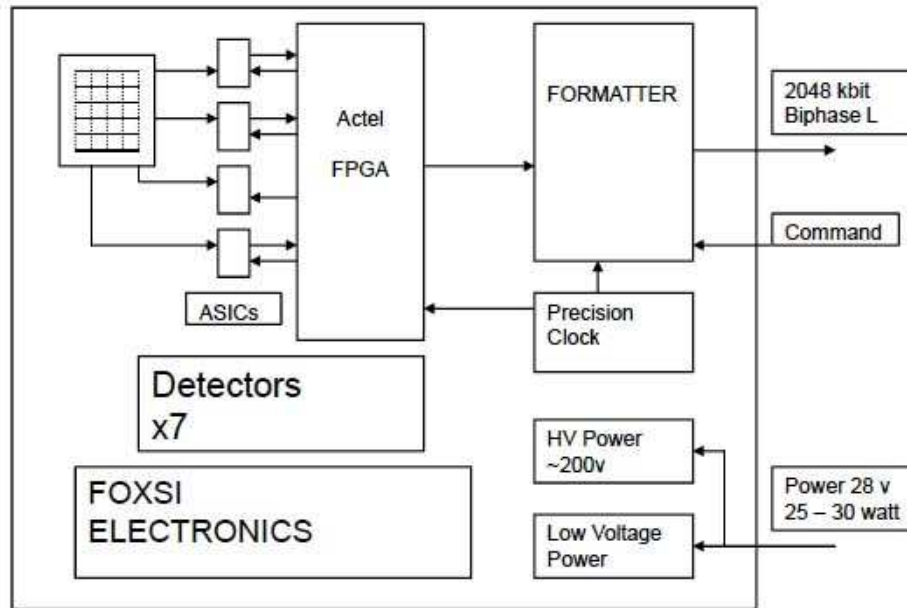


Figure 8.12: Block diagram of the *FOXSI* electronics package. Each of the 7 detectors has 4 R/O ASICs and a dedicated FPGA. Data from each FPGA is collected by a formatter FPGA (encoder) and packaged into a data packet inserted into the telemetry stream. Power, telemetry, and uplink commanding are provided by the NASA Sounding Rocket Operations (NSROC) team.

This section describes the flight detector readout system designed and constructed at SSL. Figure 8.11 shows a chart for the data flow; each of these steps will be described in detail here. Since the *FOXSI* DSSD has 128 strips on each side, 2 64-channel ASICs are required to read out each side, for a total of 4 ASICs per detector. Detector boards were fabricated with readout electronics on either side and a central cutout for a detector, which was epoxied in place with a top bond around the edges of the detector on one side. ASICs were epoxied using a conductive epoxy (TRA-DUCT 2902) to ground the body of the ASIC. The bond pads at the ends of the detector strips were then wirebonded directly to the ASIC input pads. The two sides of the detector board are electrically isolated, with floating grounds so that a potential applied between the grounds applies a bias voltage across the detector. Late in the testing phase, four  $1\ \mu\text{F}$  capacitors were added between these grounds to reduce noise in the detector bias, which led to spurious triggers and slightly degraded energy resolution; each capacitor was placed as physically closely to a detector as possible; since there was no room for such large capacitors on the detector boards themselves, the capacitors were placed on output pins on the next board up. The RC settling time after changes to the high voltage with  $4\ \mu\text{F}$  and  $10\ \text{M}\Omega$  is 40 seconds. For flight, the bias voltage during the observation time was 200V. The voltage was ramped from 0 starting 30 seconds after launch at a ramp speed

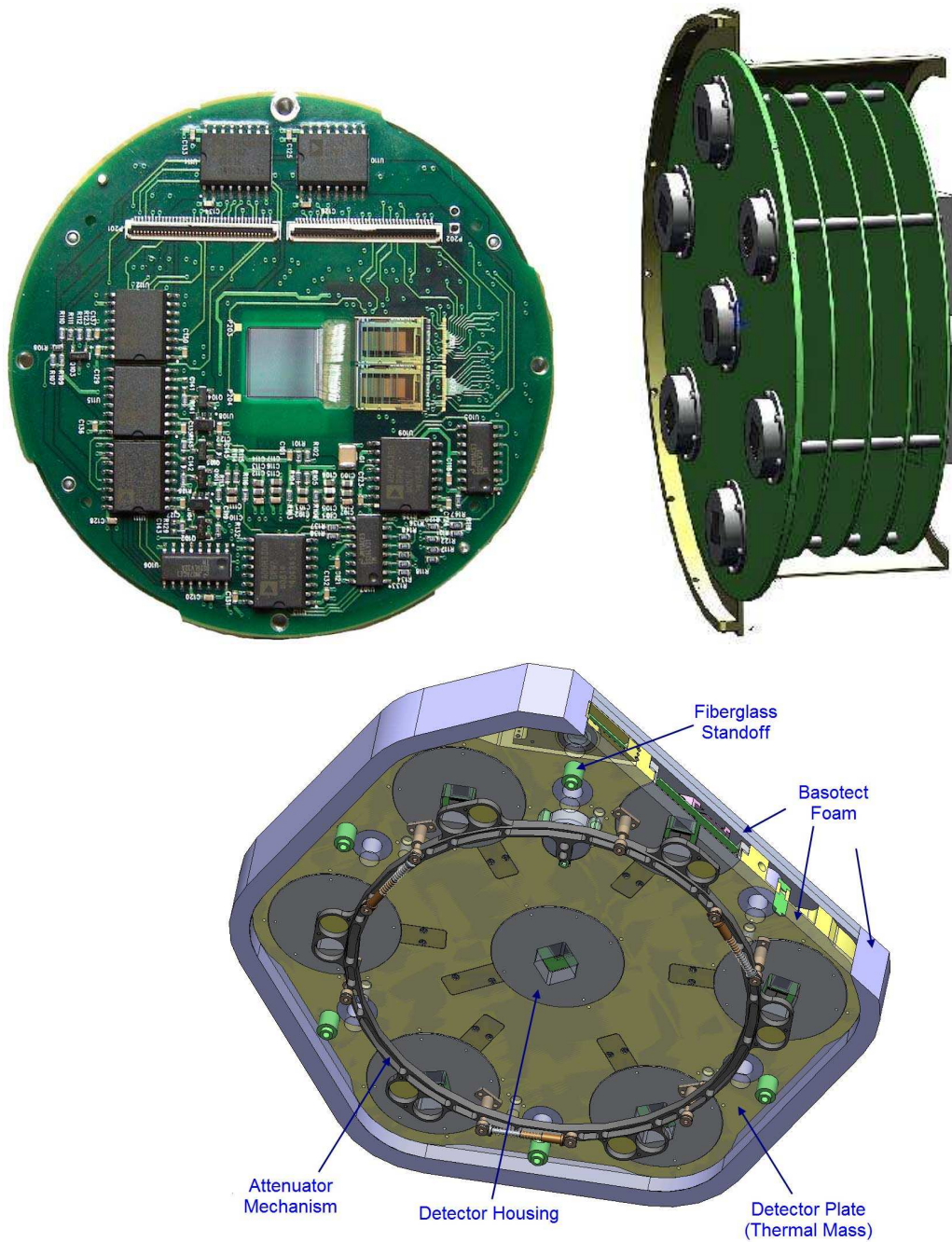


Figure 8.13: (Upper left) A photograph of the *FOXSI* detector board, showing the n-side of the detector and its two readout ASICs. (Upper right) Design showing the focal plane assembly that holds the 7 detector boards, FPGA board, formatter board, and power board. (Bottom) Design showing the attenuator mechanism. By sending a command during the flight, a pin puller is activated, allowing the spring-loaded mechanism to insert thin attenuators in front of 6 out of the 7 detectors. Images are from Krucker et al. (2011b).

of  $5\text{V s}^{-1}$  so that the detector current had time to stabilize before observations began. Table 9.1 shows a timeline of this ramp compared to the other events during the flight.

### The role of the FPGAs

ASIC control for each detector is performed by an Actel ProASIC3 A3P250 field-programmable gate array (FPGA). The tasks performed by the FPGA include sending a serial configuration register to the ASIC after power-up, sequencing ASIC modes, sending sample-and-hold pulses after receiving a trigger, clocking the Wilkinson-style ADC, and clocking out the serial data stream. See Figure 8.14 for a block diagram of the FPGA logic. An entire acquisition and readout can take up to  $955\ \mu\text{s}$  if the maximum number of ADC clocks is required. For the *FOXSI* energy range, however, the acquisition and readout time is expected to be less than  $800\ \mu\text{s}$ . This includes the pulse shaping time ( $3\ \mu\text{s}$ ), the ADC conversion time ( $< 50\ \mu\text{s}$  at  $10\ \text{MHz}$  in the *FOXSI* range), the serial readout from the ASIC ( $732\ \mu\text{s}$  at  $1\ \text{MHz}$ ), and various transition times required by the FPGA ( $\sim 15\ \mu\text{s}$ ). The FPGA temporarily stores data for a single event in an internal SRAM and outputs the data via either of two DAQ interfaces (described in the next section). The FPGA can also accept commands via either of these interfaces to change the ASIC configuration register and sampling times, or to turn on an automatic trigger mode.

Because the flight telemetry rate is limited to  $2\ \text{Mbps}$ , some basic data reduction is performed in the FPGA. For each ASIC, the FPGA selects the highest-value channel as well as the two adjacent channels, to properly include charge sharing between adjacent strips. Approximately 17% and 20% of p- and n-side events, respectively, have charge shared among  $> 1$  strip, and  $< 1\%$  of events have charge shared among  $> 2$  strips (Ishikawa et al. 2011). Therefore, the 3-strip selection in the FPGA will account for the entire collected charge in  $> 99\%$  of events. In addition to the 3-strip selection, the FPGA records the common-mode noise value for each ASIC and the time at which either p-side ASIC triggered (from a 16-bit clock counter with  $100\ \text{ns}$  resolution). The FPGA also stores a single bit for each channel indicating whether that channel value exceeded a digital threshold; this “channel mask” may be useful for diagnosing mistaken hits due to low-energy noise, or for identifying multiple hits due to flux rates above  $\sim 300,000\ \text{hits s}^{-1}\ \text{detector}^{-1}$  (which would cause significant pileup within the slow shaping time). Because the ASIC does not output the common-mode value for negative charges due to a design error, the FPGA computes the common-mode noise value for each n-side ASIC by averaging all channel signals. Calculating an average is computationally simpler than calculating a median value and thus requires fewer FPGA resources; because the n-side values will not be used for energy reconstruction, this discrepancy does not introduce any error into the analysis.

### The formatter

Each of the seven detectors has a dedicated FPGA that handles the data from all 4 ASICs (2 n-side and 2 p-side). A “formatter” FPGA then collects the data from all seven

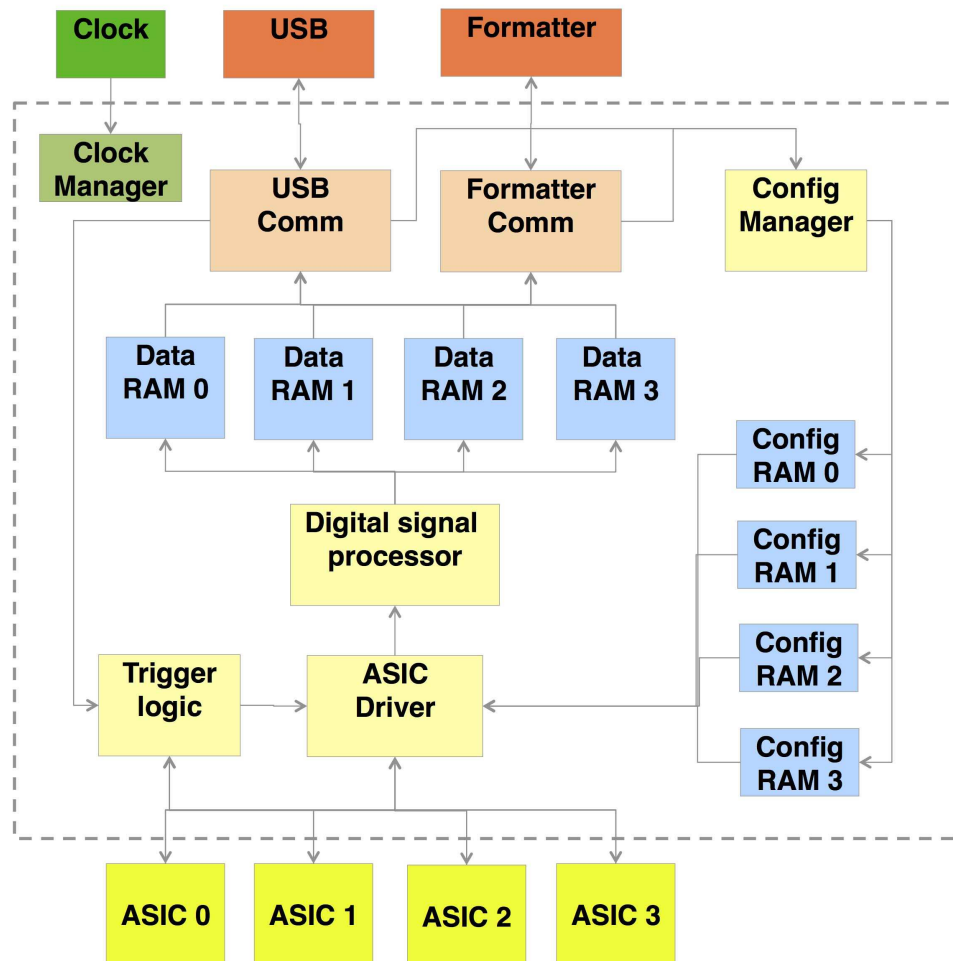


Figure 8.14: Block diagram of the FPGA functions, including SRAM memory, communication, timing, and processing modules. For simplicity, several FPGA modules are left out of the diagram and several buses are condensed into single lines. Boxes outside the dashed line are external to the FPGA. Each detector has a dedicated FPGA, which is interrogated independently by the formatter.

detector FPGAs and packages it for insertion into the 2048 kbps biphas-L telemetry stream. Data frames are made up of 256 16-bit words and are transmitted at a fixed rate of 500 frames/second (2 ms per frame). The *FOXSI* payload includes no onboard processor and no memory storage for multiple events, so no more than one event per detector can be recorded in each 2 ms frame window.

The formatter data packet for a single frame is shown in Figure 8.15. Housekeeping information at the beginning of each packet includes sync words, frame time, information on the bias voltage, detector and electronics temperatures, and the attenuator state, followed by the detector data. Detector data includes the channel mask, 3-strip values, and common-mode noise value for each ASIC and an overall detector trigger time. It should be noted that for each event, half the output data will not contain real event data (because the event is normally found in two ASICs only: one on the p-side and one on the n-side). However, retaining 3-strip data from all four detector ASICs may provide useful pedestal data for diagnostic purposes, properly accounts for split-charge events between neighboring strips in the center of the detector, and is logically simpler as it does not require comparison between data from different ASICs (which may have different gains and pedestals). If no trigger was detected during the 2 ms frame time, the data packet contains zero values for that detector.

The formatter is used to package data during flight. However, another readout system was developed for laboratory test purposes and allows readout of ASIC data directly from the dedicated detector FPGAs through a USB connection to a DAQ computer. A parallel-to-USB FT245RL chip with an internal FIFO is used to output this data. Using this interface, the entire ASIC data packets are retained with no data reduction. This interface is useful for identifying and diagnosing connectivity or configuration problems, and was used for much of the testing and calibration described later in this chapter.

## DAQ software

The data acquisition computer is an iMac running a dedicated DAQ program written by the *FOXSI* team (especially Dr. Steven Christe) in C++ using the FLTK graphics libraries (Spitzak et al. 1998). Alternate versions of the software can accept data either from the formatter (flight mode) or from the USB interface (testing mode). The formatter version displays live data from the seven detectors simultaneously, as well as individual detector spectra and an overall time profile (not corrected for livetime). This software was used to view data from the experiment during the rocket flight and was also used for testing and calibration in the lab.

## Mechanical systems

To ensure low-noise performance, the detectors were kept at a temperature below  $-15$  degrees Celsius during the data collection portion of the flight. This was accomplished by mounting the detectors in an aluminum focal plane (see Figure 8.13) that served as a large thermal mass. Prior to the rocket launch, the detectors and thermal mass were cooled to

Word	0	1	2	3	4	5	6	7
0	Sync1	Sync2	Time1(MSB)	Time2	Time3(LSB)	Frame Counter1	Frame Counter2	Housekeeping 0
8	Cmd Count	Command1	Command2	Housekeeping 1	FormatterStatus	0	HV value/status	Housekeeping 2
16	Status 0	Status 1	Status 2	Housekeeping 3	Status 3	Status 4	Status 5	Status 6
24	Detector 0 Time	0ASIC0 mask0	0ASIC0 mask1	0ASIC0 mask2	0ASIC0 mask3	0Strip0A Energy	0Strip0B Energy	0Strip0C Energy
32	0 Cmn Mode0	0ASIC1 mask0	0ASIC1 mask1	0ASIC1 mask2	0ASIC1 mask3	0Strip1A Energy	0Strip1B Energy	0Strip1C Energy
40	0 Cmn Mode1	0ASIC2 mask0	0ASIC2 mask1	0ASIC2 mask2	0ASIC2 mask3	0Strip2A Energy	0Strip2B Energy	0Strip2C Energy
48	0 Cmn Mode2	0ASIC3 mask0	0ASIC3 mask1	0ASIC3 mask2	0ASIC1 mask3	0Strip3A Energy	0Strip3B Energy	0Strip3C Energy
56	0 Cmn Mode3	Detector 1 Time	1ASIC0 mask0	1ASIC0 mask1	1ASIC0 mask2	1ASIC0 mask3	1Strip0A Energy	1Strip0B Energy
64	1Strip0C Energy	1 Cmn Mode0	1ASIC1 mask0	1ASIC1 mask1	1ASIC1 mask2	1ASIC1 mask3	1Strip1A Energy	1Strip1B Energy
72	1Strip1C Energy	1 Cmn Mode1	1ASIC2 mask0	1ASIC2 mask1	1ASIC2 mask2	1ASIC2 mask3	1Strip2A Energy	1Strip2B Energy
80	1Strip2C Energy	1 Cmn Mode2	1ASIC3 mask0	1ASIC3 mask1	1ASIC3 mask2	1ASIC1 mask3	1Strip3A Energy	1Strip3B Energy
88	1Strip3C Energy	1 Cmn Mode3	Detector 2 Time	2ASIC0 mask0	2ASIC0 mask1	2ASIC0 mask2	2ASIC0 mask3	2Strip0A Energy
96	2Strip0B Energy	2Strip0C Energy	2 Cmn Mode0	2ASIC1 mask0	2ASIC1 mask1	2ASIC1 mask2	2ASIC1 mask3	2Strip1A Energy
104	2Strip1B Energy	2Strip1C Energy	2 Cmn Mode1	2ASIC2 mask0	2ASIC2 mask1	2ASIC2 mask2	2ASIC2 mask3	2Strip2A Energy
112	2Strip2B Energy	2Strip2C Energy	2 Cmn Mode2	2ASIC3 mask0	2ASIC3 mask1	2ASIC3 mask2	2ASIC1 mask3	2Strip3A Energy
120	2Strip3B Energy	2Strip3C Energy	2 Cmn Mode3	Detector 3 Time	3ASIC0 mask0	3ASIC0 mask1	3ASIC0 mask2	3ASIC0 mask3
128	3Strip0A Energy	3Strip0B Energy	3Strip0C Energy	3 Cmn Mode0	3ASIC1 mask0	3ASIC1 mask1	3ASIC1 mask2	3ASIC1 mask3
136	3Strip1A Energy	3Strip1B Energy	3Strip1C Energy	3 Cmn Mode1	3ASIC2 mask0	3ASIC2 mask1	3ASIC2 mask2	3ASIC2 mask3
144	3Strip2A Energy	3Strip2B Energy	3Strip2C Energy	3 Cmn Mode2	3ASIC3 mask0	3ASIC3 mask1	3ASIC3 mask2	3ASIC1 mask3
152	3Strip3A Energy	3Strip3B Energy	3Strip3C Energy	3 Cmn Mode3	Detector 4 Time	4ASIC0 mask0	4ASIC0 mask1	4ASIC0 mask2
160	4ASIC0 mask3	4Strip0A Energy	4Strip0B Energy	4Strip0C Energy	4 Cmn Mode0	4ASIC1 mask0	4ASIC1 mask1	4ASIC1 mask2
168	4ASIC1 mask3	4Strip1A Energy	4Strip1B Energy	4Strip1C Energy	4 Cmn Mode1	4ASIC2 mask0	4ASIC2 mask1	4ASIC2 mask2
176	4ASIC2 mask3	4Strip2A Energy	4Strip2B Energy	4Strip2C Energy	4 Cmn Mode2	4ASIC3 mask0	4ASIC3 mask1	4ASIC3 mask2
184	4ASIC1 mask3	4Strip3A Energy	4Strip3B Energy	4Strip3C Energy	4 Cmn Mode3	Detector 5 Time	5ASIC0 mask0	5ASIC0 mask1
192	5ASIC0 mask2	5ASIC0 mask3	5Strip0A Energy	5Strip0B Energy	5Strip0C Energy	5 Cmn Mode0	5ASIC1 mask0	5ASIC1 mask1
200	5ASIC1 mask2	5ASIC1 mask3	5Strip1A Energy	5Strip1B Energy	5Strip1C Energy	5 Cmn Mode1	5ASIC2 mask0	5ASIC2 mask1
208	5ASIC2 mask2	5ASIC2 mask3	5Strip2A Energy	5Strip2B Energy	5Strip2C Energy	5 Cmn Mode2	5ASIC3 mask0	5ASIC3 mask1
216	5ASIC3 mask2	5ASIC1 mask3	5Strip3A Energy	5Strip3B Energy	5Strip3C Energy	5 Cmn Mode3	Detector 6 Time	6ASIC0 mask0
224	6ASIC0 mask1	6ASIC0 mask2	6ASIC0 mask3	6Strip0A Energy	6Strip0B Energy	6Strip0C Energy	6 Cmn Mode0	6ASIC1 mask0
232	6ASIC1 mask1	6ASIC1 mask2	6ASIC1 mask3	6Strip1A Energy	6Strip1B Energy	6Strip1C Energy	6 Cmn Mode1	6ASIC2 mask0
240	6ASIC2 mask1	6ASIC2 mask2	6ASIC2 mask3	6Strip2A Energy	6Strip2B Energy	6Strip2C Energy	6 Cmn Mode2	6ASIC3 mask0
248	6ASIC3 mask1	6ASIC3 mask2	6ASIC1 mask3	6Strip3A Energy	6Strip3B Energy	6Strip3C Energy	6 Cmn Mode3	CHECKSUM

Figure 8.15: The 256-word formatter data packet for *FOXSI*. The first three rows (light green) contain sync, time, and housekeeping information. This is followed by detector-specific information, shown here in colored blocks. Each detector section includes the trigger time (if any) followed by a 4-word hit channel mask, 3-strip data (10 bits + 6 bits addressing), and the common mode value for each of the four ASICs per detector. The text at the bottom describes the encoding of temperature and voltage information in the housekeeping data.

$\sim -30$  degrees by a cooler that circulates cold nitrogen through a channel in the focal plane. At launch, the cooling supply was disconnected. Thermal modeling predicted a rise in temperature of  $< 2$  degrees during the flight; data from thermal vacuum tests will be discussed in section 8.3.7.

To thermally isolate the detectors and thermal mass from the rest of the payload, the focal plane is blanketed in a double layer of Basotect foam covered with aluminized mylar. Fiberglass standoffs connect the focal plane to the payload structure. Slots in the blanket layers allow the passage of flexible circuits from the detector boards to outside electronics. The electronics board are stacked in the following order: (1) an “FPGA board” with one FPGA for each detector, with a connector for the optional USB readout; (2) the formatter board with a single FPGA that formats all detector data into a telemetry frame; and (3) a power board to generate the needed analog and digital voltages from an external 28V power supply.

Aluminum attenuators are mounted on a spring-loaded fixture and could be inserted in front of six of the seven detectors by issuing a command to the formatter. These attenuators could be activated in case of excessively high count rates (and were not used during the flight). To simplify design, de-insertion during flight is not possible. Figure 8.13 shows a model of the attenuator mechanism.

### Cooling accident

In February of 2012, the *FOXSI* payload was brought to the White Sands Missile Range for alignment, integration, and a launch attempt. Approximately three weeks before launch, a cooler malfunction cooled the seven flight detectors down to liquid nitrogen temperatures in  $\sim 10$ – $15$  minutes. This accident proved destructive to many of the readout ASICs on the detector boards, as differential thermal expansion produced cracks in the ASICs (see Figure 8.16). Several of the detector boards had three ASICs still functional. If an n-side ASIC fails, imaging data is lost for half of the detector, while if a p-side ASIC fails, both imaging and spectra are lost for one half. It was also unknown whether the ASIC cracks would become worse with the vibration of the rocket launch. With these doubts, and without a full set of backup detectors, the decision was made to postpone *FOXSI*'s launch and rebuild the system.

The ISAS team provided extra sets of remaining detectors and ASICs, and the summer of 2012 was spent epoxying and wirebonding the detectors and ASICs and testing/calibrating two new sets of detectors (a flight set and a backup set). Since not enough ASICs were left to construct 14 new boards, four detector boards were produced with a different, but similar, iteration of the ASIC known as the VATA 450.2. This ASIC is optimized for a higher energy range than *FOXSI* but still performs reasonably well in the 5–15 keV range. However, all seven detectors in the flight set use the original ASIC (the VATA451). The calibration results presented in this chapter are those from the summer 2012 detector sets; results from the earlier, broken, set of detectors is not included. An exception is made for two detectors (#15 and #28) that showed no ill effects after the cooling accident. These

detectors were recalibrated and found to have good performance, and were thus included as backup detectors for the next launch attempt.

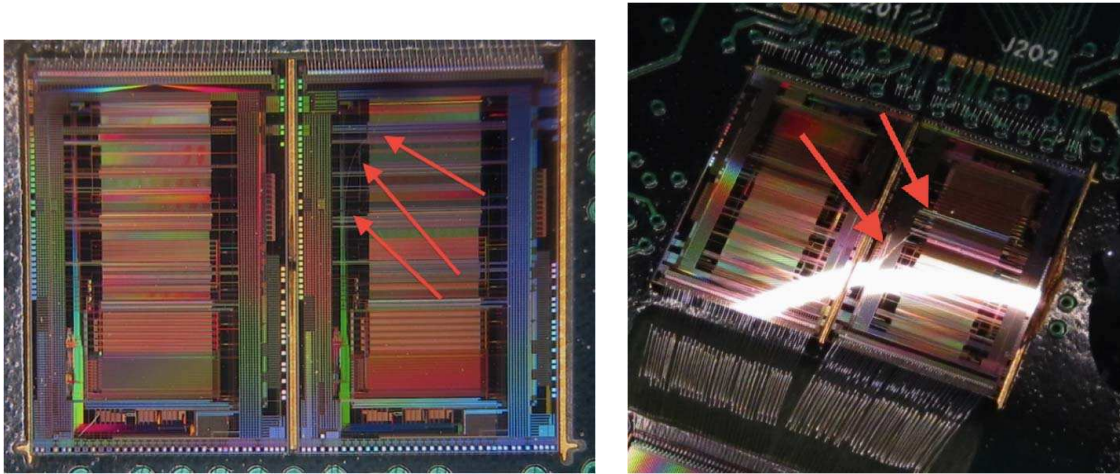


Figure 8.16: Photographs of selected ASICs with visible fractures after the cooling accident. Differential thermal expansion cracked the chips, rendering them inoperable.

## 8.3 *FOXSI* detector testing and calibration

Although testing of a prototype detector system had previously been conducted at ISAS (see section 8.2.3), the detectors needed to be tested in the readout system and mechanical assembly that would be used during flight, and each detector needed to be fully characterized individually. Since preliminary tests had found that a bias voltage of 200V was sufficient to fully deplete the detector, this value was chosen for the bias voltage during flight. All detector testing at SSL was conducted by Dr. Shin-nosuke Ishikawa and myself.

### 8.3.1 Experimental setup

A total of 14 detectors were calibrated in two sets of seven. For each set, seven detectors were installed in the flight focal plane. The focal plane was blanketed with double layers of Basotect foam and aluminized mylar as if for flight, in order to maintain a cold internal temperature. An external 28V power supply was used to power the detectors and electronics boards; during flight, this power will be supplied by an onboard battery.

Cooling during detector calibration was accomplished by the same system that will be used during the flight: a Sigma Systems Programmable Cryogenic Cooling System. The cooler contains a solenoid valve that controls coolant (liquid nitrogen) flow, feedback temperature sensors, and a digital display box for entering commands. The cooler can also

be controlled by a remote computer via an RS-232 interface. Liquid nitrogen was supplied to the cooler from a nearby dewar. A hose from the cooler attached to a nozzle on the focal plane, allowing cold nitrogen to enter a central channel in the focal plane and cool the entire thermal mass. Early testing found a large temperature gradient between detector boards during initial cooling, with the detector located closest to the nitrogen inlet reaching temperatures up to 15 degrees below those of the other detectors. An insulated inner tube was added to the entrance channel to reduce the temperature differential to  $\sim 10$  degrees, a differential that resolves within a few minutes as the system equalizes. Each of the tests described here was performed with the focal plane at a temperature of  $-25 \pm 5$  degrees Celsius.

Two modes of operation were used for calibration. In one mode, the ASICs were triggered after a fixed period of time and all strips were read out. This mode was useful for taking pedestal data with no source present. In the second mode (flight mode), data is collected from the detectors only after an ASIC trigger, indicating a detector signal above the threshold.

### 8.3.2 Noisy strips

The first calibration step was to identify noisy detector strips. Data were taken in the absence of an X-ray source by allowing the strips to trigger on noise. Strips with the highest-value data were then disabled. This process was repeated until no noise triggers were observed over a 10-second interval. Typically, the one or two strips nearest the edge of the detector were noisy, most likely due to nonuniform field effects. Since the n-sides of the detectors have higher trigger noise (as well as poorer energy resolution), all n-side triggers are normally disabled and events are triggered on the p-side only. Based on these results, it was determined that disabling 4 edge strips (2 on either side of the p-side) is sufficient for suppressing noisy triggers during flight. This setting was hard-coded into the FPGA code. If additional strips were to appear noisy during flight, an uplink command could be sent to disable these strips and/or raise the threshold value for that ASIC. (These functions turned out to not be necessary during the flight.)

### 8.3.3 Gain calibration

Next, to determine the gain for each strip, data were taken using three radioactive isotopes: Am-241, Ba-133, and Fe-55. Significant X-ray lines and sample activities are shown in Table 8.3. The locations of these peaks were identified in the detector ADC histograms as reference points, and a spline function was fit to these points to determine the ADC value to energy conversion function for every strip. Figures 8.17 and figure 8.18 show examples of raw ADC histograms and calibrated energy spectra for one detector. The FWHM of the calibrated 13.9 keV Am-241 line was measured for each ASIC of each detector; this is the number quoted as the energy resolution for *FOXSI*. A histogram of this value for all the

---

Isotope	Activity	Prominent lines	Minimum X-ray events collected
Fe-55	3.1 $\mu$ Ci	5.89 keV (Mn $K\alpha$ )	20,000
Ba-133	21 $\mu$ Ci	30.62, 30.97 keV (Cs $K\alpha$ ) 34.92, 34.98 keV (Cs $K\beta$ )	100,000
Am-241	1.0 mCi	13.76, 13.95 keV (Np $L\alpha$ ) 17.75, 17.99 keV (Np $L\beta$ ) 20.78 keV (Np $L\gamma$ ) 59.54 keV (Am $\gamma$ )	200,000

---

Table 8.3: Information on the radioactive sources used for gain calibration. The activity, prominent lines, and approximate number of X-ray events collected for each detector is shown. Closely spaced lines are not resolved; a weighted peak was measured.

VATA451 ASICs measured is in Figure 8.19. A breakdown of calibration results by detector is in Appendix B.

### 8.3.4 Low-energy efficiency

For most energies, the efficiency of the detector can be obtained by considering the photoabsorption of X-rays by a 500  $\mu$ m thick silicon wafer (see Figure 8.9). However, the efficiency of the system near its low energy threshold is influenced by the energy resolution of the VATA451 fast shaper. The low-energy cutoff is determined by the gain setting and resolution of the fast shaper, which is followed by a discriminator. Due to uncertainty in the fast shaper, photons of energy less than the nominal discriminator level may sometimes trigger the system, and occasionally photons of energy greater than the nominal value might fail to cause a trigger. The gain of the trigger as a function of energy  $\epsilon$  is an error function with width  $\sigma$  centered around the mean threshold energy  $\epsilon_{thr}$ :

$$\text{Efficiency} = \text{erf} \left( \frac{\epsilon - \epsilon_{thr}}{\sqrt{2}\sigma} \right) \quad (8.16)$$

To measure this function, a procedure from Saito (2011) was used. The threshold value is adjustable via a parameter in the ASIC control register. Data from an Fe-55 source were taken for many threshold values. Fe-55 decays to Mn, which has a  $K\alpha$  line at 5.90 keV. The count rate in this line decreases as the threshold value is raised as efficiency is lost at the line energy. Figure 8.20 shows an example of the 5.9 keV line count rate for different values of the threshold parameter. A complementary error function was fit to this data determining

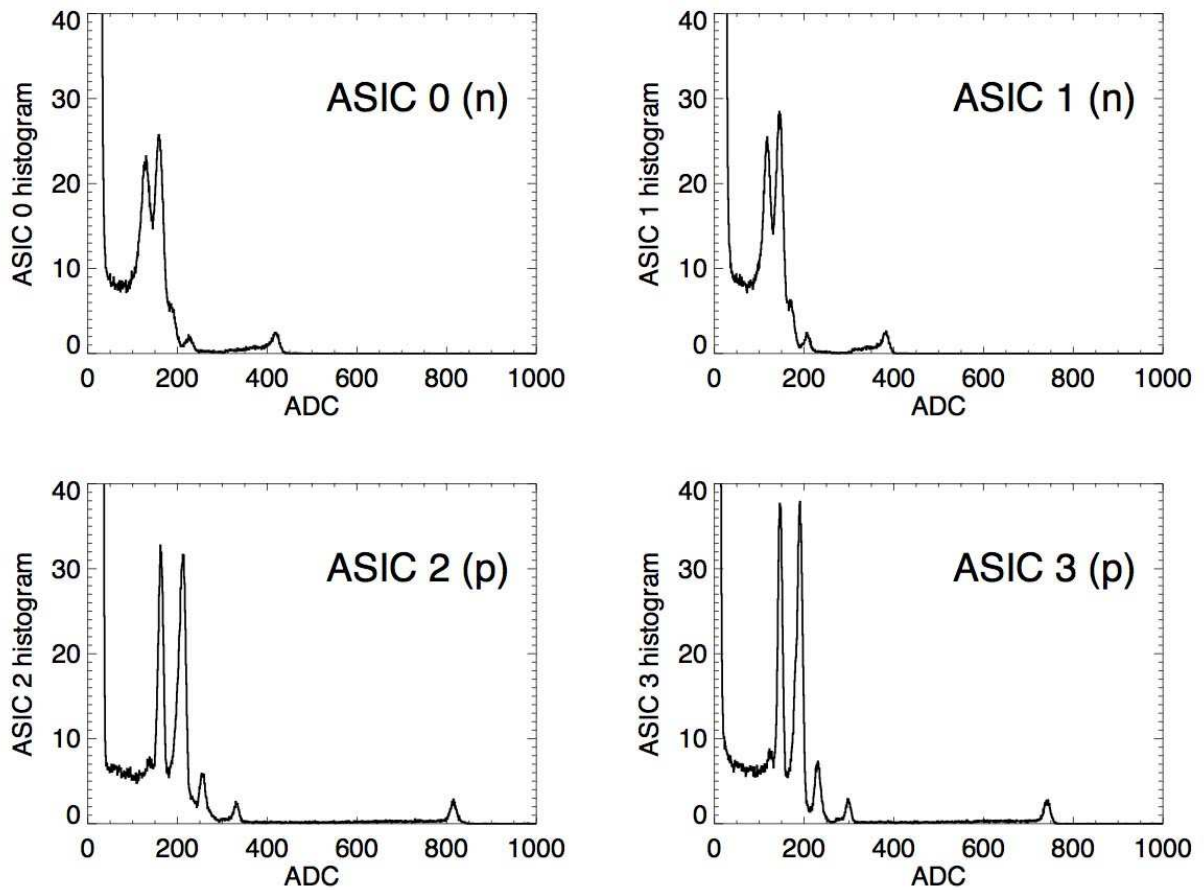


Figure 8.17: Uncalibrated Am-241 spectra taken with detector 101, in raw ADC values with the common-mode values subtracted. Spectra for each ASIC is shown; the relatively poor performance of the n-side as compared to the p-side is evident.

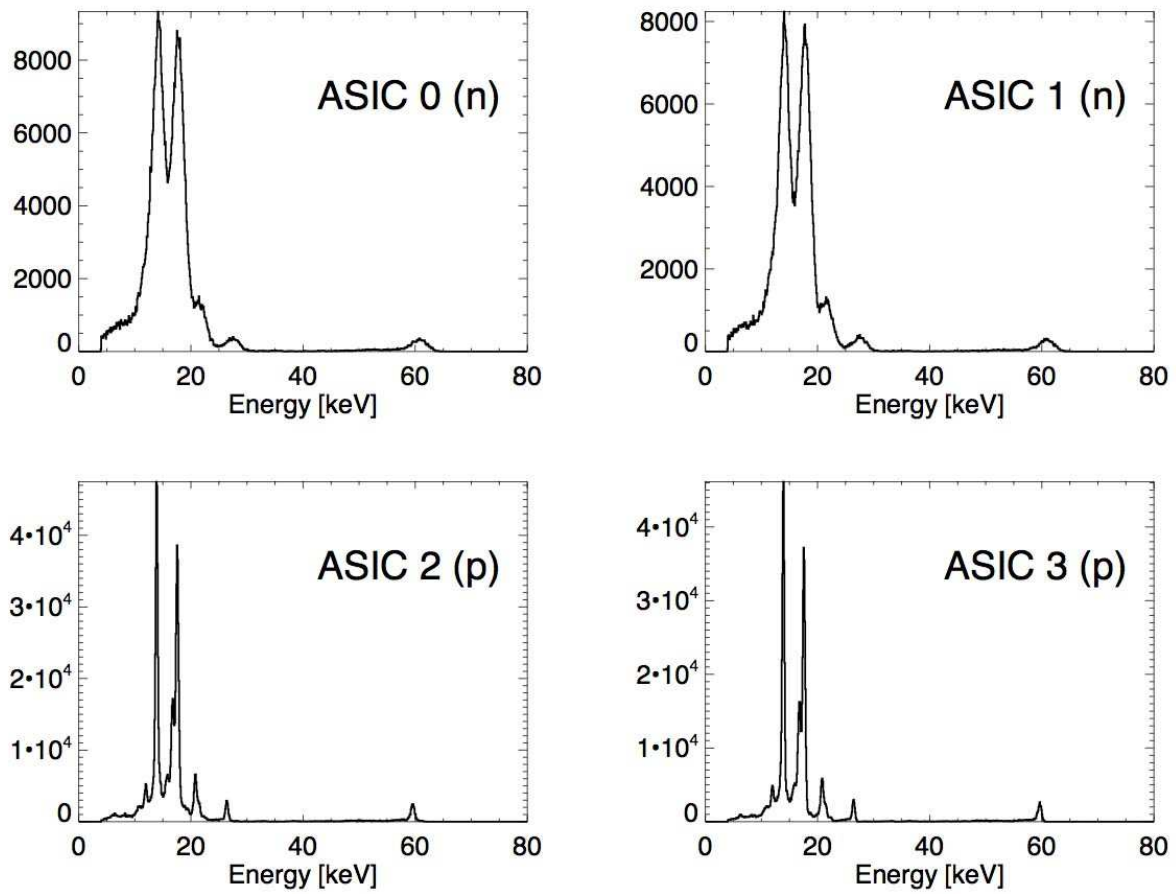


Figure 8.18: Calibrated Am-241 spectra for all ASICs of detector 101.

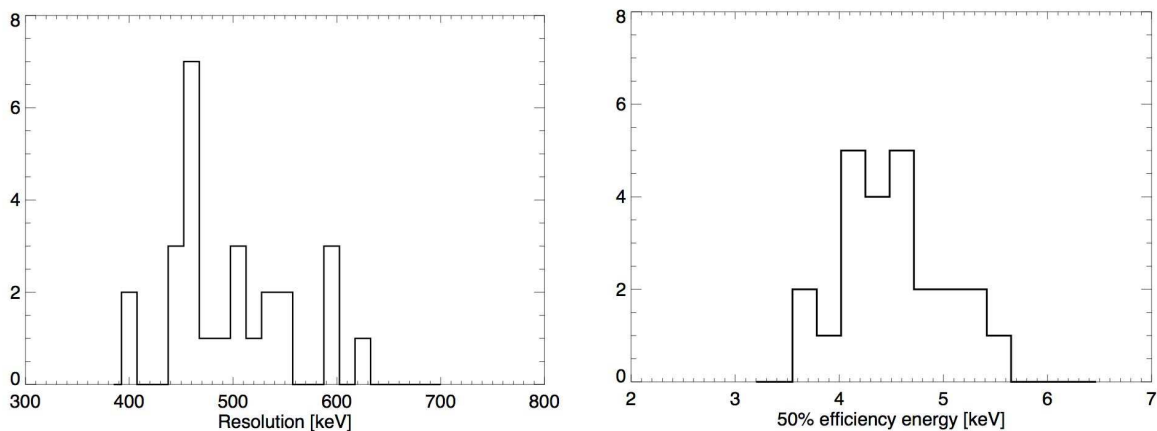


Figure 8.19: Histograms of (left) the energy resolution at the 13.9 keV Am-241 line and (right) the threshold energy at which the system is 50% efficient for all detectors with the *FOXSI* VATA451 ASIC. The values were measured separately for each p-side ASIC. Some detectors were read out with a different iteration of this ASIC, the VATA450; these detectors were not used for flight and are not included in this histogram.

the overall normalization (meaningless for our purposes), the mean value  $\epsilon_{thr}$  (which also sets the calibration of the threshold value in the ASIC control register), and the width  $\sigma$  of the threshold. The bottom panel of Figure 8.20 shows the efficiency determined by the fit to the count rates in the upper panel. An efficiency curve averaged over all the p-side ASICs of the flight detectors was shown earlier in Figure 8.9. Appendix B includes efficiency curves for all the detectors tested, and a histogram of the energy at which 50% efficiency is attained is shown in Figure 8.19.

### 8.3.5 Imaging tests

To test the imaging capability of the detectors, a qualitative test was performed. A mask was placed 1 inch in front of each detector, containing a pattern of fine wires forming a letter ‘F’ and two lines. An Am-241 source (chosen for its high intensity) was placed  $\sim 6$  inches in front of the mask so that much of the source flux was absorbed by the wires, producing an easily recognizable image on the detector. This image was used as an aid in reconstructing the geometry of the detector. An example is shown in Figure 8.21. This test was not performed for the new sets of detectors built after the cooling accident as it was deemed unnecessary since the geometry was already known.

During the X-ray alignment of the *FOXSI* optics and detectors, focused images of the X-ray beam were produced, which serve as an additional imaging test. The process was described in Section 7.4.5 and images are shown in Appendix A.

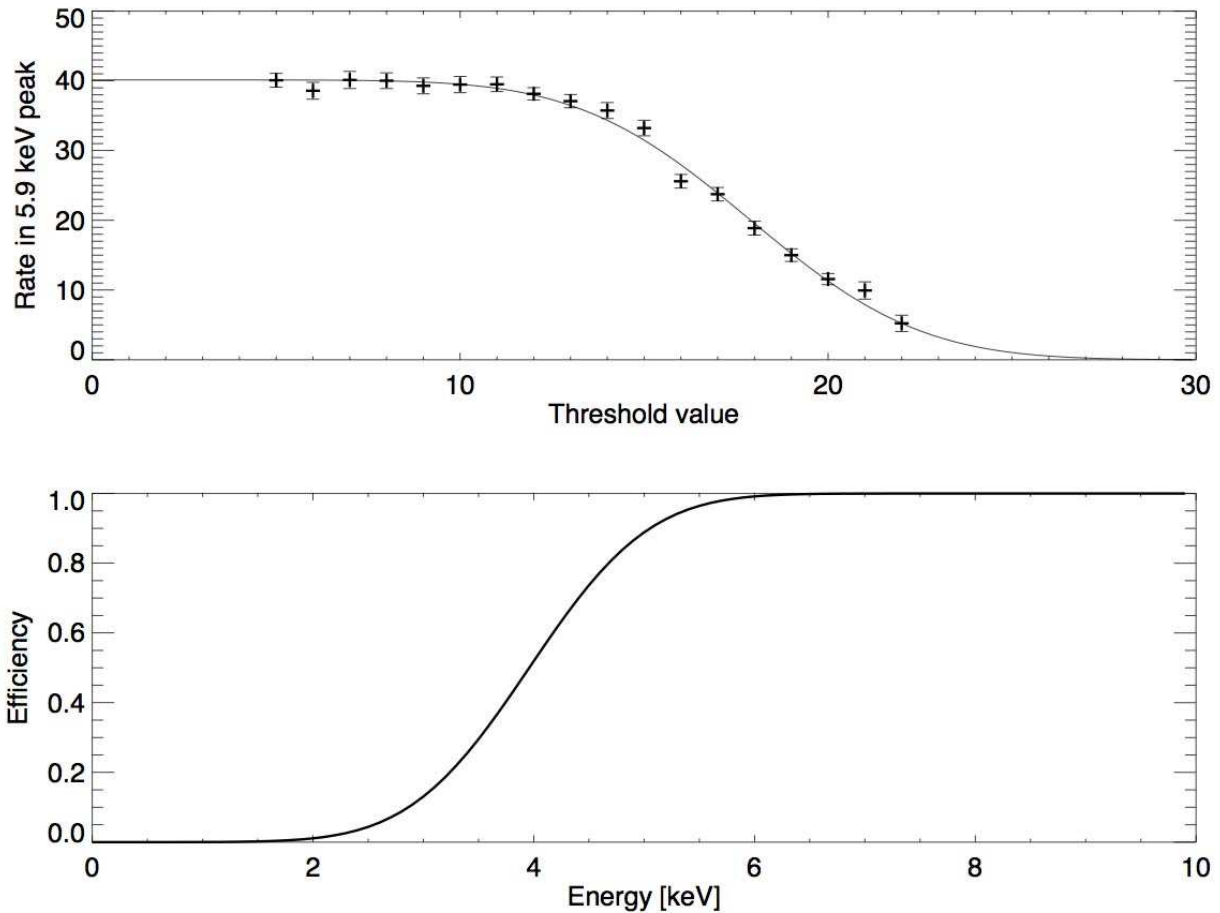


Figure 8.20: Example of the measurement of the detector efficiency near the low energy threshold. (Top) Measured count rates in the Fe-55 5.9 keV peak, with the best fit curve overplotted. Error bars are statistical uncertainties. (Bottom) The corresponding efficiency for a threshold value of 12; this is the value chosen for flight. This measurement is for one p-side ASIC of detector 101.

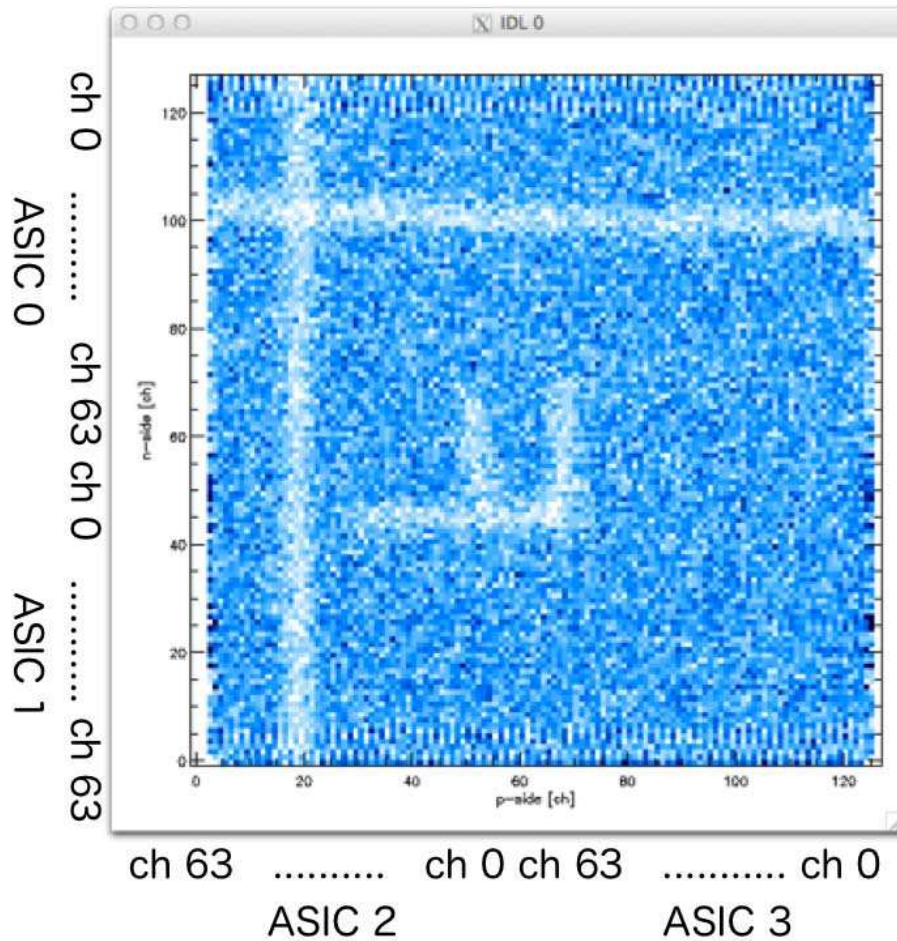


Figure 8.21: An image test for one of the first *FOXSI* detectors tested at SSL. The mask ('F' plus two lines) made by fine lines of solder is clearly visible. At the top and bottom of the image a checkered pattern indicates the locations of wirebonding pads, which alter the collection properties of the underlying detector volume (Ishikawa et al. 2011).

### 8.3.6 Livetime measurement

In order to reconstruct accurate photon fluxes, it is necessary to know the livetime of the system. This is accomplished by recording trigger times in the data packet. The formatter provides each detector FPGA with a 16-bit clock counter that counts at 10 MHz. When a trigger is received from an ASIC, the FPGA latches the next clock counter value so that there is 100 ns precision in the trigger time. This trigger time is recorded in the data frame preceding each detector data section. The clock counter value is also checked and recorded at the beginning of each formatter data frame. By comparing the detector trigger time with the formatter time *of the previous frame*, the livetime for that acquisition can be calculated. The formatter sequentially interrogates each detector for its data. A detector does not accept triggers while data is being delivered to the formatter (approximately 1/7 of the observing time). A detector becomes live (ready for acquisition) immediately after delivering its last data word and remains live until a trigger is received or the next interrogation by the formatter, whichever comes first. It should be noted that detector triggers are independent of each other, and the seven detector livetimes are out of phase due to the sequential readout by the formatter. During data analysis, if no trigger was recorded for a given data frame, 6/7 of the frame time is added onto the livetime for the next acquisition (since the detector is always dead for 1/7 of a frame time).

#### Pseudo-trigger measurement

The livetime counter performance was tested using a “pseudo-trigger” system, which is FPGA logic that supplies false triggers with pseudorandom timing that average a given rate. The rate is adjustable within a certain range from the DAQ computer. The system is based on that used by Saito (2011). The pseudotrigger system was used during lab testing only and is not used during flight.

Several 30- to 60-second data runs were taken with various pseudotrigger rates. A pseudotrigger counter is inserted in the formatter data packet so that the actual trigger rate can be determined. For each data set the actual pseudotrigger rate, a raw measured rate with no livetime correction, and the measured rate determined from the livetime distribution were recorded. As discussed in section 8.1.7, a histogram of livetime  $t$  for a trigger rate  $R$  should follow a distribution proportional to  $e^{-Rt}$ . The rate  $R$  was determined by a linear fit to a natural log plot of the livetime distribution. An example of a livetime distribution for one pseudotrigger rate with the best exponential fit overlaid is shown in the left panel of Figure 8.22. Results for various pseudotrigger rates are shown in the right panel. The calculated trigger rate matches the actual pseudotrigger rate to within the error bars (from the exponential fit) for all but one of the data points, indicating that the livetime counting system is functioning correctly. Figure 8.22 also shows the raw count rates recorded in the detector with no livetime correction. At extremely low count rates the raw rates are close to the actual rates, but there is always a minimum deadtime of 14.3% (1/7) of the collecting time while the data is delivered to the formatter.

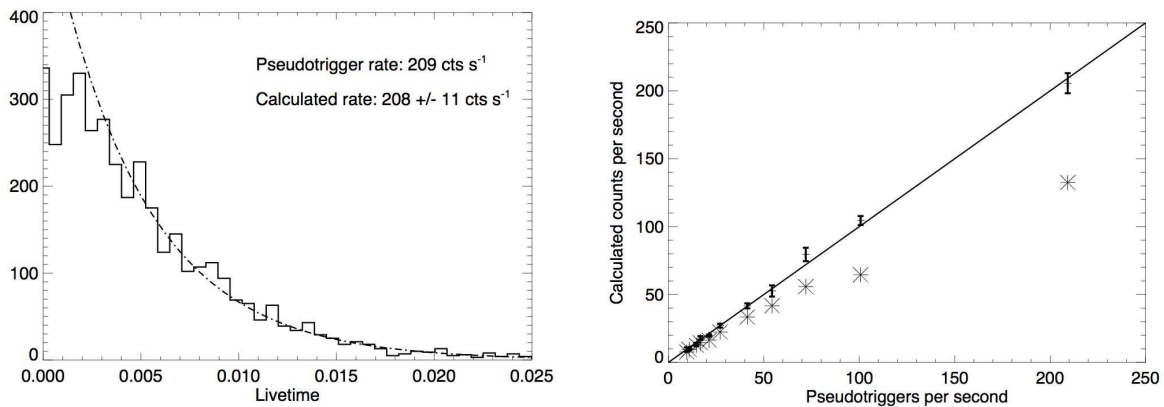


Figure 8.22: (Left) Example of an exponential fit to a distribution of measured livetimes (on an arbitrary y-axis scale). The pseudotrigger rate for this data run (as measured by a counter inserted in the data packet) is 209 counts per second. (Right) Results of pseudotrigger testing of the livetime system. Stars show raw measured count rates with no livetime correction; data points with error bars are the rates determined by fitting exponential curves to the livetime distribution; error bars are those from the fit. Each pseudotrigger rate was tested for 30–60 seconds.

### X-ray flux measurements

As discussed in section 7.4.5, X-ray alignment checks were done prior to launch at White Sands using an X-ray generator set at 30 kV and  $< 4$  mA. While preparing the X-ray generator for the alignment check, the current was slowly raised to the nominal setpoint and measurements were taken (from the detector on which the X-ray generator was trained at the time) in order to check the livetime calculation. The relationship between the X-ray rate and generator current is not well calibrated but should be linear, though not necessarily proportional (because the generator produces small but nonzero flux in the absence of an applied current). Count rates at the detector were determined by fitting the measured livetimes in the same way as for the pseudotrigger trigger rate measurements discussed previously; results are shown in Figure 8.23.

#### 8.3.7 Thermal vacuum tests

Prototype tests at ISAS determined that the detector resolution and low energy threshold are not significantly affected by temperature variations as long as the temperature remains below  $\sim -10^{\circ}\text{C}$  (Saito et al. 2010). As discussed in section 8.2.4, the rocket carries no onboard cooling system. The detectors are cooled prior to launch and are dependent on the thermal mass of the focal plane to stay cold.

During a rocket flight the payload spends most of its time in a varying, low-pressure en-

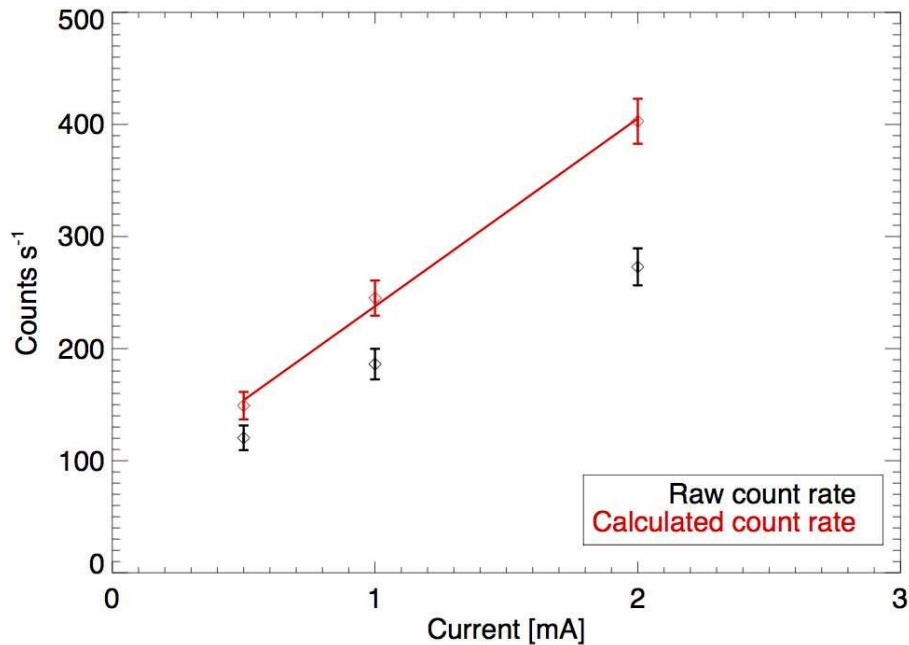


Figure 8.23: Count rates measured from an X-ray generator 20 meters in front of the payload, with X-rays focused by the optics onto detector 6. Black data points are the raw measured count rates, with no livetime correction. Red data points are the rates reconstructed by fitting the livetime distribution. The red line shows a linear fit to the data.

vironment, so payload electronics are not able to effectively transfer away heat convectively. Therefore, thermal vacuum tests were necessary in order to test that (1) the detectors remained below  $-10^{\circ}\text{C}$ , and (2) the electronics outside the focal plane did not heat up during flight (*or* cool down during pre-flight cooling) outside their specified operating ranges. These tests were done in the SSL Snout1 vacuum chamber in November 2011. Thermistors were epoxied to seven detector boards, which were installed in the focal plane and insulated as if for flight. One nonfunctional detector was included and a thermistor was epoxied directly to this detector (labeled detector 2 in the test results). Additional thermistors were placed on the FPGA board, formatter board, an oscillator and the FPGA on the formatter board, and a prototype power board (since the flight power board was not yet available). With all boards connected, the current drawn on the 28V bench power supply was  $\sim 0.6\text{A}$ .

To prepare for the test, the detectors were cooled down to  $< -25^{\circ}\text{C}$  with the vacuum chamber door open, using the Sigma cooler/controller. To simulate the rocket launch, the coolant hose was quickly disconnected from the focal plane, the vacuum chamber door closed, and the chamber pump turned on within a few seconds. The chamber was pumped down as quickly as possible, reaching  $< 1$  Torr in about 5 minutes and  $< 0.001$  Torr in about 10 minutes. Thermistor readings indicated that the detector board temperatures did not rise

more than  $7^{\circ}\text{C}$  in the 21 minutes for which the test is run. (Note that this is longer than the ascent plus observation time of the rocket; the test was run long because we cannot closely replicate the pressure environment of the rocket as it ascends.)

A second test was conducted with a heated canopy (“heat shroud”) at  $65\text{--}70^{\circ}\text{C}$  partially surrounding the electronics assembly to simulate the hot rocket skin. Temperature data from this test are shown in Figure 8.24. The cooling system was disconnected at approximately time  $t=73$  minutes. At this time detector board temperatures ranged from  $-38$  to  $-33^{\circ}\text{C}$ . The temperature differences between detectors were due to their locations in the focal plane; those detectors (1 and 7) located closest to the cooling inlet tend to reach colder temperatures than the others during cooldown. As discussed in section 8.2.4, insulating tubing was later added to the focal plane in order to reduce this temperature difference, which also disappears after an appropriate equilibrating time. The test was conducted for approximately 30 minutes (again, much longer than the ascent plus observing time), during which time the detector board temperatures rose  $9\text{--}11^{\circ}\text{C}$ . An exception was detector 1, which rose  $16^{\circ}\text{C}$ . Being closest to the coolant inlet, this detector also heats up the fastest when the cooling hose is removed. None of the temperatures rose high enough that detector performance would be affected, so the thermal design was deemed sufficient. Figure 8.24 also shows temperatures during the test of the focal plane assembly itself (middle panel) and of the electronics boards located outside the blanketed focal plane (bottom panel). The electronics boards ranged from  $-5$  to  $20^{\circ}\text{C}$  with the exception of an oscillator on the formatter board and a metal plate that served as a heat sink for the electronics (both purple lines in the bottom panel).

## 8.4 Chapter summary

The detectors designed by the ISAS team proved sufficient to meet *FOXST*'s needs of good angular and spectral resolution as well as a low threshold. These qualities were attained using thin double-sided silicon strip detectors cooled to  $-25^{\circ}\text{C}$  and dedicated readout ASICs. For future missions requiring a higher energy range, a higher- $Z$  material such as CdTe is likely to be used.

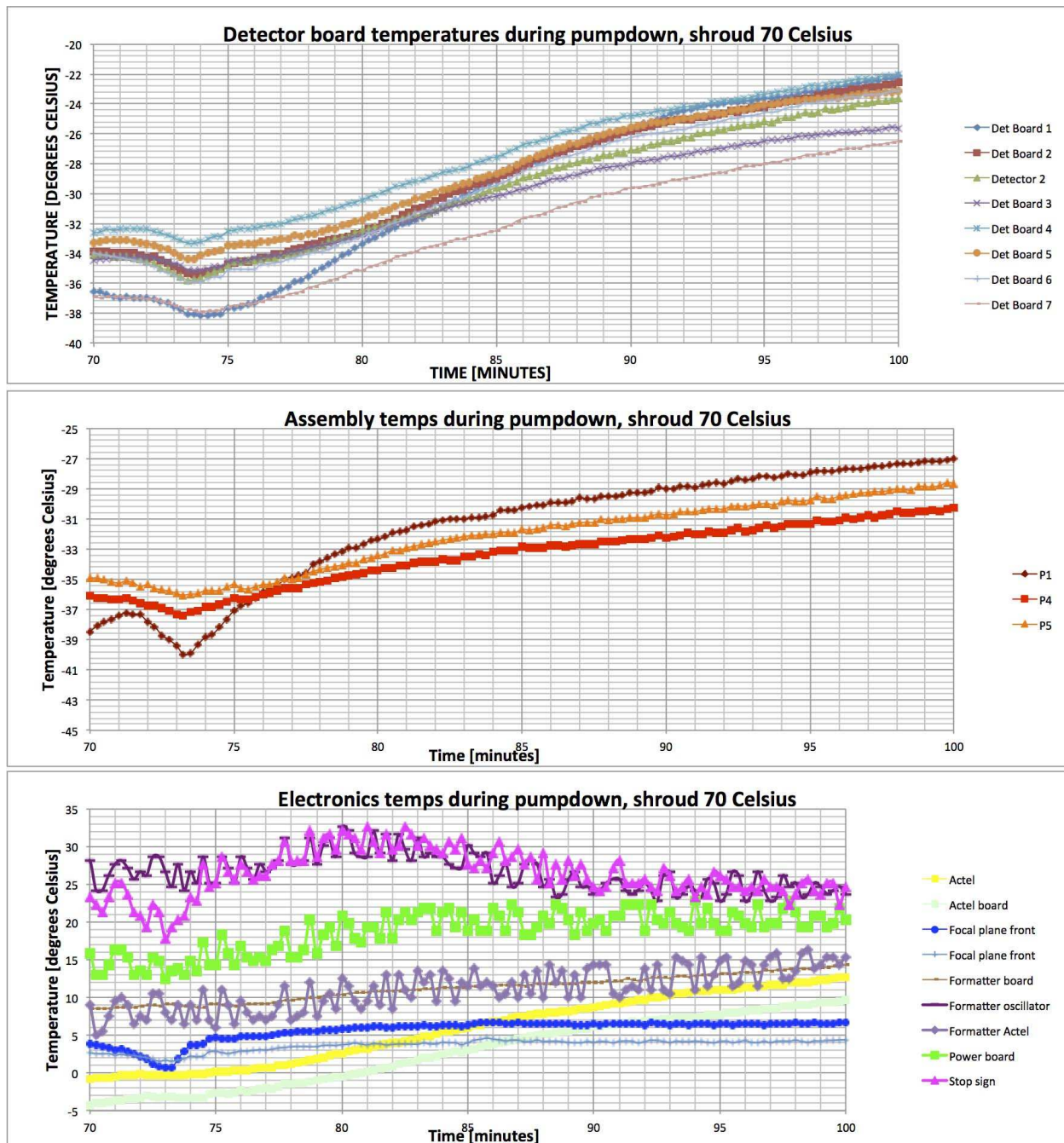


Figure 8.24: Results from one thermal vacuum test, with a 65–70°C heat shroud. (Top) Temperatures on the seven detector boards (and one detector itself). Detector 1 tends to reach the coldest temperatures and also heat up the fastest because of its location near the cooling inlet. (Middle) Temperatures from thermistors on the focal plane assembly itself. (Bottom) Temperatures on electronics boards located outside the blanketed focal plane. The hottest components are an oscillator on the formatter board and an aluminum plate serving as a heat sink for the electronics stack.

# Chapter 9

## FOXSI's first flight

### Abstract

The *FOXSI* sounding rocket payload was flown for the first time on November 2, 2012. In its 6.5-minute observation interval above 150 km *FOXSI* observed four targets on the Sun, including both the quiet Sun and active regions, with a field of view of  $\sim 16 \times 16$  arcmin<sup>2</sup>. Due to fortunate timing, a *GOES* class B2.7 microflare was observed simultaneously by *FOXSI* and *RHESSI*. The flight was a comprehensive success, with both hard X-ray images and spectra obtained. These observations constitute the first focused spectroscopic images of the Sun above 5 keV. This system will summarize the supporting systems on the payload and give a description of *FOXSI*'s flight, along with a preliminary presentation of *FOXSI* microflare data.

### 9.1 The *FOXSI* payload

#### 9.1.1 Experiment section

The *FOXSI* sounding rocket payload consists of a 22-inch-diameter segment housing the experiment (2.7 meters in length) and 17.26-inch-diameter segments for the other rocket systems. The mechanical structure of the experiment section of the payload was designed and built at SSL and centers around a 2-meter aluminum tube with the optics and detectors mounted on aluminum support structures at either end (Krucker et al. 2011b). See Figure 9.1 for a labeled diagram of the experiment section. The tube is attached to the rocket skin via a ring at the optics end; the rest of the experiment structure (including the detector end) is cantilevered from this point. Anchoring the experiment to the rocket skin at one end instead of two ensures that stresses across the rocket cannot produce a misalignment of the optics and detectors. The entire payload is wrapped in a multilayer insulating (MLI) blanket for thermal isolation from the hot rocket skin, which is expected to reach a temperature of

$\sim 150$  °C. After the rocket stages separate, a shutter door is revealed and then opens to expose the optics. The payload is rotated so that the optics end faces the Sun and then rotates back downward before landing.

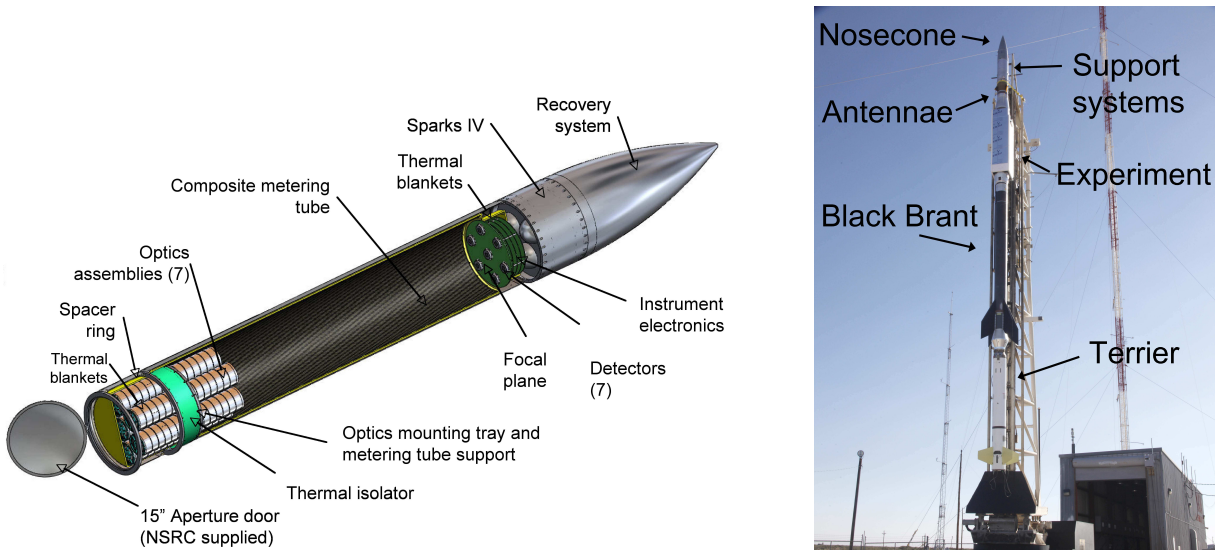


Figure 9.1: (Left) Schematic of the experimental section of the *FOXSI* payload. (Right) Photograph of the *FOXSI* rocket on the launch rail at White Sands. The experiment section is enclosed in a styrofoam box for temperature control. Non-flight equipment (liquid nitrogen, a cooling controller, and temperature sensor monitors) was located on the launch rail next to the experiment section. The two rocket stages include Black Brant and Terrier motors.

### 9.1.2 Other systems

The additional supporting systems of the payload are provided by the NASA Sounding Rocket Operations Contract (NSROC), a division of Orbital Sciences Corporation. The front of the rocket consists of a “nose cone” containing the payload recovery system (parachute). Electronics sections contain the battery for experiment power, two transmitters for telemetry data and one antenna for uplink commands. An S-19 guidance system is used for attitude control. Black Brant and Terrier stages were used as the rocket motors to achieve a flight apogee of  $\sim 300$  km. Shown in Figure 9.1 is a photograph of the rocket with some of these components labeled.

Payload pointing is performed by the Solar Pointing Attitude Rocket Control System (SPARCS). The system contains coarse, intermediate, and fine Sun sensors and uses a pneumatic system and ring laser gyros to maneuver. SPARCS can achieve pointing accuracy of within 30 arcseconds in pitch and yaw and  $\sim 1$  degree in roll with high stability (NASA/SRP 2005). To take advantage of this capability, a payload must be aligned to the SPARCS

(visible light) sensors, a difficult task for an X-ray instrument since solar X-rays cannot be measured on the ground. (If they were, then optical light and X-rays from the Sun could be used to illuminate the two systems at once, enabling them to be aligned.) For this flight the alignment was not optimal but deemed sufficient; improvements in the system will be made before the next launch.

To carry out the alignment, two mirrors were added to the optics plate. One mirror was permanently fixed to the optics plate but it was not possible to position it with the plane of the mirror precisely perpendicular to the optical axis. For this reason a second (removable and adjustable) mirror could be placed over the pinhole used for the payload X-ray alignment described in Section 7.4.5. The payload was first aligned so that the laser shining through the pinhole was centered on the photocell (used for the X-ray alignment). The removable mirror was then placed in front of the pinhole and adjusted so that the laser beam was reflected back to its source; no more adjustments to the mirror would be made after this. An autocollimator was then used to measure the angular offsets of both of these mirrors with respect to the reflective surface of the SPARCS fine sensor. Shims were added to this sensor to bring it in alignment (to  $<30$  arcseconds) with the removable mirror (and therefore with the optical axis of the experiment). The angular offset between the fine sensor and the fixed mirror was then measured so that the fixed mirror could be used as a reference for any changes in alignment during vibration. The co-alignment of the experiment with the SPARCS system is believed to be better than 2 arcminutes. This value was deemed sufficient due to *FOXSI*'s large field of view ( $16 \times 16$  arcmin<sup>2</sup>). For future flights, a more sophisticated alignment system will be built, probably incorporating an optical sensor and using the Sun as an alignment source.

## 9.2 Flight

*FOXSI* was launched from the White Sands Missile Range at 11:55 am MDT on November 2, 2012. The payload was launched at an 87 degree angle and reached an apogee of 331 km, with 393 seconds of observing time above 150 km (an altitude below which atmospheric absorption significantly attenuates X-rays in the *FOXSI* energy range). The instrument was recovered almost completely intact after the successful flight. Table 9.1 lists some of the key events during the flight.

### 9.2.1 Targeting

Five targets were preprogrammed into the SPARCS pointing control system, with the ability to choose between them and to make finer pointing adjustments mid-flight. The five targets covered almost the entire solar disk. In practice, only four of the targets were used; see Figure 9.2 for a map of these four targets.

- **Target 0** Southeastern quadrant, containing 2 active regions.

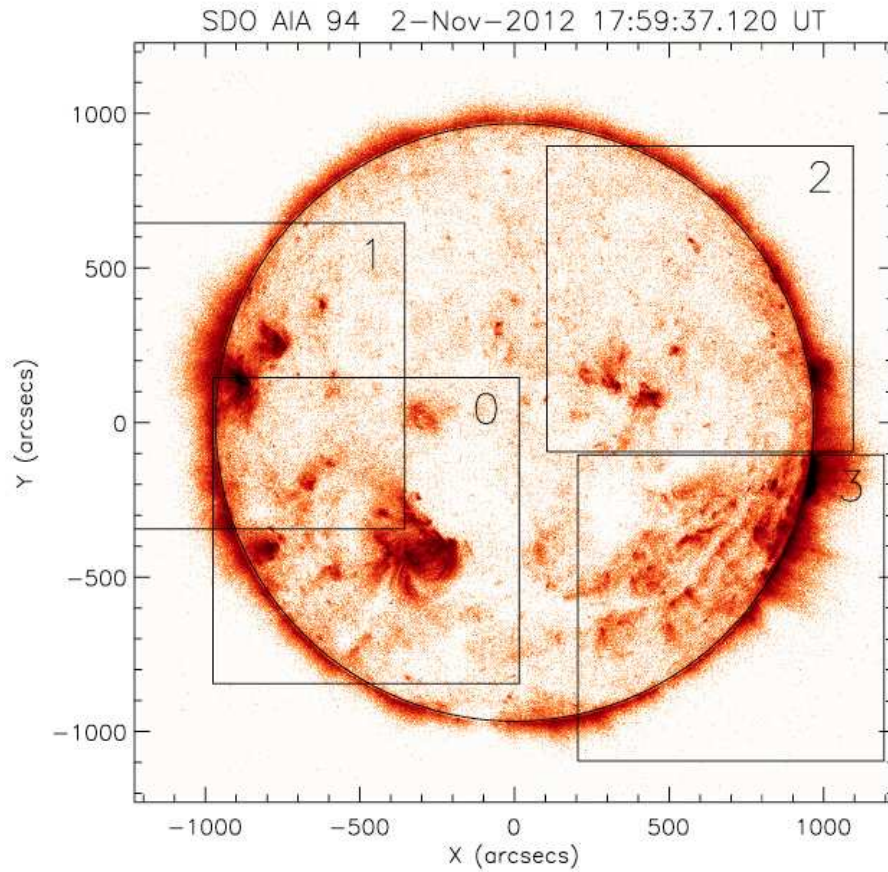


Figure 9.2: Map showing the four targets from the *FOXSI* observation, overlaid on a  $94\text{\AA}$  image from the Atmospheric Imaging Assembly (AIA) aboard the *Solar Dynamics Observatory*. Targets 0 and 1 contained active regions on the disk; target 2 contained only quiet-Sun regions, and target 3 contained an active region at the limb. The first three targets revealed extremely low count rates. A brighter source was found in the fourth target.

---

Event	Time (s)	Nominal altitude (km)
Launch (Terrier ignition)	0	0
Black Brant ignition	12.0	6.2
High voltage ramp up starts	30.0	20.3
Payload separation	64.0	88.2
Shutter door opens	67.0	94.5
High voltage reaches 200V	70.0	100
SPARCS fine mode begins / Observation window begins	107.0	170.4
Apogee	297.1	331.5
Shutter door closes / Observation window closes	500.0	147.6
Experiment powers off	565.0	15.8
Parachute deploys	696.8	4.9
Payload impact	1003.8	1.2

---

Table 9.1: Timeline of some of the key events during the *FOXSI* flight.

- **Target 1** Eastern limb, containing 1 active region.
- **Target 2** Northwestern quadrant, quiet Sun.
- **Target 3** Southwestern limb, containing 1 active region. This active region was just at the limb and produced a partially occulted microflare during the observation.

During the flight, the first three targets were observed for approximately one minute each and yielded small, unlocalized count rates ( $\sim 1\text{--}2$  counts  $\text{s}^{-1}$  detector $^{-1}$ ). Since this was not a distinguishable signal, in each case the decision was made among the science team to move on to the next target. The fourth target, in the southwest region of the disk, revealed a localized source (later discovered to be a microflare) with significantly higher rates (30–40 counts  $\text{s}^{-1}$  det $^{-1}$ ). The experiment remained targeted on this source for the remainder ( $\sim 150$  seconds) of the observation time.

### 9.2.2 Recovery and post-flight state of health

After atmospheric re-entry the payload descended via parachute and made a safe landing in the missile range. A crush bumper attached to the shutter door lessened the impact on the payload. The payload was recovered via helicopter.

Post-flight checkouts of the payload found it to be intact with one exception: one optics module had come displaced due to a failed epoxy joint. This displacement likely occurred during the vibration of the launch, as the image from this detector during the flight shows a poorer point spread function than the others, but probably worsened with the impact of landing, since post-flight X-ray alignment checks showed a drastically misaligned optic. X-ray alignment checks of all other modules showed results identical to pre-flight measurements.

### 9.3 Observations

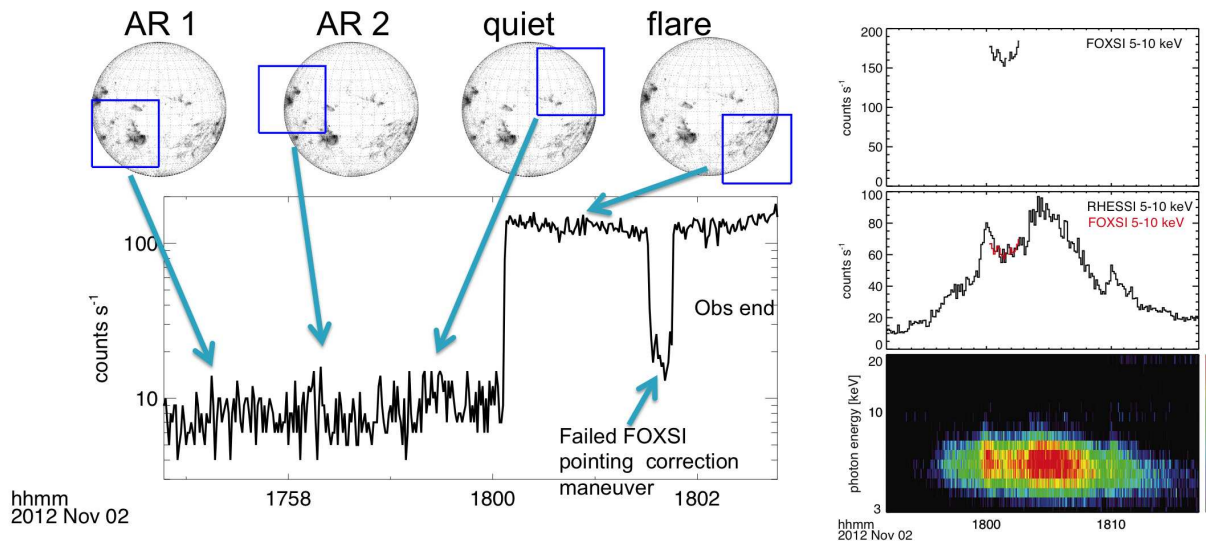


Figure 9.3: *FOXSI* count rate time profiles, integrated over energies 5–15 keV. (Left) *FOXSI* time profile for the 6.5-minute observation time, with the four successive targets approximately indicated. Little, if any, change in rates is observed among the various targets, until the microflare is observed just after 1800 UT. (Right) *FOXSI* and *RHESSI* count rates are compared for the B2.7 microflare. The top panel shows the *FOXSI* count rate over time. In the second panel, the same curve (now in red) is rescaled and overlaid on a *RHESSI* time profile (black). The bottom panel shows the *RHESSI* spectrogram. Comparing panels 1 and 2 shows that the *FOXSI* count rate was higher than that of *RHESSI*, which is expected for *FOXSI*'s superior sensitivity.

#### 9.3.1 Time profile

Figure 9.3 shows a time profile of the count rates (integrated over the entire energy range) observed by *FOXSI* during its six-minute observation. Prior to  $\sim 18:00$  UT, count

rates are very low. The jump in rates is due to the acquisition of Target 3 while the microflare was in progress. The dip in counts around 18:01:30 UT is due to a pointing maneuver that temporarily took the experiment off-target. This error was quickly rectified and the count rate restored. Around 18:03 UT the shutter door closed and the detector bias voltage began to ramp down, ending the observation interval.

The time profile shown in Figure 9.3 is integrated over all detectors. However, not all 7 detectors displayed similar behavior. Detector 3 collected drastically reduced rates as compared with the other detectors; it was this optic that became displaced during the flight and so the count rate is reduced due to lower efficiency from the off-axis optic. Detectors 0 and 2 also collected reduced rates, though not to such an extreme. An explanation for this phenomena could be the blockage of the optical path by optics blanketing. These blankets formed an inner layer within the experiment section and were fixed to the inside of the tube. It was noticed after the flight that the blankets were puffed out; insufficient venting paths had caused air to be trapped in the blankets and expand as the payload entered a low-pressure environment. Reduced efficiency due to blanket absorption could, in principle, affect fluxes measured by all the detectors, or by some of them. This may explain the reduced count rates in two of the detectors. Inspection of the spectra measured by the various detectors will reveal which of them suffered from absorption in the optical path as lower-energy X-rays should be selectively absorbed. Comparison with *RHESSI* will help to determine if all detectors were affected by this issue.

*FOXSI* count rates prior to  $\sim 1800$  UT do not show any easily recognizable signal, though the count rates are also not zero. Possible sources for the nonzero count rate are (1) background, (2) active region thermal flux, or (3) a quiet Sun signal. The strongest contributor cannot be an active region signal, because measured rates from the third target (in which no active region was included in the field of view) are not zero and may in fact be higher than the rates from the first two targets. A careful background analysis will be necessary in order to distinguish any quiet-Sun HXR signal from the background. It is clear that the simulated spectra in Figure 6.6 corresponding to high cutoff energies were not observed; however, a spectrum with a low cutoff energy ( $E_0 \lesssim 2$  keV) would be consistent with observed count rates of  $\sim 10$  counts  $s^{-1}$ .

On the right in Figure 9.3 the count rate profiles of the microflare as seen by *FOXSI* (top and middle panels) and *RHESSI* (middle and bottom panels) are compared. In the second panel, the *FOXSI* light curve has been renormalized to approximately match the scale of the *RHESSI* curve. A comparison of the top and middle panels shows that the *FOXSI* count rates were 2–3 times higher than *RHESSI*'s, which is expected for *FOXSI*'s better sensitivity. The *RHESSI* background rate in the *FOXSI* energy range was 20–30 counts  $s^{-1}$  on November 2. If the low rates observed in the first few minutes of *FOXSI*'s observations ( $\sim 10$  counts  $s^{-1}$ ) were indeed from the quiet Sun, the corresponding rate for *RHESSI* (3–5 counts  $s^{-1}$ ) would be indistinguishable from the background. This demonstrates *FOXSI*'s superior sensitivity for quiet-Sun measurements due to the decreased background of the thin strip detectors.

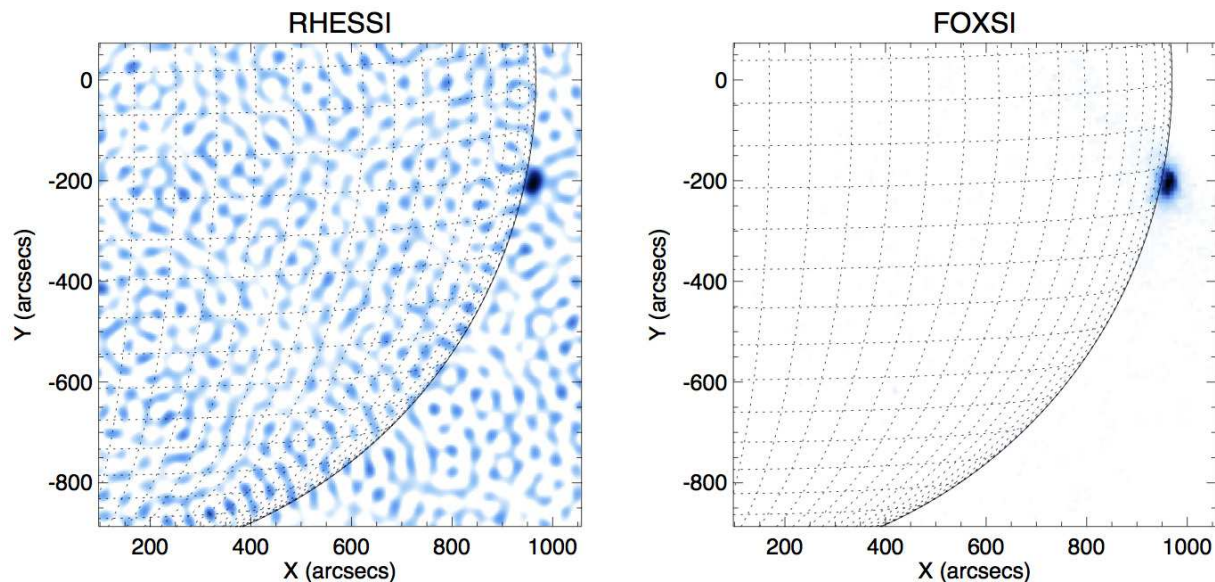


Figure 9.4: A comparison of (left) a *RHESSI* Clean image and (right) a *FOXSI* image of the B2.7 flare observing during *FOXSI*'s flight. Each image is scaled to the maximum intensity for that image. The *RHESSI* image shows artifacts that reduce the dynamic range of the instrument even far from the bright source. The *FOXSI* image is clean of such artifacts, enabling a much higher dynamic range.

### 9.3.2 Imaging

Figure 9.4 shows a comparison of a *RHESSI* Clean image of the microflare with a *FOXSI* image from one detector (detector 6). The large difference in dynamic range is apparent: the *RHESSI* image displays artifacts over the entire field of view, meaning that sources a few times fainter than the brightest source will not be distinguishable from the imaging artifacts. The *FOXSI* image displays none of these artifacts since it is a direct imager. In principle, *FOXSI*'s angular resolution (10 arcseconds) is poorer than *RHESSI*'s (2.3 arcseconds); however, the Clean *RHESSI* image shown is made using subcollimators 3–9, a common choice for *RHESSI* images, and thus has a resolution of  $\sim 10$  arcseconds FWHM. (See Chapter 3 for a description of *RHESSI*'s imaging system and its angular resolution.) In Figure 9.4, *FOXSI*'s pointing was corrected by coaligning the flare with *RHESSI*.

The source was offset by  $\sim 7$  arcmin from *FOXSI*'s optical axis, so the image is slightly distorted by the off-axis response. During the optics calibration, the FWHM of the point spread function (optics only, not including the detector resolution) was measured to be  $\sim 7$  arcsec when the source was on-axis (see Section 7.4). The measurement was repeated for an off-axis angle of 10 arcmin and the FWHM was found to be  $\sim 12$  arcsec in the radial direction and  $\sim 6$  arcsec in the radial direction (where radial and azimuthal distances are measured

with respect to the center of the field of view). If the FWHM varies linearly between source offsets of 0 and 10 arcmin (a conservative scenario), then the worst-case optics resolution at 7 arcmin off-axis is  $\sim 10.5$  arcsec in the azimuthal direction, or  $\sim 13$  arcsec including the detector angular resolution in quadrature. Deconvolution of the source structure and the point spread function of the optics will produce a more accurate image.

### 9.3.3 Spectra

Figure 9.5 shows spectra of the microflare from *FOXSI* (left) and *RHESSI* (right). Spectral fitting performed above 5 keV on the *RHESSI* data determined that the microflare had a temperature of 9 MK, which was cooler than most microflares in the statistical study of Hannah et al. (2008). The emission measure was  $5 \times 10^{46} \text{ cm}^{-3}$ , slightly brighter than most microflares. It should be noted that the spectra shown in 9.5 are count spectra from different instruments and should not be directly compared. Once the *FOXSI* response (including the effect of the attenuation by thermal blankets) is well understood then a photon spectrum will be fit and directly compared with that of *RHESSI*.

### 9.3.4 Next steps

The initial process of analyzing data from the first *FOXSI* flight will include two main goals. First, *FOXSI* and *RHESSI* observations of the microflare will be compared in order to ensure that *FOXSI*'s sensitivity and instrument response are well understood. The relative capabilities of the two instruments in terms of imaging and spectroscopy will be evaluated. Next, with this instrument knowledge cemented, attention will turn to the quiet-Sun measurements to determine if a significant nanoflare signal was observed. A detailed study of the expected background will be conducted and the observed signal will be compared with this background. Count rates and spectra from the three distinct targets (not including the flare) will be compared for differences. Some of the target regions include significant area off-disk, so the on- and off-disk fluxes will be compared to see if the signal really is solar in nature. Finally, the detectors will be coregistered and integrated into a single image for each target, which may reveal localization of sources on the solar disk. This image will also be compared with EUV and SXR brightenings as measured by AIA on the *Solar Dynamics Observatory* and the X-ray Telescope (XRT) aboard *Hinode*. These instruments show the locations of thermal signatures (possibly from nanoflares); if *FOXSI* counts correspond to these brightenings it would suggest the presence of a nonthermal nanoflare signal.

## 9.4 Conclusions

*FOXSI* has successfully demonstrated the use of HXR focusing optics for solar observations. These optics provide sensitivity and dynamic range far superior to those of *RHESSI*,

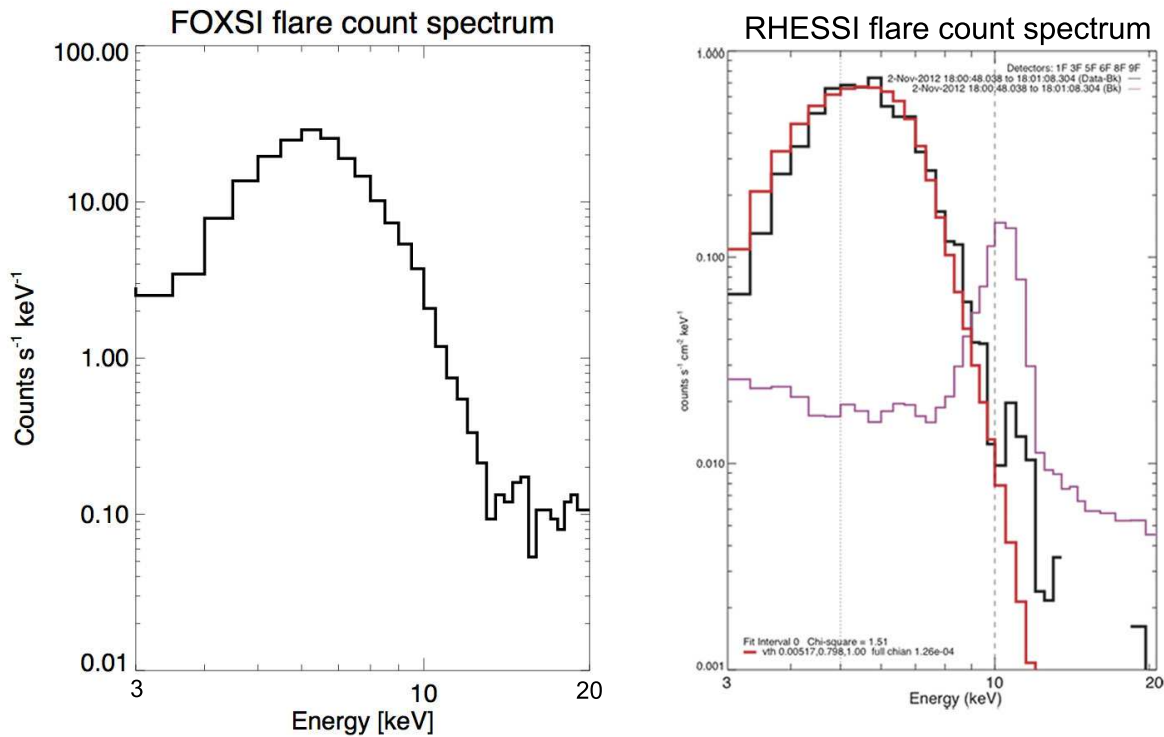


Figure 9.5: Microflare count spectra from (left) the *FOXSI* sounding rocket and (right) the *RHESSI* spacecraft. *RHESSI* spectral fitting reveal that the flare had a temperature of 9 MK and an emission measure of  $5 \times 10^{46} \text{ cm}^{-3}$ .

which was previously the most sensitive solar HXR observer. With HXR images and spectra produced, *FOXSI*'s first flight was deemed a comprehensive success.

The occurrence of a microflare during the *FOXSI* flight was an unexpected but very welcome opportunity. Comparison with simultaneous *RHESSI* measurements of the flare will undoubtedly be essential in assessing *FOXSI*'s sensitivity and imaging capabilities. Careful modeling of the background HXR flux will reveal whether low rates were measured from the quiet Sun. If present, this signal would be the first HXR signal recorded from the quiet Sun; if absent then new upper limits will be placed.

# Chapter 10

## Future work and conclusions

### 10.1 Future work

#### 10.1.1 *RHESSI* studies

Studies of coronal HXR sources in solar flares using *RHESSI* will continue to rely on partial occultation of the flare by the solar disk in order to be able to study faint sources without the presence of bright footpoints. The Two-step Clean technique (Krucker et al. 2011a) described in Chapter 5 will prove useful for studying extended, faint sources in the corona even for on-disk flares.

The analyses in Chapters 4 and 5 both find accelerated electrons in rarely observed locations: in ejected plasma forming the start of a CME, and at the base of an EUV jet. Further studies should be done to determine if these are common occurrences. In the case of the CME result, HXR studies could help to determine if energetic electrons are the source of the unusually high thermal energy (several times greater than the kinetic energy) observed in CMEs (e.g. Landi et al. 2010).

For observations in the solar cycle 24 maximum, the Atmospheric Imaging Assembly (AIA) aboard the *Solar Dynamics Observatory* will provide important context information. AIA includes high-cadence, full-Sun images in several EUV filters, allowing for accurate fitting of the temperatures, emission measures, and densities in hot coronal structures. Radio measurements will continue to be essential in assessing the coronal magnetic field, locations of Type III-emitting electrons, and locations and spectra of energetic electrons (observed via gyrosynchrotron emission).

#### 10.1.2 Solar observations with *NuSTAR*

As described in Chapter 7, the astrophysics spacecraft *NuSTAR* launched in June 2012 and is successfully taking data. Harrison et al. (2010) provides an overview of the instrument. *NuSTAR* is a HXR observer employing grazing-incidence Wolter I optics for highly sensitive astrophysics observations of faint HXRs from black holes, galactic centers, supernovae, and

other targets. At the end of *NuSTAR*'s two-year primary phase, it will begin to include solar targets in its observing plan, with as much as 2–3 weeks per year of solar observation. *NuSTAR* observes in the 5–80 keV energy range.

Since the instrument was designed to study faint galactic and not intense solar sources, the throughput is limited to several hundred counts per second. The instrument is therefore less appropriate than *RHESSI* for studying large, bright flares of *GOES* class C, M, or X. Instead, *NuSTAR*'s advances in solar observations will be similar to the intended targets of the *FOXSI* rocket: the study of nonthermal HXRs from quiet-Sun nanoflares and detailed study of active region temperatures. With an effective area  $\sim 7$  times that of *FOXSI*, a *NuSTAR* solar observation of 1 minute would allow a search for HXRs from quiet-Sun nanoflares with as much sensitivity as *FOXSI*'s flight. In addition, *NuSTAR* could observe the western solar limb for 1–3 days after an active region has rotated off the disk in order to observe coronal sources in partly occulted flares. Larger, on-disk flares could be studied in tandem with *RHESSI*, with *RHESSI* observing the intense impulsive phase while the much higher sensitivity of *NuSTAR* allows for study of the early pre-impulsive phase, when signatures of particle acceleration are likely to be observed.

### 10.1.3 *FOXSI-1* and *FOXSI-2*

*FOXSI* work in the next year will be focused on interpretation of the data from the first flight. There will be at least three areas of investigation: (1) *FOXSI* and *RHESSI* observations of the microflare will be compared in order to assess *FOXSI*'s overall sensitivity and the validity of its photon flux reconstruction. (2) A detailed study of *FOXSI*'s background will be performed in order to determine if a quiet-Sun signal was observed. If present, these will be the first measured HXR signals from the quiet Sun; if not observed, a more stringent upper limit will be set. (3) The consequences of *FOXSI*'s active-region observations will be assessed. Since few or no counts were recorded from the active regions, they must be cooler and/or fainter than expected. Supporting observations by the X-ray Telescope (XRT) and the Extreme-ultraviolet Imaging Spectrometer (EIS) aboard the *Hinode* spacecraft will inform this analysis. *FOXSI* observations will thus set upper limits on active region emission from 4–15 keV.

*FOXSI* has been funded by NASA's Low Cost Access to Space program for a second flight, to take place in 2014. This mission will include two important upgrades to the instrument. Three small-diameter mirrors will be fabricated and added to each optics module. The smaller diameter, and thus smaller grazing angle, will significantly increase effective area at higher energies (extending *FOXSI*'s energy range up to  $\sim 20$  keV) as well as increase the effective area across the entire energy range. See 6.3 for a plot of *FOXSI-2*'s effective area in comparison with the first rocket payload. The detectors will be upgraded to cadmium telluride (CdTe) detectors with a 60  $\mu\text{m}$  pitch. Detectors with good high-energy efficiency (such as CdTe) are essential to any spacecraft mission to study solar HXRs, so use of these detectors will be an excellent precursor to a future spacecraft concept.

Lessons learned from the first *FOXSI* rocket provide an important starting point in

planning the second flight. Since it is now known that HXR count rates measured by *FOXSI* from the quiet Sun are extremely low (or nonexistent), every effort will be made to maximize sensitivity by reducing material in the optical path and lowering the low-energy threshold of the detector to the extent possible. A new system will be built for aligning the instrument to the SPARCS rocket pointing system, most likely utilizing a pinhole on the optics plate and an optical sensor (CCD or other detector) mounted on the detector plane. The second *FOXSI* flight will more than double *FOXSI*'s cumulative quiet-Sun statistics, since it will observe for the same time interval with better sensitivity.

#### 10.1.4 A spaceborne *FOXSI*

A rocket-borne experiment is vastly limited in that it can only observe for several minutes at a time and must fit into rocket space constraints. Since there is currently no proven way to predict flares and particle acceleration is thought to be one of the most immediate flare processes, it is not possible to time a rocket launch to perform flare studies. (In this respect *FOXSI* was extraordinarily fortunate to observe a microflare during its first flight.) In order to take advantage of the HXR observing improvements offered by *FOXSI* it is necessary to put the technology on a spaceborne observatory.

A spaceborne *FOXSI* could have a focal length of 10 meters by using an extendable boom similar to that of *NuSTAR*, allowing appreciable response up to  $\sim 80\text{--}90$  keV. Optics could be constructed via the electroformed nickel replication (ENR) described in Chapter 7 or the slumped glass technique used for *NuSTAR* (though in this case improved angular resolution would be required to achieve the  $\lesssim 10$  arcsec resolution required to separate footpoints). Cadmium telluride (CdTe) or cadmium zinc telluride (CdZnTe) detectors, described in Chapter 8, would provide the necessary efficiency at higher energies than silicon can.

A *FOXSI* instrument is one of those included in both the Reconnection and Microscale (RAM) (Bookbinder et al. 2003) and Solar Eruptive Events (SEE) 2020 mission concepts (Lin et al. 2010; Lin et al. 2011). The SEE 2020 mission, not yet proposed, could include both a focusing HXR instrument and a gamma-ray imager/polarimeter similar to the GRIPS instrument (Shih et al. 2012) to perform imaging spectroscopy of energetic electrons and ions, along with several other instruments for context SXR, EUV, and white-light measurements. The main intention of the SEE concept is to understand explosive energy release in flares and CMEs, which are so often related that they can be referred to as a single entity: a “solar eruptive event.” The SEE mission, with its wide array of instruments, would be able to better understand the acceleration of electrons and ions in eruptive events, particle acceleration in CME shocks, and the evolution of coronal plasma during such events, including flare- and CME-related heating (Lin et al. 2010).

## 10.2 Conclusion

With the maximum of solar cycle 24 drawing near, and with the long lead times required to propose, design, and build a spaceborne mission, right now is the time to start planning instruments to observe the solar cycle 25 maximum. A spacecraft such as the SEE mission, carrying instruments to measure HXR, gamma rays, and energetic neutrals, could cover the same energy range as *RHESSI* does with far superior (10–1000 times better) sensitivity and could thus advance the field much farther than *RHESSI* has. (The fact that three instruments would be required to replace or improve on *RHESSI* is a testament to the innovation and success of its design.)

This dissertation has shown that there are technologies developed and ready to improve sensitivity and dynamic range for solar HXR observations. These improvements are required for the systematic study of faint coronal HXR sources necessary to identify and quantify the electron acceleration region. Advances in cadmium telluride device fabrication techniques now allow detectors to be manufactured with high efficiency throughout the HXR range but with a less extreme temperature requirement than that of germanium. Grazing-incidence focusing optics, long the standard for SXR instruments, are now available in the HXR range on a reasonable timescale and budget. These optics will be able to image faint coronal sources even in the presence of sources up to 1000 times brighter.

Necessary observations for future instruments include: (1) HXR measurements of energetic electrons in the acceleration region in order to compare their spectra to that predicted by various acceleration theories; (2) measurement of faint HXR from energetic electron beams escaping the flare region along field lines open to interplanetary space; (3) observations with fine time resolution in order to study time-of-flight effects similar to those found in Aschwanden et al. (1995); (4) investigation of nanoflares both in active regions and in the quiet Sun in order to weigh their contributions to coronal heating. All of these measurements are within the capabilities of a spaceborne HXR observer utilizing direct focusing optics.

At the same time this dissertation has shown that there is still a wealth of information on faint coronal HXR sources to be gained by means of *RHESSI* data. Partial occultation of flares, in particular, can allow the study of faint coronal sources by obscuring the bright footpoints. The combination of *RHESSI* and AIA data is a powerful partnership, with *RHESSI* offering data on flare-accelerated electrons and AIA contributing thermal parameters of the ambient plasma (densities and temperatures). Joint studies throughout the solar cycle 24 maximum will determine if heating by energetic electrons is an important energy input for CMEs (as in Chapter 5), which could have important consequences for CME formation theories. The presence of accelerated electrons in EUV jets, as presented in Chapter 4, is a surprising result and an effort should be made to understand the origin of these electrons.

# Appendix A

## FOXSI optics calibration results

This appendix displays results of the calibration of the *FOXSI* optics calibration at the Stray Light Facility at the NASA/Marshall Space Flight Center. As described in Chapter 7, the half power diameter (HPD) and the FWHM of the point spread function (PSF) were measured as an assessment of the optics' imaging capabilities. Plots were prepared by Steven Christie.

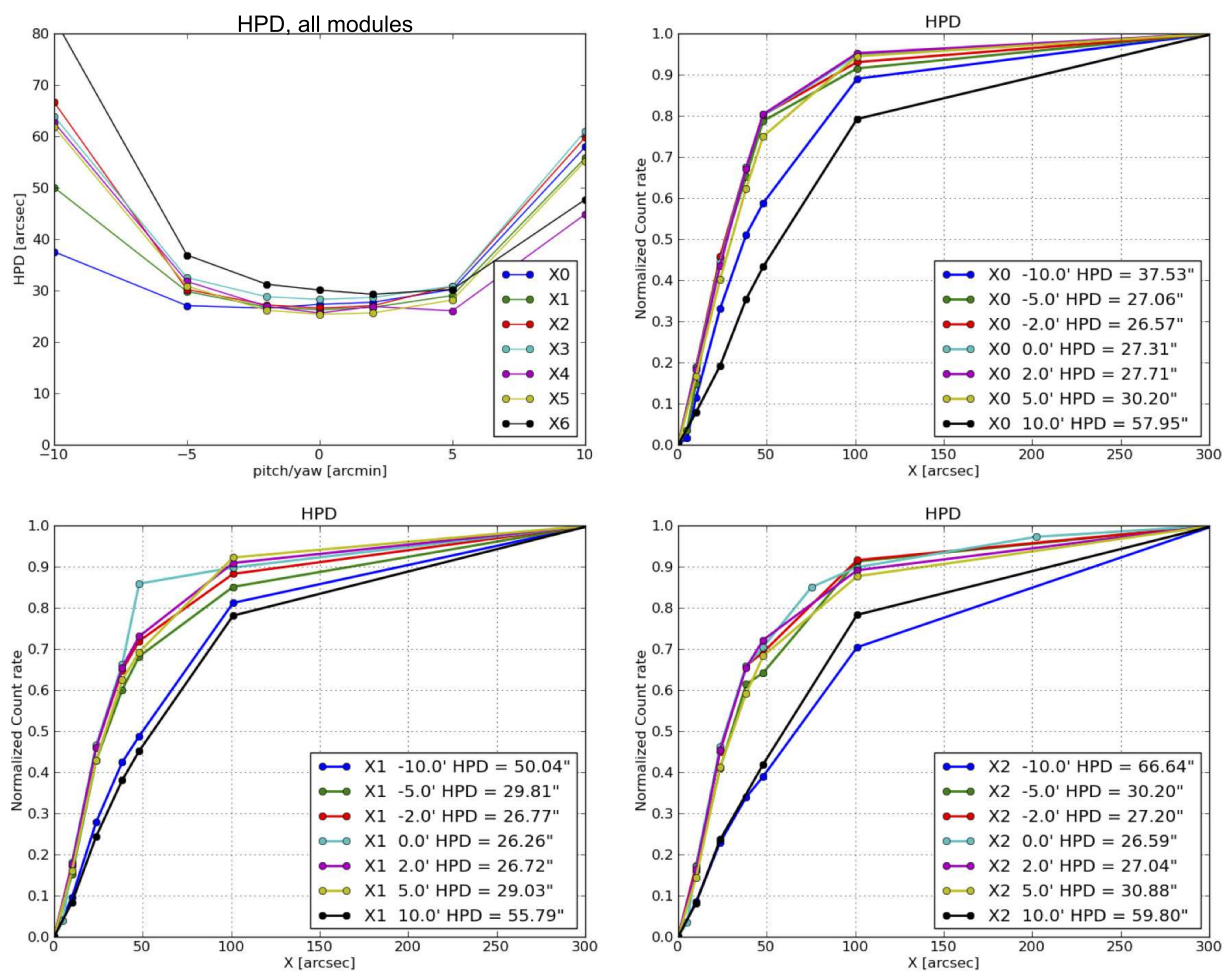


Figure A.1: The HPD was measured by taking data with various sized pinholes placed over a detector. The extrapolated pinhole size (in arcseconds) that encompasses half the flux measured by the largest pinhole is taken to be the HPD. The top left plot is a summary showing this measurement for all the optics modules (labeled X0–X6) for an on-axis and several off-axis configurations. Detailed plots showing the actual measurements for each module follow in this and the next figure.

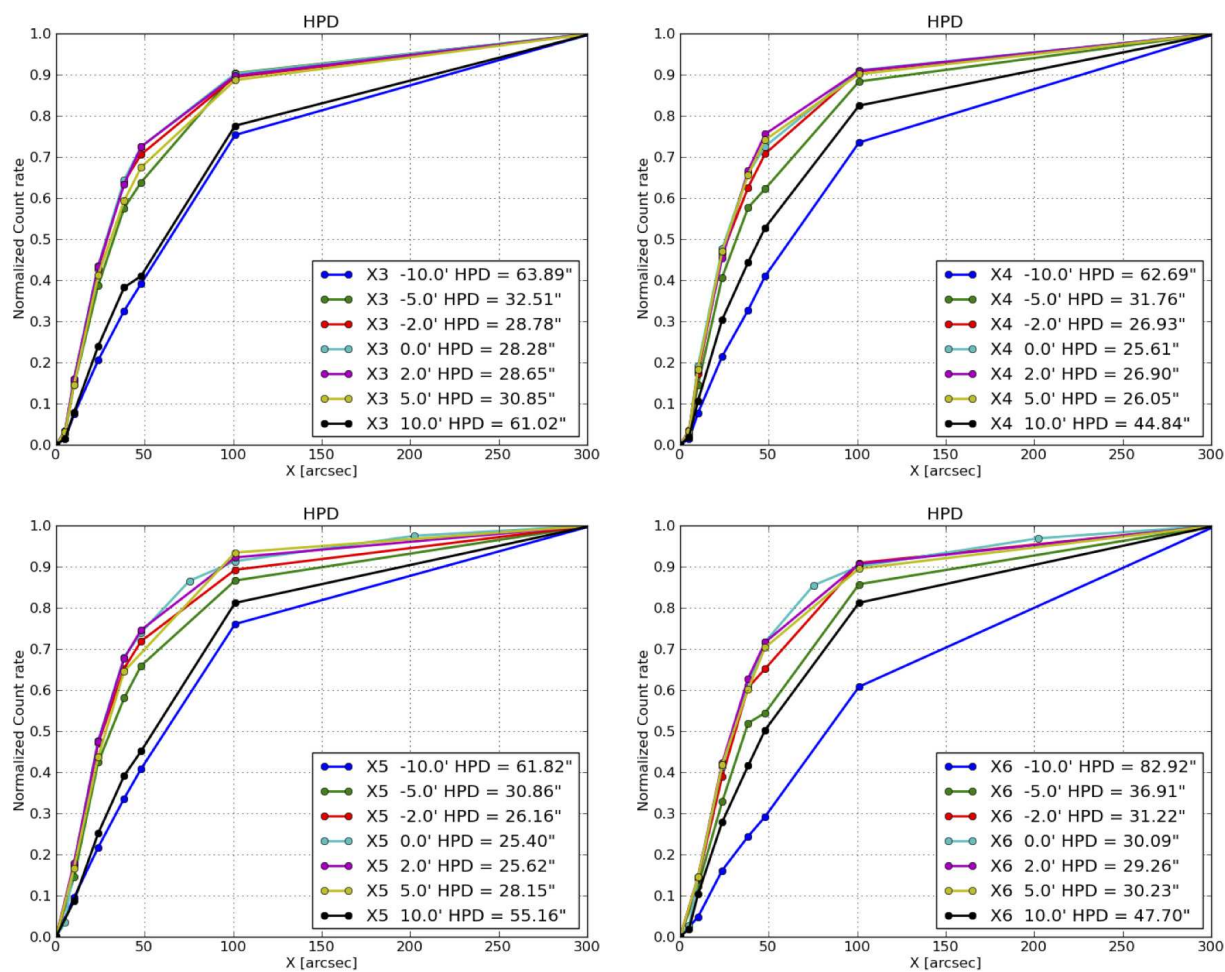


Figure A.2

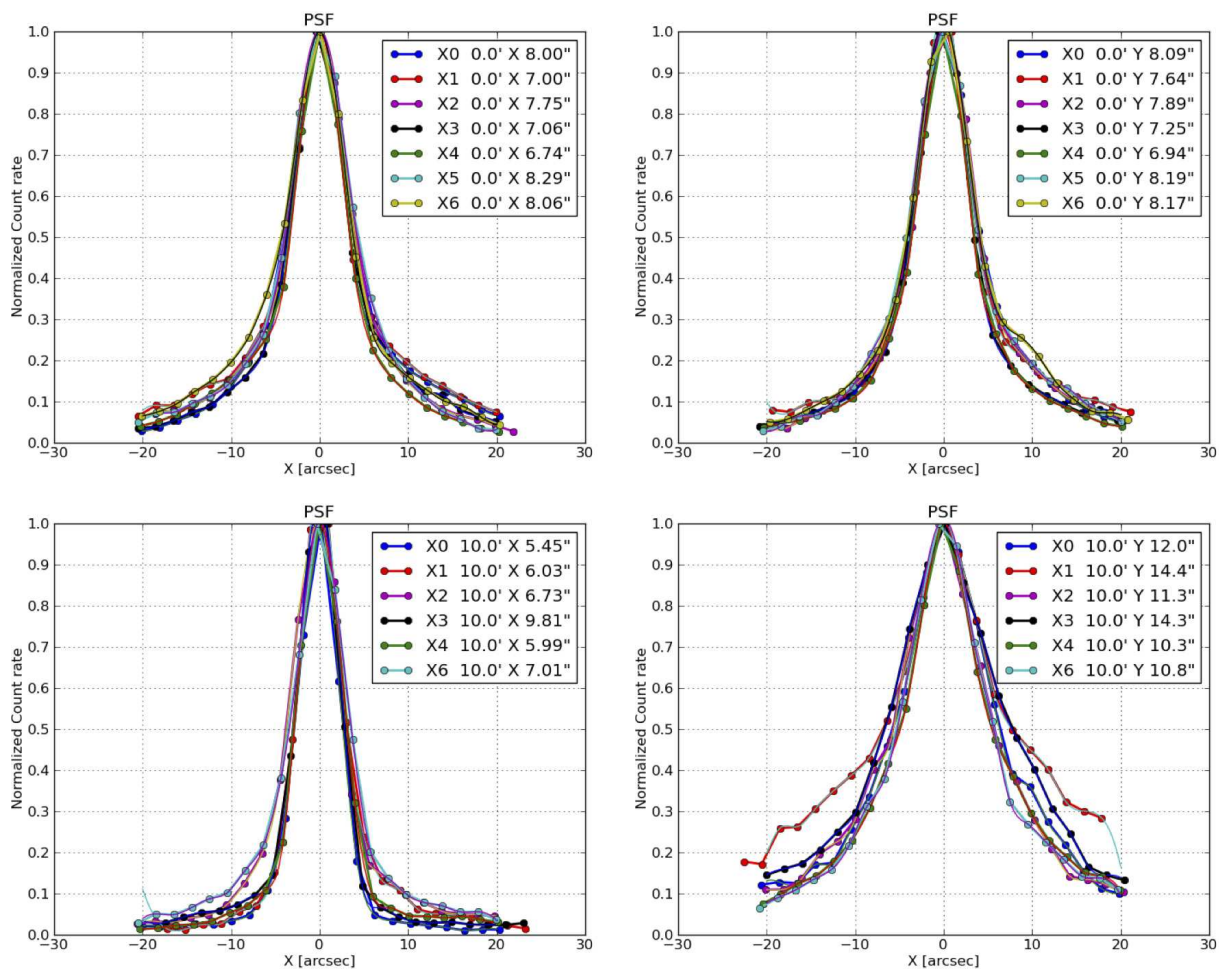


Figure A.3: The PSF was measured by stepping a single-pixel detector across the core of the focused X-ray image. This measurement was performed for an on-axis (top panels) and for one off-axis (10 arcminutes, bottom panels) position. The FWHM in both dimensions is shown for each module. The off-axis PSF is squeezed in the radial direction and elongated in the azimuthal direction, with respect to the center of the field of view.

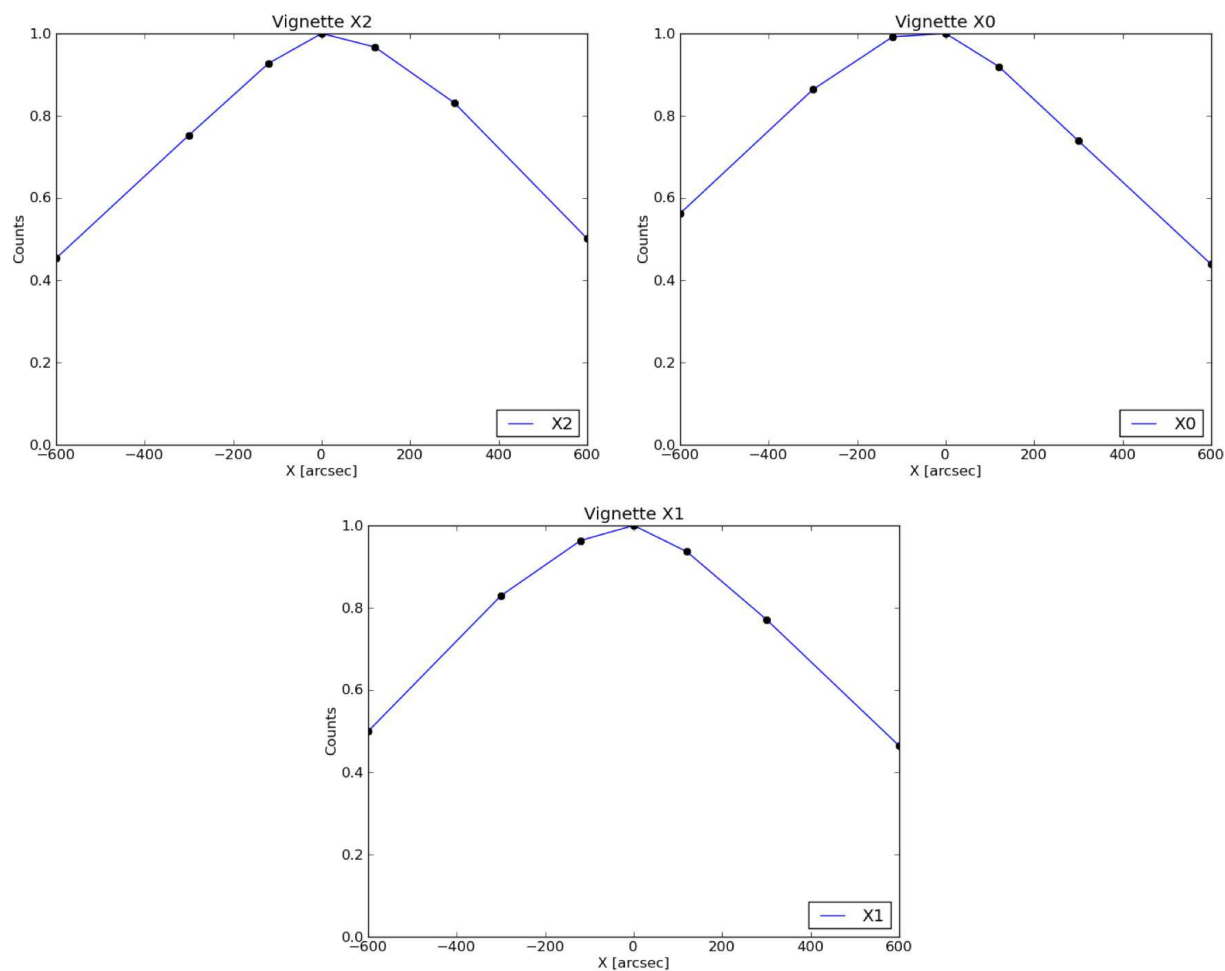


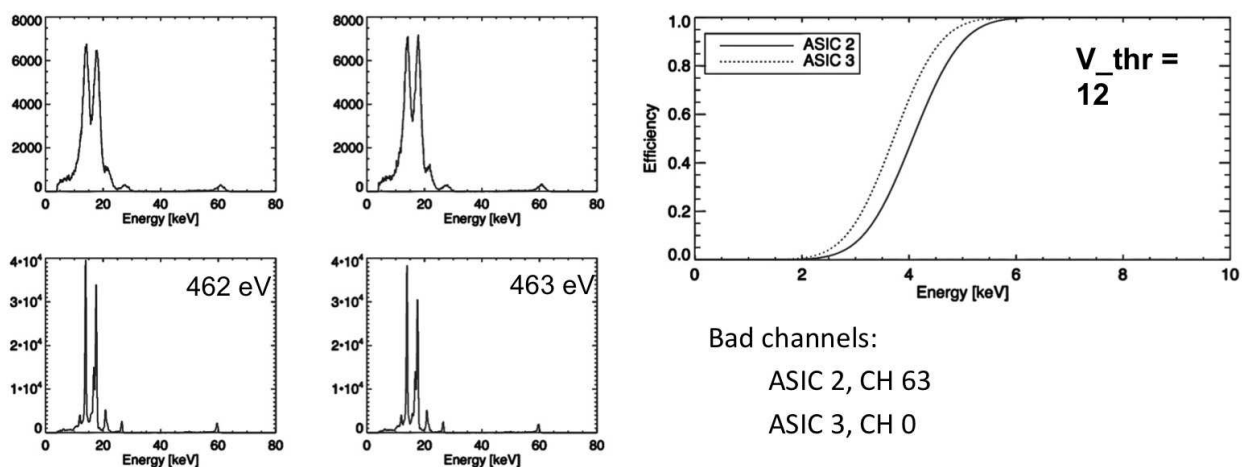
Figure A.4: Shown here is the “vignette” of the field of view, or the maximum flux recorded for several off-axis angles, for three optics modules. The effective area of the optics decreases with off-axis angle since some X-rays are incident on the mirror at an angle too large to reflect well. These plots show that the optics response falls by a factor of two approximately 600 arcseconds (10 arcminutes) away from the center (on-axis). The edges of the detector field of view are  $\sim 480$  arcseconds off-axis, where the response is  $\sim 0.6$  times the on-axis response.

## Appendix B

### FOXSI detector calibration results

These figures show the results of the calibration of each *FOXSI* flight detector (as well as the backup detectors). Measurements were carried out at the Space Sciences Laboratory using three radioactive sources: Am-241, Ba-133, and Fe-55. Details of the measurements and a summary of the results are given in Chapter 8. Here, results are shown for the individual detectors. A calibrated Am-241 is shown along with the calculated FWHM of the 13.9 keV line for each p-side ASIC. The righthand plots show the efficiency measured near the low-energy threshold for each p-side ASIC. Any bad channels and special comments are noted.

## Detector 102 (Flight board)



## Detector 103 (Flight board)

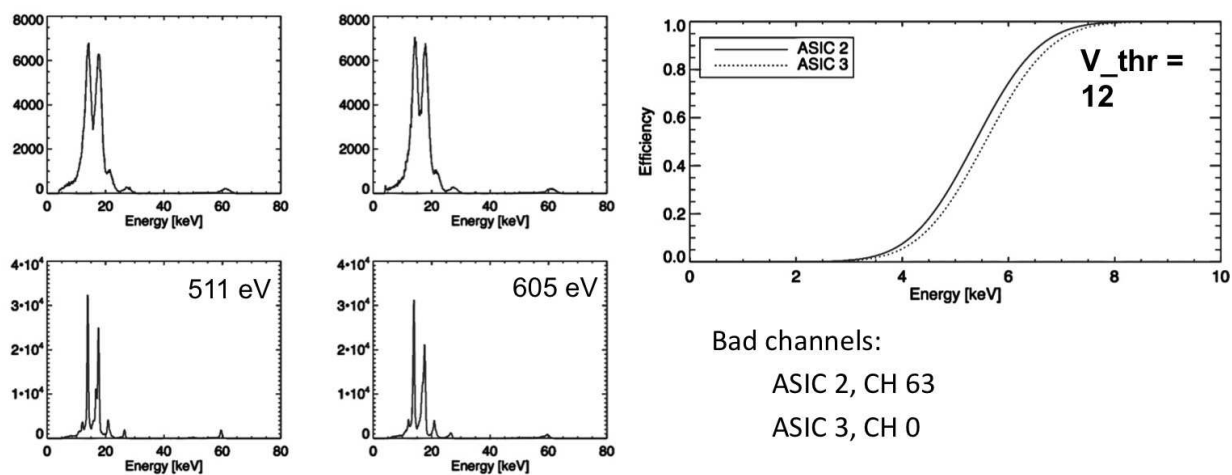
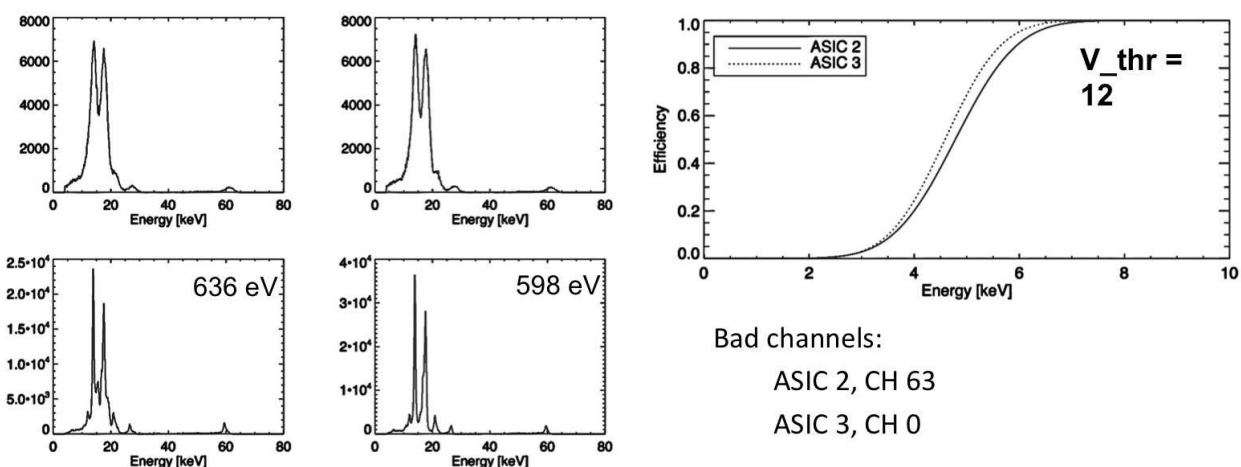


Figure B.1

## Detector 104 (Flight board)



## Detector 105 (Flight board)

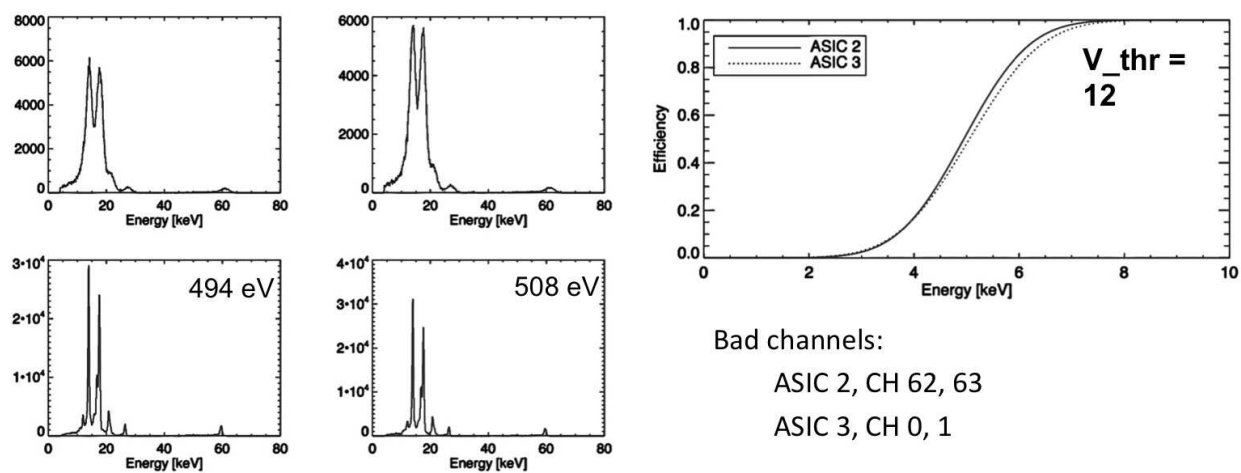
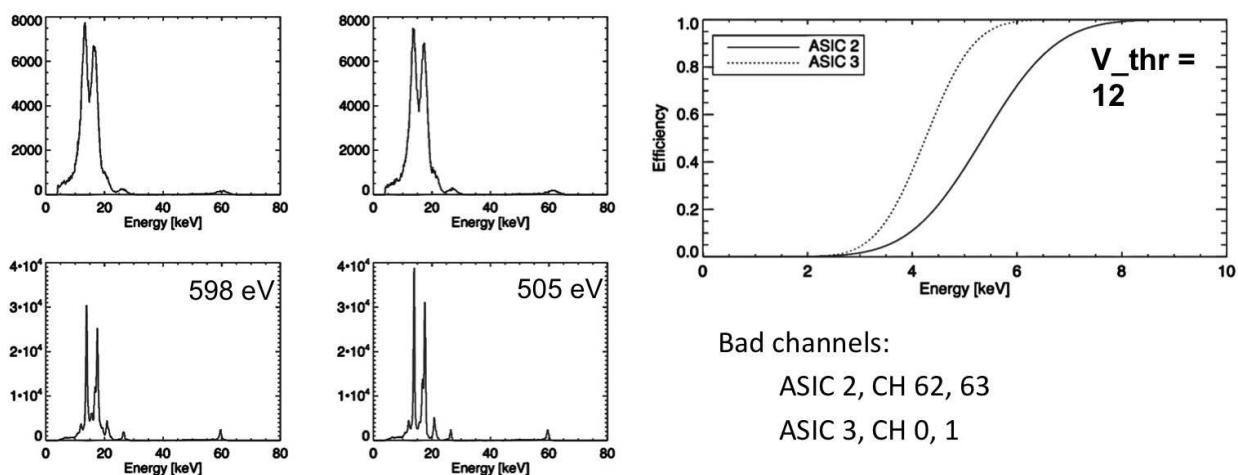


Figure B.2

## Detector 106 (Flight board)



## Detector 108 (Flight board)

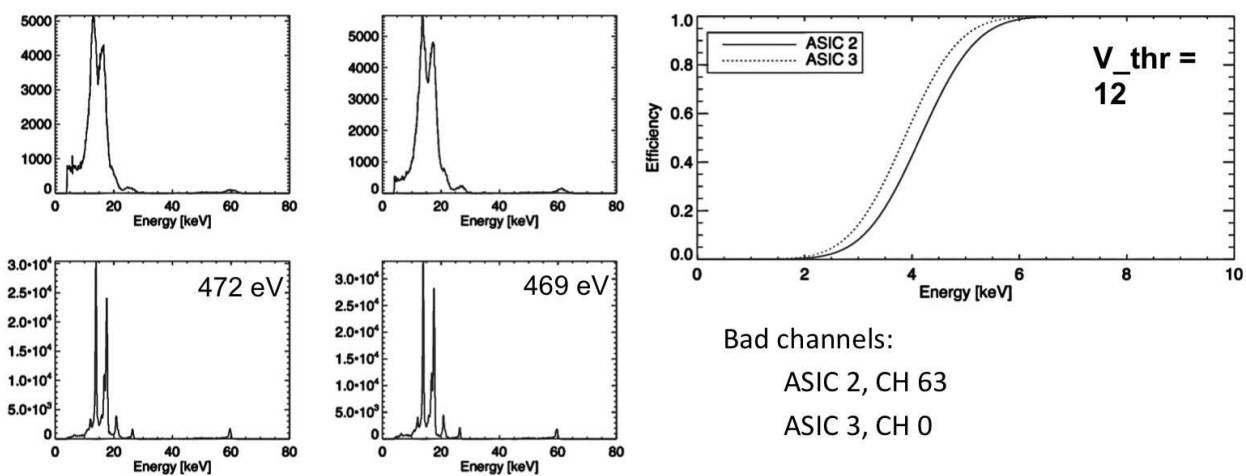
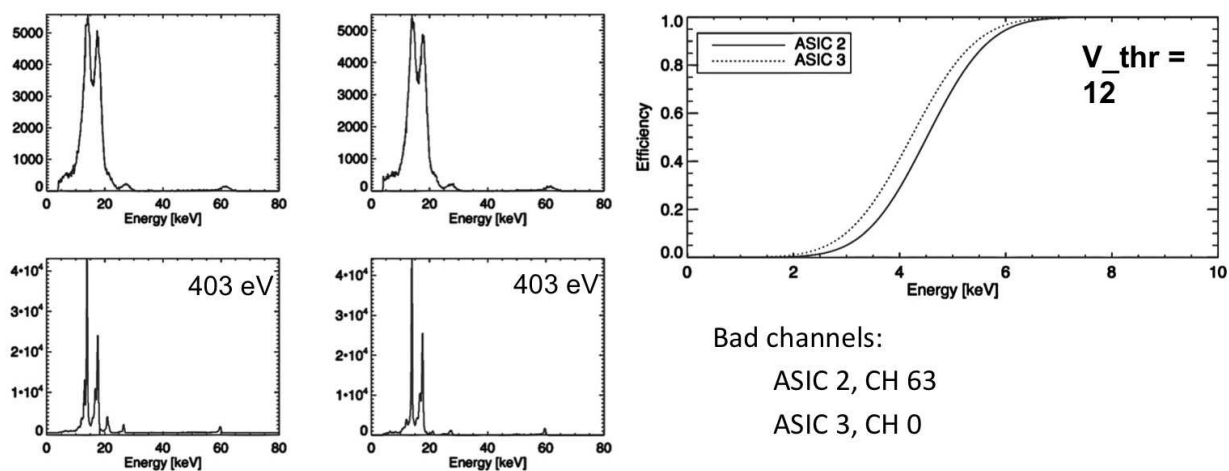


Figure B.3

## Detector 109 (Flight board)



## Detector 101 (Backup board)

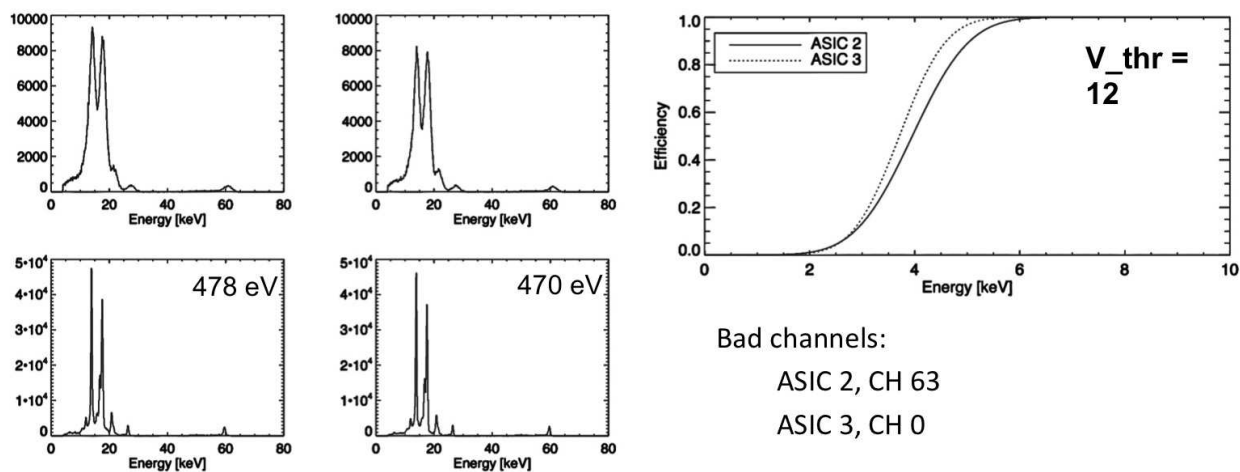
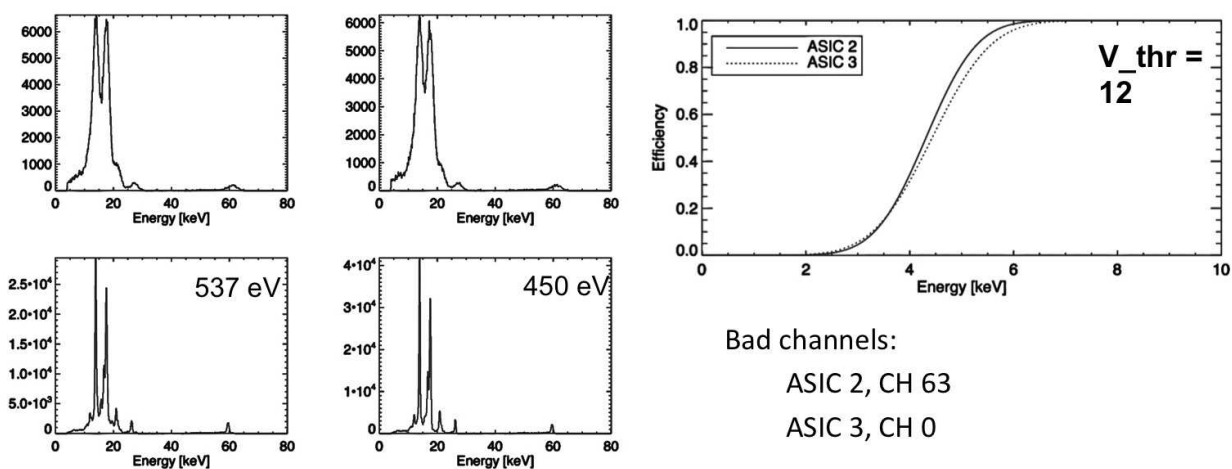


Figure B.4

## Detector 3 (Backup board)



## Detector 36 (Backup board)

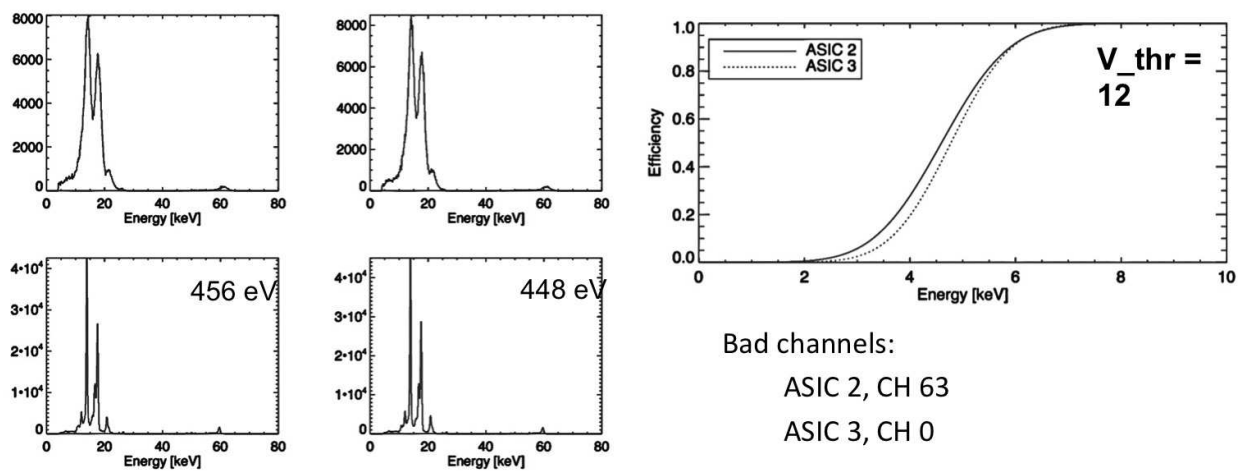
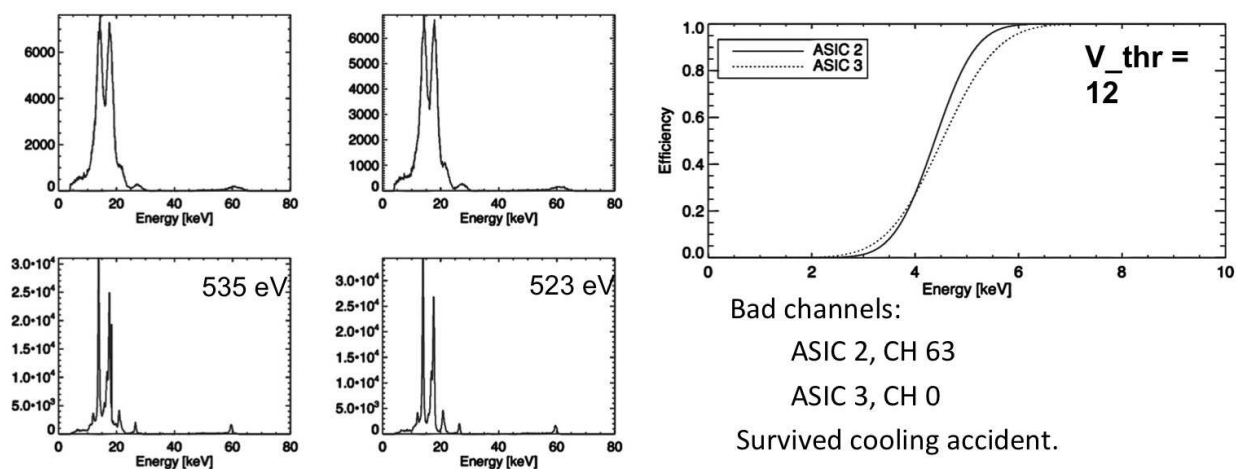


Figure B.5

## Detector 15 (Backup board)



## Detector 28 (Backup board)

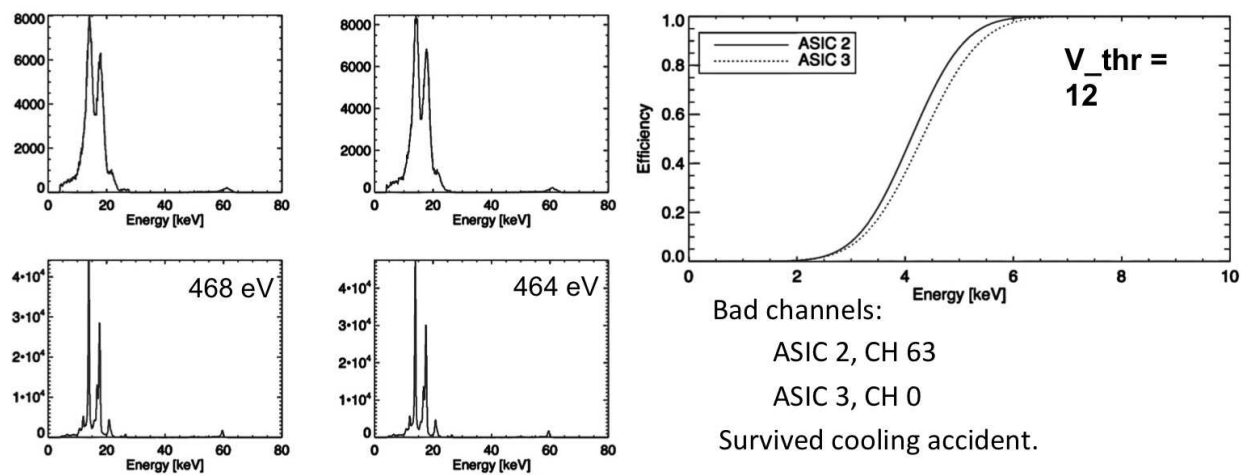
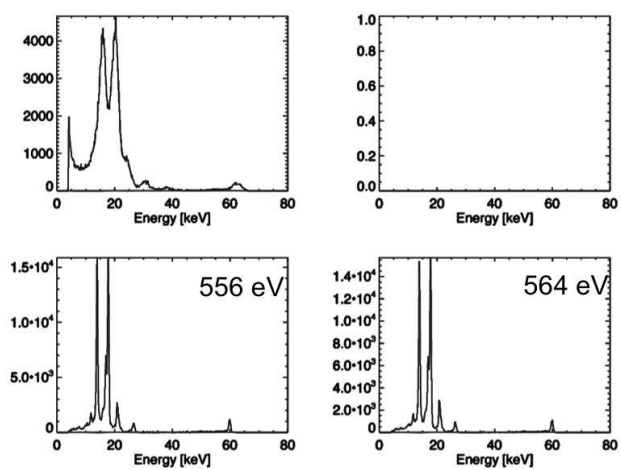


Figure B.6

## Detector 107 (Backup board)



Bad channels:

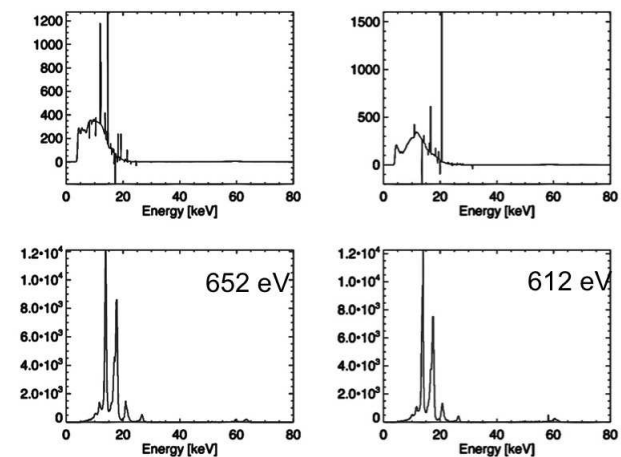
ASIC 2, CH 62, 63

ASIC 3, CH 0, 1

Data is missing from ASIC 1.

R/O problems prevented efficiency test.

## Detector 110 (Backup board)



Bad channels:

ASIC 2, CH 60, 61, 62, 63

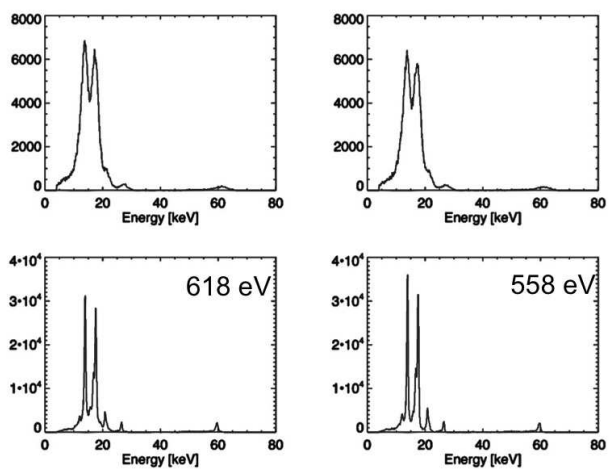
ASIC 3, CH 0, 1, 2, 3

ASICs are VATA450 (not the FOXSI ASIC)

N-side resolution with this ASIC is poor.

Figure B.7

## Detector 114 (Backup board)



Bad channels: unknown

R/O problems prevented efficiency test.

Figure B.8

## Appendix C

### FOXSI X-ray alignment results

Shown here are X-ray images produced during the alignment of the *FOXSI* optics and detectors. As described in Section 7.4.5, the source was an X-ray generator placed 20 meters in front of the payload. Since the object distance was finite, the rays are not focused to a perfect spot; instead, a ring is produced by the optics on the detectors. The concentricity and intensity uniformity of the rings can be used to evaluate the angular alignment of the optics.

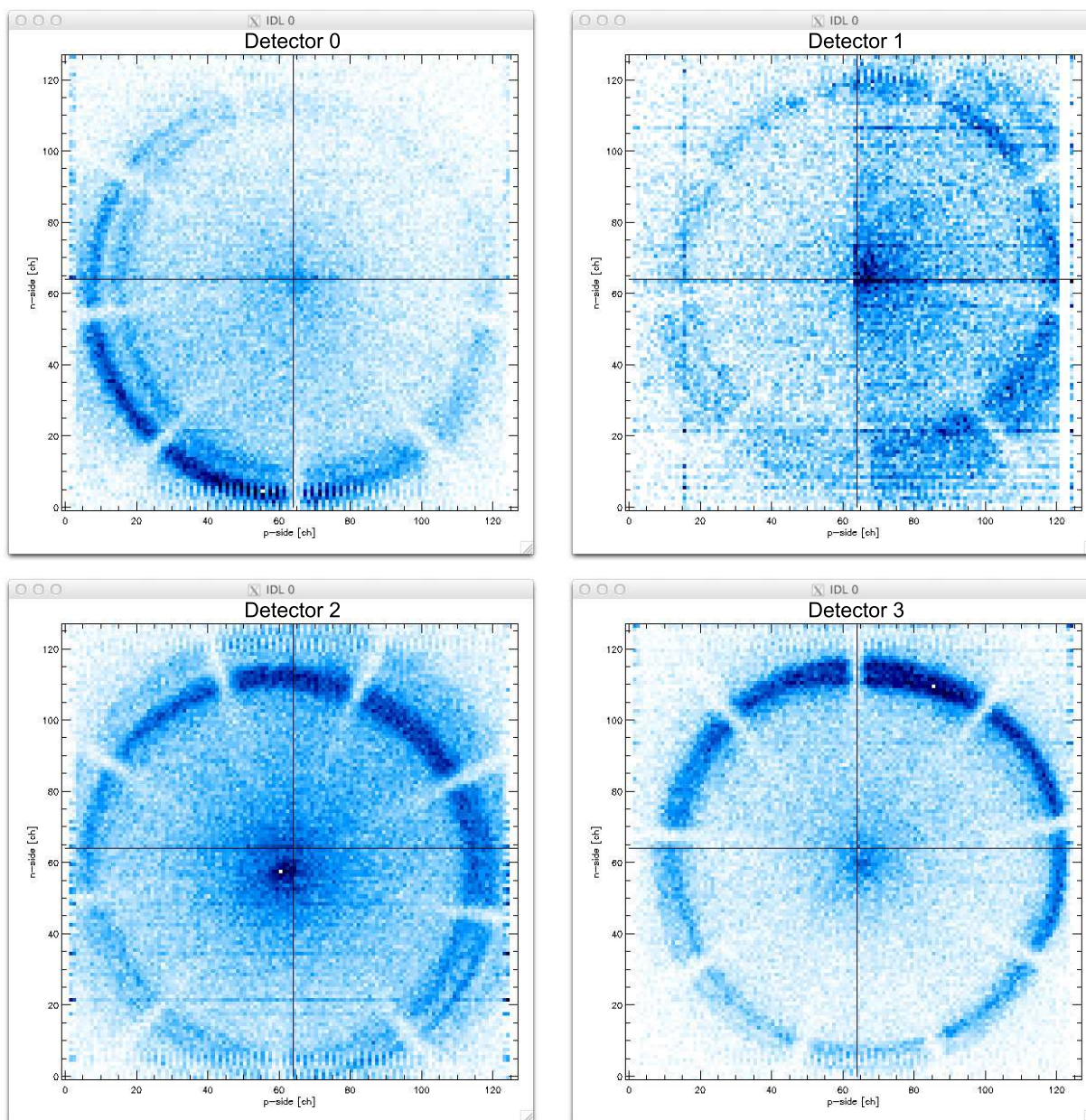


Figure C.1: X-ray images for detectors 0–3. Optic 0 (upper left) is the least well-aligned (2 arcmin), while most of the other optics are aligned to  $<1$  arcmin. Problems with a readout ASIC result in poorer quality data for detector 1 (upper right).

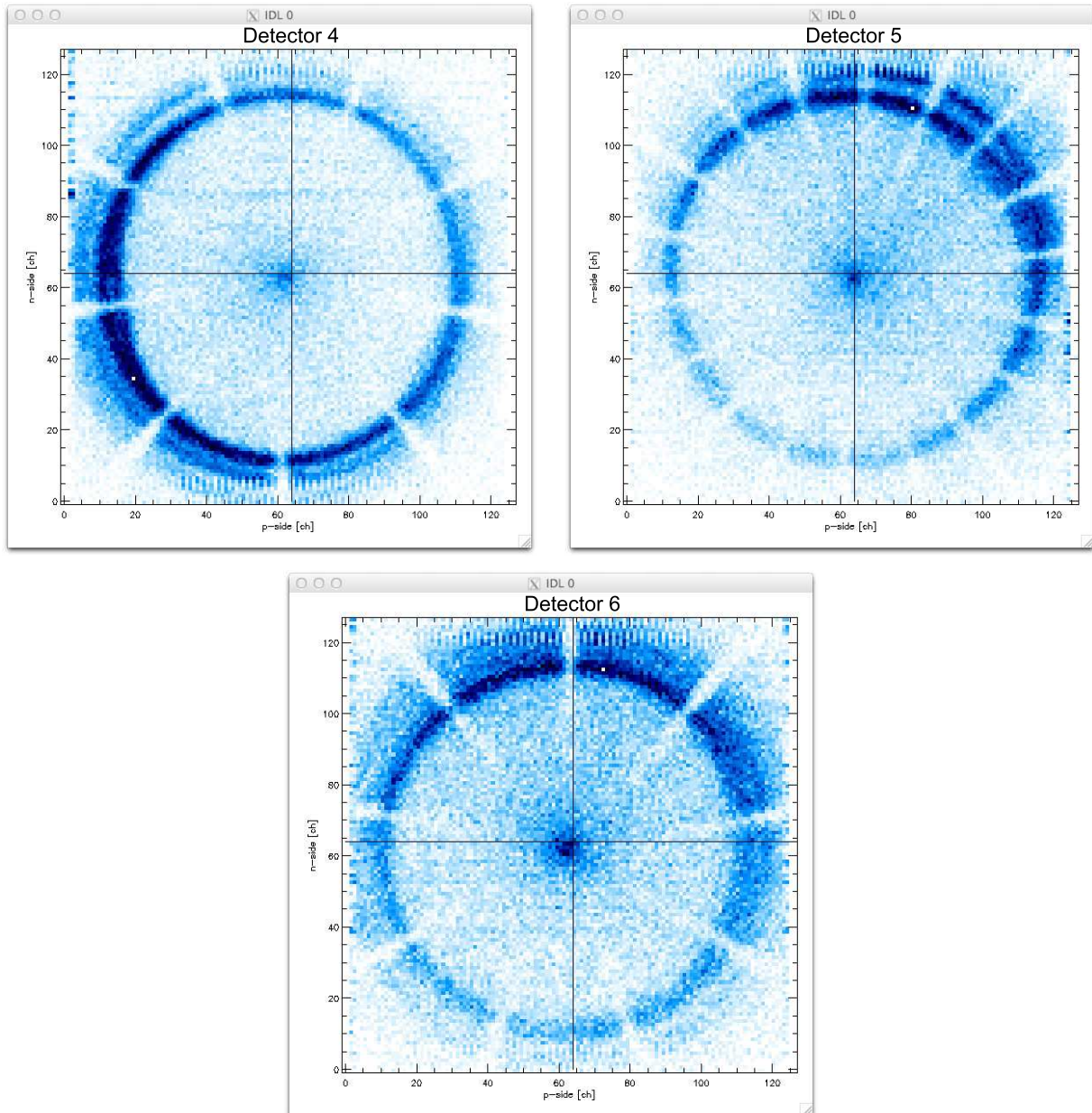


Figure C.2: X-ray images for detectors 4–6. In the detector 5 (upper right) image, more spokes (corresponding to slats in the spider supports) are apparent because of a phase offset between spider supports on either side of the module.

# Bibliography

- Akmal, A., Raymond, J. C., Vourlidas, A., et al. 2001, *ApJ*, 553, 922
- Alexander, D., & Fletcher, L. 1999, *Sol. Phys.*, 190, 167
- Als-Nielsen, J., & McMorrow, D. 2011, *Elements of modern X-ray physics* (Wiley)
- Arai, Y., Miyoshi, T., Unno, Y., et al. 2010, *Nuclear Instruments and Methods in Physics Research A*, 623, 186
- Aristov, V. V., Grigoriev, M. V., Kuznetsov, S. M., et al. 2000, *Optics Communications*, 177, 33
- Aschenbach, B. 1985, *Reports on Progress in Physics*, 48, 579
- Aschenbach, B., Briel, U. G., Haberl, F., et al. 2000, in *Society of Photo-Optical Instrumentation Engineers (SPIE) Conference Series*, ed. J. E. Truemper & B. Aschenbach, Vol. 4012, 731–739
- Aschwanden, M. 2006, *Physics of the solar corona: an introduction with problems and solutions* (Springer)
- Aschwanden, M. J., & Boerner, P. 2011, *ApJ*, 732, 81
- Aschwanden, M. J., Schwartz, R. A., & Alt, D. M. 1995, *ApJ*, 447, 923
- Aschwanden, M. J., Tarbell, T. D., Nightingale, R. W., et al. 2000, *ApJ*, 535, 1047
- Bai, T., Hudson, H. S., Pelling, R. M., et al. 1983, *ApJ*, 267, 433
- Bain, H., Krucker, S., Glesener, L., & Lin, R. P. 2012a, in *American Astronomical Society Meeting Abstracts 220*, Vol. 220, 508.04
- Bain, H. M., & Fletcher, L. 2009, *A&A*, 508, 1443
- Bain, H. M., Krucker, S., Glesener, L., & Lin, R. P. 2012b, *ApJ*, 750, 44
- Bastian, T. S. 2003, *Advances in Space Research*, 32, 2705
- Bastian, T. S., Benz, A. O., & Gary, D. E. 1998, *ARA&A*, 36, 131
- Battaglia, M., Bisello, D., Contarato, D., et al. 2009, *Journal of Instrumentation*, 4, 4007
- Battaglia, M., Bussat, J.-M., Contarato, D., et al. 2008, *IEEE Transactions on Nuclear Science*, 55, 3746
- Benz, A. O. 2008, *Living Reviews in Solar Physics*, 5, 1
- Benz, A. O., & Krucker, S. 2002, *ApJ*, 568, 413
- Birn, J., & Hesse, M. 2001, *J. Geophys. Res.*, 106, 3737
- Bookbinder, J., DeLuca, E., Cheimets, P., et al. 2003, in *Astronomical Telescopes and Instrumentation, International Society for Optics and Photonics*, 436–452
- Brooks, D. H., Warren, H. P., Williams, D. R., & Watanabe, T. 2009, *ApJ*, 705, 1522

- Brown, J. C. 1971, *Sol. Phys.*, 18, 489
- Carmichael, H. 1964, NASA Special Publication, 50, 451
- Carrington, R. C. 1859, *MNRAS*, 20, 13
- Caspi, A., & Lin, R. P. 2010, *ApJ*, 725, L161
- Cassak, P. A., Drake, J. F., & Shay, M. A. 2006, *ApJ*, 644, L145
- Chae, J., Qiu, J., Wang, H., & Goode, P. R. 1999, *ApJ*, 513, L75
- Chen, F. 1984, *Introduction to plasma physics and controlled fusion. Volume 1: Plasma physics* (Plenum Press, New York, NY (United States))
- Chen, L.-J., Bhattacharjee, A., Puhl-Quinn, P. A., et al. 2008, *Nature Physics*, 4, 19
- Chen, Q., & Petrosian, V. 2012, *ApJ*, 748, 33
- Cheng, X., Zhang, J., Liu, Y., & Ding, M. D. 2011, *ApJ*, 732, L25
- Chifor, C., Isobe, H., Mason, H. E., et al. 2008, *A&A*, 491, 279
- Christe, S., Hannah, I. G., Krucker, S., McTiernan, J., & Lin, R. P. 2008a, *ApJ*, 677, 1385
- Christe, S., Krucker, S., & Lin, R. P. 2008b, *ApJ*, 680, L149
- Christe, S., Krucker, S., & Saint-Hilaire, P. 2011, *Sol. Phys.*, 270, 493
- Christe, S. D. 2007, PhD thesis, University of California, Berkeley
- Cirtain, J. W., Golub, L., Lundquist, L., et al. 2007, *Science*, 318, 1580
- Clark, S. 2007, *The Sun Kings: the unexpected tragedy of Richard Carrington and the tale of how modern astronomy began* (Princeton University Press)
- Cornwell, T. J., & Evans, K. F. 1985, *A&A*, 143, 77
- de Jager, C. 1963, *Bull. Astron. Inst. Netherlands*, 17, 209
- De Pontieu, B., McIntosh, S. W., Hansteen, V. H., & Schrijver, C. J. 2009, *ApJ*, 701, L1
- De Pontieu, B., McIntosh, S. W., Carlsson, M., et al. 2011, *Science*, 331, 55
- Del Río, M. S., & Dejus, R. J. 2004, in *American Institute of Physics Conference Series*, Vol. 705, American Institute of Physics Conference Series, ed. T. Warwick, J. Arthur, H. A. Padmore, & J. Stöhr, 784–787
- Drake, J. F., Swisdak, M., Che, H., & Shay, M. A. 2006a, *Nature*, 443, 553
- Drake, J. F., Swisdak, M., Schoeffler, K. M., Rogers, B. N., & Kobayashi, S. 2006b, *Geophys. Res. Lett.*, 33, 13105
- Dulk, G. A. 1985, *ARA&A*, 23, 169
- Edwards, P. J., & McCracken, K. G. 1967, *J. Geophys. Res.*, 72, 1809
- Ehle, M., Breittellner, M., Dahlem, M., et al. 2001, *XMM-Newton Users' Handbook*: [http://xmm.vilspa.esa.es/xmm\\_user\\_support/external/documentation/uhb\\_frame.shtml](http://xmm.vilspa.esa.es/xmm_user_support/external/documentation/uhb_frame.shtml)
- Ehrenberg, W. 1949, *Journal of the Optical Society of America* (1917-1983), 39, 741
- Emslie, A., Dennis, B., Hudson, H., & Lin, R., eds. 2011, *High-Energy Aspects of Solar Flares*, (Space Science Reviews special issue), Vol. 159 (Springer Netherlands), 10.1007/s11214-011-9815-7
- Engelhaupt, D. E., Ramsey, B. D., O'Dell, S. L., Jones, W. D., & Russell, J. K. 2000, in *Society of Photo-Optical Instrumentation Engineers (SPIE) Conference Series*, ed. R. B. Hoover & A. B. Walker, Vol. 4138, 154–163
- Feffer, P. T., Lin, R. P., Slassi-Sennou, S., et al. 1997, *Sol. Phys.*, 171, 419
- Fermi, E. 1949, *Physical Review*, 75, 1169

- Fisher, G. H., Canfield, R. C., & McClymont, A. N. 1984, *ApJ*, 281, L79  
— . 1985, *ApJ*, 289, 425
- Fivian, M., Hemmeck, R., McHedlishvili, A., & Zehnder, A. 2002, *Sol. Phys.*, 210, 87
- Fletcher, L., & Hudson, H. S. 2002, *Sol. Phys.*, 210, 307  
— . 2008, *ApJ*, 675, 1645
- Foullon, C., Verwichte, E., Nakariakov, V. M., Nykyri, K., & Farrugia, C. J. 2011, *ApJ*, 729, L8
- Gao, F., Campbell, L. W., Devanathan, R., et al. 2007, *Nuclear Instruments and Methods in Physics Research B*, 255, 286
- Giacconi, R., Reidy, W. P., Zehnpfennig, T., Lindsay, J. C., & Muney, W. S. 1965, *ApJ*, 142, 1274
- Giacconi, R., & Rossi, B. 1960, *J. Geophys. Res.*, 65, 773
- Gibson, E. 1977, *The quiet sun.*, by Gibson, E.. Translated from the English edition. Moskva: Mir, 408 p., 1
- Glesener, L., Krucker, S., & Lin, R. P. 2012, *ApJ*, 754, 9
- Golub, L., Deluca, E., Austin, G., et al. 2007, *Sol. Phys.*, 243, 63
- Gopalswamy, N., Yashiro, S., Michalek, G., et al. 2009, *Earth Moon and Planets*, 104, 295
- Gubarev, M., Alexander, C., & Ramsey, B. 2005, in *Society of Photo-Optical Instrumentation Engineers (SPIE) Conference Series*, ed. O. Citterio & S. L. O'Dell, Vol. 5900, 232–238
- Gubarev, M., Ramsey, B., Engelhaupt, D., Kester, T., & Speegle, C. 2006, in *Society of Photo-Optical Instrumentation Engineers (SPIE) Conference Series*, Vol. 6266
- Handy, B. N., Acton, L. W., Kankelborg, C. C., et al. 1999, *Sol. Phys.*, 187, 229
- Hannah, I., Fletcher, L., & Kontar, E. P. 2012, in *American Astronomical Society Meeting Abstracts #220*, Vol. 220, 322.02
- Hannah, I. G., Christe, S., Krucker, S., et al. 2008, *ApJ*, 677, 704
- Hannah, I. G., Hudson, H. S., Hurford, G. J., & Lin, R. P. 2010, *ApJ*, 724, 487
- Hannah, I. G., Hurford, G. J., Hudson, H. S., Lin, R. P., & van Bibber, K. 2007, *ApJ*, 659, L77
- Hannah, I. G., & Kontar, E. P. 2012, *A&A*, 539, A146
- Harrison, F. A., Boggs, S., Christensen, F., et al. 2010, in *Society of Photo-Optical Instrumentation Engineers (SPIE) Conference Series*, Vol. 7732
- Henke, B., Gullikson, E., & Davis, J. 1993, *Atomic data and nuclear data tables*, 54, 181
- Heyvaerts, J., & Priest, E. 1983, *Astronomy and Astrophysics*, 117, 220
- Heyvaerts, J., Priest, E. R., & Rust, D. M. 1977, *ApJ*, 216, 123
- Hirayama, T. 1974, *Sol. Phys.*, 34, 323
- Hodgson, R. 1859, *MNRAS*, 20, 15
- Holman, G. D. 1985, *ApJ*, 293, 584
- Holman, G. D., Sui, L., Schwartz, R. A., & Emslie, A. G. 2003, *ApJ*, 595, L97
- Howard, R. A., Moses, J. D., Vourlidas, A., et al. 2008, *Space Sci. Rev.*, 136, 67
- Hubbell, J. H., & Seltzer, S. M. 2004, *Tables of X-Ray Mass Attenuation Coefficients and Mass Energy-Absorption Coefficients (version 1.4)*

- Hudson, H. S. 1991, *Sol. Phys.*, 133, 357
- Hudson, H. S., Canfield, R. C., & Kane, S. R. 1978, *Sol. Phys.*, 60, 137
- Hudson, H. S., Kosugi, T., Nitta, N. V., & Shimojo, M. 2001, *ApJ*, 561, L211
- Hurford, G. 2006, *User's Guide to Visibilities*
- Hurford, G. J., Krucker, S., Lin, R. P., et al. 2006, *ApJ*, 644, L93
- Hurford, G. J., Schwartz, R. A., Krucker, S., et al. 2003, *ApJ*, 595, L77
- Hurford, G. J., Schmahl, E. J., Schwartz, R. A., et al. 2002, *Sol. Phys.*, 210, 61
- Ishikawa, S., Watanabe, S., Aono, H., et al. 2008, in *Nuclear Science Symposium Conference Record, 2008. NSS'08. IEEE, IEEE*, 440–443
- Ishikawa, S., Saito, S., Tajima, H., et al. 2011, *IEEE Transactions on Nuclear Science*, 58, 2039
- Jackson, J. D. 1962, *Classical Electrodynamics* (New York: Wiley)
- Janesick, J., & Putnam, G. 2003, *Annual Review of Nuclear and Particle Science*, 53, 263
- Jiang, Y. C., Chen, H. D., Li, K. J., Shen, Y. D., & Yang, L. H. 2007, *A&A*, 469, 331
- Kane, S. R., McTiernan, J., Loran, J., et al. 1992, *ApJ*, 390, 687
- Kerdraon, A., & Delouis, J.-M. 1997, in *Lecture Notes in Physics*, Berlin Springer Verlag, Vol. 483, *Coronal Physics from Radio and Space Observations*, ed. G. Trottet, 192
- Kim, Y.-H., Moon, Y.-J., Park, Y.-D., et al. 2007, *PASJ*, 59, 763
- Kirkpatrick, P., & Baez, A. V. 1948, *Journal of the Optical Society of America* (1917-1983), 38, 766
- Klimchuk, J. A. 2001, in *Washington DC American Geophysical Union Geophysical Monograph Series*, Vol. 125, 143
- Knoll, G. F. 2000, *Radiation detection and measurement* (Wiley, USA)
- Kokubun, M., Nakazawa, K., Enoto, T., et al. 2010, in *Society of Photo-Optical Instrumentation Engineers (SPIE) Conference Series*, Vol. 7732
- Kopp, R. A., & Pneuman, G. W. 1976, *Sol. Phys.*, 50, 85
- Krucker, S., & Benz, A. O. 1998, *ApJ*, 501, L213
- Krucker, S., Benz, A. O., Bastian, T. S., & Acton, L. W. 1997, *ApJ*, 488, 499
- Krucker, S., Hudson, H. S., Glesener, L., et al. 2010, *ApJ*, 714, 1108
- Krucker, S., Kontar, E. P., Christe, S., Glesener, L., & Lin, R. P. 2011a, *ApJ*, 742, 82
- Krucker, S., & Lin, R. P. 2002, *Sol. Phys.*, 210, 229
- . 2008, *ApJ*, 673, 1181
- Krucker, S., Saint-Hilaire, P., Christe, S., et al. 2008a, *ApJ*, 681, 644
- Krucker, S., White, S. M., & Lin, R. P. 2007, *ApJ*, 669, L49
- Krucker, S., Battaglia, M., Cargill, P. J., et al. 2008b, *A&A Rev.*, 16, 155
- Krucker, S., Christe, S., Glesener, L., et al. 2011b, in *Society of Photo-Optical Instrumentation Engineers (SPIE) Conference Series*, Vol. 8147
- Kumar, A., & Rust, D. M. 1996, *J. Geophys. Res.*, 101, 15667
- Landi, E., Raymond, J. C., Miralles, M. P., & Hara, H. 2010, *ApJ*, 711, 75
- Lee, J.-Y., Raymond, J. C., Ko, Y.-K., & Kim, K.-S. 2009, *ApJ*, 692, 1271
- Lemen, J. R., Title, A. M., Akin, D. J., et al. 2012, *Sol. Phys.*, 275, 17
- Lin, R., Caspi, A., Krucker, S., et al. 2010, *National Academies Solar and Heliophysics*

- Decadal Survey White Papers  
Lin, R. P. 1974, *Space Sci. Rev.*, 16, 189  
— . 2011, *Space Sci. Rev.*, 159, 421  
Lin, R. P., Dennis, B. R., Hurford, G. J., et al. 2002, *Sol. Phys.*, 210, 3  
Lin, R. P., Krucker, S., Caspi, A., et al. 2011, in *AAS/Solar Physics Division Abstracts #42*, 2204  
Liu, W., Petrosian, V., Dennis, B. R., & Jiang, Y. W. 2008, *ApJ*, 676, 704  
McTiernan, J. M. 2009, *ApJ*, 697, 94  
Messmer, P., Benz, A. O., & Monstein, C. 1999, *Sol. Phys.*, 187, 335  
Miceli, M., Reale, F., Gburek, S., et al. 2012, *A&A*, 544, A139  
Mozer, F. S., Bale, S. D., & Phan, T. D. 2002, *Physical Review Letters*, 89, 015002  
NASA/SRP. 2005, *NASA Sounding Rocket Program Handbook (NASA)*  
Neupert, W. M. 1968, *ApJ*, 153, L59  
Nitta, N. V., Mason, G. M., Wiedenbeck, M. E., et al. 2008, *ApJ*, 675, L125  
Øieroset, M., Phan, T. D., Fujimoto, M., Lin, R. P., & Lepping, R. P. 2001, *Nature*, 412, 414  
Parker, E. N. 1957, *J. Geophys. Res.*, 62, 509  
— . 1963, *ApJS*, 8, 177  
— . 1972, *ApJ*, 174, 499  
— . 1983, *ApJ*, 264, 642  
— . 1988, *ApJ*, 330, 474  
Parnell, C. E., & Jupp, P. E. 2000, *ApJ*, 529, 554  
Peterson, L. E., Schwartz, D. A., Pelling, R. M., & McKenzie, D. 1966, *J. Geophys. Res.*, 71, 5778  
Petrosian, V., & Liu, S. 2004, *ApJ*, 610, 550  
Petschek, H. E. 1964, *NASA Special Publication*, 50, 425  
Phillips, K. 1995, *Guide to the Sun* (Cambridge University Press)  
Phillips, K. J. H., Chifor, C., & Landi, E. 2005, *ApJ*, 626, 1110  
Pulupa, M. P., Bale, S. D., & Kasper, J. C. 2010, *Journal of Geophysical Research (Space Physics)*, 115, 4106  
Ramsey, B. D. 2005, *Experimental Astronomy*, 20, 85  
Ramsey, B. D., Elsner, R. F., Engelhaupt, D., et al. 2004, in *Society of Photo-Optical Instrumentation Engineers (SPIE) Conference Series*, ed. O. Citterio & S. L. O'Dell, Vol. 5168, 129–135  
Ramsey, B. D., Alexander, C. D., Apple, J. A., et al. 2002, *ApJ*, 568, 432  
Raulin, J. P., Kundu, M. R., Hudson, H. S., Nitta, N., & Raoult, A. 1996, *A&A*, 306, 299  
Raymond, J. C., Krucker, S., Lin, R. P., & Petrosian, V. 2012, *Space Sci. Rev.*, 47  
Reeves, K. K., & Golub, L. 2011, *ApJ*, 727, L52  
Riley, P., & McComas, D. J. 2009, *Journal of Geophysical Research (Space Physics)*, 114, 9102  
Roy, J. R. 1973, *Sol. Phys.*, 28, 95  
Saint-Hilaire, P., Krucker, S., Christe, S., & Lin, R. P. 2009, *ApJ*, 696, 941

- Saint-Hilaire, P., Krucker, S., & Lin, R. P. 2008, *Sol. Phys.*, 250, 53  
— . 2010, *ApJ*, 721, 1933
- Saito, S. 2011, Master's thesis, University of Tokyo, Tokyo
- Saito, S., Ishikawa, S.-N., Watanabe, S., et al. 2010, in *Society of Photo-Optical Instrumentation Engineers (SPIE) Conference Series*, Vol. 7732
- Savcheva, A., Cirtain, J., Deluca, E. E., et al. 2007, *PASJ*, 59, 771
- Schmahl, E. J., Pernak, R. L., Hurford, G. J., Lee, J., & Bong, S. 2007, *Sol. Phys.*, 240, 241
- Schmelz, J. T., Jenkins, B. S., Worley, B. T., et al. 2011, *ApJ*, 731, 49
- Schmelz, J. T., Kashyap, V. L., Saar, S. H., et al. 2009, *ApJ*, 704, 863
- Schwartz, D. A., David, L. P., Donnelly, R. H., et al. 2000, in *Society of Photo-Optical Instrumentation Engineers (SPIE) Conference Series*, ed. J. E. Truemper & B. Aschenbach, Vol. 4012, 28–40
- Schwartz, R. A., Csillaghy, A., Tolbert, A. K., et al. 2002, *Sol. Phys.*, 210, 165
- Sellin, P., Davies, A., Lohstroh, A., Ozsan, M., & Parkin, J. 2005, *Nuclear Science, IEEE Transactions on*, 52, 3074
- Servagent, N. 2007, *Semiconductor sensors and applications: Fundamentals of Semiconductor physics (SCIRN-PRN - Universit du Maine)*
- Shibata, K., & Magara, T. 2011, *Living Reviews in Solar Physics*, 8, 6
- Shibata, K., Nozawa, S., & Matsumoto, R. 1992a, *PASJ*, 44, 265
- Shibata, K., Shimojo, M., Yokoyama, T., & Ohyama, M. 1997, in *Astronomical Society of the Pacific Conference Series*, Vol. 111, *Magnetic Reconnection in the Solar Atmosphere*, ed. R. D. Bentley & J. T. Mariska, 29
- Shibata, K., Tajima, T., Steinolfson, R. S., & Matsumoto, R. 1989, *ApJ*, 345, 584
- Shibata, K., Ishido, Y., Acton, L. W., et al. 1992b, *PASJ*, 44, L173
- Shih, A. Y., Lin, R. P., Hurford, G. J., et al. 2012, in *Society of Photo-Optical Instrumentation Engineers (SPIE) Conference Series*, Vol. 8443
- Shimizu, T. 1995, *PASJ*, 47, 251
- Shimojo, M., Hashimoto, S., Shibata, K., et al. 1996, *PASJ*, 48, 123
- Smith, D. M., Lin, R. P., Turin, P., et al. 2002, *Sol. Phys.*, 210, 33
- Somov, B. V., & Kosugi, T. 1997, *ApJ*, 485, 859
- Space Studies Board, A., Space Engineering Board, D. o. E., on a Decadal Strategy for Solar, P. S. N. R. C. C., & (Heliophysics), S. P. 2012, *Solar and Space Physics: A Science for a Technological Society (The National Academies Press)*
- Spieler, H. 2005, *Semiconductor detector systems*, Vol. 12 (Oxford University Press, USA)
- Spitzak, B., et al. 1998, *FLTK: Fast light toolkit*. Available: <http://www.ftk.org/>.
- Sturrock, P. A. 1966, *Nature*, 211, 695
- Sui, L., & Holman, G. D. 2003, *ApJ*, 596, L251
- Sweet, P. A. 1958, in *IAU Symposium*, Vol. 6, *Electromagnetic Phenomena in Cosmical Physics*, ed. B. Lehnert, 123
- Sylwester, J., Kowalinski, M., Gburek, S., et al. 2012, *ApJ*, 751, 111
- Tajima, H., Nakamoto, T., Tanaka, T., et al. 2004, *IEEE Transactions on Nuclear Science*, 51, 842

- Takeda, S., Takahashi, T., Watanabe, S., et al. 2008, SPIE Newsroom
- Tandberg-Hanssen, E., & Emslie, A. G. 1988, *The physics of solar flares* (Cambridge and New York, Cambridge University Press)
- Tsuneta, S., & Naito, T. 1998, *ApJ*, 495, L67
- Veronig, A. M., & Brown, J. C. 2004, *ApJ*, 603, L117
- Viatour, L. 2006, <http://www.lucnix.be/main.php>
- Wang, Y.-M., Pick, M., & Mason, G. M. 2006, *ApJ*, 639, 495
- Warren, H. P., Brooks, D. H., & Winebarger, A. R. 2011, *The Astrophysical Journal*, 734, 90
- Wilkinson, D. 1950, *Proceedings of the Cambridge Philosophical Society*, Cambridge, England, 46
- Windt, D. L. 1998, *Computers in Physics*, 12, 360
- Withbroe, G. L., & Noyes, R. W. 1977, *ARA&A*, 15, 363
- Wolter, H. 1951a, *Annalen der Physik*, 444, 65
- . 1951b, *Annalen der Physik*, 444, 57
- Yokoyama, T., & Shibata, K. 1996, *PASJ*, 48, 353
- Zimovets, I., Vilmer, N., Chian, A. C.-L., Sharykin, I., & Struminsky, A. 2012, *A&A*, 547, A6
- Zweibel, E. G., & Yamada, M. 2009, *ARA&A*, 47, 291